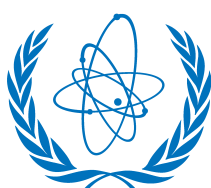# ATOMIC AND PLASMA–MATERIAL INTERACTION DATA FOR FUSION

## VOLUME 13

**IAEA**
International Atomic Energy Agency

# IAEA SAFETY RELATED PUBLICATIONS

## IAEA SAFETY STANDARDS

Under the terms of Article III of its Statute, the IAEA is authorized to establish or adopt standards of safety for protection of health and minimization of danger to life and property, and to provide for the application of these standards.

The publications by means of which the IAEA establishes standards are issued in the **IAEA Safety Standards Series**. This series covers nuclear safety, radiation safety, transport safety and waste safety, and also general safety (i.e. all these areas of safety). The publication categories in the series are **Safety Fundamentals, Safety Requirements** and **Safety Guides**.

Safety standards are coded according to their coverage: nuclear safety (NS), radiation safety (RS), transport safety (TS), waste safety (WS) and general safety (GS).

Information on the IAEA's safety standards programme is available at the IAEA Internet site

http://www-ns.iaea.org/standards/

The site provides the texts in English of published and draft safety standards. The texts of safety standards issued in Arabic, Chinese, French, Russian and Spanish, the IAEA Safety Glossary and a status report for safety standards under development are also available. For further information, please contact the IAEA at P.O. Box 100, A-1400 Vienna, Austria.

All users of IAEA safety standards are invited to inform the IAEA of experience in their use (e.g. as a basis for national regulations, for safety reviews and for training courses) for the purpose of ensuring that they continue to meet users' needs. Information may be provided via the IAEA Internet site or by post, as above, or by e-mail to Official.Mail@iaea.org.

## OTHER SAFETY RELATED PUBLICATIONS

The IAEA provides for the application of the standards and, under the terms of Articles III and VIII.C of its Statute, makes available and fosters the exchange of information relating to peaceful nuclear activities and serves as an intermediary among its Member States for this purpose.

Reports on safety and protection in nuclear activities are issued in other publications series, in particular the **Safety Reports Series**. Safety Reports provide practical examples and detailed methods that can be used in support of the safety standards. Other IAEA series of safety related publications are the **Provision for the Application of Safety Standards Series**, the **Radiological Assessment Reports Series** and the International Nuclear Safety Group's **INSAG Series**. The IAEA also issues reports on radiological accidents and other special publications.

Safety related publications are also issued in the **Technical Reports Series**, the **IAEA-TECDOC Series**, the **Training Course Series** and the **IAEA Services Series**, and as **Practical Radiation Safety Manuals** and **Practical Radiation Technical Manuals**. Security related publications are issued in the **IAEA Nuclear Security Series**.

# ATOMIC AND PLASMA–MATERIAL INTERACTION DATA FOR FUSION

## VOLUME 13

INTERNATIONAL ATOMIC ENERGY AGENCY
VIENNA, 2007

The volumes of ATOMIC AND PLASMA–MATERIAL INERACTION DATA FOR FUSION are published by the International Atomic Energy normally once a year.

For these volumes, papers, letters and reviews are accepted which deal with the following topics:

— Elementary collision processes in fusion plasmas involving photons, electrons, ions, atoms and molecules;
— Collision processes of plasma particles with surfaces of fusion relevant materials;
— Plasma-material interaction phenomena, including the thermophysical response of materials.

Each submitted contribution should contain fusion relevant data and information in either of the above areas. Original contributions should provide new data, using well established methods. Review articles should give a critical analysis or evaluation of a wider range of data. They are normally prepared on the invitation by the Editor or on prior mutual consent. Each submitted contribution is assessed by two independent referees.

Every manuscript submitted must be accompanied by a *disclaimer* stating that the paper has not been published and is not being considered for publication elsewhere. If no copyright is claimed by the authors, the IAEA automatically owns the copyright of the paper.

Manuscripts and correspondence should be addressed to: The Editor, ATOMIC AND PLASMA–MATERIAL INERACTION DATA FOR FUSION, International Atomic Energy Agency, Wagramer Strasse 5, P.O. Box 100, 1400 Vienna, Austria.

# COPYRIGHT NOTICE

# Foreword

Plasmas generated in fusion energy research cover a wide range of conditions involving electron temperature, electron density and plasma constituents, as well as electric and magnetic fields. Performing diagnostics on such plasmas is a complex problem requiring many different types of atomic and molecular (A+M) data. The typical plasmas in fusion research naturally divide into a core region and an edge/divertor region, and the physical conditions differ significantly between these two regions.

There is a need to use soft X-ray spectroscopy as well as optical spectroscopy for diagnostics in the core region. This requires information on the emission properties of the plasma under the core conditions. Information about several different processes for atomic species relevant to the plasma is needed in this process. Some data can be measured directly in experimental devices such as the electron beam ion trap (EBIT). This type of measurement would prove very useful in furthering databases for plasma diagnostics of core regions. Heating beams are used to raise the core temperature and doped beams are used for diagnostic purposes. Thus, beam spectroscopy is an important consideration in the core region. Radiation from impurities in the edge region is very important in understanding the formation of advanced discharge regimes (transport barriers).

Temperatures are significantly lower in the edge/divertor region and there is a relatively high population of neutral species. Molecules will also form in this region, requiring extensive data on a variety of molecular processes for diagnostic procedures. Processes such as charge exchange will also be important for diagnostic purposes in the edge — data needed for diagnostics include radiative as well as collision processes. Collision processes include both electron and heavy particle collisions.

The importance of generating new data for support of diagnostics in fusion plasmas led to a strong recommendation at the 12th meeting of the A+M Subcommittee of the International Fusion Research Council in May 2000 to initiate a Coordinated Research Project (CRP) to address data needs in this area. The Atomic and Molecular Data Unit of the International Atomic Energy Agency initiated the CRP on "Atomic and Molecular Data for Fusion Plasma Diagnostics" in 2001. Results from this CRP will be incorporated into the A+M Data Unit databases and will be available through the worldwide-web for global access by researchers. These data will be of interest not only for direct fusion applications, but in other research plasma studies used in accelerators, environmental research and other fields.

The work of the CRP was completed in 2005. During the course of the Coordinated Research Project, new data were generated for a variety of processes impacting on a number of diagnostic procedures for fusion plasmas:

spectral observations near the strike zone and divertor (where alpha particles interact with molecules) require a variety of cross-section data that have been measured and calculated during the current work programme;

helium beam diagnostics from fast to thermal require cross-section data for both electron and proton impact, that have been generated during the current work programme;

data have been produced for use in the determination of species from light elements such as helium, boron and hydrocarbons, as well as heavy elements such as tungsten;

large amounts of data on spectral properties were generated to assist in the spectral analysis of plasma emissions;

X-ray emissions from impact on surfaces have been studied and quantified;

data have been generated for use in hydrogen charge exchange spectroscopy for the determination of the flow and temperature of impurities in the divertor region.

The CRP on "Atomic and molecular data for plasma diagnosis" has been very successful in meeting all of the objectives established at the beginning of the project. The present volume of *Atomic and Plasma–Material Interaction Data for Fusion* represents the results of the co-ordinated efforts of leading experimental and theoretical groups.

The IAEA takes this opportunity to acknowledge the CRP participants for their dedicated efforts and contribution to this volume.

# Contents

# Feasibility studies of a charge exchange recombination diagnostic for measurement of impurity flows in the divertor of the DIII–D tokamak

*N.H. Brooks[1], N.S. Wolf[2], W.P. West[1], S. Loch[2], M.O. Mullane[4], R.E. Olson[5], T.E. Evans[1], R.L. Boivin[1]*

[1] General Atomics, San Diego, California, USA

[2] Lawrence Livermore National Laboratory, Livermore, California, USA

[3] Auburn University, Auburn, Alabama, USA

[4] University of Strathclyde, Glasgow, Scotland, UK

[5] University of Missouri-Rolla, Rolla, Missouri, USA

## Abstract

Charge exchange recombination, a well-established technique for measuring impurity flows and ion temperature in the core of tokamak plasmas, was evaluated for measuring the same plasma parameters in the divertor region of the DIII–D tokamak. Because divertor temperatures are typically much lower than those in the core, different charge exchange reaction processes must be considered. A combination of experimental measurements and code modeling were carried out to quantify the expected signal-to-background ratio. In conclusion, it was determined that a divertor charge exchange recombination diagnostic is not feasible, even employing lock-in detection methods to extract a beam-modulated signal from background radiation at the same wavelength.

## 1. Introduction

The use of charge exchange recombination (CER) spectroscopy for measuring impurity flows in the divertor of a tokamak was evaluated through a combination of experimental measurements and code modeling. Basic atomic physics calculations played a central role in the modeling: rate coefficients from the ADAS database [1] were employed for assessing the background emission from the thermal background plasma, and Monte Carlo trajectory (CTMC) calculations [2] were used for estimating the state-selective CER emission in the path of a diagnostic neutral beam.

Fluid-flow models of the scrape-off layer and divertor regions of tokamak plasmas predict complicated two-dimensional flow patterns, with some regions of the divertor exhibiting flow away from the target plate (reverse flow) under some conditions. To have confidence in the extrapolation of modeling results to ITER-like divertor conditions, fluid codes such as the LLNL's UEDGE need to be validated in current devices against experimental measurements of impurity flow velocity, $V$, and ion temperature, $T_i$ in current devices. CER has been proposed as a means to obtain $V$ and $T_i$ near the elevation of the divertor X-point, with the

centimeter-scale spatial resolution necessary to map the strong spatial gradients predicted in the flow patterns.

CER spectroscopy is a well-established technique for measuring radial profiles of $V$, $T_i$ and $n_i$ in the core of tokamak plasmas. Initial work in the field focused on the measurement of impurity densities in the hot core of tokamaks by detection in the ultraviolet of the prompt $\Delta n = 1$ decay of the daughter ions arising from charge exchange of fast neutral beam atoms with fully stripped, low-$Z$ impurities [3]; successful observation of the visible transitions emitted by daughter ions in excited levels with high $n$-values [4] opened the possibility for measurement of spectral profiles with optical multichannel detectors and high resolution spectrometers; the simplicity of imaging and transmitting visible radiation led to widespread use of CER spectroscopy for deduction of core temperature and velocity profiles on tokamaks equipped with fast neutral, heating beams [5]. More recently, diagnostic beams of small cross-section [6] have enabled similar measurements on fusion devices which do not employ fast neutral beams for auxiliary plasma heating.

In Section 2, the successes and limitations of passive spectroscopic measurements are reviewed. Candidate

impurities for active CER measurements are discussed in Section 3, the physical layout of the proposed CER diagnostic for DIII–D is described in Section 4, and anticipated signal-to-background ratios are presented in Section 5. Techniques to deal with low signal to background are given in Section 6. The prospects for success in such a measurement are reviewed in Section 7.

## 2. Passive spectroscopic measurements

Passive spectroscopic techniques have been used successfully to measure temperatures and flow velocities of impurity ions in the DIII–D divertor [7–9]. One notable success of this effort was the confirmation of an elongated region of reverse flow predicted by the UEDGE fluid model. However, the impurity species accessible by visible spectroscopy are limited to low charge states generally concentrated near the divertor targets. Though thermal charge exchange (CX) was successfully used to access the He-like ion of carbon, its CX line was measurable only when deuterium gas was puffed so strongly that both divertor legs detached [10].

As shown in Fig. 1, passive spectrometer measurements of divertor flow rely on line-integrated measurements along quasi-tangential viewchords. When viewed in projection on a poloidal cross section of the MHD flux configuration, the straight line paths appear as hyperbolas. Because the emission from a specific impurity ion is usually localized to a thin sheet defined by contours of constant electron temperature, the passive measurement, though line-integrated, often yields a velocity for a rather well-defined location. The Doppler width and shift of a spectral line are obtained from the measured line shape by least square fitting to a theoretical profile based on the nonlinear, Zeeman/Paschen-Bach magnetic splitting. Passive spectroscopic measurements have been performed on DIII–D with electron
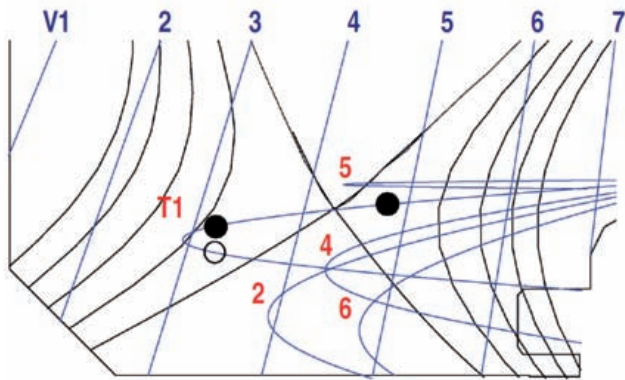
impact-excited lines between 4000 and 9000 Å from the $D^0$, $C^0$, $C^+$, $B^+$ and $C^{2+}$ ions.

Thermal CX of deuterium (in the excited $n = 2$ state) with $C^{4+}$ has also been measured under atypical conditions. The solid black circles along chord T1 in Fig. 1 represent the positions of the $C^{4+}$ flows when strong gas puffing causes detachment of both divertor legs. The magnetic field inferred from the magnetic splitting of each of these velocity components gives the major radius of its emission zone.

Fig. 2 shows the measured line C IV (7–6) line profile in both vertical and tangential views when the intensity of this otherwise weak line is dramatically increased by thermal CX processes. Since the vertical view (left box) is normal to the flow direction along the nearly toroidal magnetic field lines in the divertor, the fit to the profile in this view provides a fiducial for the rest wavelength of the line. In the quasi-tangential view (right box), the central pi-component of each $\Delta\ell = 1$ transition is suppressed, giving rise to a multi-peaked envelope for the individual, Doppler-broadened features comprising the ensemble of magnetically split $\Delta\ell = 1$ transitions. Here, the measured C IV line profile is fit to a linear superposition of two theoretical C IV line profiles, with $T_i$, $V_i$ and magnetic field B treated as independent fitting parameters for each profile. Though the wavelength shifts for the separate emission sources in inner and outer legs are opposite (inner leg is red-shifted, outer leg is blue-shifted), the impurity ion flow is toward the divertor target in both cases, due to the continuous helical path of the open field lines connecting inner and outer divertor targets.

## 3. Candidate impurities for active CER

Active CX offers a means to detect the dominant ion in the divertor and to measure its temperature $T_i$ and flow velocity $V$ in the vicinity of the X-point. Through a combination of modeling [11,12] and measurement, the most promising impurity elements and charge states were identified: for lithium and beryllium, these are the fully stripped ions; for boron and carbon, the He-like charge states. Injected lithium has been ruled out for CER measurements, because an experiment conducted on DIII–D revealed that its CX lines overlap those of intrinsic boron. Beryllium was rejected, because of the onerous safety requirements associated with use of this toxic material. Additionally, its CX lines overlap those of intrinsic carbon. Boron and carbon are already present in DIII–D: the former due to its periodic deposition as a thin surface film to getter oxygen and control wall recycling of deuterium [13]; the latter as the graphite armor which forms the plasma-facing wall. By puffing their dust into the SOL continuously, the abundance of the non-recycling impurities boron and carbon can potentially be enhanced in the divertor without raising core concentrations significantly.

The spatial distributions of the He-like charge states of boron and carbon are shown in Fig. 3 for a UEDGE code



**Figure 1.** Design of the DIII–D lower divertor showing vertical and quasi-tangential views together with an outline of a separatrix. The solid circles are the locations where C IV flows have been measured from the 7726 Å feature (see Fig. 2).
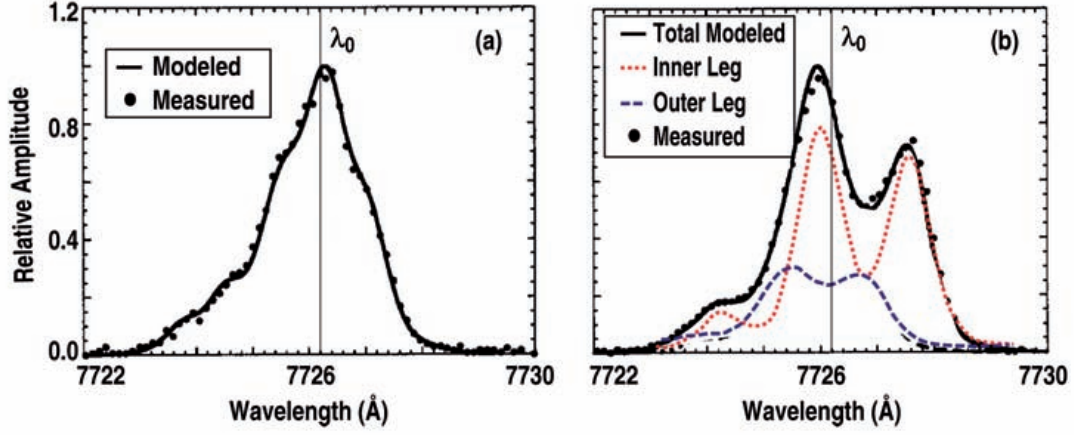
**Figure 2.** (a) Fitted spectrum of the 7726 Å feature observed along view V4 (see Fig. 1 [10]). (b) Fitted spectrum for the quasi-tangential view T1 showing both red- and blue-shifted components.
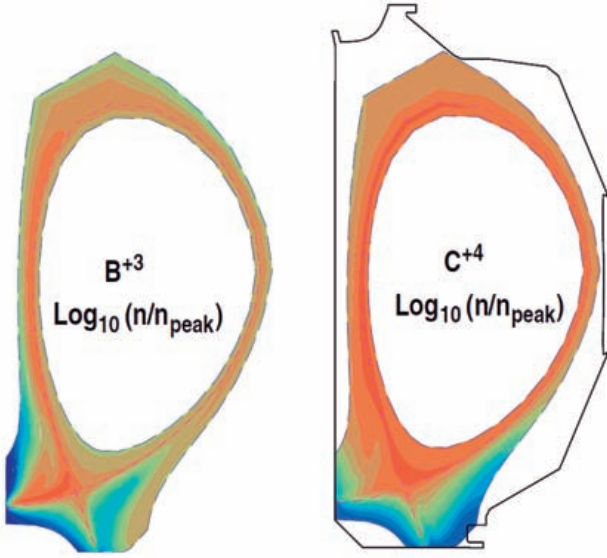


**Figure 3.** Normalized density distributions of the He-like ions of boron and carbon displayed with red corresponding to the peak value, blue to ~$10^{-5}$ of the peak value.

calculation with $P_{beam}$ = 1.5 MW, $\langle n_e \rangle = 10^{13}$, and $B_t$ = 2.0 T. For these particular low-$Z$ atoms, the He-like charge state is the dominant impurity in the vicinity of the X-point. Candidate CER reactions of these impurity ions with a hydrogen diagnostic beam are listed in Table I, along with the visible emission lines associated with the prompt $\Delta n = 1$ decay of the excited, Li-like daughter species. Wavelengths for reactions with the fully stripped $Li^{+3}$ and $Be^{+4}$ are also shown. On DIII–D, the lines of B and C were found to be free of spectral contamination from other, close-lying lines. The C IV (7–6) transition can be easily seen in the path of the DIII–D neutral heating beams as its crosses the scrape-off layer at the outer midplane. Signal-to-background ratio for the CER signal at this location is typically 1:1.

It should be noted that high spectral resolution and multichannel spectral detection is required to fit the CER lines from Li-like daughter ions, because of their asymmetric, multi-bumped profile. The complex profile is the result of a large wavelength separation between the multiple $\Delta\ell = 1$ transitions comprising a given $\Delta n = 1$ transition in the Li-like ions. This situation is in sharp contrast to that of H-like daughter ions, such as $Li^{2+}$ and $Be^{3+}$, where the separation associated with different $\Delta\ell = 1$ transitions is much smaller than the magnetic splitting. For H-like daughter ions, the spectral profile of the CER line formed by the envelope of the Doppler-broadened, magnetic components is symmetric. In the case of symmetric line profiles, Doppler shifts can be measured with a system comprised of just two detectors outfitted with sawtooth – shaped, spectral transmission filters [14]. Concentrating all the light on just two spot detectors dramatically reduces photon statistical noise and permits the full power of lock-in detection to be realized.

## 4. Physical layout of the proposed divertor CER system

The feasibility of mounting a Russian diagnostic neutral beam manufactured by the Budker Institute in the DIII–D Machine Hall was demonstrated for the oblique orientation shown in Fig. 4. A hydrogen diagnostic beam with the highest energy current available from Budker Institute (55 keV/amu) was chosen. A deuterium beam was ruled out because the 2x higher mass of deuterium isotope entails a significant penalty in beam penetration efficiency. A desired spatial resolution of 1 cm in the radial direction limits the beam cross section, and thereby, the beam neutral current to 2 A for the currently available, long pulse rf sources. The Budker diagnostics beam is capable of modulation at 500 Hz. As described later, synchronous detection of the CER signal at the modulation frequency was a key element of the proposed system. The PixelVision

**Table I.** Charge Exchange Reactions for Various Low-Z Impurities of the Ionic Charge States Dominant in the Divertor Region

| Candidate CX Processes | State-Selective from Daughter Ion | Visible | Emission |
|---|---|---|---|
| | $(n - n')$ | $\lambda(Å)$ | $\sigma(10^{-18} \text{ cm}^2)^{(a)}$ |
| $Li^{3+} + H^0 \Rightarrow (Li^{2+})^* + H^+$ | (5–4) | 4499 | 6.0 |
| | (6–5) | 8282 | 2.2 |
| $Be^{4+} + H^0 \Rightarrow (Be^{3+})^* + H^+$ | (6–5) | 4659 | 8.8 |
| | (7–6) | 7226 | 3.0 |
| $B^{3+} + H^0 \Rightarrow (B^{2+})^* + H^+$ | (5–4) | 4498, 4487 | 6.0 |
| | (6–5) | 8284, 8262 | 2.2 |
| $C^{4+} + H^0 \Rightarrow (C^{3+})^* + H^+$ | (6–5) | 4660 | 8.8 |
| | (7–6) | 7726 | 3.0 |

(a) For 55 keV $H^0(n=1)$ [2].
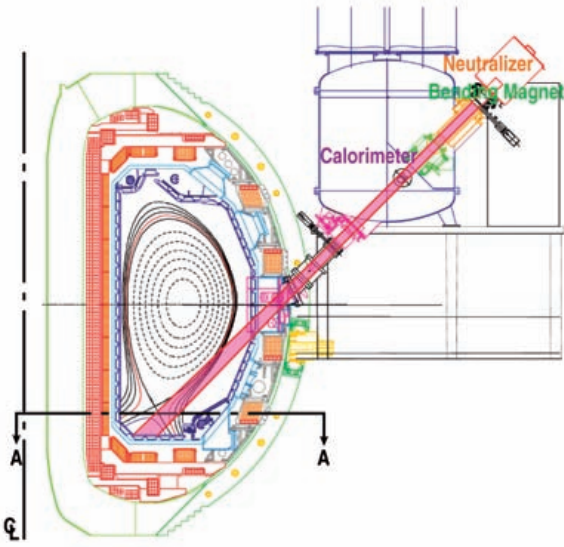


**Figure 4.** Installation layout for a Budker diagnostics beam injector firing into the DIII–D divertor.

camera employed in the core CER systems on DIII–D [15] is capable of 1 kHz framing rate; its use on a high throughput, high resolution spectrometer would permit capturing the CER spectral profile during each ON and OFF phase of the modulated diagnostics beam.

The crossed geometry of tangential view cone and injected beam shown in Fig. 5 defines a limited path length from which CER emission is collected. Background radiation from electron impact excitation is collected from the entire path of the viewchord through the divertor plasma; CER signal is present only in the short segment where viewchord and beam intersect.

Spatial resolution is set by the excursion in major radius of the tangential chord in spanning the diameter of the neutral beam. The magnetic field is specified by the average major radius of the viewchord across this span. In contrast with passive spectroscopy, where multiple emission zones along the viewchord may contribute to the spectral profile

and their locations in radius must be distinguished by fitting the measured profile to one or more line profiles with magnetic field as a free parameter, active CER spectroscopy provides a single emission zone at a well-defined location.

## 5. Signal-to-background ratio

A low signal-to-background ratio is the central challenge facing CER measurements in the divertor. This is the result of a spatially extended region of cool plasma in the divertor: it gives rise to background emission by electron impact excitation of the daughter charge state (and dielectronic recombination to the daughter charge state) which is much larger than that typical for core CER measurements. Fig. 6 compares the contribution to the divertor background emission from electron impact excitation of the daughter state and thermal CER from the parent state. These results were obtained by evaluating the atomic physics rates [1] over the 2-D map of divertor plasma parameters output by a UEDGE fluid modeling code. Note that electron impact excitation of the Li-like ion constitutes the dominant background emission everywhere except the region immediately in front of the inner divertor strike point.

Measurement of the C IV (7–6) transition in the path of a DIII–D heating beam at the vessel midplane shows a CER signal-to-background ratio of rough unity; in the divertor, the signal-to-background ratio can be expected to be much lower. Divertor modeling calculations of the C IV CER signal, combined with measurements of the background signal in the divertor, predict a signal-to-background ratio in the range $10^{-2}$ to $10^{-3}$.

Model calculations of the expected CER signal were performed for the oblique injection shown in Fig. 4. Fig. 7 is a plot of the predicted attenuation of the beam versus vertical distance below the vessel midplane, together with the anticipated CER signal in tangential view. Also plotted are the local plasma values of $n_e$ and $T_e$ given by the UEDGE model. The case illustrated here, as seen in the insert left, is
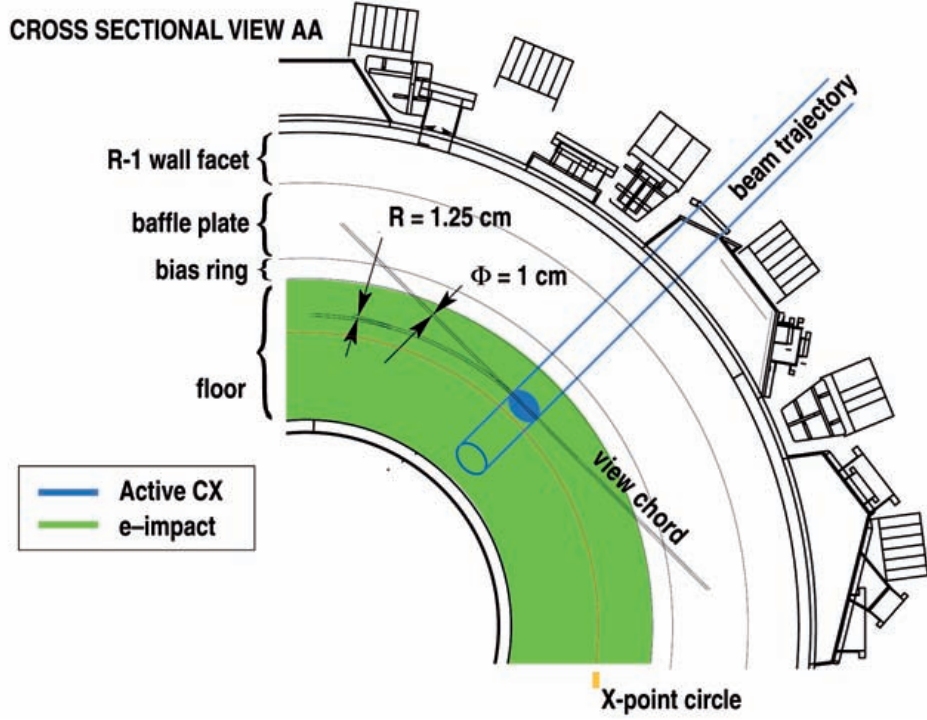
**Figure 5.** Plan view of the crossed geometry between downward-injected beam and horizontal, tangential viewchord.
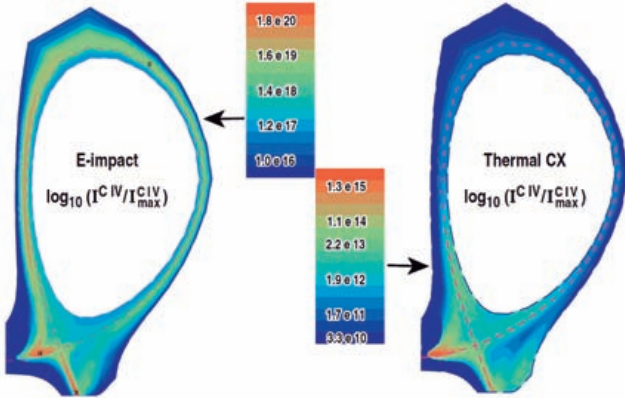


**Figure 6.** Relative intensities of the background C IV (7–6) emission from electron impact of $C^{3+}$ and thermal CX with $C^{4+}$ shown with displaced color scales spanning over nine decades in intensity.

injection just inboard of the divertor X-point. In the insert right, the figure is rotated 90 deg, so that its $Z$-axis is horizontal, making more intuitive the relationship between the beam path and the horizontal axis of the plot box. Since the beam crosses the core plasma's pedestal en route to the divertor, less than 25% of the beam neutrals survive to CX in the area of interest. Nevertheless, the relative peak in the CER signal comes from the divertor region, because of the dominant He-like charge state of carbon.

In the model calculation shown in Fig. 7, attenuation of the hydrogen beam results from the processes listed below, namely, impact ionization arising from collisions with electrons and deuterons, as well as CX with deuterons and fully stripped carbon.

$$
\begin{aligned}
H^0_{beam} + e &\Rightarrow p + 2e \\
H^0_{beam} + p &\Rightarrow p + p + e \\
H^0_{beam} + p &\Rightarrow p + H^0 \\
H^0_{beam} + C^{6+} &\Rightarrow p + \left(C^{5+}\right)^*.
\end{aligned}
$$
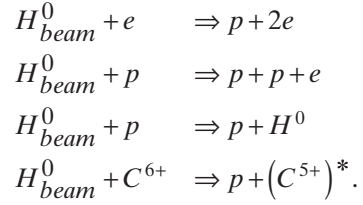
The beam loss $\Delta n$ in a distance $\Delta s$ along the 1-D path is calculated using Eq. (1) below

$$
\Delta n_{beam} = n_{beam} \sum_i n \; X_i \; \Delta s + n^*_{beam} \sum_i n \; X^*_i \Delta s \quad (1)
$$

where $n_{beam}$ is the surviving beam density, $X_i$ are the rate coefficients for beam atom loss by electron impact ionization, proton impact ionization, and charge transfer with protons and fully stripped carbon ions, and $n$ is electron density, proton density or fully stripped carbon density, as appropriate for the loss process. Rate coefficients for proton impact ionization and charge transfer are calculated by simply multiplying cross section by the beam velocity. The second term on the right represents beam loss resulting from interaction with atoms in the $n = 2$ excited level. At 55 keV, beam neutrals excited into the $n = 2$ level make a negligible contribution to the total loss rate.

5
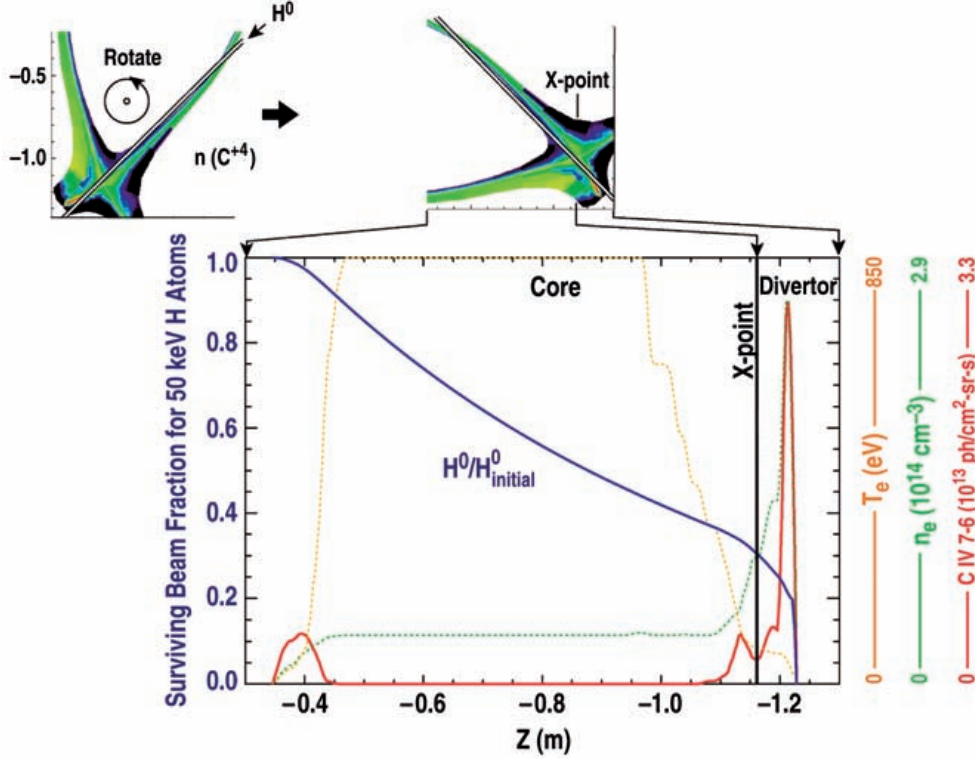
**Figure 7.** Plot of beam attenuation $H^0/H^0_{initial}$ and C IV (7–6) CER signal versus vessel elevation $Z$, along with the local values of $n_e$ and $T_e$ of the UEDGE target plasma. The color inserts show the beam path superposed on the UEDGE solution for the $C^{4+}$ density distribution.

The calculated CER signal is based on CTMC calculations for 40 keV atoms [2] — since the cross section peaks between 40 and 50 keV, the value at 55 keV should be similar. The predicted CER signal is compared with the measured background along tangential chords on DIII–D during a shot with similar parameters: specifically, the L–mode period preceding the high gas puffing phase in which the thermal CX profile in Fig. 2 was measured. The ratio of signal to background, so derived, is a little less than $10^2$. To detect a signal so deeply buried in the background requires special techniques.

## 6. Techniques for extracting small signals from the background

Digital lock-in techniques utilizing a modulated diagnostic beam were evaluated for extracting a weak signal from a strong background. The Budker diagnostic beam is capable of square wave modulation at frequencies up to 500 Hz. By synchronizing a PixelVison CCD camera with 1 kHz framing rate to the ON/OFF phases of the modulated beam, lock-in detection of the weak CER signal may be accomplished by post processing of the digital data recorded every millisecond. For an analysis time long compared with the beam modulation period (2 ms), the difference between the camera framing data summed over the beam ON periods and those summed over the OFF periods comprises a measure of the CER signal at the modulation frequency with a frequency bandwidth equal to the reciprocal of the analysis time. Such a summation is readily executed using a correlation function with values of +1 and –1, respectively, for the ON and OFF phases of the beam. Shifting the CER measurement from zero frequency to 500 Hz by the digital lock-in method described above improves the signal-to-background ratio, if the power spectrum of the background light has an inverse frequency dependence.

More sophisticated conditional averaging techniques can also be applied to the digitally recorded data. For example, in ELMing discharges, the correlation function may be zeroed during phases containing ELMs to extract an average value of $T_i$ and $V$ between ELMs, and vice versa. The result of applying such digital lock-in techniques yields the value of $T_i$ and $V$, time-averaged over the number of ON/OFF pulses used in the correlation function. A balance must be struck between choosing an analysis time long enough to give a good signal-to-noise ratio, yet short enough to ensure that steady plasma conditions obtain. ELMing H-mode, QH-mode and stochastic edge plasmas are examples of operating regimes with relatively long periods of steady conditions.

Fig. 8 illustrates the deviation during ELMing H-mode of the plasma's inherent noise frequency spectrum from that of white noise. Comparing the normalized power spectrum of the chord-integrated B III line (the background signal for a CER measurement) in ELMing H-mode and ELM-free H-mode, a broad secondary peak is visible at the ELM frequency. If this frequency is close to the beam modulation
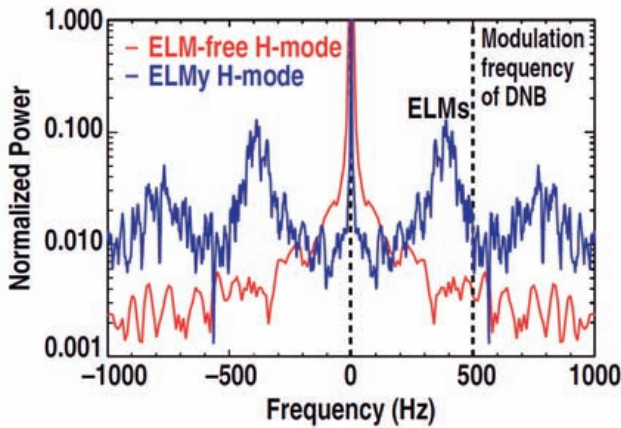
**Figure 8.** Normalized power spectrum of the B III emission signal in the DIII–D divertor for ELMy and ELM-free H-modes.

frequency, little benefit is gained by displacing the CER signal measurement from zero frequency to that of the beam modulation. Though this plot makes ELM-free H-mode look like a more suitable candidate for lock-in detection, one should not be misled. Plasma density rises uncontrollably during ELM-free H-mode reducing the appropriate duration for time-averaging while increasing attenuation of the diagnostic beam which reaches the X-point region.

## 7. Assessment of feasibility

An estimate of the minimum signal-to-background ratio for which the photon noise on an individual spectral resolution element exceeds the signal-to-noise requirement for decent least-squares line-fitting has been derived for a lock-in analysis interval of 1 s. This approach relies on (1) a calculation of component efficiencies for a realistic system extending from the collection telescope inside vacuum all the way to a CCD detector on the spectrometer, and (2) the ACX source intensity based on CTML cross sections and UEDGE model calculations of plasma parameters. If the background is ten times the signal, the measurement is doable. If background is one hundred times the signal, photon noise alone prevents success. If micro-instabilities in the divertor contribute more noise at the modulation frequency than photon statistics, the signal-to-background ratio must be higher for the diagnostic to succeed. Our current estimate of signal-to-background is roughly 1:100. Based on this fact, a decision was made that a divertor CX diagnostic is not feasible on DIII–D employing the He-like charge states of boron or carbon as the target for the CX reaction.

As stated earlier, the high resolution required to fit the asymmetric line profiles of the $\Delta\ell = 1$ transition ensemble from Li-like ions leads to low signal on each pixel of the detector array. If fully stripped lithium or beryllium were usable as a target ion — as would be the case in a boron-free machine with a lithium first wall or a carbon-free machine with beryllium first wall — the outlook would be much more favorable, because a Doppler shift, at least, can be measured with the light split between only two detectors. Unfortunately, neither lithium nor beryllium is a realistic candidate for use on DIII–D.

## Acknowledgment

## References

[1] LOCH, S., Auburn University, O'MULLANE, M., University of Strathclyde, private communication.

[2] OLSON, R.E., University of Missouri at Rolla, private communication.

[3] ISLER, R.C., MURRAY, L.E., KASAI, S., DUNLAP, J.L., BATES, S.C., EDMONDS, P.H., LAZARUS, E.A., MA, C.H., MURAKAMI, M., Phys. Rev. Lett. **24** (1981) 2701.

[4] FONCK, R.J., GOLDSTON, R.J., KAITA, R., POST, D.E., Appl. Phys. Lett. **42** (1983) 239.

[5] GROEBNER, R.J., BROOKS, N.H., BURRELL, K.H., ROTTLER, L., Appl. Phys. Lett. **43** (1983) 920; ISLER, R.C., Plasma Phys. Contr. Fusion **36** (1994) 171-208.

[6] IVANOV, A.A., et al., Rev. Sci. Instrum. **71** (2000) 10.

[7] ISLER, R.C., BROOKS, N.H., WEST, W.P., LEONARD, A.W., McKEE, G.R., Phys. Plasmas **6** (1999) 541.

[8] ISLER, R.C., BROOKS, N.H., WEST, W.P., LEONARD, A.W., McKEE, G.R., PORTER, G.D., J. Nucl. Mater. **266-269** (1999) 376.

[9] ISLER, R.C., et al., Phys. Plasmas **6** (1999) 1837.

[10] ZANIOL, B., et al., Phys. Plasmas **8** (2001) 4386.

[11] PORTER, G.D., et al., Phys. Plasmas **7** (2000) 3663.

[12] EVANS, T.E., FINKENTHAL, D.F., FENSTERMACHER, M.E., LEONARD, A.W., PORTER, G.D., WEST, W.P., J. Nucl. Mater. **266-269** (1999) 1034.

[13] HOLTROP, K.L., JACKSON, G.L., KELLMAN, A.G., LEE, R.L., WEST, W.P., WOOD, R.D., WHYTE, D.G., "Characterization of Wall Conditions in DIII–D," J. Vac. Sci. Technol. A (1997) 678.

[14] PAUL, S., "A high-speed optical diagnostic for measuring Doppler shift using interference filters," 15th High Temperature Plasma Diagnostics Conf., San Diego, California, 2004, to be published in Rev. Sci. Instrum.

[15] GOHIL, P., BURRELL, K.H., GROEBNER, R.J., SERAYDARIAN, R.P., Rev. Sci. Instrum. **61** (1990) 2949.

# Charge exchange data for alpha particles interacting with atoms and molecules

*R. Hoekstra[1], D. Bodewits[1], S. Knoop[1], R. Morgenstern[1], L. Méndez[2], L.F. Errea[2], C. Illescas[2], A. Macías[2], B. Pons[2#], A. Riera[2], F. Aumayr[3], HP. Winter[3]*

[1] KVI Atomic Physics, Rijksuniversiteit Groningen, Zernikelaan 25, NL 9747 AA Groningen, Netherlands

[2] Laboratorio Asociado al CIEMAT de Física Atómica y Molecular en Plasmas de Fusión, Departamento de Química, Universidad Autónoma, Cantoblanco, 28049 Madrid, Spain

[3] Institut für Allgemeine Physik, Technische Universität Wien, Wiedner Hauptstrasse 8-10, A-1040 Vienna, Austria

## Abstract

We have reviewed the status of charge exchange data for collisions between slow (impact energy below 1 a.u. = 25 keV/amu) alpha particles and some selected atoms and molecules. Because at low energies charge transfer between alpha particles and atomic hydrogen turns out to have a negligibly small cross section, low-abundant neutral atomic and molecular species with large cross section can be of great relevance for the charge state distribution of helium ions in colder plasma regions. Gaps or inconsistencies in the data are found, particularly at the lower energies (E = 1 keV/amu).

## 1. Introduction

Helium "ash" is one of the end products of the D-T fusion reactions in future burning fusion plasmas and will constitute an important issue for various reasons. Inside the hot plasma core an intense flux of newly born fast alpha particles may possibly give rise to plasma instabilities. Moreover, the He influx increases $Z_{eff}$, the mean plasma ion charge which is of direct relevance for bremsstrahlung loss. Rapid He removal will be needed to keep the He concentration at a sufficiently low level. On the other hand, alpha particles which have been slowed-down by elastic collisions into the cooler outer plasma boundary can recombine along various pathways into excited $He^+$ and $He^0$ states and thus contribute to radiative cooling [1]. The latter helps to accommodate the large power flux from the inner plasma onto the first wall and the divertor target plates. In addition, radiative cooling modifies plasma density and temperature profiles in the plasma edge which are important for plasma transport. Strong gradients in these profiles can induce socalled internal transport barriers (ITP) which have been shown to strongly improve the overall plasma confinement.

In view of this rather complex scenario it is evident that a satisfactory understanding of the transport behaviour and charge balance of neutral and ionized He in the plasma boundary is highly desirable. Near the first wall a relevant fraction of neutral atoms and molecules which are being desorbed and sputtered from the material boundary is available for charge exchange (CX - electron capture) reactions with the alpha particles and heavier impurity ions. Such CX reactions involve sizeable cross sections [2] and can therefore play a rather important role.

Radiation from excited states produced by CX has recently also been found responsible for far-UV and X-ray emission from comets and other astrophysical objects [3-5].

In order to understand and assess the particular role of CX in connection with alpha particles, a sufficient knowledge of respective cross sections is necessary. In this paper we review the status of charge exchange data for alpha particles interacting with atoms and molecules. It is attempted to add to the figures with the data compilations a

---

# Permanent address: CELIA, Université de Bordeaux I, 351, Cours de Libération, 33405 Talence CEDEX, France

curve representing our cross section recommendation based on the presently available data. Otherwise, uncertainties and unresolved issues will be described. Throughout the report there will be extensive referring to original papers. Nevertheless it is realized that the list of references will be far from complete. A table of papers on charge transfer by alpha particles giving energy ranges, methods, and kind of results can be found on the webpages of the IAP Vienna (http://www.iap.tuwien.ac.at/www/atomic/cxdatabase/).

The key charge exchange process is in most alpha-neutral systems, single-electron capture (SEC), which can be represented as:

$$He^{2+} + B \rightarrow He^{+}(nl) + B^{+}$$
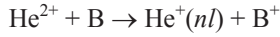
with B the neutral target gas that acts as electron donor and *nl* the principal and angular momentum quantum numbers of the state into which the electron is captured. Apart from SEC, bound-double electron capture (BDC)

$$He^{2+} + B \rightarrow He^{0}(nln'l') + B^{2+}$$
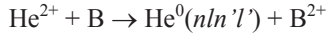
and transfer ionization (TI)

$$He^{2+} + B \rightarrow He^{+}(nl) + B^{2+} + e$$

are charge transfer processes that can occur too. The final outcome of the TI reaction, i.e., a singly charged helium ion, a doubly charged target ion and a free electron can in principle also result from autoionizing double-electron capture (ADC) or innershell capture followed by target autoionization. The latter process is unlikely to happen at energies far below 25 keV/amu. As doubly-excited helium states are much weaker bound than the initial binding energy of the two least bound target electrons, ADC is expected to be of relevance only at higher collision energies. It should be noted that in many experiments on total charge exchange, the socalled charge-changing experiments only the charge state of the projectiles is determined. Therefore in this kind of experiments contributions from TI are included in the present charge-changing cross sections.

Electron capture processes have been studied by a whole variety of experimental techniques: charge-state analysis in crossed-beam, gas cell, ion guide, and merged beam configurations, Translational Energy Spectroscopy (TES), Photon Emission Spectroscopy (PES), and Recoil Ion Momentum Spectroscopy (RIMS) using either supersonic target beams or laser-cooled targets.

TES, PES and RIMS give access to state selective charge transfer cross sections. In PES experiments the photon emission subsequent to charge transfer into an excited state is measured. In this way line emission cross sections ($\sigma_{nl-n'l'}$) are obtained. In TES experiments the energy gained or lost by the projectile ion is determined while in RIMS the recoil momentum of the target is

determined. The energy gain or loss by the projectile ion and the component of target recoil momentum along the ion beam axis, can be related to the difference in electronic binding energy before and after the interaction. Because of the hydrogen-like nature of the He$^{+}$ ions (cf. Fig. 1) these methods can only produce *n*-shell selective capture cross sections ($\sigma_n$).

For single-electron capture, the total cross sections is linked to TES and PES data as follows:

$$\sigma_{sec} = \Sigma\, \sigma_n \text{ or } \sigma_{sec} = \Sigma\, \sigma_{np-1s} + \sigma_1 + \sigma(2s)$$

which can also be used for consistency checks between different data sets. Here $\sigma(2s)$ represents the metastable *2s* population cross section. The 2s state can be populated by direct capture and it can also accumulate population via *np* $\rightarrow$ *2s* transitions, see Fig. 1. The only unknown is the direct electron capture contribution $\sigma_{2s}$ to $\sigma(2s)$ because $\sigma_1$ is known from the TES experiments and the *np* $\rightarrow$ *2s* contributions to $\sigma_{2s}$ can be calculated from the corresponding *np* $\rightarrow$ *2s* transitions via their respective branching ratios. For example $\sigma_{3p-2s}$ is equal to $(0.12/0.88)\, \sigma_{3p-1s}$, see Fig. 1.

At several keV/amu energy, a (near) statistical distribution over the angular momenta is a common feature of one-electron capture by multicharged ions (see e.g. [2,6]) and therefore it presents another consistency check between PES and TES data.

Theoretical treatment of electron capture in ion-atom collision at energies below ~25 keV/amu is carried out by employing close-coupling expansions in terms of molecular or atomic wave functions (see e.g. [2,6,7]). For energies E > 50 eV/amu, a semiclassical treatment is applied, and a quantal description for lower energies. Although the methods are well-established, the applications are in general scarce for many-electron systems, because of the difficulty
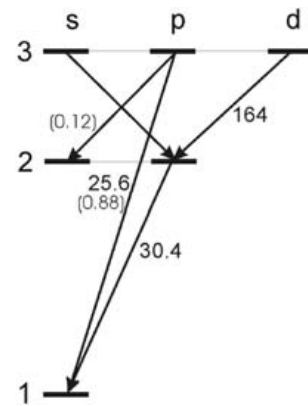


**Figure 1.** Part of the HeII decay scheme, indicated are the wavelengths (in nm) of the relevant transitions. The numbers in brackets refer to the branching ratios.

of evaluating the atomic or molecular wave functions. At impact energies larger than the maximum of the electron capture cross section, ionization starts to be sizeable and pseudostates are added to the basis to describe the ionization continuum. The definition of these pseudo-states has been considered in many works, but again the applications are restricted to one-electron systems. In the region near the maximum of the total electron capture cross section, classical (CTMC) methods [8] have been also applied, although, at these relatively low energies, an improved initial distribution [9] is required to accurately evaluate electron capture cross sections (see [10]).

The description of electron capture in ion- molecule collisions cannot be carried out by simply extending the methods applied to ion-atom collisions because of the presence of internal molecular motions. The simplest approach, useful in general at high impact energies, is the Franck-Condon (FC) approximation, where the internuclear distances of the molecule are kept fixed at their equilibrium values. More sophisticated treatments employ the sudden approximation for rotation and vibration [11,12], or only for rotation, as in the so-called IOSA method [13]. However, these methods have not been applied to $He^{2+}$ -molecule collisions, as a consequence of the complexity of the calculation of three-centre electronic wavefunctions for these systems. For example (see [14]), in $He^{2+}$ + $H_2$ collisions, and for infinitely separated subsystems, the energy of the entrance channel lies above that of $He^+(1s)$ + $H_2^{2+}$ + $e^-$, which is the limit of the two Rydberg series $He(1snl)$ + $H_2^{2+}$, and $He^+(1s)$ + $H_2^+(n\lambda)$, but these Rydberg series cannot be completely removed from the basis set (e.g. using block-diagonalization techniques [15]), since BDC to $He(1s2l)$ and $He(1s3l)$, as well as dissociative single electron capture to $He^+(1s)$ + $H_2^+(n\lambda)$ are important processes. Besides, states correlated to $He^+(n=2)$ + $H_2^+$ $(1\sigma_g)$

are higher in energy than the entrance channel and must also be included in the dynamical basis set, since these states are the main products of the electron capture at E > 2keV/amu.

## 2. Charge exchange data for alpha particles

As charge transfer at low impact energy proceeds in a (near-) resonant manner a simple "resonant" charge transfer model as the over-the-barrier model (e.g. [16]) can be used to get an idea about the final states which are most likely populated. From the over-the-barrier model one derives for single-electron capture the following relation between the resonant, final binding energy and the ionization potential, $I_{pot}$, of the electron donor:

$$E_{final} = 1.26\ I_{pot}$$

Table 1 summarizes the estimations for the final binding energies for collisions of $He^{2+}$ on the electron donor species discussed in this paper.

From the comparison with the actual binding energies of the n-shells in $He^+$ it is clear that except for the alkali and metastable targets one expects the $He^+(n = 2)$ shell to be predominantly populated. Except for the alkalis it is seen that there is a considerable mismatch between resonant final binding energies and actual state energies in $He^+$. From this one may expect that cross sections for SEC decrease with decreasing collision energy.

### 2.1. Atomic electron donors

#### 2.1.1. $He^{2+}$ - H

As it constitutes a real, asymmetric three-particle problem, the interaction of alpha particles with atomic hydrogen is the benchmark system of charge-transfer theory.

**Table 1.** Estimates based on the over-the-barrier model of final binding energies in one-electron capture in collisions of alpha particles on neutral targets.

| Target | $I_{pot}$ (eV) | $E_{final}$ (eV) | Target | $I_{pot}$ (eV) | $E_{final}$ (eV) | $E_{binding}$ He$^+$(n) (eV) | |
|--------|--------|--------|--------|--------|--------|--------|--------|
| H | 13.6 | 17.1 | K | 4.3 | 5.4 | n = 1 | 54.4 |
| He | 24.6 | 31.0 | H(n=2) | 3.4 | 4.3 | n = 2 | 13.6 |
| O | 13.6 | 17.1 | $H_2$ | 16.1 | 20.3 | n = 3 | 6.0 |
| Ne | 21.6 | 27.2 | CO | 13.7 | 17.3 | n = 4 | 3.4 |
| Li | 5.4 | 6.8 | $CH_4$ | 12.5 | 15.8 | n = 5 | 2.2 |
| Na | 5.1 | 6.4 | $H_2O$ | 13.6 | 17.1 | n = 6 | 1.5 |

A whole arsenal of approaches has been applied, e.g. [17-33]. In general there is excellent agreement (10%) between the different calculated cross sections for SEC.

Based on the wealth of data, recommended cross sections have been assessed and presented in the ORNL Redbook [34] and in the IAEA "Atomic and Plasma-Material Interaction Data for Fusion" [35] series. At energies above 1 keV/amu, there are only very minor differences between the two data sets. At lower energies the data sets start to deviate. The IAEA data are larger than the ORNL one by a factor of ~2.5 at 0.1 keV/amu. Here the IAEA data follow the theoretical results of van Hemert *et al.* [23], which were found to be in close agreement with PES measurements at energies above 0.2 keV/amu [36]. The IAEA data set is shown in Fig. 2 on both a logarithmic and a linear scale to illustrate the general behaviour of SEC cross sections. At that time no SEC cross sections were given for energies below 0.1 keV/amu, but from the energy trend they are likely to be very small ($\ll 10^{-18}$ cm$^2$).

At lower energies, a quantal treatment is required. Besides the early calculation of van Hemert *et al.* [23], the system has been considered recently by employing reaction coordinates (hyperspherical close-coupling and common reaction-coordinate approaches) [37,38], and the hidden crossings approach [39], leading to accurate values of the SEC cross sections at very low collision energies. These theories predict the SEC cross section to decrease by 10 orders of magnitude when only reducing the energy from 0.1 keV/amu to 0.01 keV/amu. Based on the recent calculations [37-39] it is proposed to adapt the IAEA recommended curve as depicted in Fig. 2. The fact that at energies below 0.1 keV/amu charge transfer between He$^{2+}$- H is basically

inhibited implies that even small amounts of other neutral constituents in the divertor and edge plasma may determine the rate at which alpha particles charge exchange.

At E > 25 keV/amu, where ionization starts to be sizeable, CTMC [10] and close coupling calculations including pseudostates have been carried out. In particular, several works have considered electron capture in He$^{2+}$-H collisions as a benchmark system to test the definition of these pseudostates. For example, one-centre atomic expansions have been enlarged by means of the basis set generator method of [40]. Two-centre pseudostates have been applied in Refs. [41, 42], and three-centre expansions in [26]. A similar approach in the framework of the molecular method has been applied in [43], where the molecular basis was enlarged by adding Gaussian functions centered on an intermediate point of the internuclear axis. Good general agreement is found between different approaches also at high impact energies. There seems to be no reason to change the earlier recommendations. In addition the fundamental data have been used successfully in modelling beam emission spectroscopy and charge exchange spectroscopy observations based on D heating beams [44].

### 2.1.2. He$^{2+}$ - He

Fig. 3 shows the 1990 recommended data from the ORNL Redbook [34] for SEC and BDC in collisions of 50 eV/amu to 20 keV/amu alpha particles on He. While the SEC cross section decreases at lower energies, BDC increases gradually. This is basically a manifestation of the symmetric resonance nature of two-electron capture in the He$^{2+}$- He system, first pointed out by Lichten [45] and then
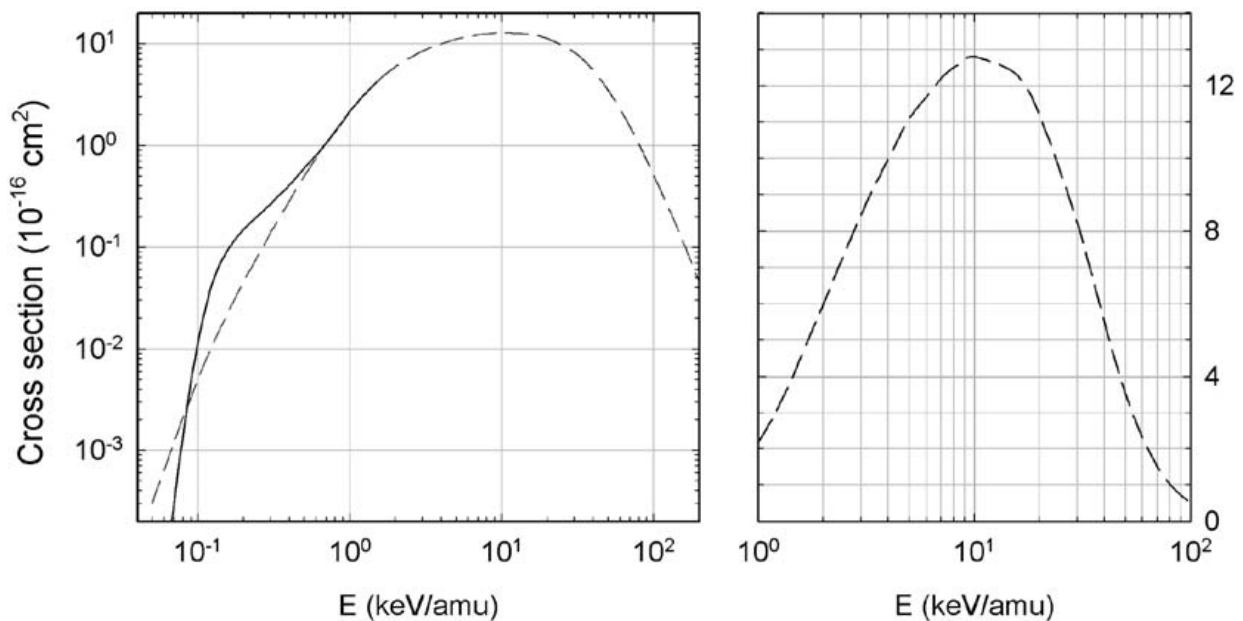


**Figure 2.** Recommended (– – – Janev and Smith [35]) single electron capture cross sections for He$^{2+}$ - H collisions on a logarithmic (left panel) and linear (right panel) cross section scale. Present recommendation: ————.

confirmed by molecular calculations [46-48]. More recent theoretical [49] and experimental [50] work seem not to support the acclaimed estimated accuracy of 20% of the Redbook recommendation.

### 2.1.3. $He^{2+}$ - Li

In connection to the use of keV Li beams for plasma-edge diagnostics [51-53], a lot of work has been done on electron, proton and multiply charged ion impact on Li. The status of inelastic cross sections for particle interactions with Li has been reviewed in detail [51,55]. Based on data for a variety of ions, Wutte *et al.* [51] have given a recommended cross section expression for SEC by multiply charged ions. The data for alphas are in excellent agreement with their recommendation.

On the level of state selective cross sections it is seen that the n = 3 level is dominantly populated (e.g. [56-61]) in line with the aforementioned estimate based on a simple over-the-barrier picture. Comparing state selective TES

[60,62] and PES [56,58,63] data with theoretical predictions ([57,62]) very good agreement is found.

### 2.1.4. $He^{2+}$- O

Because of the difficulty of producing dense atomic oxygen targets only two experiments have been performed with $He^{2+}$ ions interacting with atomic oxygen. As can be seen from Fig. 4 the available data are limited to energies of several keV/amu and higher.

Accidentally the ionization potential of atomic oxygen is the same as the ionization potential of atomic hydrogen (see Table 1), therefore one may be inclined to expect a similar cross sectional behavior of SEC for O as for H. However note that for O the maximum of the SEC cross section is found at somewhat higher energy and that it exceeds the one of H by approximately 50%. With decreasing energy, SEC on O seems to decrease much faster than on H, at 2 keV/amu the atomic oxygen cross section is already smaller than the one of H by a factor of 5-6. This may be due to flux drawn by BDC and TI, channels which
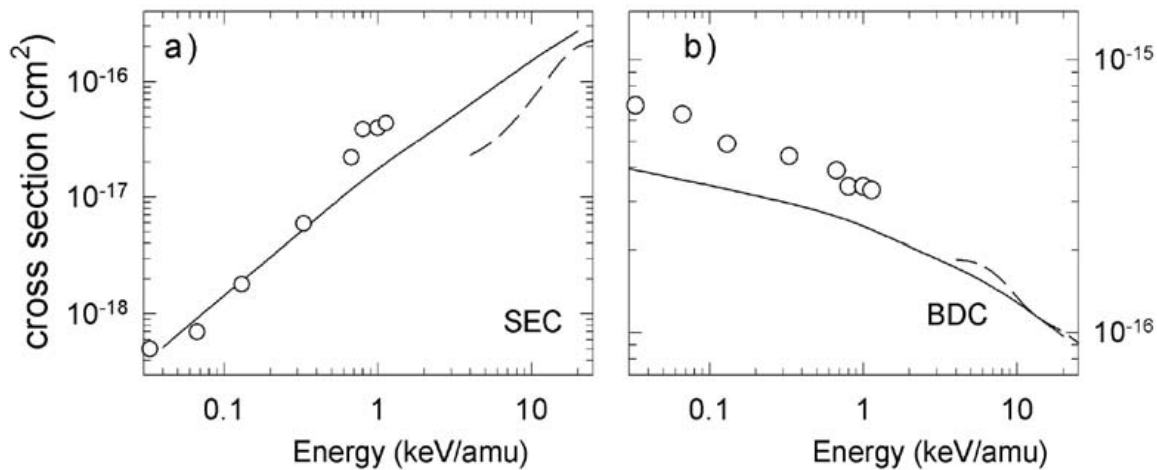


**Figure 3**. Electron capture cross sections for $He^{2+}$ - He collisions: a) SEC: ——— Redbook [34], – – – Fritsch [49], O - Okuno [50]. b) BDC as panel a).
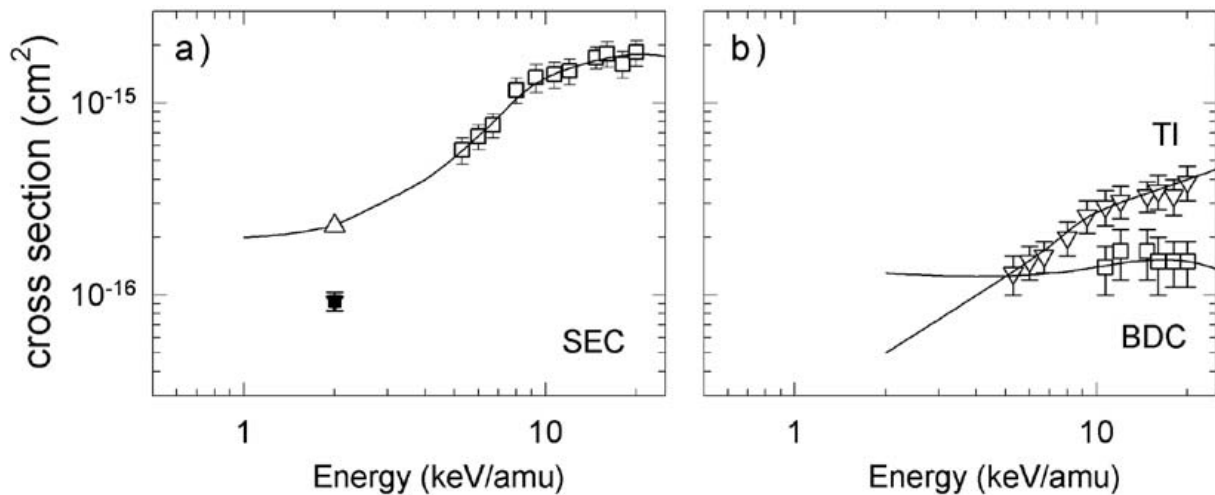


**Figure 4.** Electron capture cross sections for $He^{2+}$ - O collisions: a) SEC: □ - Thompson et al. [65], ■ - McCullough et al. [64], △ - McCullough et al. [64] renormalized by a factor of 2.5, b) BDC (□) and TI (▽) - Thompson et al. [65].
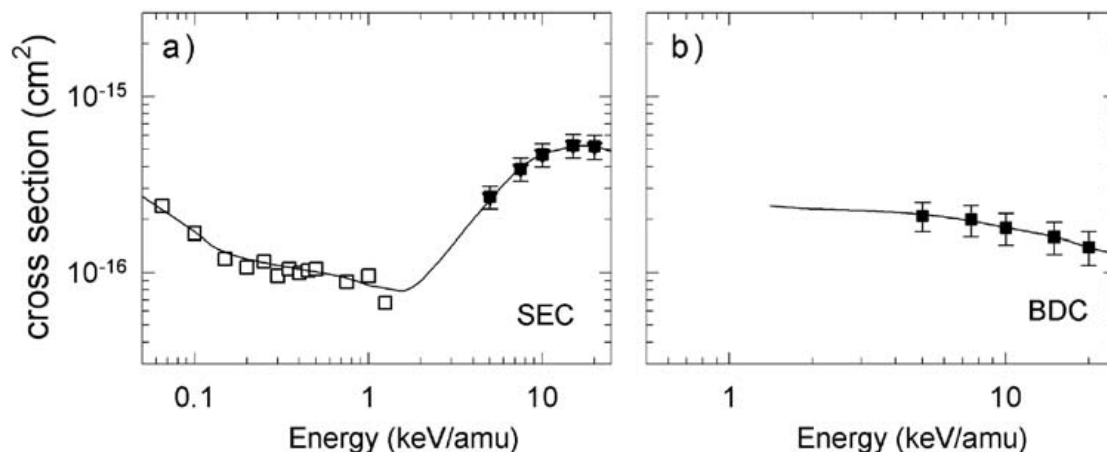
**Figure 5.** Electron capture cross sections for $He^{2+}$ - Ne collisions: a) SEC: □ - Abdelrahman et al. [67], ■ - Rudd et al. [66]. b) BDC as panel a) .

are non-existent in the case of atomic hydrogen. But, it is of note that the complementary measurement by McCullough *et al.* [64] on $O_2$ which is used as reference seems to be too low by a factor of ~2.5 (see section $He^{2+}$- $O_2$). Therefore it is proposed to renormalize the cross section given by McCullough *et al.* [64] by a factor of 2.5. This renormalized value is used for the determination of the preferred cross section curve.

Without further experimental or theoretical data it is hard to estimate whether the SEC cross section will continue to decrease with decreasing energy or whether it will first level off and then increase again at lower energy. Considering the cross sectional behavior of for example Ne and the heavier molecules the latter scenario seems most likely.

### 2.1.5. $He^{2+}$ - Ne

The data for $He^{2+}$ - Ne interactions are shown in Fig. 5. At energies going from 20 to 5 keV/amu the SEC cross sections decrease [66], in a manner similar to atomic hydrogen and oxygen. The measurements of Abdelrahman *et al.* [67], clearly show that this decrease stops at about 2 keV/amu, where the SEC cross section is reduced to just below $10^{-16}$ cm$^2$. At lower energies the cross section increases slowly, reaching again a value of $3\times10^{-16}$ cm$^2$ at 50 eV/amu.

The cross section for two-electron capture (BDC) seems to rise slowly with decreasing energy, although an extrapolation towards energies below a few keV/amu is rather uncertain.

### 2.1.6. $He^{2+}$ - Na

The $He^{2+}$ - Na(3s) system has been studied by a whole arsenal of experimental and theoretical methods: charge-changing measurements, both non-coincident [68] and coincident [69], Trans-lational Energy Spectroscopy [61,70], Photon Emission Spectroscopy [71-73], close

coupling techniques [61,74-76] and the Classical Trajectory Monte Carlo method [73,77].

As can be seen from Fig. 6, there is good agreement between theoretical and experimental data sets, except that at energies above 10 keV/amu the Sturmian-type AO calculations predict smaller cross sections [76]. From the comparison between the non-coincident and coincident data of DuBois and Toburen [68] and DuBois [69], respectively, it is clear that at least at energies below 25 keV/amu there is no significant contribution from transfer ionization to the single electron capture cross sections. Therefore, in assessing a "recommended" curve for total one-electron capture it was decided to follow the experimental data [61,68,69] and use a shape similar to the CTMC results [73,77]. This implies that the recommended curve exceeds the CTMC cross sections by approximately 15%.
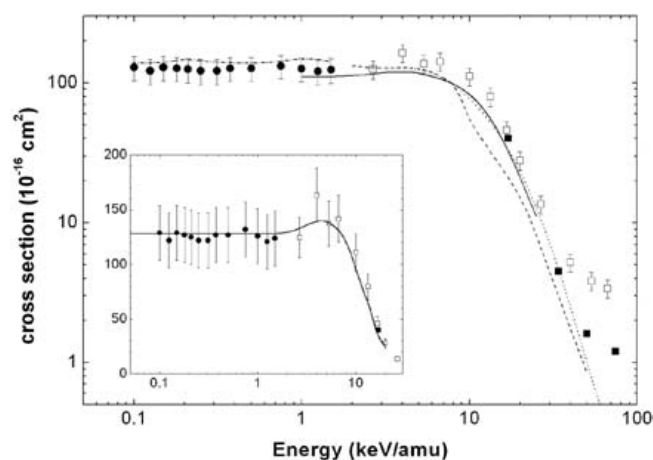


**Figure 6.** Single electron capture in $He^{2+}$ - Na: ● - Schweinzer and Winter [61], □ - DuBois and Toburen [68], ■ - DuBois [69], ——— Knoop et al. [77], – – – Jain and Winter [76], ·················· Shingal et al. [74], — · — · — Schweinzer and Winter [61]. Inset) ——— Recommended SEC cross section.

While for Li and K the SEC cross sections decrease at energies below 1 keV/amu, they remain constant for Na. For the low energies (0.05 – 1 keV/amu) we assume a constant cross section of $128 \times 10^{-16}$ cm$^2$. Although the ionization potentials of the alkalis differ only slightly, the difference in the cross sectional behavior at low energy between on the one hand Na and on the other hand Li and K can be understood on basis of the respective potential energy curves [61].

Because of the large binding energy difference between the 3s valence electron and the 2p$^6$ core electrons of Na BDC is much smaller than SEC [68].

### 2.1.7. He$^{2+}$- Ar

As Ar gas is often used to enhance radiative cooling, fractions of Ar may be present in the colder edge regions of the plasma (T = 1 keV). To our knowledge only experimental data exists at much higher energies (3.3 – 150 keV/amu) [66,78-80]. At the lowest energy of 3.3 keV/amu the SEC and BDC cross sections determined by Shah and Gilbody [78] amount to $7 \times 10^{-16}$ and $2.5 \times 10^{-16}$ cm$^2$, respectively. From the energy dependence it may be expected that the cross sections will decrease towards lower energy. However, considering the cross sectional behavior of for example Ne and the heavier molecules an increase at lower energy is just as likely. New data at energies well below 1 keV/amu are highly desirable.

### 2.1.8. He$^{2+}$ - K

The data depicted in Fig. 7 stem from the combined experimental and theoretical work of Schweinzer and Winter [61]. The cross sections for alphas colliding on K ($110 \times 10^{-16}$ cm$^2$) are slightly smaller than for collisions on Na ($\sim 130 \times 10^{-16}$ cm$^2$) and decrease at lower energy. The decrease towards lower energies is confirmed by Landau Zener type calculations (LZM, in Fig. 7) and atomic orbital expansion calculations with different basis sets (AO7 and AO13, in Fig. 7). At several keV energy, the cross sections seem well-predicted by the over-the-barrier model under assumption of a 50% transfer probability ($\sigma_{COM}$) [61].



**Figure 7.** Single electron capture in He$^{2+}$ - K: Both experimental and theoretical data are from Schweinzer and Winter [61], see text.

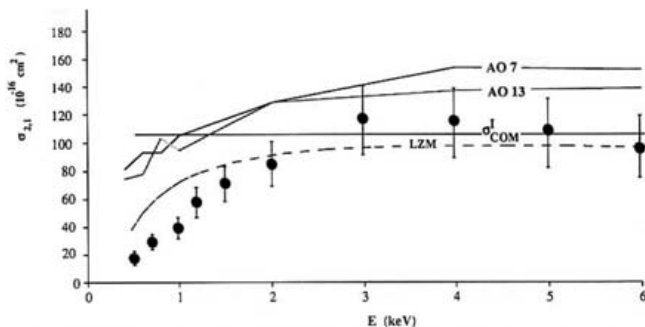In experiments on metastable He$^+$(2s) ion production in collisions of He$^{2+}$ on K, Shah and Gilbody [81] showed that in the energy range of 3.3 to 20 keV/amu, the SEC cross section decreases from approximately $130 \times 10^{-16}$ cm$^2$ to $20 \times 10^{-16}$ cm$^2$.

### 2.1.9. He$^{2+}$ - Metastable excited atoms

Neutral metastable particle densities are low as compared to ground state neutral densities. The metastable atoms of prime interest are H* in injected neutral beams and in the edge or divertor regions. He* is of direct relevance for charge exchange recombination spectroscopy (CXRS) based on He beams. The importance of metastable donors in CXRS on injected neutral beams stems from the fact that high-n levels, which radiate in the visible, can be populated directly (see e.g. [44,82]).

At scaled energies (collision energies multiplied by $4q^{-0.5}$ [35,83]) below 10 keV/amu, the cross section for SEC from H* (H(n = 2)) seems to be well approximated by $75q \times 10^{-16}$ cm$^2$. The scaling is primarily based on CTMC calculations [84] for B$^{5+}$ and Ne$^{10+}$. Specific CTMC calculations [82] for He$^{2+}$ yielded cross sections of $\sim 120 \times 10^{-16}$ cm$^2$ about 20% lower than the general expression deduced for multiply charged ions.

At energies between 2 and 6 keV/amu similar values of SEC cross sections are obtained by adiabatic promotion model [29] and close-coupling [85,86] calculations. However, these approaches predict the SEC cross section to decrease strongly at lower energies. At 0.5 keV/amu the cross section seems already to be reduced by a factor of 10 or more to approximately $\sim 10 \times 10^{-16}$ cm$^2$.

In addition a few calculations have been performed for metastable He* [49, 87-89].

Laboratory experiments on H* and He* are very unlikely to be performed in the near future, but one may get an idea about the cross sections by comparison to experimental data from alkali and excited alkali targets [83] which have similar ionization potentials as H* and He*. Some data on charge transfer from excited alkalis is available from TES and PES experiments (e.g. [66,86,87]).

## 2.2. Molecular electron donors

### 2.2.1. He$^{2+}$- H$_2$

Inelastic collisions of He$^{2+}$ with molecular hydrogen have attracted a lot of attention in connection with the modelling of He ash removal in the divertor region [1] because if it is readily neutralized it is no longer magnetically confined and it may diffuse back into the core plasma thereby deteriorating plasma properties. At NIFS (Japan), a lot of work has been done on cold recombining He plasmas produced by puffing neutral gasses into a He plasma [92-95]. A prompt and very strong HeI($1s3l \rightarrow 1s2l'$) line emission has been observed when H$_2$ was puffed into the He plasma, hinting at strong double-electron capture directly
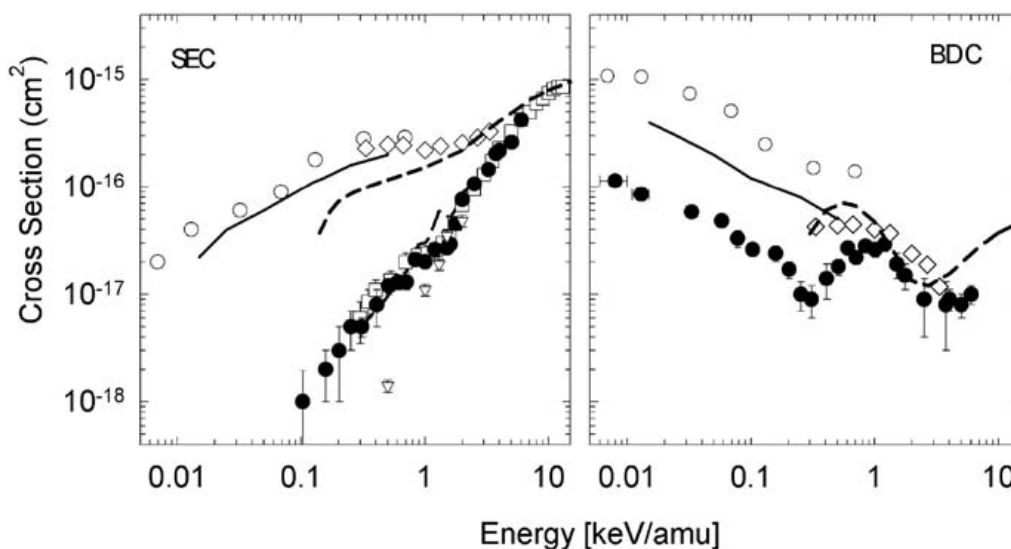
**Figure 8.** 2002 status of single and double electron capture in He$^{2+}$ - H$_2$. SEC: Total charge changing results: ○ - Okuno et al. [97], ◊ - Kusakabe et al. [98], ——— Shimakura et al. [99], – – – Redbook [34], TES data Hodgkinson et al [100]): ▽ - n=2; PES data 2p: ● - Juhász et al. [101], □ - Hoekstra et al. [36, 102]. BDC: As SEC panel except ● - 1s2p $^1$P [101].

into the He($1s3l$) states. However, in PES experiments no evidence for strong direct two-electron capture into the He($1s3l$) states is found [96].

In spite of the apparent simplicity of this system, not only state selective but also total cross sections for He$^{2+}$ - H$_2$ collisions are not well established, in particular not at energies relevant for edge and divertor plasma. This is illustrated in Fig. 8, which depicts the Redbook [34] evaluation of the SEC and BDC cross sections together with attenuation [98] and ion guide [97] measurements extending to lower energies. In addition it is of note that the TES data for capture into the He$^+$(n=2) shell fall below the PES data for He$^+$(2p).

At energies above several keV/amu, theoretical calculations [103-105] for state selective SEC are in good agreement with experiments [102,106]. One-electron model calculations [107] at energies below 1 keV/amu are in good accord with the He$^+$(2p) data of PES experiments (cf. Fig. 8). This is somewhat remarkable as at these energies TES experiments have shown that one-electron capture is completely dominated by dissociative SEC [100,108,109]. At these energies where dissociative charge transfer is the dominant process, large discrepancies between total cross sections from different experiments are noticeable, cf. Fig. 8.

Calculations have been carried out for SEC and BDC, where the H$_2$ molecule was approximated by two atoms with an average ionization potential [99]. Although the calculated BDC cross sections are smaller by a factor of 2-3, this calculation supports the results of Okuno et al. [97] at E < 1 keV/amu. BDC is predicted to proceed into the He($1s3l$) states which, as mentioned above, is not observed in PES

experiments [96]. Concerning SEC, the main output of the calculation is He$^+$($2l$) + H$_2^+$($1\sigma_g$). This is in contrast with experiments which show dissociative one-electron capture into He$^+$(1s) to dominate [100,108,109].

In recent Franck-Condon calculations, Errea *et al.* [110] used two methods to address the problem: A close-coupling expansion in terms of *ab initio* three-centre wavefunctions, which allowed to simultaneously describe dissociative and nondissociative SEC, and BDC, and a model potential approach using the independent particle model [111]. It yielded total SEC cross sections above the experimental values [110], but showing better agreement with the results of Kusakabe *et al.* [98] than with those of Nutt *et al.* [112], whose cross sections are probably too small [113], and therefore, further experimental work is required to determine total SEC cross sections.

The total SEC cross section of Nutt *et al.* [112] was used to normalize the experiment of Hodgkinson *et al.* [100], which is probably the explanation of the discrepancy illustrated in Fig. 9, where the cross section for population of He$^+$(2p) + H$_2^+$($1\sigma_g$) of Ref. [101] is larger (almost a factor of 10 at 500eV/amu) than the cross section for non-dissociative SEC; i.e. for formation of He$^+$($2l$) + H$_2^+$($1\sigma_g$) (renormalization of the TES data to the total cross sections of Okuno *et al.* [97] would reduce the difference to a factor of 2-3). Unfortunately, the calculation of Ref. [110] is not useful to support any experiment at low energy because of the limitation of the Franck-Condon approximation employed. In this respect, the calculation indicates that vibrational effects are sizeable at energies below 1 keV/amu, and therefore a large scale close-coupling vibronic calculation,

15
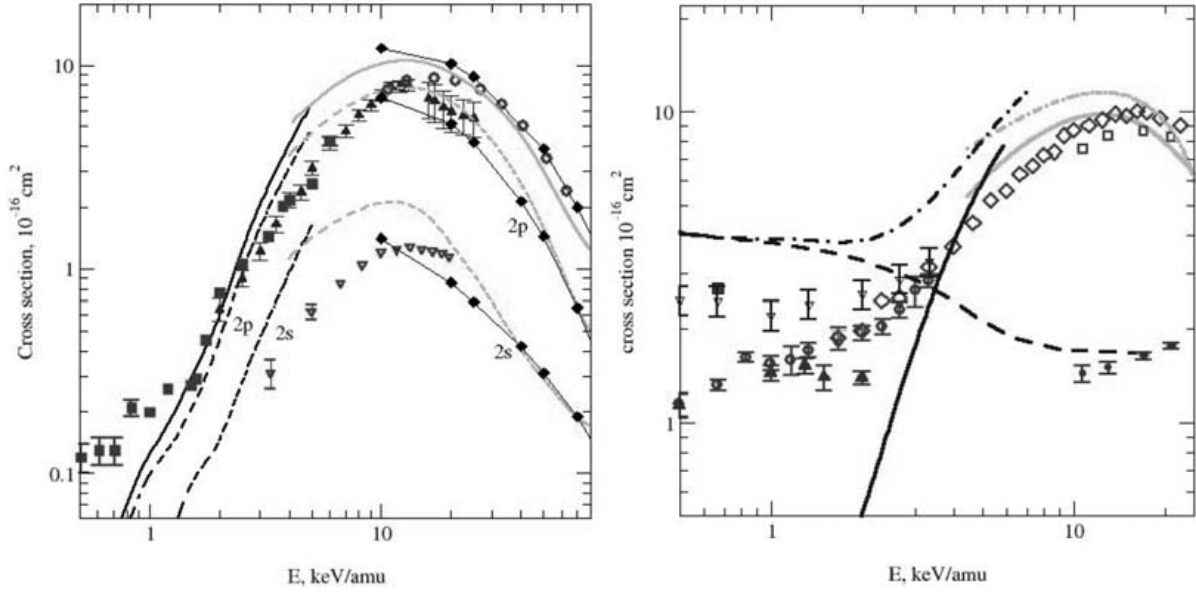
**Figure 9.** Left panel: Cross sections for nondissociative SEC: Total cross sections: O, [113]; full line, [110]. Cross sections for SEC into He$^+$(2s) + H$_2^+$(1σ$_g$):▽, [114]; dashed curve labelled 2s, [110]. Cross sections for SEC into He$^+$(2p) + H$_2^+$(1σ$_g$):▲, [102]; ■, [101], dashed curve labelled 2p, [110]. -♦-, CTMC calculations with a hydrogenic initial distribution.

Right panel: Comparison of calculations of Ref. [110] and experimental results for SEC in He$^{2+}$ + H$_2$ collisions. Total cross sections for SEC: dash-dotted curve, [110]; ◊, [106]; O, [112]; ▽, [98]. Total cross sections for nondissociative SEC: full curves, [110]; □, [115]. Total cross sections for dissociative SEC: dashed curves, [110]; ●, [115]; ▲, [100]. In both panels black curves are ab initio calculations and grey curves model potential calculations from [110].
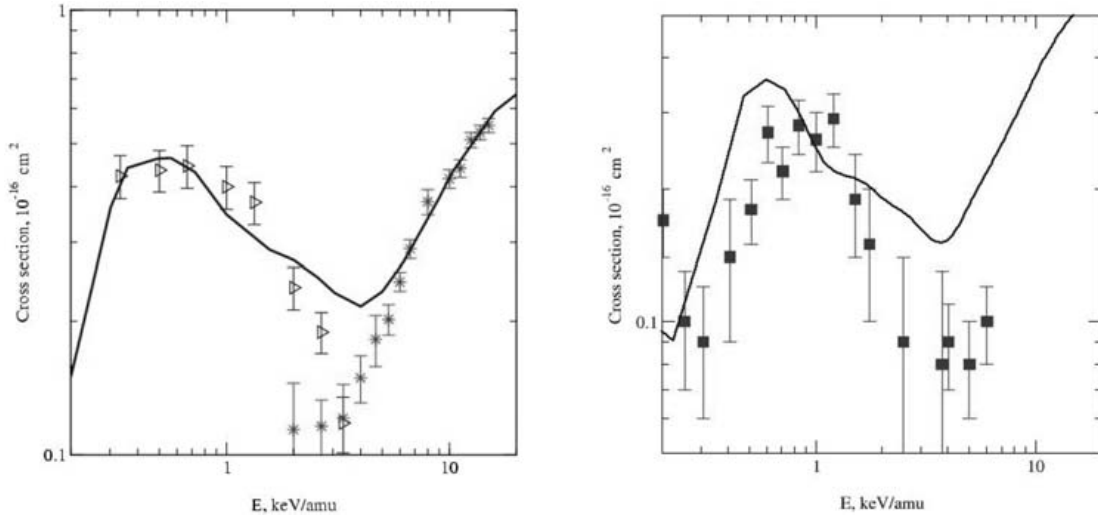


**Figure 10.** Detailed comparison of the results of the calculation by the Madrid group [110] for total BDC (left panel) and BDC into He(1s2p $^1$P) (right panel). Experimental data: ▷ - Kusakabe et al. [98], ✳ - Shah and Gilbody [106], ■ - Juhász et al. [101].

including continuum wavefunctions is required to accurately evaluate total SEC cross sections.

At E > 1 keV/amu, theoretical and experimental data agree for total non-dissociative and partial cross sections for transition to He$^+$(2s, 2p) + H$_2^+$(1σ$_g$). Fig. 9 includes new CTMC results obtained by applying the independent particle model and the same effective potential employed and an improved hydrogenic initial distribution (see [116]) constructed as a superposition of ten microcanonical

ensembles in order to yield a good fit of both momentum and spatial quantal densities. Partial cross sections have been obtained by applying the method of Ref. [117]. Good agreement is found between close-coupling, CTMC, and experimental results for E > 20keV/amu.

General good agreement is found for E > 100 eV/amu between theory and experiment for BDC cross sections shown in Fig. 10, probably because this cross section is less sensitive than SEC to vibrational effects (see [110]).
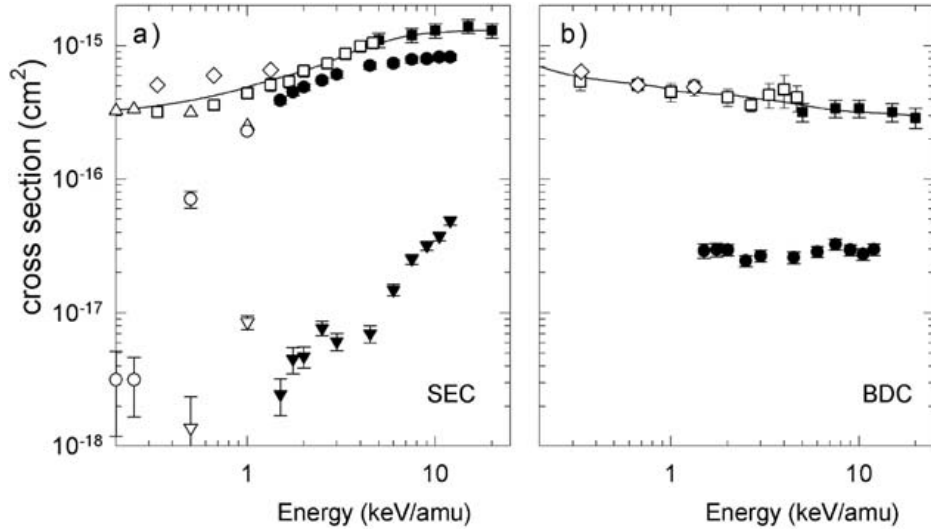
**Figure 11.** Single and double electron capture in He$^{2+}$ - CO. a) SEC: Total charge changing results: ▼ - Rudd et al. [66] ▼ - Čadež et al. [118], ◊ - Ishii et al. [119]; TES data (Kearns et al. [120]): ○ - n=2, ▽ - n=3, △ - n=1; PES data (Bodewits et al. [121]): ● - 2p, ○ - 3p. b) BDC: As panel a) except ● - 1s2p $^1$P (Bodewits et al. [121]).
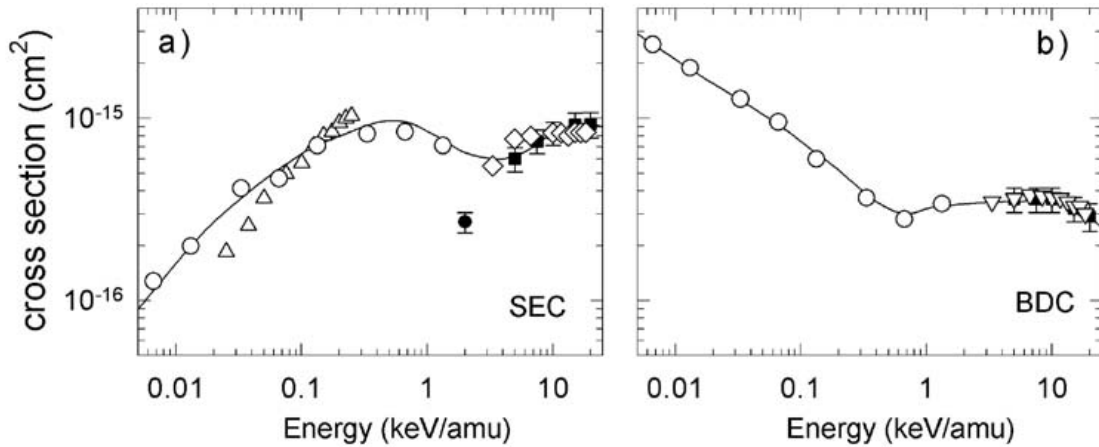


**Figure 12.** Electron capture cross sections for He$^{2+}$ - O$_2$ collisions: a) SEC: ○ - Ishii et al. [119], ◊ - Rudd et al. [66], ● - McCullough et al. [64], ▽ - Shah and Gilbody [78], △ - Kamber et al. [122]. b) BDC as panel a) .

### 2.2.2. He$^{2+}$- CO

Fig. 11 shows the SEC data for carbon monoxide. The energy behaviour is similar as for He$^{2+}$- H$_2$ collisions, again at low energy SEC is dominated by dissociative electron capture into the He$^+$(1s) ground state [120,109], while at higher energy non-dissociative capture into He$^+$(n = 2) dominates. There is mutual consistency between TES [120] and PES [121] data. At energies around and below 1 keV/amu, as for molecular hydrogen, there are some differences between total SEC cross sections, in this case the difference amounts to a factor of 2.

In contrast to the H$_2$ case, BDC into He(1s2p $^1$P) constitutes only a small fraction (~10%) of the total BDC. Due to spin conservation only singlet states can be populated

in collisions on H$_2$, while for CO also the triplet channels are accessible.

### 2.2.3. He$^{2+}$- O$_2$

Fig. 12 shows a compilation of the SEC and BDC data for collisions on molecular oxygen. It is clear from the figure that there are some apparent inconsistencies between the different data sets. The TES cross section of McCullough *et al.* [64] is based on the extrapolation of the lowest data points of Shah and Gilbody [78]. On basis of the present data a renormalization by a factor of 2.5 is proposed.

The state selective TES data of Kamber *et al.* [122] and Albu *et al.* [109] show that below 200 eV/amu, dissociative capture dominates over non-dissociative capture. The dominance of non-dissociative capture at energies of 1 and

2 keV/amu is also evident from the work of Martin *et al.* [123] and McCullough *et al.* [64].

### 2.2.4. $He^{2+}$- $CH_4$

The data sets for $He^{2+}$- $CH_4$ are depicted in Fig. 13. Total SEC cross sections have been obtained by Rudd *et al.* [66] at energies above 7.5 keV/amu. Recently the energy range has been expanded towards lower energies by beam attenuation measurements by the Queens University, Belfast group [121]. As for the other molecular targets one observes that below approximately 1 keV/amu, SEC is dominated by dissociative charge exchange. For this collision system there is very good agreement between the state selective TES and PES data [121].

### 2.2.5. $He^{2+}$- $H_2O$

A detailed discussion on SEC in $He^{2+}$ - $H_2O$ is given in the paper by Seredyuk *et al.* [124] in which TES, PES and Fragment Ion Spectroscopy data are presented and compared with results of approximate theoretical calculations. Some additional data on two-electron capture are summarized by Bodewits *et al.* [121].

## 3. Conclusions

We have compiled and reviewed charge exchange data for collisions between slow alpha particles and a whole series of atoms and molecules. It is evident from the data that in particular at the lower energies (E $\chi$ 1 keV/amu) which are of most relevance for edge and divertor plasma modeling many gaps and inconsistencies in the data exist. Strikingly enough even for the simplest and most studied $He^{2+}$- molecule system, $He^{2+}$- $H_2$, uncertainties of factors of 2 are still associated to the total charge exchange cross sections. Because at low energies charge transfer in $He^{2+}$- H has a negligibly small cross section, low-abundant neutral atomic and molecular species with large cross section can be of great relevance for the charge state distribution of helium ions in colder plasma regions. However, for many of those atoms and molecules data at the relevant energies are scarce or fully lacking.

## Acknowledgment

## References

[1] JANEV, R.K., (ed.), *Atomic and Molecular Processes in Fusion Edge Plasmas,* (Plenum, New York, 1995) and Comm. At. Mol. Phys., **26** (1991) 83.

[2] JANEV, R.K., WINTER, HP., Phys. Rep., **117** (1985) 265.

[3] LISSE, C.M., DENNERL, K., ENGLHAUSER, J., HARDEN, M., MARSHALL, F.E., MUMMA, M.J., PETRE, R., PYE, J.P., RICKETTS, M.J., SCHMITT, J., TRÜMPER, J., WEST, R.G., Science, **274** (1996) 205.

[4] KRASNOPOLSKY, V.A., MUMMA, M.J., ABBOTT, M., FLYNN, B.C., MEECH, K.J., YEOMANS, D.K., FELDMAN, P.D., COSMOVICI, C.B., Science, **277** (1997) 1488.

[5] CRAVENS, T.E., Science **296** (2002) 1042.

[6] FRITSCH, W., LIN, C.D., Phys. Rep., **202** (1991) 1.

[7] ERREA, L.F., MACÍAS, A., MÉNDEZ, L., RIERA, A., in *The Physics of Multiply and Highly Charged Ions*, p. 237 (Ed. Fred J. Currell, Kuwer Academic Publishers, Dordrecht, 2003)

[8] ABRINES, R., PERCIVAL, I.C., Proc. Phys. Soc. **88** (1966) 873.

[9] HARDIE, D.J.W., OLSON, R.E., J. Phys. B: At. Mol. Phys. **16** (1983) 1983.

[10] ILLESCAS, C., RIERA, A., Phys. Rev. A **60** (1999) 4546.

[11] SIDIS, V., Adv. Atom. Molec. Phys. **26** (1990) 161.

[12] ERREA, L.F, GORFINKIEL, J.D., MACÍAS, A., MÉNDEZ, L., RIERA, A., J. Phys. B: At. Mol. Opt. Phys. **30** (1997) 3855.

[13] BAER, M., Adv. Chem. Phys. **82** (1992) 187.

[14] ERREA, L.F., MACÍAS, A., MÉNDEZ, L., PONS, B., RIERA, A., J. Chem. Phys. **128** (2003) 325.

[15] MACÍAS, A., RIERA, A., Phys. Rep. **81** (1982) 299.

[16] NIEHAUS, A., J. Phys. B: At. Mol. Phys. **19** (1986) 2925.

[17] WINTER, T.G., HATTON, G.J., Phys. Rev. A. **21** (1980) 793.

[18] KIMURA, M., THORSON, W.R., Phys. Rev. A. **24** (1981) 3019.

[19] BRANSDEN, B.H., NOBLE, C.J., CHANDLER, J., J. Phys. B: At. Mol. Phys. **16** (1983) 4191.

[20] FRITSCH, W., Phys. Rev. A. **38** (1988) 2664.

[21] FRITSCH, W., J. Physique. Coll. **50** (1989) 87.

[22] ERREA, L.F., GÓMEZ-LLORENTE, J.M., MÉNDEZ, L., RIERA, A., J. Phys. B: At. Mol. Phys. **20** (1987) 6089.

[23] VAN HEMERT, M.C., VAN DISHOEK, E.F., VAN DER HART, J.A., KOIKE, F., Phys. Rev. A. **31** (1985) 2227.

[24] SHINGAL, R., LIN, C.D., J. Phys. B: At. Mol. Opt. Phys. **22** (1989) L445.

[25] LÜDDE, H.J., DREIZLER, R.M., J. Phys. B: At. Mol. Phys. **15** (1982) 2713.

[26] WINTER, T.G., Phys. Rev. A. **37** (1988) 4656.

[27] ERREA, L.F., MAIDAGAN, J.M., MÉNDEZ, L., RIERA, A., J. Phys. B: At. Mol. Opt. Phys. **24** (1991) L387.

[28] ERREA, L.F., HAREL, C., JOUIN, H., MAIDAGAN, J.M., MÉNDEZ, L., PONS, B., RIERA, A., Phys. Rev. A. **46** (1992) 5617.

[29] KRSTIĆ, P.S., JANEV, R.K., Phys. Rev. A. **47** (1993) 3894.

[30] HOSE, G., Phys. Rev. A. **51** (1995) 2222.

[31] HOSE, G., Phys. Rev. A. **56** (1997) 1364.

[32] HAREL, C., JOUIN, H., PONS, B., At. Data. Nucl. Data Tables **68** (1998) 279.

[33] FUKUDA, H., ISHIHARA, T., Phys. Rev. A. **46** (1992) 5531.

[34] BARNETT, C.F., HUNTER, H.T., KIRKPATRICK, M.I., ALVAREZ, I., CISNEROS, C., PHANEUF, R., *Atomic Data for Fusion,* vol. 1 (Oak Ridge National Laboratory, ORNL-6086/V1, 1990)

[35] JANEV, R.K., SMITH, J.J., Atomic and Plasma – Material Interaction Data for Fusion, **4** (1993) 1.

[36] HOEKSTRA, R., SCHLATMANN, A.R., DE HEER, F.J., MORGENSTERN, R., J. Phys. B: At. Mol. Opt. Phys. **22** (1989) L603.

[37] LEE, T.G., LE ANH TU, LIN, C.D., J. Phys. B: At. Mol. Opt. Phys. **36** (2003) 4081.

[38] LE ANH TU, LIN, C.D., ERREA, L.F., MÉNDEZ, L., PONS, B., RIERA, A., Phys. Rev. A. **69** (2004) 062703.

[39] KRSTIĆ, P.S., J. Phys. B: At. Mol. Opt. Phys. **37** (2004) L217.

[40] HENNE, A., LÜDDE, H.J., DREIZLER, R.M., J. Phys. B: At. Mol. Opt. Phys. **30** (1997) L565.

[41] TOSHIMA, N., Phys. Rev. A. **50** (1994) 3940.

[42] KUANG, J., LIN, C.D., J. Phys. B: At. Mol. Opt. Phys. **29** (1996) 1207.

[43] ERREA, L.F., HAREL, C., ILLESCAS, C., JOUIN, H., MÉNDEZ, L., PONS, B., RIERA, A., J. Phys. B: At. Mol. Opt. Phys. **31** (1998) 3199.

[44] ANDERSON, H., VON HELLERMANN, M., HOEKSTRA, R., HORTON, L.D., HOWMAN, A.C., KONIG, R.W.T., MARTIN, R., OLSON, R.E., SUMMERS, H.P., Plasma. Phys. Controll. Fusion **40** (2000) 781.

[45] LICHTEN, W., Phys. Rev. **131** (1963) 229.

[46] LÓPEZ, V., MACÍAS, A., PIACENTINI, R.D., RIERA, A., YÁÑEZ, M.J., J. Phys. B: At. Mol. Phys. **11** (1978) 2889.

[47] HAREL, C., SALIN, A., J. Phys. B: At. Mol. Phys. **13** (1980) 785.

[48] KIMURA, M., J. Phys. B: At. Mol. Phys. **21** (1988) L19.

[49] FRITSCH, W., J. Phys. B: At. Mol. Opt. Phys. **27** (1994) 3461.

[50] OKUNO, K., Atomic and Plasma – Material Interaction Data for Fusion, **10** (2002) 163.

[51] SCHORN, R.P., WOLFRUM, E., AUMAYR, F., HINTZ, E., RUSBÜLDT, D., WINTER, HP., Nucl. Fusion. **32** (1992) 351.

[52] WOLFRUM, E., AUMAYR, F., WUTTE, D., WINTER, HP., HINTZ, E., RUSBÜLDT, D., SCHORN, R.P., Rev. Sci. Instrum. **64** (1993) 2285.

[53] McCORMICK, K., FIEDLER, S., KOCSIS, G., SCHWEINZER, J., ZOLETNIK, S., Fusion Engineering and Design. **34-35** (1997) 125.

[54] WUTTE, D., JANEV, R.K., AUMAYR, F., SCHNEIDER, M., SCHWEINZER, J., SMITH, J.J., WINTER, HP., At. Nucl. Data. Tabl. **65** (1997) 155.

[55] SCHWEINZER, J., BRANDENBURG, R., BRAY, I., HOEKSTRA, R., AUMAYR, F., JANEV, R.K., WINTER, HP., At. Nucl. Data. Tabl. **72** (1999) 239.

[56] KADOTA, K., DIJKKAMP, D., VAN DER WOUDE, R.L., DE BOER, A., PAN GUANG YAN, DE HEER, F.J., J. Phys. B: At. Mol. Phys. **15** (1982) 3275.

[57] FRITSCH, W., LIN, C.D., J. Phys. B: At. Mol. Phys. **16** (1983) 1595.

[58] DIJKKAMP, D., BOELLAARD A., DE HEER, F.J., Nucl. Instrum. Meth. B. **9** (1985) 377.

[59] ERMOLAEV, A.M., HEWITT, R.N., McDOWELL, M.R.C., J. Phys. B: At. Mol. Phys. **20**, (1987) 3125.

[60] AUMAYR, F., SCHWEINZER, J., WINTER, HP., J. Phys. B: At. Mol. Phys. **22** (1989) 1027.

[61] SCHWEINZER, J., WINTER, HP., J. Phys. B: At. Mol. Opt. Phys. **23** (1990) 3881.

[62] SCHWEINZER, J., WUTTE, D., WINTER, HP., J. Phys. B: At. Mol. Opt. Phys. **27** (1994) 137.

[63] HOEKSTRA, R., WOLFRUM, E., BEIJERS, J.P.M., DE HEER, F.J., WINTER, HP., MORGENSTERN, R., J. Phys. B: At. Mol. Opt. Phys. **25** (1992) 2587.

[64] McCULLOUGH, R.W., McLAUGHLIN, T.K., KOIZUMA, T., GILBODY, H.B., J. Phys. B: At. Mol. Opt. Phys., **25** (1992) L193.

[65] THOMPSON, W.R., SHAH, M.B., GILBODY, H.B., J. Phys. B: At. Mol. Opt. Phys. **29** (1996) 2847.

[66] RUDD, M.E., GOFFE, T.V., ITOH, A., Phys. Rev. A. **32** (1985) 2128.

[67] ABDELRAHMAN, M., AUMAYR, F., WINTER, HP., to be published (2005)

[68] DuBOIS, R.D., TOBUREN, L.H., Phys. Rev. A. **31** (1985) 3603.

[69] DuBOIS, R.D., Phys. Rev. A. **34** (1986) 2738.

[70] GIELER M., AUMAYR, F., SCHWEINZER, J., KOPPENSTEINER, W., HUSINSKY, W., WINTER, HP., LOZHKIN, K., HANSEN, J.P., J. Phys. B: At. Mol. Opt. Phys. **26** (1993) 2137.

[71] DEHONG, Y., JIARUI, L., ZIMING, L., FENG, Y., GUANGYAN, P., DUANWEI, W., SHIANG, S., Phys. Rev. A. **39** (1989) 2931.

[72] SCHLATMANN, A.R., HOEKSTRA, R., FOLKERTS, H.O., MORGENSTERN, R., J. Phys. B: At. Mol. Opt. Phys. **25** (1992) 3155.

[73] SCHIPPERS, S., BODUCH, P., VAN BUCHEM, J., BLIEK, F.W., HOEKSTRA, R., MORGENSTERN, R., OLSON, R.E., J. Phys. B: At. Mol. Opt. Phys. **28** (1995) 3271.

[74] SHINGAL, R., NOBLE, C.J., BRANSDEN, B.H., J. Phys. B: At. Mol. Opt. Phys. **19** (1987) 793.

[75] KUMAR, A., LANE, N.F., KIMURA, M., Phys. Rev. A. **42** (1990) 3861.

[76] JAIN, A., WINTER, T.G., J. Phys. B: At. Mol. Opt. Phys. **29** (1996) 4675.

[77] KNOOP, S., OLSON, R.E., OTT, H., HASAN, V.G., MORGENSTERN, R., HOEKSTRA, R., J. Phys. B: At. Mol. Phys., submitted (2005).

[78] SHAH, M.B., GILBODY, H.B., J. Phys. B: At. Mol. Phys., **7** (1974) 256.

[79] BAYFIELD, J.E., KHAYRALLAH, G.A., Phys. Rev. A. **11** (1975) 920.

[80] BARAGIOLA, R.A., NEMIROVSKY, I.B., Nucl. Instrum. Meth. **110** (1973) 511.

[81] SHAH, M.B., GILBODY, H.B., J. Phys. B: At. Mol. Phys., **7** (1974) 637.

[82] HOEKSTRA, R., ANDERSON, H., BLIEK, F.W., VON HELLERMANN, M., MAGGI, C.F., OLSON, R.E., SUMMERS, H.P., Plasma Phys. Controll. Fusion. **40** (1998) 1541.

[83] JANEV, R.K., Phys. Lett. A., **160** (1992) 67.

[84] OLSON, R.E., J. Phys. B: At. Mol. Phys. **13** (1980) 483.

[85] BLANCO, S.A., FALCÓN, C.A., REINHOLD, C.O., CASAUBÓN, J.I., PIACENTINI, R.D., J. Phys. B: At. Mol. Phys. **20** (1987) 6295.

[86] JOUIN, H., HAREL, C., J. Phys. B: At. Mol. Opt. Phys. **24** (1991) 3219.

[87] BLIEK, F.W., FOLKERTS, H.O., MORGENSTERN, R., HOEKSTRA, R., MENG, L., OLSON, R.E., FRITSCH, W., VON HELLERMANN, M., SUMMERS, H.P., Nucl. Instr. Meth. B. **98** (1995) 195.

[88] RABLI, D., GARGAUD, M., McCARROLL, R., Phys. Rev. A.**64** (2001) 022707.

[89] FOLKERTS, H.O., BLIEK, F.W., MENG, L., OLSON, R.E., MORGENSTERN, R., J. Phys. B: At. Mol. Opt. Phys. **27** (1994) 3475.

[90] GIELER, M., AUMAYR, F., WEBER, M., WINTER, HP., SCHWEINZER, J., J. Phys. B: At. Mol. Opt. Phys. **26** (1993) 2153.

[91] SCHLATMANN, A.R., HOEKSTRA, R., MORGENSTERN, R., OLSON, R.E., J. Phys. Rev. Lett. **71** (1993) 513.

[92] SATO, K., TAKIYAMA, K., ODA, T., FURUKANE, U., AKIYAMA, R., MIMURA, M., OTSUKA, M., TAWARA, H., J. Phys. B: At. Mol. Opt. Phys. **27** (1994) L651.

[93] ODA, T., FURUKANE, U., TAKIYAMA, K., SATO, K., TAWARA, H., Fusion. Eng. Design. **34-35** (1997) 773.

[94] ODA, T., SATO, K., NAMBA, S., KUSAKABE, S., TAKAHARA, K., TAWARA, H., KATSUTA, T., TAKIYAMA, K., FURUKANE, U., J. Nucl. Mater. **241-243** (1997) 1238.

[95] NAMBA, S., NOMURA, I., IWASAKI, K., TAKIYAMA, K., FURUKANE, U., ODA, T., SATO, K., J. Nucl. Mater. **266-269** (1999) 1157.

[96] LUBINSKI, G., JUHÁSZ, Z., MORGENSTERN, R., HOEKSTRA, R., Phys. Rev. Lett., **86** (2001) 616.

[97] OKUNO, K., SOEJIMA, K., KANEKO, Y., J. Phys. B: At. Mol. Opt. Phys. **25** (1992) L105.

[98] KUSAKABE, T., YONEDA, H., MIZUMOTO, Y., KATSURAYAMA, K., J. Phys. Soc. Japan **59** (1990) 1218.

[99] SHIMAKURA, N., KIMURA, M., LANE, N.F., Phys. Rev. A. **47** (1993) 709.

[100] HODGKINSON, J.M., McLAUGHLIN, T.K., McCULLOUGH, R.W., GEDDES, J., GILBODY, H.B., J. Phys. B: At. Mol. Opt. Phys. **28** (1995) L393.

[101] JUHÁSZ, Z., LUBINSKI, G., MORGENSTERN, R., HOEKSTRA, R., Atomic and Plasma – Material Interaction Data for Fusion, **10** (2002) 25.

[102] HOEKSTRA, R., FOLKERTS, H.O., BEIJERS, J.P.M., MORGENSTERN, R., DE HEER, F.J., J. Phys. B: At. Mol. Opt. Phys. **27** (1994) 2021.

[103] SHINGAL, R., LIN, C.D., Phys. Rev. A. **40** (1989) 1302.

[104] FRITSCH, W., Phys. Rev. A. **46** (1992) 3910.

[105] MENG, L., OLSON, R.E., FOLKERTS, H.O., HOEKSTRA, R., J. Phys. B: At. Mol. Opt. Phys., **27** (1994) 2269.

[106] SHAH, M.B., GILBODY, H.B., J. Phys. B: At. Mol. Phys., **11** (1978) 121.

[107] SAHA, B.C., LANE, N.F., KIMURA, M., Phys. Rev. A. **44** (1991) R1.

[108] AFROSIMOV, V.V., LEIKO, G., PANOV, M., Sov. Tech. Phys. **25** (1980) 3133.

[109] ALBU, M., AUMAYR, F., WINTER, HP., Int. J. Mass. Spec. **233** (2004) 239.

[110] ERREA, L.F., MACÍAS, A., MÉNDEZ, L., PONS, B., RIERA, A., J. Phys. B: At. Mol. Opt. Phys. **36** (2003) L135.

[111] McGUIRE, J.H., WEAVER, L., Phys. Rev. A. **16** (1977) 41.

[112] NUTT, W.L., McCULLOUGH, R.W., BRADY, K., SHAH, M.B., GILBODY, H.B., J. Phys. B: At. Mol. Phys., **11** (1978) 1457.

[113] GILBODY, H.B., Private communication (2003).

[114] SHAH, M.B., GILBODY, H.B., J. Phys. B: At. Mol. Phys., **9** (1976) 1933.

[115] SHAH, M.B., McCALLION, P., GILBODY, H.B., J. Phys. B: At. Mol. Phys., **22** (1989) 3983.

[116] SHAH, M.B., McGRATH, C., ILLESCAS, C., PONS, B., RIERA, A., LUNA, H., CROTHERS, D.S.F., O'ROURKE, S.F.C., GIIBODY, H.B., Phys. Rev. A. **67** (2003) 010704.

[117] BECKER, R.L., McKELLAR, A.D., J. Phys. B: At. Mol. Phys. **17** (1984) 3923.

[118] ĆADEŽ, I., GREENWOOD, J.B., CHUTJIAN, A., MAWHORTER, R.J., SMITH S.J., NIIMURA, M., J. Phys. B: At. Mol. Opt. Phys. **35** (2002) 2515.

[119] ISHII, K., OKUNO, K., KOBAYAHI, N., Phys. Scr. T. **80** (1999) 176.

[120] KEARNS, D.M., GILLEN, D.R., VOULOT, D., GREENWOOD, J.B., McCULLOUGH, R.W., GILBODY, H.B., J. Phys. B: At. Mol. Opt. Phys. **34** (2001) 3401.

[121] BODEWITS, D., HUISMANS, Y., HOEKSTRA, R., SEREDYUK, B., McCULLOUGH, R.W., TIELENS, A.G.G.M., Astrophys. J., submitted for publication (2005)

[122] KAMBER, E.Y., ABU-HAIJA, O., FERGUSON, S.M., Phys. Rev. A. **65** (2002) 062717.

[123] MARTIN, S.J., STEVENS, J., POLLACK, E., Phys. Rev. A. **43** (1991) 3503.

[124] SEREDYUK, B., McCULLOUGH, R.W., TAWARA, H., GILBODY, H.B., BODEWITS, D., HOEKSTRA, R., TIELENS, A.G.G.M., SOBOCINSKI, P., PESIC, P., HELLHAMMER, R., SULIK, B., STOLTERFOHT, N., ABU-HAIJA, O., KAMBER, E.Y., Phys. Rev. A. **71** (2005) 022705.

# Experimental study on inner shell ionization cross sections by electron impact

*Luo Zhengming, An Zhu*

Key Laboratory of Radiation Physics and Technology of Ministry of Education and Institute of Nuclear Science and Technology, Sichuan University, Chengdu 610064, China

**Abstract**

The experimental measurements of electron-impact inner shell ionization cross sections of some middle and high Z elements, which are able to be used in fusion reactor first wall, within the energy region 8-40 keV were reported. The thin targets with thick substrates are used in the experiment to avoid the difficulty of preparing self-supporting thin targets. The influence of the reflected electrons from the substrates of thin targets on ionization cross section measurements has been corrected by a method based upon bipartition model of electron transport. The measured cross sections are compared with existing data and some theoretical prediction and empirical formulas. The further improvement of measurement precision is discussed.

## 1. Introduction

Accurate electron-impact inner-shell ionization cross section data are necessary for precisely measuring the impurity density in fusion plasma. The radiation energy loss of impurity elements in fusion plasma is one of the key factors for determining the fusion efficiency. Moreover, a large number of impurity elements in plasma will be able to trigger plasma instability and influence on the stable operation of fusion reactors. Therefore the measurement of the impurity element density in fusion plasma is crucial for the determination of radiation energy loss of impurity elements and the stable operation of fusion reactor. In general, the determination of impurity density in plasma is based on the measurement of characteristic X-rays emitted from impurity elements, therefore the accurate electron-impact inner-shell ionization cross section data are necessary to obtain the impurity density through using this method. For a long time, however, accurate and systematic electron-impact inner-shell ionization cross section data for main impurity elements in fusion plasma such as C, O, N, Fe, Ni, Cu, Mo and W have been very scarce [1-2]. In recent years, due to the improvement of experimental method, our group has carried out systematic experimental measurements for some impurity elements. This paper gives a summary on the measurement data on electron-impact inner shell ionization cross sections for impurity elements Fe, Ni, Cu, Mo and W [3-7].

It is well known that inner shell ionization cross sections by electron impact have been a subject of experimental and theoretical study for many years [1-2]. The study

is significant not only for fusion research, but also for understanding the basic interaction between electrons and atoms, X-ray microanalysis, inertia confinement fusion and so on. Unfortunately, a recent survey [2] shows that, for a wide range of elements, knowledge of inner shell ionization cross sections by electron impact is meager and of poor quality, especially in the threshold energy region, namely 5-30 keV. This energy region is specially important for fusion technique. Therefore, we carried out a project to perform a systematic measurement of inner-shell ionization cross sections by electron impact for those elements for which cross-section data are lacking.

In existing experimental measurements for inner shell ionization cross sections, the self-supporting thin target is widely used. One of the main criteria for a good thin target is that the target thickness be thin enough to fulfill the condition of a thin target, namely, $\Delta E << E$ where E and $\Delta E$ denote the incident energy of electrons and the energy loss of incident electrons passing through a thin target, respectively. This condition leads to great difficulties in preparing self-supporting thin targets. As a result, a new method was developed to avoid this difficulty in our group. Instead of using a self-supporting thin target, we use thin targets with thick substrate, which are easily prepared by a vacuum coating technique. The reflected electrons from the thick substrate will penetrate the thin target again and induce additional ionization of target atoms, which will increase the counting number of characteristic X-rays in the Si(Li) detector, requiring a correction of the measured cross sections. The correction method we adopted is a simple iterative procedure, in which reflection energy spectra of

incident electrons from thick substrate can be precisely calculated using the bipartition model of electron transport. The correction method has been applied to the analyses of experimental data of the elements Ni, Fe, Cu, Mo and W and preliminary success was attained.

## 2. Measurement method and data corrections

For the measurement of electron impact inner shell ionization cross sections by using thin targets with thick substrate two important corrections should be considered. Firstly, as mentioned above, the electrons reflected from the substrate will re-enter into the thin target and ionize target atoms once again and inevitably lead to a systematic overestimation of the measured cross sections, therefore the systematic error in the measurement must be corrected. Secondly, when an electron passes through a thin target, it undergoes a large number of elastic collisions with the target atomic nuclei. This multiple scattering will lead to increase the length of the electron trajectory in the thin target, because of electron deflection and the zigzag way of electrons inside the target. Under thin target conditions, this effect is proportional to the square of the atomic number and to the geometric thickness. Obviously if the atomic weight of the target element is larger and the electron energy is lower, this effect is more notable. Due to the multiple scattering, the electron path length within the target will be greater than the straight penetrating length in the thin target, this factor could lead to another additional X-ray counting number, therefore, this influence of electron multiple scattering in the thin target on the measurement should also be corrected. The correction can be done by using EGS4, a Monte Carlo code, which is used to calculate the ratio of electron mean path length to the electron straight penetrating length in the thin target [8].

For the measurements of K-shell ionization cross sections by electron impact for middle Z elements such as Fe, Ni, Cu, Mo and so on, the influence of thick substrate on measurement is important and was corrected. However, the influence of electron multiple scattering was not considered due to its lesser importance. For this case the measurement formula for K-shell ionization cross section by electron impact is as follows

$$Q_K(E) = \frac{4\pi N_K(E)A\cos\theta}{\Omega\eta N_e N_A Dd\omega_k}\left[1+\frac{I_\beta}{I_\alpha}\right] - \cos\theta\int_{E_{th}}^{E}\phi_{ref}(E')Q(E')dE' \quad (1)$$

surface of substrate, is calculated by using the bipartition model of electron transport [9,10] and is given in Ref. [3]. $\eta\Omega/4\pi$ is the total detection efficiency for $K_\alpha$ X-rays. The angle between the incident beam direction and the vertical direction of the target plane is denoted as $\theta$. After performing a simple iteration to Eq. (1), the corrected K-shell ionization cross sections $Q_K(E)$ can be obtained. If $\phi_{ref}(E)$ are assumed to vanish, then uncorrected cross sections, actually as the initial values of the iteration

procedure, are obtained. In general, the corrected cross sections, compared with the uncorrected ones, will decrease 10-30%.

For measuring L-shell X-ray production cross sections for heavy elements, a formula similar to Eq.(1) could be found. The final X-ray production cross section for the $L_i$-shell characteristic X-ray, $\sigma_{L_i}$ is given as follows

$$\sigma_{L_i}(E) = \frac{4\pi}{\Omega\eta}\frac{N_{L_i}(E)A\cos\theta}{N_e N_A RDd} - \cos\theta\int_{E_{th}}^{E}\phi_{ref}(E')\sigma_{L_i}(E') \ dE' \quad (2)$$

where $N_{L_i}$ is the X-ray counting number for $L_i$-shell characteristic X-ray, the subscript $i$ indicates α, β or γ, $R$ denotes the ratio of the mean path length of multiple scattered electrons in thin target to the electron straight penetrating length in thin target. The symbol $\sigma_{L_i}(E')$ represents the production cross sections induced by the electrons with energy $E'$. Other symbols have the same meanings as in Eq. (1) and can also be solved by an iteration procedure. In order to obtain $L$-shell mean ionization cross sections of the target elements it is necessary to measure the total X-ray production cross section, because the mean ionization cross section $\bar{\sigma}_L$ for L-shell of target atoms is related to the total X-ray production cross section $\sigma_L$ via

$$\bar{\sigma}_L = \sigma_L/\bar{\omega}_L = (\ \sigma_\alpha + \sigma_\beta + \sigma_\gamma\ )/\bar{\omega}_L \quad (3)$$

where $\bar{\omega}_L$ is the L-shell mean fluorescence yield whose definition is as follows [11]:

$$\bar{\omega}_L = \frac{\omega_1^{ef}/I_1 + \omega_2^{ef}/I_2 + \ 2\omega_3^{ef}/I_3}{1/I_1 + 1/I_2 + 2/I_3} \quad (4)$$

Here, $I_i$ denotes the ionization energy of the $i$-th subshell, the Coster-Kronig corrected subshell effective fluorescence yields are evaluated using the following relations:

$$\omega_1^{ef} = \omega_1 + f_{12}\omega_2 + (f_{13} + f_{12}f_{23})\omega_3, \quad (5)$$

$$\omega_2^{ef} = \omega_2 + f_{23}\omega_3, \quad (6)$$

$$\omega_3^{ef} = \omega_3, \quad (7)$$

with $\omega_i$ being the fluorescence yield for the $i$-th subshell and $f_{ij}$ the Coster-Kronig transition probability between the $i$-th and $j$-th subshells.

## 3. Experiments

We have used two experimental equipments. One is a scanning electron microscope, which supplies a stable electron beam with 0-25 keV and a target chamber. The

experimental equipment is mainly used to measure K-shell ionization cross section of lower and middle Z elements by electron impact. The other is an electron gun with a target chamber on an experimental platform for an electron electrostatic accelerator refitted by us, which provided an electron beams with energy 5-40 keV. The latter is mainly used to measure L-shell X-ray production cross sections.

The inner shell ionization cross sections were deduced from characteristic X-ray counting number. The schematic diagram of our experimental setup is demonstrated in Fig. 1. For the first experimental setup, the characteristic X-rays emitted by targets were detected by an ORTEC Si(Li) detector with an energy resolution of 180 eV (full width at half maximum) for Mn $K_\alpha$ X-rays and electron beam charges were collected by a deep Faraday cup and recorded with an ORTEC 439 digital current integrator. Targets were placed at 10° with respect to the beam direction and the Si(Li) detector was positioned at 70° to the electron beam. The incident energies of electrons were determined by the end point of bremsstrahlung spectra [12] obtained by a data acquisition system: a multiple channel analyzer (ORTECMEA916) that has been energy calibrated. With this method, the incident energies of electrons can be measured within an uncertainty of 0.1 keV. To reduce counting error caused by pulse pile-up effects, electron beam current was adjusted to be about 1 nA. The detection efficiency calibration of this system was conducted using standard radioactive sources, i.e. $^{241}$Am, $^{137}$Cs, $^{55}$Fe and $^{54}$Mn, and $^{57}$Co, provided by the National Institute of Metrology of China. The uncertainty of the calibrated efficiency is believed to be no more than 5%. For the secondsetup, the targets were placed at 45° with respect to the beam direction and the Si(Li) detector was positioned at 90° to the electron beam. A typical X-ray spectrum for tungsten is shown in Fig. 2.

Targets enriched to 99.9% with the thickness range $\bar{\sigma}_L$ $5-40 \mu g/cm^2$ were employed in our experiments. Therefore, the values of ($\Delta$E/2)/E are restricted to be less than 0.005. The targets, evaporated onto an aluminum foil or mylar film thicker than the range of electrons with incident energy, were manufactured at China Institute of Atomic Energy (CIAE) using a vacuum coating technique in which the thickness of targets was monitored and measured by a quartz oscillator. The uncertainty of the target thickness did not exceed 10%. The homogeneity of the targets was tested by probing the targets with the electron beam while registering the emitted X-rays. The reproducibility of the measured cross sections was also checked, and repeatedly measured cross sections were found to be consistent within an uncertainty of 1.3%.
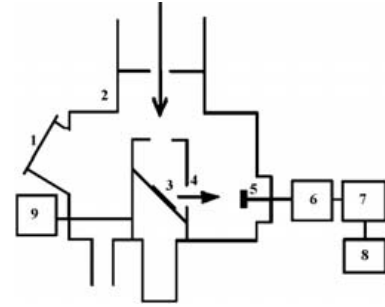


**Figure 1.** Block diagram of the equipment. 1. View window; 2. Chamber; 3. Target; 4. Faraday cup; 5. Si(Li) detector; 6. Preamplifier; 7. Main amplifier; 8. MCA; 9. Charge integrator.
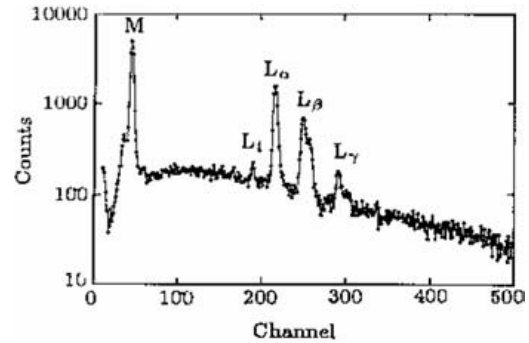


**Figure 2.** L-shell X-ray energy spectrum emitted from tungsten target at incident electron energy of 30 keV.

## 4. Results and discussion

The new experimental method of thin target with thick substrate has been used to measurement of electron-impact inner shell ionization cross sections for many elements since 1994. The measured elements include Sc, Ti, V, Cr, Mn, Fe, Co, Ni, Cu, Zn, Ge, Se, Y, Zr, Nb, Mo, Ru, Ag, In, Sn, Hf, W, Ir, Au [13-27]. Among them Fe, Ni, Cu, Mo and W are interesting to fusion technique. We summarize the measurement results of inner shell ionization cross sections for Fe, Ni, Cu, Mo and W elements in two tables.

In Table 1, the final measurement data of K-shell ionization cross sections for Fe, Ni, Cu and Mo, for which the correction of ionization contribution by electrons reflected from substrate has been made, are given. Figs. 3-6 show comparisons of our measurement results with existing experimental data, theoretical prediction and empirical formulas [28-38].

**Table 1.** Corrected K-shell ionization cross sections for Fe, Ni, Cu, Mo by electron impact

| $E_i$ (keV) | $Q_k^{Fe}$ (barn) | $Q_k^{Ni}$ (barn) | $Q_k^{Cu}$ (barn) | $Q_k^{Mo}$ (barn) |
|---|---|---|---|---|
| 7.9 | 106(±12) | | | |
| 9.0 | | 80(±8) | | |
| 9.4 | | | 20(±2) | |
| 10.0 | 363(±42) | 105(±12) | | |
| 11.6 | | | 155(±18) | |
| 12.0 | 482(±59) | 350(±45) | | |
| 13.6 | | | 257(±29) | |
| 14.2 | 613(±78) | | | |
| 15.4 | | | 303(±34) | |
| 16.0 | | 480(±54) | | |
| 16.3 | 680(±88) | | | |
| 17.7 | | | 375(±41) | |
| 18.4 | 690(±91) | | | |
| 19.7 | | | 381(±42) | |
| 20.0 | | 512(±60) | | |
| 20.4 | 683(±93) | | | |
| 21.0 | | | | 15.5(±1.4) |
| 21.7 | | | 412(±44) | |
| 22.0 | | | | 27.8(±2.7) |
| 22.3 | 707(±100) | | | |
| 24.0 | | | 398(±48) | 37.9(±3.4) |
| 25.0 | 698(±98) | 547(±75) | | |
| 26.0 | | | 397(±43) | 49.8 (±4.1) |
| 28.0 | | | | 60.9(±5.2) |
| 30.0 | | 517(±73) | | 70.7(±6.6) |
| 32.0 | | | | 76.7(±8.1) |
| 34.0 | | 517(±73) | | 87.0((±8.5) |
| 36.0 | | | | 94(±10) |
| 38.0 | | | | 107(±12) |
| 40.0 | | | | 130(±17) |

In Table 2, the measurement data of L-shell ionization cross sections for W are given. Corrections for the substrate effect and the electron multiple scattering within the target (including forward-, backward- scattering) have been carried out. Figs. 7-10 show comparisons of our measurement results with existing experimental data, theoretical prediction and empirical formulas [39-41].
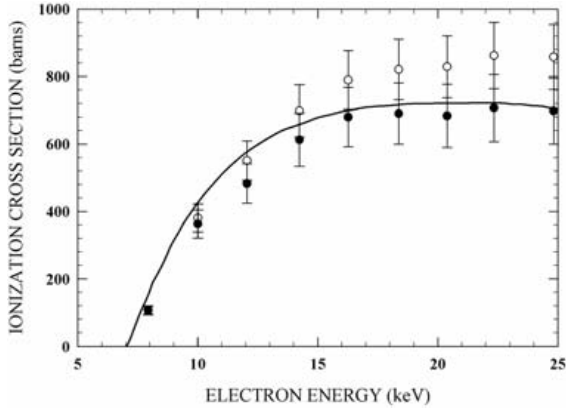
**Figure 3.** The K-shell ionization cross sections by electron impact for Fe as a function of electron energies. Open circles are the uncorrected measured data [5]. Full circles are the corrected measured data [5]. The full curve is the results of the empirical formula given by Casnati et al [28].
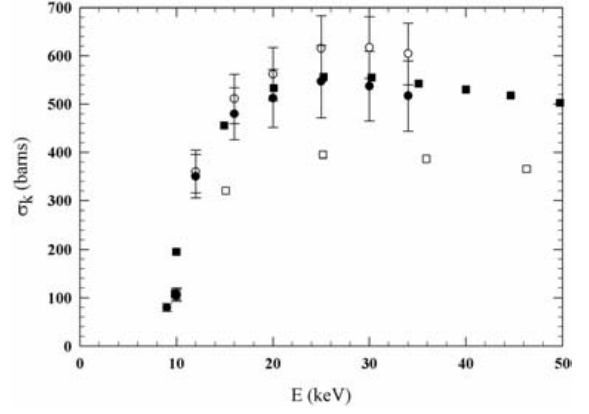


**Figure 4.** Uncorrected (open circle) and corrected (full circle) Ni K-shell ionization cross sections by electron impact [3]. Experimental data of K-shell ionization cross sections for Ni are also shown by full squares [30], and open squares [31] respectively.

**Table 2.** Measured values of partial production cross sections of electron-impact W-L-shell ionization

| E (keV) | $\sigma_{L\alpha}$ (barn) | $\sigma_{L\beta}$ (barn) | $\sigma_{L\gamma}$ (barn) | $\sigma_{LT}$ (barn) | $\overline{\sigma}_{LI}$ (barn) |
|---------|---------|---------|---------|---------|---------|
| 11.0 | 14.3±1.3 | 1.4±1.1 | | 15.7±2.4 | 58.1±8.9 |
| 12.0 | 35.2±2.6 | 9.4±1.9 | 1.7±0.4 | 46.3±4.9 | 171.5±18.1 |
| 13.0 | 58.7±3.9 | 25.7±2.4 | 4.8±0.9 | 89.2±7.2 | 330.4±26.7 |
| 14.0 | 88.2±5.7 | 46.3±3.6 | 9.1±1.4 | 143.6±10.7 | 531.9±39.6 |
| 15.0 | 101.7±6.7 | 64.3±4.7 | 10.4±2.1 | 176.4±13.5 | 653.3±50.0 |
| 16.0 | 120.1±7.8 | 86.9±6.2 | 11.4±3.2 | 218.4±17.2 | 808.9±63.7 |
| 17.0 | 141.9±9.1 | 100.7±6.9 | 13.1±2.4 | 255.7±18.4 | 947.0±68.1 |
| 18.0 | 157.9±9.8 | 105.8±7.3 | 14.8±2.7 | 276.8±19.6 | 1025±72.6 |
| 19.0 | 155.8±9.8 | 114.1±7.5 | 16.1±1.9 | 286.1±19.2 | 1060±71.1 |
| 20.0 | 163.5±10.6 | 117.4±8.1 | 18.8±2.8 | 299.8±21.5 | 1110±79.6 |
| 22.0 | 163.5±10.6 | 132.2±8.9 | 20.9±4.3 | 316.9±23.8 | 1174±88.1 |
| 24.0 | 167.1±10.7 | 121.3±8.4 | 21.0±3.0 | 309.0±22.1 | 1144±81.9 |
| 26.0 | 166.7±10.7 | 128.1±8.6 | 21.6±3.4 | 316.6±22.7 | 1172±84.1 |
| 28.0 | 155.4±9.6 | 122.3±7.6 | 19.2±2.3 | 296.2±19.5 | 1097±72.2 |
| 30.0 | 150.4±9.5 | 117.2±7.9 | 17.5±2.6 | 284.5±20.0 | 1054±74.1 |
| 32.0 | 146.3±10.0 | 110.3±9.2 | 15.7±8.6 | 271.8±27.8 | 1008±103 |
| 34.0 | 140.3±12.5 | 107.9±17.3 | 15.2±7.5 | 263.2±37.3 | 974.8±138 |
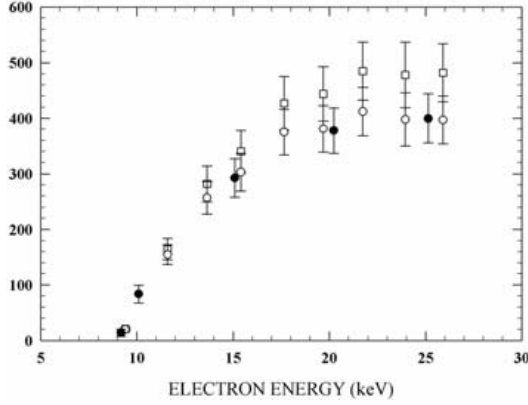
**Figure 5.** Cu K-shell ionization cross sections as a function of electron energy. The present uncorrected (open squares) and corrected data (open circle) as well as Shima's data (full circle) are plotted [4,12].
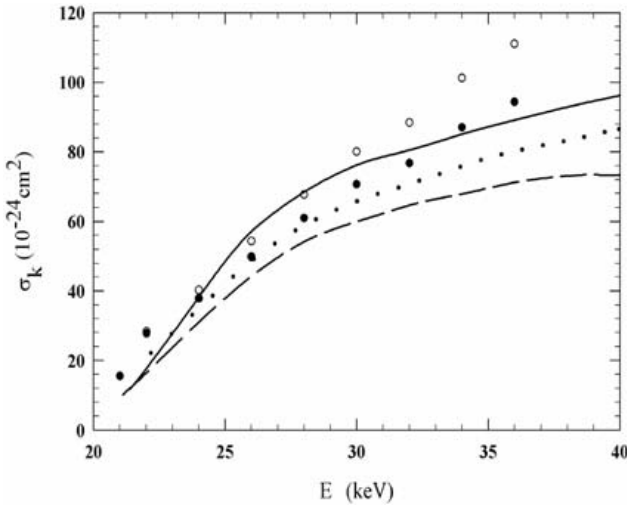


**Figure 6.** K-shell ionization cross sections for Mo as a function of electron energy. Solid line is empirical approach of Ref. [28]. Dotted line is empirical approach of Ref. [38]. Solid line is theoretical calculation of Ref. [35]. Full circles are corrected data. Open circles are uncorrected data [6].

The partial production cross sections of $L_\alpha$, $L_\beta$, $L_\gamma$ X-rays, the total production cross sections and the mean ionization cross sections of W-$L$-shell as functions of incident electron energy are shown in Figs. 7-10. The experimental cross sections of $L_l$ X-ray have not been evaluated due to its poor peak counts.

The binary encounter approximation (BEA) proposed by Gryzinski [39], which is suitable for theoretical calculation of the $L$-shell ionization cross section at present, can be written as

$$\sigma_i = b_i(\sigma_0 / I_i^2)g_i(x) \,, \qquad (8)$$

and

$$g_i(x) = \frac{1}{x}\left(\frac{x-1}{x+1}\right)^{3/2}\left[1+\frac{2}{3}\left(1-\frac{1}{2x}\right)\ln\left[2.7+(x-1)^{1/2}\right]\right], (9)$$

where $b_i$ is the number of electrons in the sub-shell $L_i$ ($i = 1$, 2 and 3), $x = E / I_i$, $E$ is the incident electron energy, $I_i$ is the ionization energy of the $i$-th sub-shell, and $\sigma_0 = 6.56 \times 10^{-14}$ cm$^2$. This classical scaling apparently predicts the same value of $f(E / I_i)$ at the same $E / I_i$ for all sub-shells.

Another theoretical calculation was proposed by McGuire [40] which can be written as

$$\sigma_i(I_i)^\alpha = f(E/I_i) \,, \qquad (10)$$

where $\alpha \neq 2$. This differs from the K-shell ionization, in which a simple scaling law $\sigma_{1s}(I_{1s})^2 = f(E/I_{1s})$ is adapted for all elements in the non-relativistic limit. This non-classical scaling law predicts the same feature of $f(E/I_{1s})$ only when the sub-shells have the same orbital angular momentum, such as $2p_{1/2}$ and $2p_{3/2}$.

For comparison of experimental data with the above two theories, from which only obtained the ionization cross sections of three sub-shells $L_1$, $L_2$, $L_3$ of tungsten, therefore we have to convert them into the partial production cross sections. The conversion formulas can be taken from Ref. [42]. The partial production cross sections $\sigma_{L\alpha}$, $\sigma_{L\beta}$, and $\sigma_{L\gamma}$ are functions of $L_1$-, $L_2$-, and $L_3$-subshell ionization cross sections $\sigma_{L_1}$, $\sigma_{L_2}$ and $\sigma_{L_3}$ as below

$$\sigma_{L\alpha} = \frac{\Gamma_{M4,5-L3}}{\Gamma_{total-L3}}\omega_3\left[\sigma_{L3} + f_{23}\sigma_{L2} + (f_{13} + f_{12}f_{23})\sigma_{L1}\right], \quad (11)$$

$$\sigma_{L\beta} = \frac{\Gamma_{N1,5-L3}+\Gamma_{O4,5-L3}}{\Gamma_{total-L3}}\omega_3\left[\sigma_{L3} + f_{23}\sigma_{L2} + (f_{13} + f_{12}f_{23})\sigma_{L1}\right]$$
$$+ \frac{\Gamma_{M4-L2}}{\Gamma_{total-L2}}\omega_2\left[\sigma_{L2} + f_{12}\sigma_{L1}\right] + \frac{\Gamma_{M2,3-L1}}{\Gamma_{total-L1}}\omega_1\sigma_{L1}$$
$$(12)$$

$$\sigma_{L\gamma} = \frac{\Gamma_{N1,4-L2}+\Gamma_{O4-L2}}{\Gamma_{total-L2}}\omega_2\left[f_{12}\sigma_{L1} + \sigma_{L2}\right] + \frac{\Gamma_{N2,3-L1}+\Gamma_{O2,3-L1}}{\Gamma_{total-L1}}\omega_1\sigma_{L1}$$
$$(13)$$

where $\Gamma_{M4,5-L3}$ and $\Gamma_{total-L3}$ are the X-ray emission rates for $L_\alpha$ ($M_{4,5}$-$L_3$ transition) and total X-rays (M-, N-, O-$L_3$ transition) respectively; $\omega_3$ is the fluorescence yield for $L_3$-shell. In Eq. (12) and Eq. (13) the corresponding parameters have a meaning similar to that in Eq. (5). The parameters in Eqs. (3-7) and Eqs. (11-13) are taken from Refs. [43-45].

From Figs. 7-10 we can come to the conclusion that the near-threshold experimental values are close to the predictions by McGuire provided that both corrections of the substrate reflection and multi-scattering have been made, and at higher energies the corrected experimental results
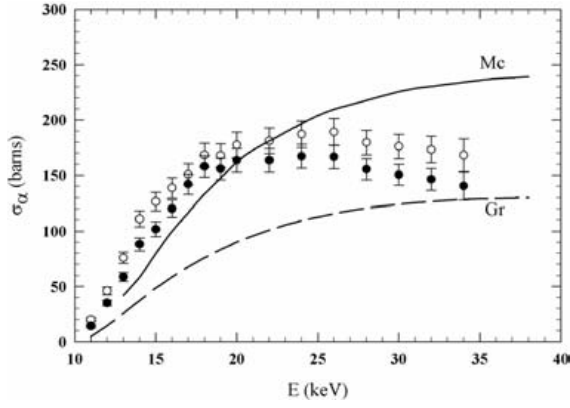
**Figure 7.** Experimental values of $L_\alpha$-rays production cross sections for tungsten [7]. The symbol Gr indicates Gryzinski's theory [39]. Mc indicates McGuire's theory [40]. The hollow symbols are experimental values and the filled symbols are corrected experimental values for the reflected electron effect.
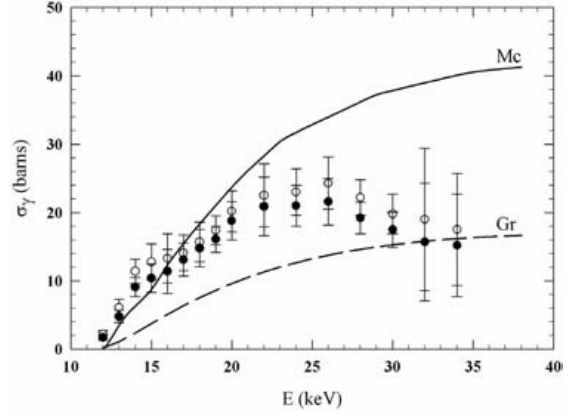


**Figure 9.** Experimental values of $L_\gamma$-rays production cross sections for tungsten {7}. The symbol Gr indicates Gryzinski's theory [39]. Mc indicates McGuire's theory [40]. The hollow symbols are experimental values and the filled symbols are corrected experimental values for the reflected electron effect.
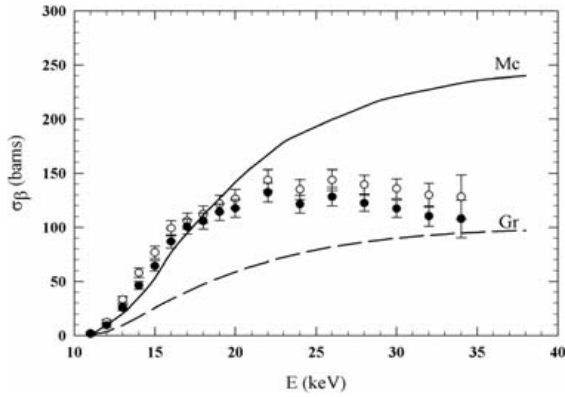


**Figure 8.** Experimental values of $L_\beta$-rays production cross sections for tungsten [7]. The symbol Gr indicates Gryzinski's theory [39]. Mc indicates McGuire's theory [40]. The hollow symbols are experimental values and the filled symbols are corrected experimental values for the reflected electron effect.
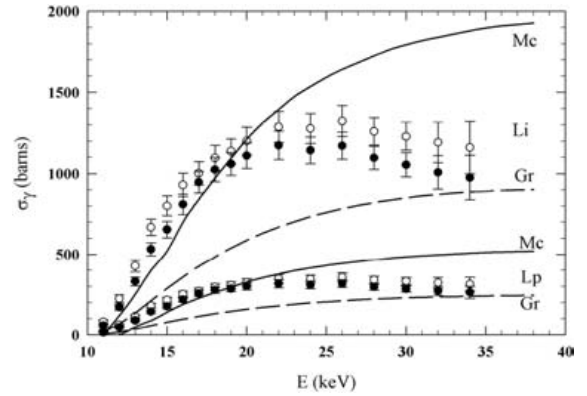


**Figure 10.** Total production cross sections (Lp) and ionization cross sections (Li) of tungsten as functions of electron impact energy. The hollow symbols are experimental values and the filled symbols are corrected experimental values. The symbol Gr indicates Gryzinski's theory [39]. Mc indicates McGuire's theory [40].

tend to the predictions by Gryzinski, but the corrected measured values are still higher than the theoretical predictions at near threshold. Therefore even more works on lower-energy electron impact may be necessary.

Since we started to study inner shell ionization cross sections by electron impact in the beginning of the 1990s, some improved measurement methods for upgrading the experimental accuracy have been successively advanced and refined. These measurement methods include: the correction for the additional X-ray counting number resulting from electrons reflected from substrate, the correction for the additional X-ray counting number resulting from the zigzag path length of incident electrons in thin target due to multiple scattering, improvement of the measurement of thin target thickness by using RBS technique, extension of the Si(Li) detector calibration curve to low energy range by using the

bremsstrahlung spectrum emitted from thick carbon. A new scanning electron microscope will be used to measure the inner shell ionization cross sections. Based on the research we have done, all developed techniques in our group will be systemically used to determine the inner shell ionization cross sections with higher accuracy.

## Acknowledgements

# References

[1] POWELL, C.J., Rev. Mod. Phys. **48** (1976) 33.

[2] LONG, X.G. et al. At. Data Nucl. Data Tables **45** (1990) 353.

[3] LUO, Z.M., AN, Z., HE, F.Q., LI, T.H., LONG, X.G., PENG, X.F., J. Phys. B: At. Mol. Opt. Phys. **29** (1996) 4001.

[4] AN, Z., LUO, Z.M., LI, T. H, WANG, L.M., Phys. Rev. A **54** (1996) 3067.

[5] LUO, Z.M., AN, Z., LI, T.H., WANG, L.M., ZHU, Q., XIA, X.Y., J. Phys. B: At. Mol. Opt. Phys. **30** (1997) 2681.

[6] HE, F.Q, PENG, X.F., LONG, X.G., LUO, Z.M., AN, Z., Nucl. Instrum. Meth. Phys. Res. B **114** (1996) 213.

[7] PENG, X.F, HE, F.Q., LONG, X.G., LUO, Z.M., AN, Z., Chinese Phys. **9** (2000) 749.

[8] NELSON, W.R., HIRAYAMA, H., ROGERS, D.W.O., The EGS4 code system SLAC- Report-265 Stanford Linear Accelerator Center (1985)

[9] LUO, Z.M., Phys. Rev. B **32** (1985) 812.

[10] LUO, Z.M., Phys. Rev. B **32** (1985) 824.

[11] ISHII, K. et al. Phys.Rev. A **15 (**1977) 906.

[12] WOLTERS, U., MEYER, D., WIESEMANN, K., J. Phys. D: Appl. Phys. **31** (1998) 2112.

[13] PENG, X.F., HE, F.Q., LONG, X.G., LUO, Z.M., AN, Z., Phys. Rev. A **58** (1998) 2034.

[14] TANG, C.H., AN, Z., LI, T.H., LUO, Z.M., Nucl. Instrum. Meth. Phys. Res. B **155** (1999) 1.

[15] AN, Z., TANG, C.H., ZHOU, C.G., LUO, Z.M., J. Phys. B. At. Mol. Opt. **33** (2000) 3677.

[16] LUO, Z.M., TANG, C.H., AN, Z., HE, F.Q., PENG, X.F., LONG, X.G., Phys. Rev. A **63** (2001) 034702.

[17] PENG, X.F., HE, F.Q., LONG, X.G., AN, Z., LUO, Z.M., Chinese Phys. **10** (2001) 31.

[18] PENG, X.F., HE, F.Q., LONG, X.G., AN, Z., LUO, Z.M., Chinese Phys. Lett. **18** (2001) 39.

[19] ZHOU, C.G, FU, Y.C., AN, Z., TANG, C.H., LUO, Z.M., Chinese Phys. Lett. **18** (2001) 531.

[20] ZHOU, C.G., AN, Z., LUO, Z.M., Chinese Phys. Lett. **18** (2001) 769.

[21] ZHOU, C.G., FU, Y.C, AN, Z., LUO, Z.M., Laser Particle Beams **13** (2001) 117.

[22] TANG, C.H., AN, Z., LUO, Z.M. et al, J. Appl. Phys. **91** (2002) 6739.

[23] TANG, C.H, LUO, Z.M., AN, Z. et al, Phys. Rev. A **65** (2001) 052707.

[24] LUO, Z.M., FU, Y.C., AN, Z., PENG, X.F., HE, F.Q., LONG, X.G., Chinese Phys. Lett. **19** (2002) 1610.

[25] ZHOU, C.G., AN, Z., LUO, Z.M., J. Phys. B. At. Mol. Opt. **35** (2002) 841.

[26] WU, Z.W., YANG, D.L., HE, F.Q., PENG, X.F., LUO, Z.M., Chinese Phys. Lett. **20** (2003) 1485.

[27] YANG, D.L., LUO, X.B., FU, Y.C., HE, F.Q., LONG, X.G., PENG, X.F., LUO, Z.M, Chinese Phys. **13** (2004) 670.

[28] CASANATI, E., TARTARI, A., BARALDI, C., J. Phys. **B**: At. Mol. Phys. **15** (1982) 155.

[29] LLOVET, X., MERLET, C., SALVAT, F., J. Phys. B: At. Mol.Opt. Phys. **35** (2002) 973.

[30] JESSENBERGER, J., HINK, W., Z. Phys. A **275** (1975) 331.

[31] POCKMAN, L.T., WEBSTER, D.L., KIRKPATRICK, P. HARWORTH, K., Phys. Rev. **71** (1947) 330.

[32] LLOVET, X., MERLET, C., SALVAT, F., J. Phys. B: At. Mol. Opt. Phys. **35** (2000) 3761.

[33] SHIMA, K., NAKAGAWA, T., UMETANI, K., MIKUMO, T., Phys. Rev. A **24** (1981) 72.

[34] GREEN, M., COSSLETT, V.E., Proc Phys Soc. London **78** (1961) 1206.

[35] RUDGE, M.R.H., SCHWARTZ, S.B., Proc. Phys. Soc. London **88** (1966) 563.

[36] LOTZ, W., Z. Phys. **206** (1967) 205.

[37] HINK, W., JESSENBERGER, J., ZIEGLER, A., Z. Phys. **226** (1969) 463.

[38] JACOBY, C., GENZ, H., RICHTER, A., J. Phys. Coll. **48**(c9) (1987) 487.

[39] GRYZINSKI, M., Phys. Rev. A **138** (1965) 336.

[40] McGUIRE, E.J., Phys. Rev. A **16** (1977) 73.

[41] CAMPOS, C.S., VASCONCELLOS, M.A.Z., LLOVET, X., SALVAT, F., Phys. Rev. A **66** (2002) 012719.

[42] SHIMA, K., NAKAGAWA, T., UMETANI, K., MIKUMO, T., Phys. Rev. A **24** (1981) 72.

[43] KRAUSE, M.O., J. Phys. Chem. Ref. Data **8** (1979) 307.

[44] LIU, Y.Z. et al., The Decay Scheme for Usual Radionuclides (in Chinese), Atomic Energy Press, Beijing (1982) 400.

[45] SCOFIELD, J.H.., At. Data Nucl. Data Tables **14** (1974) 121.

# Determination of rate coefficients for atoms and molecules (hydrocarbons and hydrogen with its isotopes) by measurement and modelling in the boundary plasma of TEXTOR

*A. Pospieszczyk[1], D. Borodin[1], S. Brezinsek[1], A. Huber[1], A. Kirschner[1], Ph. Mertens[1], G. Sergienko[1], B. Schweer[1], I.L. Beigman[2], L. Vainshtein[2]*

[1] Institut für Plasmaphysik, Forschungszentrum Jülich GmbH, EURATOM Association, Trilateral Euregio Cluster, D-52425 Jülich, Germany

[2] P.N.Lebedev Institute, Leninsky Prospect 53, 119991 Moscow, RAS, Russia

## Abstract

Rate coefficients for the excitation and ionisation of neutral as well as singly ionised particles and – predominantly – their ratios S(D) / XB, which are important for the conversion of photon into particle fluxes in ionising fusion boundary plasma, have been modelled and experimentally determined in TEXTOR and JET for fusion relevant species such as He I, Li I, C I, B I&II, O I&II, Si I&II, $H_2$, CH(D), $C_2$.

## 1. Introduction

The knowledge of particle release from Plasma Facing Components (PFC) is vital for the determination of erosion and fuelling. These processes can both limit the life time of e.g. divertor plates and the achievable density for ignition in ITER. Spectroscopic methods are the most promising tools for such measurements; however, they often suffer from an incomplete data base for the interpretation of the signals in terms of particle fluxes, predominantly for atoms as well as hydrogen molecules and hydrocarbons as these are difficult to produce quantitatively in laboratory experiments. Because of its capabilities TEXTOR offers a unique possibility to determine rate coefficients and compare them with various model calculations.

Therefore, the main activities in this project were to derive rate coefficients from known fluxes of carbon-, oxygen- and hydrogen- containing gases, which have been injected through several nozzles and injection systems into different boundary plasmas. The intensity profiles for several atomic, molecular and/or low ionisation stages are absolutely measured via spectrometric techniques in the visible and air UV range which allow the determination of effective rate coefficients for the different level populations. Collisional radiative models (CRM) are employed to compare the measured coefficients with the calculated ones for different plasma densities and temperatures. The tokamak TEXTOR with its spatially resolving and absolutely calibrated spectroscopy on limiter locks and other PFCs, which are equipped with gas injection systems, is especially suited for such kind of measurements. Several Codes (ATOM, ATCC, GKU for atoms & ions; CRMOL for hydrogen molecules; ERO for erosion and deposition) allow the calculation of level populations for boundary plasma parameter conditions. The particles investigated were Li, He, B, C, O, Si, and W as atoms and/or ions as well as hydrogen (with its isotopomeres) and hydrocarbon molecules (with their radical dissociation products).

## 2. Methods

### 2.1. Experimental studies

The way to determine fluxes in (ionising) edge plasmas is to measure the integral photon flux of a spectral line emitted by the released particles. The particle flux $\Phi_A$, density $n_A$, integrated photon flux $I_{tot}$ (with branching ratio $\Gamma_B$), ionisation rate $< \sigma_I \upsilon_e >$, excitation rate $< \sigma_{Ex} \upsilon_e >$ and the plasma with $n_e$ and $T_e$ are coupled by the following equation:

$$\Phi_A = 4\pi \frac{I_{tot}}{\Gamma_B h\nu} \frac{\int_{r_1}^{r_2} n_A(r)n_e(r) <\sigma_I \upsilon_e>_{(r)} dr}{\int_{r_1}^{r_2} n_A(r)n_e(r) <\sigma_{Ex} \upsilon_e>_{(r)} dr} \quad (1)$$

A derivation of (1) can be found in [1]. One should note here especially that a general solution of equation (1) is only possible, if $n_e(r)$, $f(v_A)$, $<\sigma_I v_e>=f_i(r)=f(T_e)$, and $<\sigma_{Ex} v_e>=f_{ex}(r)=f_{ex}(T_e)$ are precisely known at the position of the corresponding measured intensities. Since the latter condition is mostly not fulfilled because of problems of access for the relevant diagnostics, an iterative procedure is in general required. For this reason and provided the ratio $<\sigma_I v_e>/<\sigma_{Ex} v_e>$ has only a weak spatial (i.e. temperature) dependence in the region of interest, a simpler version of equation (1) can be derived:

$$\Phi_A = \frac{4\pi}{\Gamma_B} \frac{I_{tot}}{h\nu} \frac{<\sigma_I \upsilon_e>}{<\sigma_{Ex} \upsilon_e>} = 4\pi \frac{I_{tot}}{h\nu} \frac{S}{XB} \quad (2)$$

where the following identities are valid: $S \equiv <\sigma_I v_e>$, $X \equiv <\sigma_{Ex} v_e>$, and $B \equiv \Gamma_B$. The expression on the right side of this equation is also often referred in this way in the literature in respect to flux determination from integral line intensity measurements [2]. The necessary so-called $S/XB$ (in the case of molecules $D/XB$ replacing ionisation by decomposition) are normally determined from known ionisation and excitation rates, which have been either deduced from experiments or calculations. In extreme cases a CRM has to be set up which calculates the population of the excited levels from a set of rate equations.

A major problem for the quantitative evaluation of emission line measurements is - especially in the case of detection systems with interference filters - the radiation

from near-by lines or bands. Also hot limiter or wall components may disturb the evaluation of infrared lines considerably. Therefore, one often has to turn to lines which both/either are undisturbed and/or in a more accessible wavelength range of the spectrum but the excitation rates of which are unknown and no calculations exist so far for these transitions. Also in the field of molecular plasma spectroscopy many cross-sections for the observed bands are unknown. An alternative in this case is to produce spectra in the same wavelength range either in a simulator with a boundary like plasma of $10^{12} \text{cm}^{-3} < n_e < 2\times10^{13} \text{cm}^{-3}$ and $5\text{ eV} < T_e < 50\text{ eV}$ [3,4] or directly in a tokamak where the respective elements are introduced either by gas blow or laser blow off. The principle of these experiments is to reverse equation (2):

$$\frac{S}{XB} = \frac{<\sigma_I \upsilon_e>}{\Gamma <\sigma_{Ex} \upsilon_e>} = \frac{\Phi_A}{4\pi \left(I_{tot}/h\nu\right)} \quad (3)$$

and determine the effective line excitation rate (which now also includes all density dependent effects) via an absolute measurement of the intensity of the spectral line and the inward flux of atoms. This procedure has been used on TEXTOR (see Fig. 1), however, one should note here that in this way only the *ratio* of ionisation to excitation (or population) rate can be determined. These values will mainly be provided in this report; a knowledge of at least $X$ or (in most practical cases) $S$ is necessary to derive both values separately.

### 2.2. Theoretical studies

The kinetic calculations for the atoms were done by the code GKU (for a short outline see [5]). It provides the data for the level populations, intensities of the selected lines and $S/XB$ factors. Two modes - non- stationary (NS) and
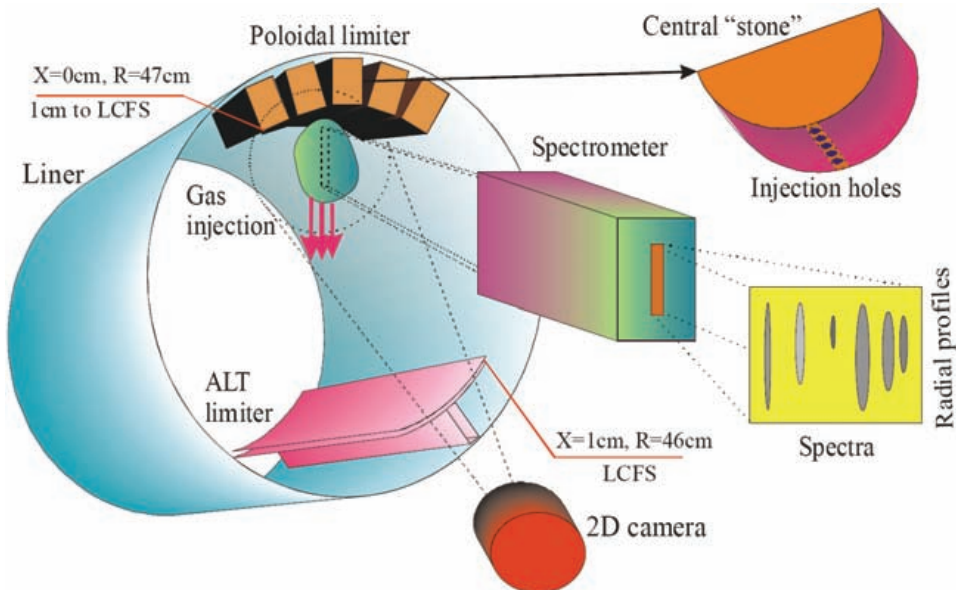


**Figure 1:** Injection and observation system as it was used on TEXTOR for the measurement of rates from gaseous constituents. The imaging spectrometer allows additionally to measure the penetration depth and, hence, the ionisation rates

quasi-stationary (QS) - are possible. The atomic data-base (ADB) for the transitions between the levels considered was calculated by the code ATOM. If any atomic characteristic is absent in the ADB, it was calculated by the code using a set of formulae ('Bates-Damgaard' for oscillator strengths, semiclassical excitation and classical ionization formulae [6]).

The code ATOM calculates atomic characteristics such as transition probabilities and rate coefficients. It is based on the one-electron, semi-empirical wave functions without configuration interaction. For the collisional characteristics, the Coulomb-Born-exchange approximation (CB) with K-matrix method for the channel interaction and normalization is used. For ionization cross-sections, besides the direct ionization from the outer shell, the contributions from the innershell ionization and excitation of autoionization levels are included. For more details see Ref. [6].

For molecules CRMs as well as a kinetic code (ERO) have been set up for the calculation of the emission characteristics of hydrocarbon radicals, which can conveniently be observed with high resolution spectroscopy in the optical wave length range (e.g. CH & CD). A similar CRM has been installed in the case of hydrogen molecules (see below).

## 3. Results

### 3.1. Lithium and carbon

Both elements are commonly used in plasma edge diagnostics for the determination of the radial electron density distribution $n_e(r)$ (via the radial light intensity profile of a Li-resonance line ($2p^2P - 2s^2S$ at 671nm)) and of the radial electron temperature distribution $T_e(r)$ (via the radial light intensity profile of a C emission line ($2s^22p^3p^3P_2 - 2s^22p^3s^3P_2$ at 910nm). Therefore, model calculations have been performed which provide good fits to the experimentally obtained light emission profiles. The elements are injected into the TEXTOR boundary plasma by the **l**aser **b**low **o**ff method (LBO) which is described in more detail in [5]. In principle, the focussed light of a ruby laser (1 J output energy) ablates small portions ($\phi = 1$–4 mm) from the rear side of a glass substrate. The ablated atoms travel to the plasma boundary with a velocity of $\upsilon = 6\times10^5$–$1.3\times10^6$ cm s$^{-1}$ depending on the power density within the laser spot and are recorded in time by a photomultiplier and in space by a Si-diode array camera, both in combination with an interference filter for the appropriate wavelength.

All collisional and allowed radiative transitions (with the exception of photo- and dielectric-recombination) are included in the transition matrix $W$. Most of the necessary atomic characteristics—transition probabilities and electron–atom collision rate coefficients—could be calculated with the general code ATOM [7]. It uses one-electron atomic wave functions for the optical (active) electron, which are solutions of the radial Schrödinger equation with an effective scaled potential and an experi-
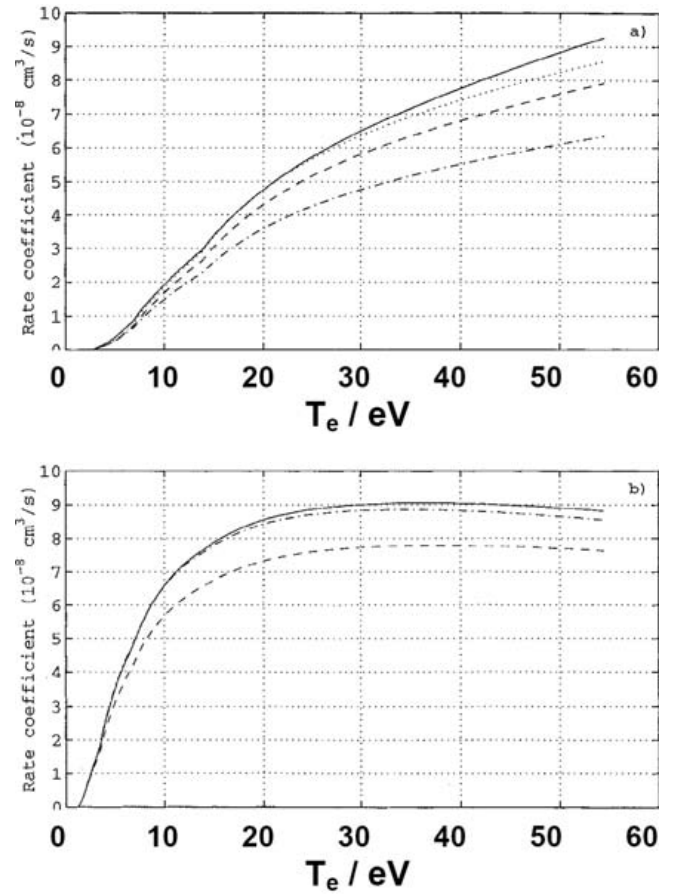


**Figure 2.** (a) Ionization rate coefficient of C atom ground state. Full curve are recommended data [8]; dashed curve is the BE approximation, dash-dot curve is the Born approximation, both from 2s and 2p shells; dotted curve is the BE approximation, from 2p shell only. (b) Ionization rate coefficient of Li atom ground state. Full curve are recommended data [8];dashed curve is the BE approximation, dotted curve is the Born approximation, both from 2s shells.

mental value for the energy. Excitation and ionization cross sections are calculated in the Born (for neutrals) or Coulomb–Born (for ions) approximation with inclusion of exchange effects by the orthogonalized function method) and normalization (by the *K*-matrix method)—BE approximation. The recommended rate coefficient for Li(2s) is compared with those calculated by the ATOM code in different approximations is displayed in Fig. 2a. The difference of the rate coefficients does not exceed 15%. Rate coefficients for Li(2s) are shown in Fig. 2b.

Fig. 3 shows the calculated Li-line intensity profiles along the beam axis. One can see that the inclusion of levels $n > 3$ changes the line profile at large densities ($>3\times 10^{12}$ cm$^{-3}$, $x > x_{lim}$) by 20% and more; $n = 9$ is large enough; even $n$=4 already provides very reasonable results.

The detailed calculations have shown that more than half of the level $n > 3$ contribution is connected with step by step ionization through excitation of $nl$ levels from the ground state.

The rest is provided by excitation of $nl$ from $2p$ and $3l$ states. It is worth mentioning that for Li ionization cross
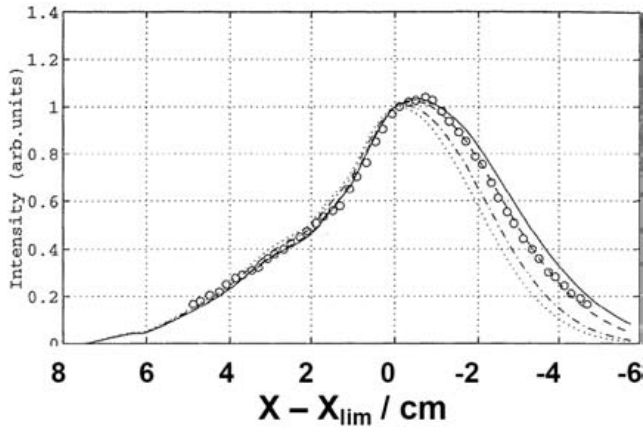
**Figure 3.** Li line profiles for $n_m$ = 3 (full curve), 4 (dashed curve), 6 (dotted curve), 9 (dash-dot curve); $n_m$ is the maximal principal quantum number of levels included; circles are experimental data. The velocity of the atomic beam is $1.25 \times 10^6$ cm s$^{-1}$; $X_{lim}$ denotes the limiter radius, which defines the last close flux surface.

sections from 2p are more than five times larger than from 2s state.

The measured and calculated intensity profiles are compared in Fig. 4. The calculated profile with $n = 4$ agrees with the experimental data. An inclusion of levels up to $n = 9$ requires a correction of the density profile. This was done by a simple constant multiplication factor to the density profiles. A value of 0.8 value is in agreement with the experimental data.

An agreement with experimental light profiles may be achieved by using a changed temperature profile. In Fig. 4a the calculated intensity profiles for three versions of $T_e(x)$ (Fig. 4b) are shown. The full curve profile provides reasonable agreement with experiment. Fig. 4c demonstrates that all three temperature versions give practically the same results for the Li line profile.

The intensity profile of the observed carbon line (909.5 nm) can yield information about the temperature profile, however, additional experimental data are necessary for a more detailed reconstruction of the temperature profile above 20 eV.

### 3.2. Helium

The disadvantages – a pulsed operation for the suprathermal beam of Li- and C-atoms – could be overcome by the use of continuous helium beams. Helium can penetrate quite far into the plasma because of its high ionisation energy of 24.9 eV and is also applied for the simultaneous measurement of $n_e(r)$ and $T_e(r)$ in the plasma edge. The line intensity ratios of the transitions in the singlet and triplet systems at the wavelengths $\lambda_1^S = 667.8$ nm ($3^1D – 2^1P$), $\lambda_2^S = 728.1$ nm ($3^1S – 2^1P$) and $\lambda_3^T = 706.5$ nm ($3^3S – 2^3P$) are calculated for a local position inside the plasma edge and compared with the values obtained from a collisional–radiative model which allows an unambiguous and simultaneous determination of the electron density and



**Figure 4.** C line (a) and Li line (c) profiles for $T_e$ profiles shown in Fig. 4b. Circles are the experimental profiles. The velocities of atomic beams are the same as in Fig. 3.
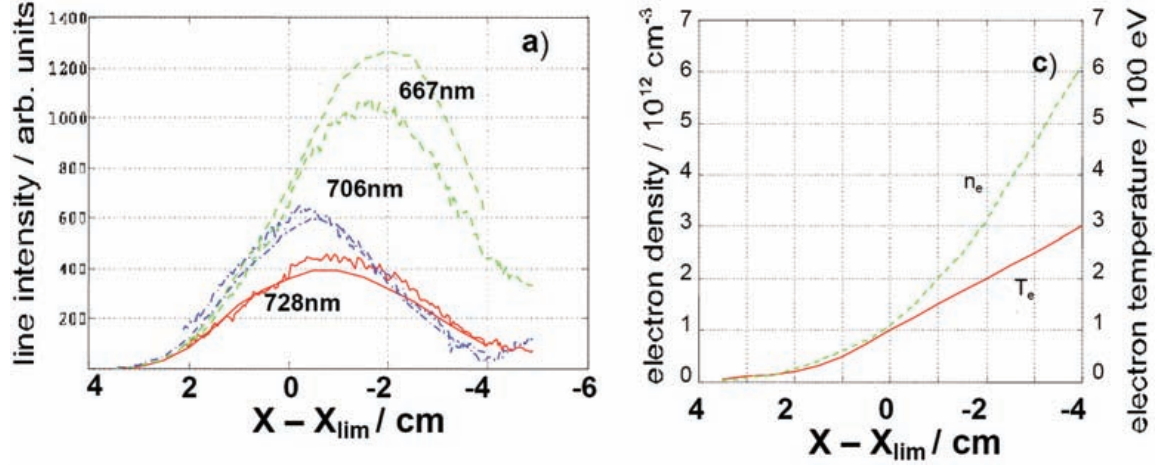
**Figure 5.** calculated (solid) and experimental (dashed) He-line profiles: a) without deuteron collisions, b) with deuteron collisions c) shows the respective electron density and temperature profiles used.
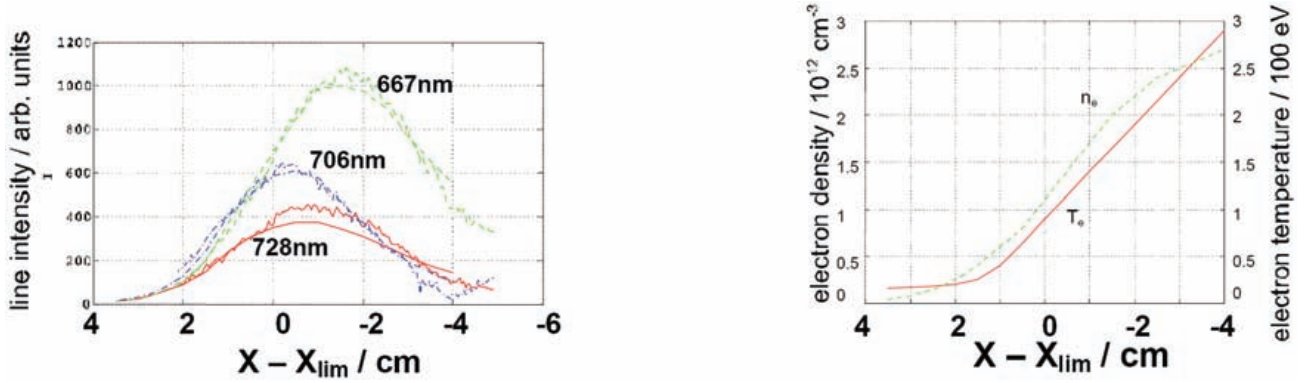


**Figure 6.** Calculated (solid) and experimental (dashed) He-line profiles: left - with deuteron collisions using a modified electron density profile - right

temperature. The profiles can be measured quasi-continuously with a time resolution of 1 ms.

However, it often turned out that a fit especially for the $\lambda_1^S = 667.8$ nm line was unsatisfactory at high plasma densities. For this purpose two codes optional to the general code ATOM, which provides for both the radial integrals, **AT**OM with **I**mpact **P**arameter **M**ethod (ATIPM with Coulomb-Born with normalisation) and **AT**OM **C**lose **C**oupling (ATCC - close coupling approach) - were developed [9]. These codes are based on the Coulomb-Born and close coupling approaches in the impact parameter representation. This representation is useful in the case when the mass and, hence, the orbital momentum of the incoming particle is large relative to electrons (p, d, etc.). He and He-like ions were used as an example to demonstrate different properties of the generalised Born calculations and to test the code ATIPM, which allow also an automatic calculation of large volumes of atomic data. ATIMP has been used to re-fit the experimental helium line emission profiles with the inclusion of deuteron collisions at high densities. The result can be seen in Fig. 5 and shows the influence of such processes. An even better fit can be obtained with a slight modification of $n_e(r)$ and $T_e(r)$. Fig. 6 displays the fits with a

double as high density profile as in Fig. 5, which allows a satisfactory agreement now between all measured and calculated He-line intensity profiles.

### 3.3. Boron

Boron is a rather important element in fusion plasma research because it has a number of advantages. This low-Z material is a good oxygen getter, and has a relatively high melting point of 2573K. The main applications of boron are the production of $B_4C$ coatings and the so-called 'boronization' [10] which means that by a special glow discharge with parts of $B_2H_6$ (diborane) or $B(CH_3)_3$ (trimethylboron) the internal surfaces of a fusion device are coated by a very thin layer of boron. This helps to improve the total confinement of the machine by the mitigation of impurity fluxes (e.g. oxygen or carbon) released from the wall. A major part within this work was to setup a CRM for boron and to compare the modelled with the experimentally determined S/XB.

The CRM for B II is very similar to the one described for O II (see below). The singly ionized boron lines seem to be more convenient than the one of the neutral boron
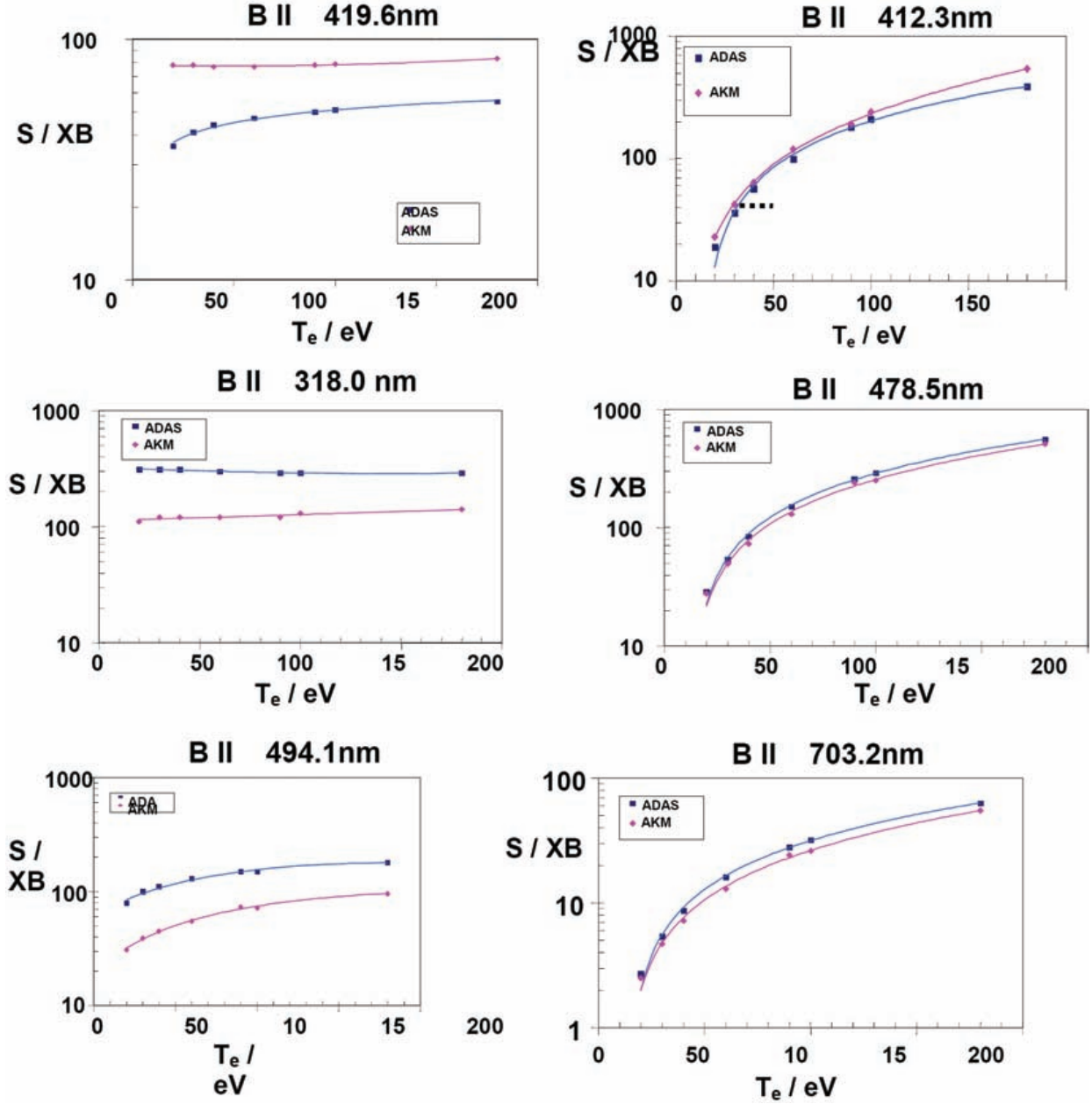
**Figure 7.** S /XB values versus $T_e$ for some of the B II lines of Table 1 in comparison with data from ADAS (■). The diamond bar represents values from a cross-calibration with a B I line at 249.7 nm, derived via the van Regemorter formula.

because both the strongest B I lines lie in the UV spectral range and the B II lines are less dependent on the dissociation processes and the properties of the injection mode. The atomic data implemented were calculated in the frame of the Coulomb-Born approach. Transitions between *2nl SL* levels for *n = 2-5*, all possible *l, S = 0; 1* (27 levels, 351 channels) were calculated by the AKM (*K*-matrix) code, transitions *2s-6l* and ionization are from ATOM.

The calculations mentioned do not take into the account the effect of the *configuration mixing* (CM). The comparison with the data obtained in the multi-configurational Hartree-Fock approach [11] shows that for transitions *2s2-2snp* this mixing can decrease the oscillator strength by a factor of about 1.5. The most important fact is the mixing between *2s2* and *2p2*. For transitions between excited states

CM is generally less important. The data were corrected using the ratios of the according oscillator strengths. Ionization cross-sections from the ground state of B II were calculated in Coulomb-Born with exchange and normalization approximations.

The results of the GKU calculations in the stationary approach for $n_e = 2\times10^{12}\text{cm}^{-3}$ and $n_e = 3.2\times10^{12}\text{cm}^{-3}$ for the respective S/XB-values are presented in Table 1 for the strongest B II lines. The temperature dependence of these values significantly depends on the population of the metastable level $2s2p^3P$. Therefore, measurements of the relative intensities between singlet and triplet lines are of particular importance.

Graphs of Tables 1 and 2, which for comparison also include numbers from ADAS [12], are provided in Fig. 7.

**Table 1a.** Calculated S/XB values as a function of electron temperature for the considered lines of BII and the 249.8nm line of BI for an electron density of $2\times10^{12}$cm$^{-3}$

| Upper level | 4f_3F | 4s_1S | 3p_3P | 4f_1F | 4p_3P | 4s_3S |
|---|---|---|---|---|---|---|
| Lower level | 3d_3D | 3p_1P | 3s_3S | 3d_1D | 3d_3D | 3p_3P |
| wavelength / nm | 412.3 | 419.6 | 703.2 | 494.1 | 478.5 | 447.3 |
| Te / eV | | | | | | |
| 20 | 2.30E+01 | 7.80E+01 | 2.50E+00 | 3.10E+01 | 2.80E+01 | 5.30E+01 |
| 30 | 4.20E+01 | 7.80E+01 | 4.70E+00 | 3.90E+01 | 4.90E+01 | 9.00E+01 |
| 40 | 6.40E+01 | 7.70E+01 | 7.20E+00 | 4.50E+01 | 7.30E+01 | 1.30E+02 |
| 60 | 1.20E+02 | 7.70E+01 | 1.30E+01 | 5.50E+01 | 1.30E+02 | 2.20E+02 |
| 90 | 1.90E+02 | 7.80E+01 | 2.40E+01 | 7.30E+01 | 2.40E+02 | 4.00E+02 |
| 100 | 2.40E+02 | 7.90E+01 | 2.60E+01 | 7.20E+01 | 2.50E+02 | 4.10E+02 |
| 180 | 5.40E+02 | 8.30E+01 | 5.50E+01 | 9.60E+01 | 5.10E+02 | 8.10E+02 |

| Upper level | 4d_3D | 5f_1F | 4d_1D | 2p_1P | 2p2_1D | [B I] 3s |
|---|---|---|---|---|---|---|
| Lower level | 3p_3P | 3d_1D | 3p_1P | 2s_1S | 2s_1P | [B I] 2p |
| wavelength / nm | 332.4 | 330.3 | 318 | 136.2 | 345.1 | 249.8 |
| Te / eV | | | | | | |
| 20 | 3.30E+01 | 1.00E+02 | 1.10E+02 | 1.10E-01 | 1.40E+00 | 3.76 |
| 30 | 5.50E+01 | 1.10E+02 | 1.20E+02 | 1.30E-01 | 2.10E+00 | 4.56 |
| 40 | 7.80E+01 | 1.20E+02 | 1.20E+02 | 1.50E-01 | 2.60E+00 | 5.12 |
| 60 | 1.30E+02 | 1.40E+02 | 1.20E+02 | 1.70E-01 | 3.40E+00 | 5.84 |
| 90 | 2.70E+02 | 1.40E+02 | 1.20E+02 | 1.90E-01 | 3.80E+00 | 6.54 |
| 100 | 2.30E+02 | 1.60E+02 | 1.30E+02 | 1.90E-01 | 4.40E+00 | |
| 180 | 4.40E+02 | 2.10E+02 | 1.40E+02 | 2.20E-01 | 5.60E+00 | |

**Table 1b.** Calculated S/XB values as a function of electron temperature for the considered lines of BII and the 249.8nm line of BI for an electron density of $3.2\times10^{13}$cm$^{-3}$

| Upper level | 4f_3F | 4s_1S | 3p_3P | 4f_1F | 4p_3P | 4s_3S |
|---|---|---|---|---|---|---|
| Lower level | 3d_3D | 3p_1P | 3s_3S | 3d_1D | 3d_3D | 3p_3P |
| wavelength / nm | 412.3 | 419.6 | 703.2 | 494.1 | 478.5 | 447.3 |
| Te / eV | | | | | | |
| 20 | 1.30E+01 | 1.20E+02 | 4.80E+00 | 2.90E+01 | 9.80E+01 | 5.60E+01 |
| 30 | 2.30E+01 | 1.20E+02 | 8.90E+00 | 3.20E+01 | 1.70E+02 | 9.50E+01 |
| 40 | 3.50E+01 | 1.10E+02 | 1.30E+01 | 3.50E+01 | 2.40E+02 | 1.40E+02 |
| 60 | 6.20E+01 | 1.10E+02 | 2.40E+01 | 3.80E+01 | 4.10E+02 | 2.20E+02 |
| 90 | 1.10E+02 | 1.00E+02 | 4.00E+01 | 4.30E+01 | 6.70E+02 | 3.70E+02 |
| 100 | 1.30E+02 | 1.00E+02 | 4.60E+01 | 4.40E+01 | 7.60E+02 | 4.20E+02 |
| 180 | 2.80E+02 | 1.00E+02 | 8.90E+01 | 5.30E+01 | 1.50E+03 | 8.20E+02 |

| Upper level | 4d_3D | 5f_1F | 4d_1D | 2p_1P | 2p2_1D | [B I] 3s |
|---|---|---|---|---|---|---|
| Lower level | 3p_3P | 3d_1D | 3p_1P | 2s_1S | 2s_1P | [B I] 2p |
| wavelength / nm | 332.4 | 330.3 | 318 | 136.2 | 345.1 | 249.8 |
| Te / eV | | | | | | |
| 20 | 3.00E+01 | 1.20E+02 | 1.40E+02 | 1.10E-01 | 1.40E+00 | 5.94 |
| 30 | 4.90E+01 | 1.30E+02 | 1.40E+02 | 1.40E-01 | 2.10E+00 | 7 |
| 40 | 6.90E+01 | 1.30E+02 | 1.40E+02 | 1.50E-01 | 2.70E+00 | 7.69 |
| 60 | 1.10E+02 | 1.30E+02 | 1.40E+02 | 1.70E-01 | 3.40E+00 | 8.49 |
| 90 | 1.90E+02 | 1.30E+02 | 1.40E+02 | 1.90E-01 | 4.20E+00 | 9.2 |
| 100 | 2.10E+02 | 1.30E+02 | 1.40E+02 | 1.90E-01 | 4.40E+00 | 9.37 |
| 180 | 4.20E+02 | 1.40E+02 | 1.50E+02 | 2.20E-01 | 5.60E+00 | |
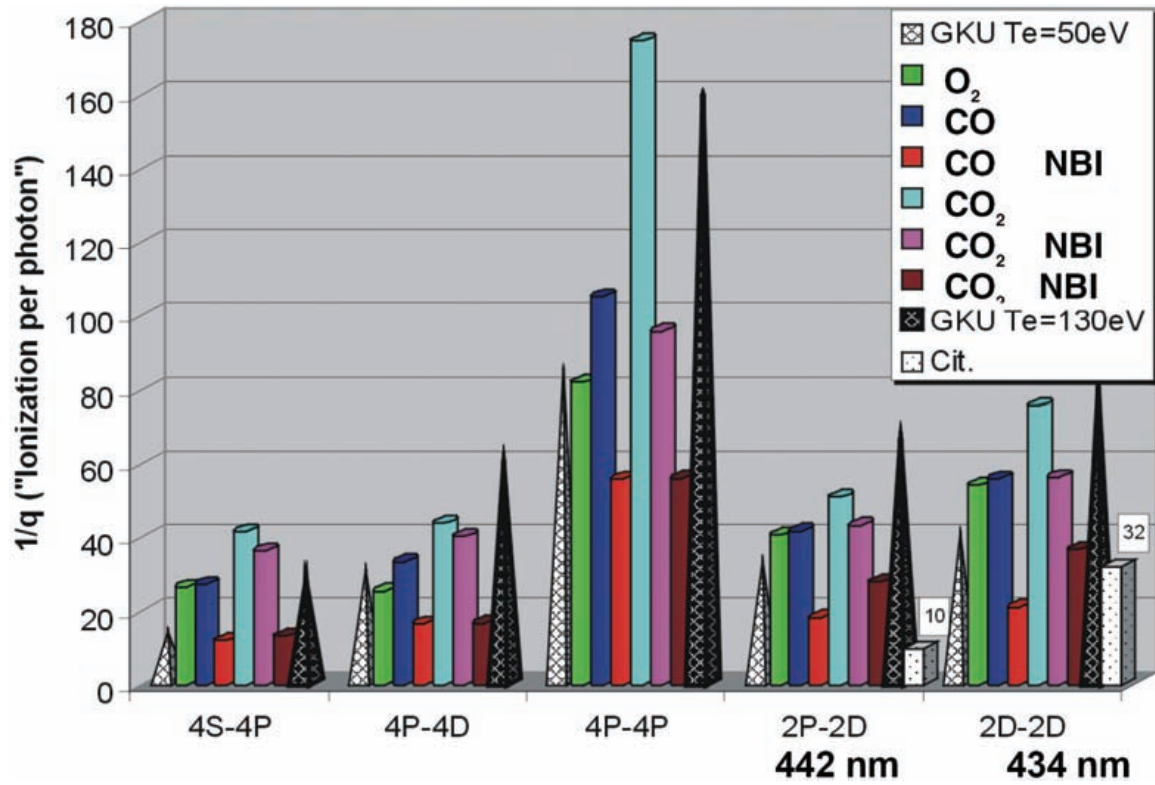
**Figure 8.** Comparison of the experimental (rods) and modelled (pyramids) *S/XB* (ionization per photon) values for different injected gases (see insert) and different plasma conditions.

The general trend is the same for both the data and the systems. For the triplet system the absolute agreement is excellent. However, data for the singlet system (which contains the ground state) differ by about a factor of 3, but do not show a temperature dependence, which favours them for the use in spectroscopic plasma edge diagnostics. The density dependence is in general small, which can be seen from the two tables. From experimental cross-calibration with a B I line at 249.7 nm, where the formula of van Regemorter [13] could be applied, an S/XB value was derived represented by the diamond bar. Therefore, the use of both the GKU- and ADAS-values can be recommended as both display the same temperature dependence. The reason for difference in absolute numbers in the singlet system is not known up to now, therefore, the most reliable values are those from the triplet system.

## 3.4. Oxygen

Spectra of the O II ion were obtained with temporal and spatial (along the poloidal radius) resolution by injecting oxygen-containing molecules through a block of the upper poloidal limiter of TEXTOR into the boundary plasma. Three different wavelength regions (466 ±10, 434 ±10, 373 ±10 nm) were observed during reproducible TEXTOR discharges with $n_e = 1 \times 10^{18} m^{-3}$, $T_e = 90$ eV at the last closed flux surface (LCFS).

The radial intensity distributions of lines corresponding to the transitions $2p^2[^3P]3s-2p^2[^3P]3p$ (components of the multiplets $^4P-^4S$, $^4P-^4P$, $^4P-^4D$, $^2P-^2D$) and $2p^2[^1D]3s-2p^2[^1D]3p$ (doublet $^2D-^2D$) were measured; the relative intensities of the lines inside the multiplets are in good agreement with theoretical data calculated in SL-coupling. An appropriate collisional-radiative model (the level list and the corresponding atomic database) has been developed and calculations have been carried out using the GKU kinetic code. Cross-sections of atomic processes have been calculated using the ATOM code in combination with the K-matrix method. With this it could be shown that the relative multiplet intensities have a weak dependence on electron density and temperature.

Absolute S/XB values for several O II lines were both measured and compared with modelled ones. The results are shown in Fig. 8 for a variety of injected oxygen containing gases and plasma conditions (e.g. with and without neutral beam (NBI) heating). There is a trend that for neutral beam heated discharges – i.e. higher plasma density – the S/XB values are somewhat smaller than for ohmic ones which may indicate the direction of a possible density dependence. Every transition range is framed by values from modelling for $T_e = 50$ eV and $T_e = 130$ eV; the numbers for the 442 and 434 nm lines have been taken from ADAS and are in agreement with the experiments for the 434 nm line, however, are in general smaller for 442 nm. Details for these measurements can be found in [14].
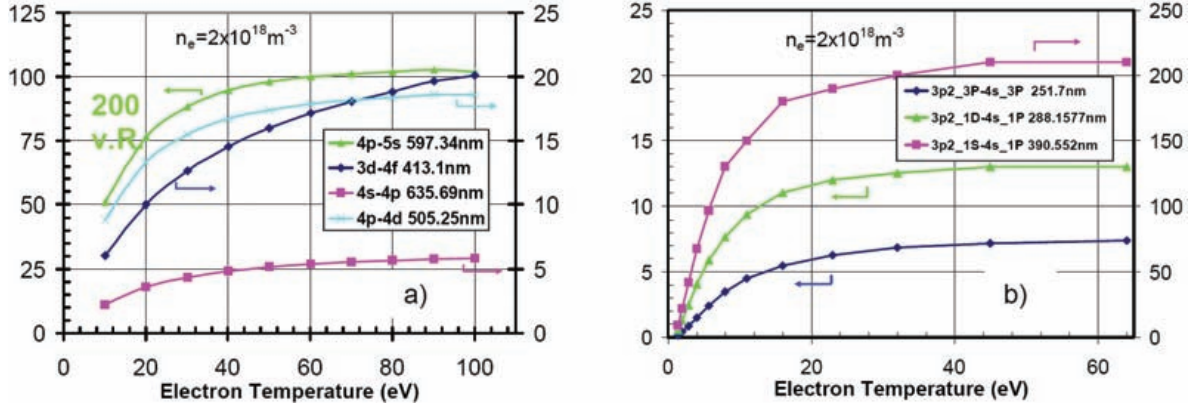
**Figure 9.** *S/XB* for several Si I-(b) and Si II-emissions (a) lines for an electron density of $2.0 \times 10^{18}$ m$^{-3}$.

## 3.5. Silicon

Measurements of Si I- and Si II-emission lines were performed in front of a test limiter under two different conditions:

a) silicon is sputtered from a silicon layer deposited on a graphite test limiter,

b) silane is puffed into the plasma through a gas inlet in the limiter head, releasing Si-atoms via dissociation of SiD$_4$ molecules.

The relative intensities of the emission lines within the multiplets were in good agreement with theoretical data calculated in the LS-coupling scheme.

The *S/XB* values have been calculated for the electron temperature range below 100 eV using the GKU kinetic code; the dependence on electron density is weak. Fig. 9a shows an example of *S/XB* ratios for Si II-emission lines for an electron density of $n_e = 2 \times 10^{18}$ m$^{-3}$. The strongest lines are the Si II-emission lines at 635.9 nm (sum over multiplet lines 634.711 and 637.137 nm) corresponding to the transition 3s$^2$($^2$S)4s–3s$^2$($^2$P)4p for which *S/XB* = 2–6 holds. Also the lines at 412.9 and 504.8 nm can be recommended for silicon flux measurements. An approximate calculation of the *S/XB* ratio for the line at 596.8 nm using the Regemorter formula [13] for the excitation rate results in a factor of two larger. This had in the past led to an overesti-

mation of silicon fluxes in [15,16]. Fig. 9b shows the *S/XB* ratio for Si I-emission lines at $n_e = 2 \times 10^{18}$ m$^{-3}$. These calculations were performed based on the assumption of a thermodynamical population of the 3p$^2$ SL terms ($^3$P, $^1$D and $^1$S). For silicon flux measurements, the Si I-emission lines at 251.7 nm (a strong emission line with *S/XB* = 7.0 for $T_e$ = 40 eV) and 288.155 nm (a strong emission line with *S/XB* = 13.0 for $T_e$ = 40 eV) seem to be the preferred choice. However, a disadvantage for the use of the Si I lines might lie in the accessibility in the UV region.

As said above, for lines with resolved fine structure, the relative intensities inside multiplets are in good agreement with the theoretical prediction. We consider below the sum over multiplet intensities, and the relative line intensities $r\lambda = I(\lambda)/I(\lambda_0)$ with respect to the line $\lambda_0$ = 412.9 nm (3d–4f). Under the assumption of identical silicon I and II fluxes, it follows that $r_\lambda = I(\lambda)/I(\lambda_0) = S/XB(\lambda_0)/SXB(\lambda)$ is valid. Fig. 10a shows the experimentally measured value $r\lambda$, performed in discharges with siliconized walls and identical plasma conditions, and the calculated $S/XB(\lambda_0)/SXB(\lambda)$ for three different Si II-emission lines for electron temperature $T_e$ = 40 eV and a local density $n_e = 2 \times 10^{18}$ m$^{-3}$ (Fig. 10b). The measured intensities ratios $I(\lambda)/I(\lambda_0)$ for the three emission lines match the calculated data ($S/XB(\lambda 0)/SXB(\lambda)$) very well: the deviation between measured and calculated values for the emission lines at 596.8 nm (sum
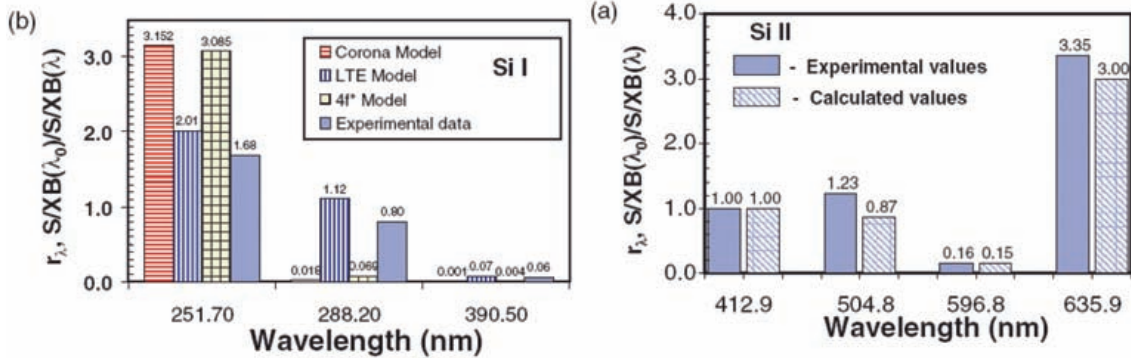


**Figure 10.** (a) Experimentally measured values $r_\lambda = I(\lambda)/I(\lambda 0)$ and calculated $S/XB(\lambda_0)/SXB(\lambda)$ for three different Si II-emission lines for an electron temperature $T_e$ = 40 eV and a density $n_e = 2 \times 10^{18}$ m$^{-3}$. (b) Comparison between the experimental ($r_\lambda$) and theoretical ($S/XB(\lambda_0)/SXB(\lambda)$) results with different model assumptions: corona, LTE and 4$f^*$-models.

**Table 2.** Comparison of absolute calculated (GKU) and measured *S/XB*-values. The exp. *S/XB* values for Si II were obtained in the experiment with $SiD_4$ puffing under the assumption, that one $Si^+$ ion and 4 deuterium atoms. The experimental *S/XB* values for Si I were obtained by cross-calibration with Si II emission lines

| | 3d-4f 412.9nm | 4s-4p 635.9nm | 4p-5s 596.8nm | 4p-4d 504.8nm |
|---|---|---|---|---|
| GKU | 14.5 | 4.95 | 90.0 | 16.5 |
| Exp. | 16.4 | 4.89 | 104.0 | 13.4 |

| | $3p^2\ ^3P-4s^3P$ 251.7nm | $3p^2\ ^1D-4s^1P$ 288.2nm | $3p^2\ ^1S-4s^1P$ 390.55nm |
|---|---|---|---|
| GKU | 7.2 | 13.0 | 210.0 |
| Exp. | 9.63 | 20.2 | 282.0 |

over multiplet lines 595.756 and 597.893 nm) and at 635.9 nm (sum over multiplet lines 634.711 and 637.137 nm) is smaller than 10% and for line 504.8 nm (sum over multiplet lines 504.1024 and 505.5984 nm) is about 29%.

One can see from Table 2 that the measured and theoretical values for the Si II emission lines are in reasonable agreement within a deviation of 30%. However, as mentioned above, the experimentally measured values for Si I lines match the calculated ones only when a thermodynamical population of $3p^2$ SL terms ($^3P$, $^1D$ and $^1S$) is assumed. More details for these measurements can be found in Ref. [17].

### 3.6. Hydrogen

Measurements at graphite limiters in TEXTOR indicated that, under cold surface conditions, the release is dominantly molecular [18]. If molecules are not taken into account, the Balmer-$\alpha$ measurement, a standard method for total hydrogen flux determination, leads to an underestimation of the total hydrogen flux $\Gamma_{tot}= \Gamma_A+ \Gamma_M$ by a factor up to two [19]. Thus, the measurement of $\Gamma_M$ – the molecular part of $\Gamma$ – is crucial. Fulcher-$\alpha$-band spectroscopy allows us to determine $\Gamma_M$ via the factor D/XB (the equivalent of S/XB for molecules), which is needed to convert the Fulcher-$\alpha$-band photons into the connected molecular flux. In general $\Gamma_{tot}$ cannot be determined from the Fulcher-band and the Balmer-$\alpha$ photon flux without additional information about the molecule to atom ratio and the number of atoms, which are released as such on the surface. Nevertheless, in the case of the not actively heated limiter in TEXTOR, we are able — with knowledge of the molecular flux $\Gamma_M$ — to determine $\Gamma_{tot}$ from the line emission of Balmer-$\alpha$. We can introduce an effective $(S/XB)_{eff}$ value which takes into account the molecular contribution in the conversion value empirically and thus 'corrects' the measured Balmer-$\alpha$ photon flux, $\phi_D$. $(S/XB)_{eff}$ is not constant but depends on the molecular flux, or more precisely, implicitly on the ratio of molecular to

atomic flux. $(S/XB)_{eff}$ may be written as $(S/XB)_{eff}$ = S/XB $(1 + (2\eta\Gamma_{D2}/\Gamma_{tot}))$, where $\eta$ is often nearly 1 under the conditions of a cold carbon wall.

In TEXTOR, experiments in deuterium have been performed to investigate the dependence of $\Gamma_M$ on the plasma parameters and validate the factor D/XB – calculated by a collisional radiative model (CRMOL) – in the range covered. For a correct conversion of the measured molecular photon flux one has to sum up the intensities of all lines belonging to a specific electronic transition band – for hydrogen Fulcher-$\alpha$ the $3p^3\Pi_u$ and the $2s^3\Sigma^+_g$ state. In practice this is – especially for hydrogen with its many line spectrum – a tedious matter. Therefore, a lot of effort has been put into a method to determine the full Fulcher-$\alpha$ emission from the measurement of a restricted number of lines. This technique has been described in [20] and will no longer be discussed here.

To determine D/XB, calibration experiments using an effusive nozzle have been done. For one plasma parameter set $6.5 \times 10^{19}$ $D_2$ particles have been injected and a comparison between both particle and photon fluxes results in a value for D/XB.

For an accurate calibration, several critical points have to be considered:

(a) The recycling flux has to be excluded from the injected flux. This can be achieved by using a nozzle with minimised surface area far away from other recycling objects as well as by a background subtraction.

(b) The injected amount has to be small enough to avoid any disturbances of the plasma and large enough for sufficient intensity. For this purpose, the injected flux has been limited to a low percentage of the usual recycling flux.

(c) Finally, the observation volume has to be large enough to detect all photons resulting from the injection.

A summation over all intensities and an additional extrapolation to the asymptotic value yields the photon flux and a D/XB value of 980±245 for $n_e$ = 0.5×10^18 m^{-3} and $T_e$ = 50eV is obtained. The collisional radiative model for hydrogen CRMOL [21] was used to take into account the $T_e$ and $n_e$ dependence of the relevant rate coefficients D and X and thus of D/XB. In addition to dissociation and ionisation, other loss processes like dissociative attachment were included in the calculations. CRMOL solves the coupled rate equations and provides the rate coefficients for the loss and excitation processes as a function of $n_e$ and $T_e$. Fig. 11 displays the variation of D/XB between 500 and 7000 in the respective TEXTOR boundary layer parameter range. A comparison with the calibration data suggests that D/XB varies between 750 and 1500 over the observed area. CRMOL calculates a value of 1040 for the region of maximum emission at r = 47 cm. Thus, the injection experiment confirms the model in the low $n_e$ regime.
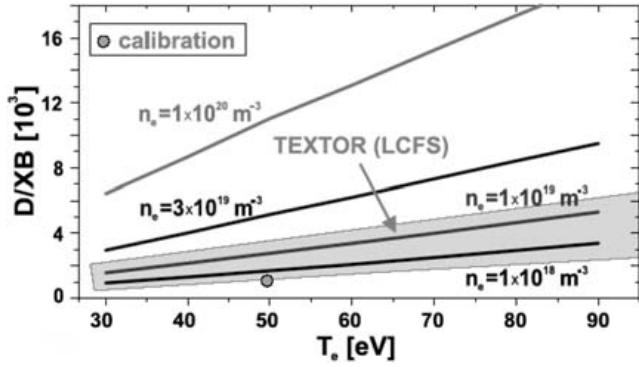
**Figure 11.** CRMOL calculations for the conversion factor D = XB. The experimentally obtained value is also indicated.

As pointed out above, the summation of all lines from the Fulcher-$\alpha$ emission band can be a difficult task especially in cases where all vibrational bands cannot be observed simultaneously during one discharge. Therefore, it would be highly desirable to have D/XBs at one's disposal which provide numbers for the vibrational branches individually. So it is only necessary to determine the intensity of a single vibrational transition. The respective D/XB values are shown in Table 3. More details of the respective experiments and values obtained can be found in Ref. [22].

*3.7. Hydrocarbons*

A reliable determination of hydrocarbon fluxes is a vital task since the introduction of carbon as PFC in fusion plasma devices. However, what looked promising after the work of [3] has turned out to be a major challenge in plasma wall interaction research. Strong discrepancies from the general trend have been reported by [23,24], but the reasons for these are still unclear – there might be stronger varying rates with density and temperature than published, problems in the molecular physics, and last but not least, influences from the emitting surfaces themselves on the measured molecular bands. Therefore, a clarification of the quantities used is urgently necessary.

Nearly all information about the molecular release of hydrocarbons from PFCs is presently obtained via the observation of molecular band radiation from CH/D (Gerö band: $A^2\pi$-$X^2\Delta$ around 430nm) and $C_2$ (Swan band: $d^3\Pi$-$a^3\Pi$ around 500nm) in the visible part of the spectrum. Whereas $C_2$ may still display some properties of the starting molecule ($C_2H_y$), the CH radical is at the very end of a long (and variable) dissociation chain via $CH_y^{(+)}$ ($1\le y \le 4$). Therefore, it may not be surprising that in the latter case the results from different machines look different. The underlying molecular processes and problems of molecular spectroscopy cannot be discussed here, although the latest developments in modelling and experiments will be presented. Further information about such processes and the (molecular) spectroscopy connected can be found in Ref. [25].

In the past simulations have been carried out using rate coefficients from Ehrhardt–Langer [26] for the different dissociation products starting from $CH_4$ have been used. These are compared to those using recent data from Brooks and co-workers [27,28] (for electron reactions) and from Janev et al. [29] (for proton reactions). Proton reactions play a major role at very low temperatures and lead in general to an increase of the D/XB. The rate coefficients for reactions between protons and $CD_2$ or CD radicals given from Janev are smaller than corresponding values according to Ehrhardt–Langer. In total, this results in smaller total rate coefficients for the data of Brooks/Janev.

Fig. 12 shows the influence of the different rate coefficients on photon efficiency D/XB. Only the temperature dependence is shown because the density does not affect D/XB under the simplifying assumptions. In general, the total rate coefficients according to Brooks/Janev are smaller for CD radicals. This results in longer lifetimes of these species and thus to a smaller value of D/XB compared to calculations where Ehrhardt–Langer data are used. This difference is particularly large at higher plasma temperatures but tends to decrease with decreasing temperature down to 5 eV and then increases again slightly with a further decrease of temperature. The increase of D/XB with decreasing temperature below $\approx 5$ eV is a result of a decreasing rate coefficient for excitation of the CD band [30], independent on the used rate coefficient database.

As already pointed out the presence of a surface during the chemical erosion process might lead to modifications of the D/XB value because of different erosion probabilities for virgin and for deposited carbon. With Brooks/Janev data eroded methane molecules return to a surface still as hydrocarbon because of low rate coefficients at high temperatures. From modelling of deposited layers on limiters in TEXTOR [31] it was concluded that the sticking of re-deposited carbon is very low. Since zero sticking is assumed, these hydrocarbons are re-ejected into the plasma as $CD_4$. They either return to the surface or finally leave the observation volume. Also the probability of becoming a CD radical decreases with Brooks/Janev data (the majority of
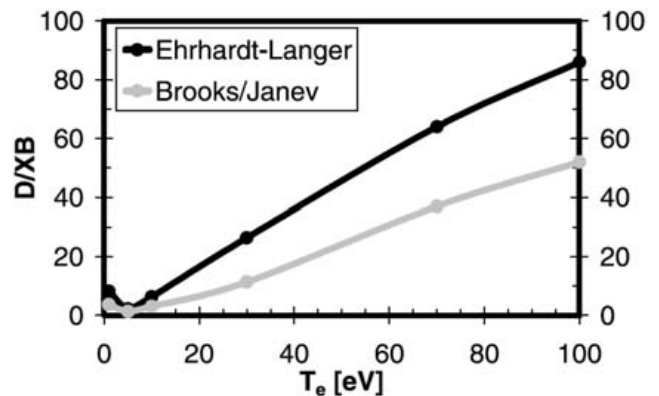


**Figure 12.** D/XB for CD from $CD_4$ in a homogenous plasma: usage of rate coefficients from the Ehrhardt–Langer database in comparison to data according to Brooks/Janev.

**Table 3.** Vibrationally resolved D/XB values for the Fulcher-α band transitions in $H_2$

### Electron density $= 1.00 \times 10^{18}$ m$^{-3}$

| $T_e$ (eV) \ $v=$ | 0 | 1 | 2 | 3 | 4 |
|---|---|---|---|---|---|
| 5.0 | 298.9 | 296.9 | 296.9 | 347.7 | 433.0 |
| 10.0 | 348.3 | 348.5 | 348.5 | 368.8 | 405.3 |
| 15.0 | 468.4 | 470.0 | 470.0 | 487.1 | 517.7 |
| 20.0 | 611.0 | 614.3 | 614.3 | 631.7 | 662.7 |
| 25.0 | 767.7 | 772.9 | 772.9 | 791.9 | 826.5 |
| 30.0 | 935.0 | 942.2 | 942.2 | 963.7 | 1004.0 |
| 35.0 | 1111.0 | 1120.0 | 1120.0 | 1145.0 | 1193.0 |
| 40.0 | 1293.0 | 1304.0 | 1304.0 | 1333.0 | 1392.0 |
| 45.0 | 1481.0 | 1494.0 | 1494.0 | 1528.0 | 1600.0 |

| $T_e$ (eV) \ $v=$ | 5 | 6 | 7 | 8 | 9 |
|---|---|---|---|---|---|
| 5.0 | 1599.0 | 1677.0 | 1766.0 | 1874.0 | 1916.0 |
| 10.0 | 933.4 | 960.0 | 984.1 | 1009.0 | 1022.0 |
| 15.0 | 1018.0 | 1038.0 | 1054.0 | 1069.0 | 1078.0 |
| 20.0 | 1207.0 | 1224.0 | 1238.0 | 1251.0 | 1259.0 |
| 25.0 | 1438.0 | 1455.0 | 1468.0 | 1481.0 | 1489.0 |
| 30.0 | 1695.0 | 1713.0 | 1726.0 | 1739.0 | 1748.0 |
| 35.0 | 1971.0 | 1989.0 | 2003.0 | 2017.0 | 2027.0 |
| 40.0 | 2261.0 | 2280.0 | 2295.0 | 2309.0 | 2321.0 |
| 45.0 | 2564.0 | 2583.0 | 2599.0 | 2614.0 | 2627.0 |

| $T_e$ (eV) \ $v=$ | 10 | 11 | 12 | 13 | 14 |
|---|---|---|---|---|---|
| 5.0 | 1898.0 | 1905.0 | 1904.0 | 1904.0 | 1899.0 |
| 10.0 | 1023.0 | 1027.0 | 1028.0 | 1028.0 | 1024.0 |
| 15.0 | 1081.0 | 1085.0 | 1087.0 | 1086.0 | 1082.0 |
| 20.0 | 1264.0 | 1268.0 | 1270.0 | 1270.0 | 1264.0 |
| 25.0 | 1495.0 | 1500.0 | 1503.0 | 1502.0 | 1496.0 |
| 30.0 | 1755.0 | 1761.0 | 1764.0 | 1762.0 | 1755.0 |
| 35.0 | 2035.0 | 2041.0 | 2044.0 | 2043.0 | 2035.0 |
| 40.0 | 2330.0 | 2337.0 | 2340.0 | 2338.0 | 2330.0 |
| 45.0 | 2637.0 | 2645.0 | 2648.0 | 2646.0 | 2636.0 |

### Electron density $= 3.20 \times 10^{18}$ m$^{-3}$

| $T_e$ (eV) \ $v=$ | 0 | 1 | 2 | 3 | 4 |
|---|---|---|---|---|---|
| 5.0 | 344.3 | 342.1 | 342.1 | 400.1 | 497.3 |
| 10.0 | 410.4 | 410.7 | 410.7 | 434.3 | 476.6 |
| 15.0 | 556.0 | 558.1 | 558.1 | 578.1 | 613.8 |
| 20.0 | 726.9 | 731.1 | 731.1 | 751.4 | 787.6 |
| 25.0 | 913.4 | 919.9 | 919.9 | 942.1 | 982.4 |
| 30.0 | 1111.0 | 1120.0 | 1120.0 | 1145.0 | 1192.0 |
| 35.0 | 1318.0 | 1329.0 | 1329.0 | 1358.0 | 1415.0 |
| 40.0 | 1532.0 | 1545.0 | 1545.0 | 1579.0 | 1647.0 |
| 45.0 | 1751.0 | 1767.0 | 1767.0 | 1806.0 | 1890.0 |

| $T_e$ (eV) \ $v=$ | 5 | 6 | 7 | 8 | 9 |
|---|---|---|---|---|---|
| 5.0 | 1829.0 | 1918.0 | 2019.0 | 2141.0 | 2190.0 |
| 10.0 | 1090.0 | 1121.0 | 1149.0 | 1178.0 | 1192.0 |
| 15.0 | 1198.0 | 1221.0 | 1240.0 | 1258.0 | 1267.0 |
| 20.0 | 1424.0 | 1444.0 | 1460.0 | 1475.0 | 1484.0 |
| 25.0 | 1697.0 | 1717.0 | 1732.0 | 1747.0 | 1756.0 |
| 30.0 | 1999.0 | 2019.0 | 2035.0 | 2050.0 | 2060.0 |
| 35.0 | 2322.0 | 2342.0 | 2358.0 | 2374.0 | 2385.0 |
| 40.0 | 2659.0 | 2680.0 | 2697.0 | 2714.0 | 2727.0 |
| 45.0 | 3008.0 | 3031.0 | 3048.0 | 3066.0 | 3080.0 |

| $T_e$ (eV) \ $v=$ | 10 | 11 | 12 | 13 | 14 |
|---|---|---|---|---|---|
| 5.0 | 2169.0 | 2177.0 | 2175.0 | 2175.0 | 2170.0 |
| 10.0 | 1193.0 | 1198.0 | 1200.0 | 1199.0 | 1195.0 |
| 15.0 | 1271.0 | 1276.0 | 1278.0 | 1277.0 | 1272.0 |
| 20.0 | 1490.0 | 1495.0 | 1498.0 | 1497.0 | 1491.0 |
| 25.0 | 1763.0 | 1769.0 | 1772.0 | 1771.0 | 1764.0 |
| 30.0 | 2068.0 | 2075.0 | 2078.0 | 2076.0 | 2068.0 |
| 35.0 | 2395.0 | 2402.0 | 2405.0 | 2403.0 | 2395.0 |
| 40.0 | 2737.0 | 2745.0 | 2748.0 | 2746.0 | 2736.0 |
| 45.0 | 3092.0 | 3100.0 | 3104.0 | 3101.0 | 3091.0 |

### Electron density $= 1.00 \times 10^{19}$ m$^{-3}$

| $T_e$ (eV) \ $v=$ | 0 | 1 | 2 | 3 | 4 |
|---|---|---|---|---|---|
| 5.0 | 447.9 | 445.2 | 445.2 | 520.0 | 645.1 |
| 10.0 | 560.2 | 561.2 | 561.2 | 592.9 | 649.7 |
| 15.0 | 771.8 | 775.6 | 775.6 | 802.8 | 851.3 |
| 20.0 | 1015.0 | 1022.0 | 1022.0 | 1050.0 | 1099.0 |
| 25.0 | 1278.0 | 1289.0 | 1289.0 | 1319.0 | 1374.0 |
| 30.0 | 1554.0 | 1568.0 | 1568.0 | 1602.0 | 1666.0 |
| 35.0 | 1840.0 | 1858.0 | 1858.0 | 1897.0 | 1974.0 |
| 40.0 | 2133.0 | 2155.0 | 2155.0 | 2200.0 | 2293.0 |
| 45.0 | 2432.0 | 2457.0 | 2457.0 | 2509.0 | 2622.0 |

| $T_e$ (eV) \ $v=$ | 5 | 6 | 7 | 8 | 9 |
|---|---|---|---|---|---|
| 5.0 | 2361.0 | 2475.0 | 2605.0 | 2761.0 | 2822.0 |
| 10.0 | 1473.0 | 1514.0 | 1551.0 | 1589.0 | 1608.0 |
| 15.0 | 1646.0 | 1676.0 | 1701.0 | 1726.0 | 1738.0 |
| 20.0 | 1968.0 | 1995.0 | 2017.0 | 2037.0 | 2049.0 |
| 25.0 | 2350.0 | 2376.0 | 2397.0 | 2416.0 | 2429.0 |
| 30.0 | 2767.0 | 2793.0 | 2814.0 | 2834.0 | 2847.0 |
| 35.0 | 3207.0 | 3235.0 | 3256.0 | 3276.0 | 3291.0 |
| 40.0 | 3664.0 | 3692.0 | 3714.0 | 3736.0 | 3752.0 |
| 45.0 | 4135.0 | 4164.0 | 4187.0 | 4210.0 | 4228.0 |

| $T_e$ (eV) \ $v=$ | 10 | 11 | 12 | 13 | 14 |
|---|---|---|---|---|---|
| 5.0 | 2795.0 | 2804.0 | 2801.0 | 2801.0 | 2795.0 |
| 10.0 | 1610.0 | 1616.0 | 1618.0 | 1618.0 | 1612.0 |
| 15.0 | 1744.0 | 1750.0 | 1753.0 | 1752.0 | 1745.0 |
| 20.0 | 2056.0 | 2063.0 | 2066.0 | 2065.0 | 2057.0 |
| 25.0 | 2438.0 | 2445.0 | 2449.0 | 2447.0 | 2438.0 |
| 30.0 | 2858.0 | 2866.0 | 2870.0 | 2868.0 | 2858.0 |
| 35.0 | 3303.0 | 3312.0 | 3316.0 | 3314.0 | 3302.0 |
| 40.0 | 3766.0 | 3776.0 | 3780.0 | 3777.0 | 3765.0 |
| 45.0 | 4242.0 | 4253.0 | 4257.0 | 4254.0 | 4240.0 |

### Electron density $= 3.20 \times 10^{19}$ m$^{-3}$

| $T_e$ (eV) \ $v=$ | 0 | 1 | 2 | 3 | 4 |
|---|---|---|---|---|---|
| 5.0 | 751.9 | 748.0 | 748.0 | 872.6 | 1080.0 |
| 10.0 | 990.9 | 994.8 | 994.8 | 1050.0 | 1149.0 |
| 15.0 | 1389.0 | 1399.0 | 1399.0 | 1448.0 | 1533.0 |
| 20.0 | 1837.0 | 1856.0 | 1856.0 | 1905.0 | 1992.0 |
| 25.0 | 2314.0 | 2341.0 | 2341.0 | 2394.0 | 2491.0 |
| 30.0 | 2810.0 | 2845.0 | 2845.0 | 2905.0 | 3016.0 |
| 35.0 | 3318.0 | 3362.0 | 3362.0 | 3429.0 | 3562.0 |
| 40.0 | 3833.0 | 3884.0 | 3884.0 | 3961.0 | 4121.0 |
| 45.0 | 4355.0 | 4413.0 | 4413.0 | 4502.0 | 4694.0 |

| $T_e$ (eV) \ $v=$ | 5 | 6 | 7 | 8 | 9 |
|---|---|---|---|---|---|
| 5.0 | 3921.0 | 4107.0 | 4317.0 | 4572.0 | 4670.0 |
| 10.0 | 2568.0 | 2638.0 | 2702.0 | 2767.0 | 2800.0 |
| 15.0 | 2919.0 | 2972.0 | 3015.0 | 3057.0 | 3078.0 |
| 20.0 | 3510.0 | 3557.0 | 3594.0 | 3628.0 | 3648.0 |
| 25.0 | 4195.0 | 4240.0 | 4274.0 | 4307.0 | 4327.0 |
| 30.0 | 4932.0 | 4976.0 | 5009.0 | 5041.0 | 5063.0 |
| 35.0 | 5701.0 | 5745.0 | 5778.0 | 5811.0 | 5834.0 |
| 40.0 | 6489.0 | 6534.0 | 6568.0 | 6601.0 | 6625.0 |
| 45.0 | 7294.0 | 7338.0 | 7373.0 | 7406.0 | 7432.0 |

| $T_e$ (eV) \ $v=$ | 10 | 11 | 12 | 13 | 14 |
|---|---|---|---|---|---|
| 5.0 | 4622.0 | 4633.0 | 4624.0 | 4623.0 | 4616.0 |
| 10.0 | 2802.0 | 2811.0 | 2815.0 | 2814.0 | 2805.0 |
| 15.0 | 3087.0 | 3097.0 | 3102.0 | 3101.0 | 3089.0 |
| 20.0 | 3660.0 | 3672.0 | 3677.0 | 3674.0 | 3661.0 |
| 25.0 | 4341.0 | 4354.0 | 4359.0 | 4356.0 | 4342.0 |
| 30.0 | 5079.0 | 5093.0 | 5098.0 | 5095.0 | 5078.0 |
| 35.0 | 5852.0 | 5866.0 | 5871.0 | 5867.0 | 5849.0 |
| 40.0 | 6644.0 | 6659.0 | 6665.0 | 6659.0 | 6640.0 |
| 45.0 | 7452.0 | 7467.0 | 7473.0 | 7467.0 | 7447.0 |

## Electron density = $1.00 \times 10^{20}$ m$^{-3}$

| $T_e$ (eV) \ $v=$ | 0 | 1 | 2 | 3 | 4 |
|---|---|---|---|---|---|
| 5.0 | 1678.0 | 1672.0 | 1672.0 | 1950.0 | 2409.0 |
| 10.0 | 2270.0 | 2290.0 | 2290.0 | 2418.0 | 2647.0 |
| 15.0 | 3195.0 | 3239.0 | 3239.0 | 3351.0 | 3549.0 |
| 20.0 | 4216.0 | 4287.0 | 4287.0 | 4401.0 | 4600.0 |
| 25.0 | 5286.0 | 5384.0 | 5384.0 | 5505.0 | 5722.0 |
| 30.0 | 6382.0 | 6507.0 | 6507.0 | 6640.0 | 6886.0 |
| 35.0 | 7492.0 | 7644.0 | 7644.0 | 7791.0 | 8078.0 |
| 40.0 | 8600.0 | 8777.0 | 8777.0 | 8942.0 | 9281.0 |
| 45.0 | 9715.0 | 9914.0 | 9914.0 | 10100.0 | 10500.0 |

| $T_e$ (eV) \ $v=$ | 5 | 6 | 7 | 8 | 9 |
|---|---|---|---|---|---|
| 5.0 | 8570.0 | 8960.0 | 9393.0 | 9925.0 | 10120.0 |
| 10.0 | 5771.0 | 5924.0 | 6063.0 | 6205.0 | 6274.0 |
| 15.0 | 6599.0 | 6716.0 | 6809.0 | 6901.0 | 6948.0 |
| 20.0 | 7925.0 | 8026.0 | 8104.0 | 8179.0 | 8220.0 |
| 25.0 | 9430.0 | 9523.0 | 9594.0 | 9660.0 | 9699.0 |
| 30.0 | 11020.0 | 11110.0 | 11180.0 | 11240.0 | 11280.0 |
| 35.0 | 12660.0 | 12750.0 | 12810.0 | 12860.0 | 12900.0 |
| 40.0 | 14320.0 | 14400.0 | 14460.0 | 14510.0 | 14540.0 |
| 45.0 | 16000.0 | 16070.0 | 16120.0 | 16170.0 | 16200.0 |

| $T_e$ (eV) \ $v=$ | 10 | 11 | 12 | 13 | 14 |
|---|---|---|---|---|---|
| 5.0 | 9998.0 | 10000.0 | 9966.0 | 9963.0 | 9958.0 |
| 10.0 | 6277.0 | 6297.0 | 6305.0 | 6303.0 | 6285.0 |
| 15.0 | 6967.0 | 6989.0 | 7000.0 | 6997.0 | 6974.0 |
| 20.0 | 8245.0 | 8269.0 | 8280.0 | 8276.0 | 8249.0 |
| 25.0 | 9727.0 | 9751.0 | 9762.0 | 9756.0 | 9728.0 |
| 30.0 | 11300.0 | 11330.0 | 11340.0 | 11330.0 | 11300.0 |
| 35.0 | 12930.0 | 12950.0 | 12960.0 | 12950.0 | 12920.0 |
| 40.0 | 14570.0 | 14590.0 | 14590.0 | 14580.0 | 14550.0 |
| 45.0 | 16220.0 | 16240.0 | 16240.0 | 16230.0 | 16200.0 |

## Electron density = $3.20 \times 10^{20}$ m$^{-3}$

| $T_e$ (eV) \ $v=$ | 0 | 1 | 2 | 3 | 4 |
|---|---|---|---|---|---|
| 5.0 | 4749.0 | 4754.0 | 4754.0 | 5546.0 | 6858.0 |
| 10.0 | 6518.0 | 6631.0 | 6631.0 | 7023.0 | 7721.0 |
| 15.0 | 9132.0 | 9355.0 | 9355.0 | 9701.0 | 10300.0 |
| 20.0 | 11940.0 | 12280.0 | 12280.0 | 12630.0 | 13220.0 |
| 25.0 | 14830.0 | 15280.0 | 15280.0 | 15640.0 | 16260.0 |
| 30.0 | 17730.0 | 18290.0 | 18290.0 | 18680.0 | 19350.0 |
| 35.0 | 20610.0 | 21290.0 | 21290.0 | 21690.0 | 22450.0 |
| 40.0 | 23450.0 | 24220.0 | 24220.0 | 24650.0 | 25520.0 |
| 45.0 | 26250.0 | 27120.0 | 27120.0 | 27590.0 | 28590.0 |

| $T_e$ (eV) \ $v=$ | 5 | 6 | 7 | 8 | 9 |
|---|---|---|---|---|---|
| 5.0 | 23180.0 | 24140.0 | 25160.0 | 26450.0 | 26850.0 |
| 10.0 | 16040.0 | 16460.0 | 16830.0 | 17200.0 | 17390.0 |
| 15.0 | 18380.0 | 18700.0 | 18960.0 | 19210.0 | 19340.0 |
| 20.0 | 21950.0 | 22220.0 | 22430.0 | 22620.0 | 22730.0 |
| 25.0 | 25900.0 | 26130.0 | 26300.0 | 26460.0 | 26550.0 |
| 30.0 | 29990.0 | 30180.0 | 30320.0 | 30450.0 | 30520.0 |
| 35.0 | 34120.0 | 34270.0 | 34380.0 | 34470.0 | 34520.0 |
| 40.0 | 38220.0 | 38330.0 | 38400.0 | 38460.0 | 38470.0 |
| 45.0 | 42290.0 | 42350.0 | 42380.0 | 42400.0 | 42380.0 |

| $T_e$ (eV) \ $v=$ | 10 | 11 | 12 | 13 | 14 |
|---|---|---|---|---|---|
| 5.0 | 26460.0 | 26370.0 | 26170.0 | 26160.0 | 26200.0 |
| 10.0 | 17400.0 | 17450.0 | 17470.0 | 17470.0 | 17420.0 |
| 15.0 | 19400.0 | 19460.0 | 19490.0 | 19490.0 | 19430.0 |
| 20.0 | 22800.0 | 22860.0 | 22890.0 | 22890.0 | 22830.0 |
| 25.0 | 26620.0 | 26670.0 | 26700.0 | 26690.0 | 26630.0 |
| 30.0 | 30570.0 | 30610.0 | 30630.0 | 30620.0 | 30560.0 |
| 35.0 | 34550.0 | 34570.0 | 34580.0 | 34560.0 | 34520.0 |
| 40.0 | 38470.0 | 38480.0 | 38470.0 | 38450.0 | 38420.0 |
| 45.0 | 42350.0 | 42330.0 | 42320.0 | 42290.0 | 42270.0 |

hydrocarbons hit the surface even before becoming a CD) which leads to significantly higher D/XB at high temperatures (Fig. 13).

Compared with experimental values [32], the modelled D/XB values are up to a factor of 100 higher for Brooks/Janev whereas the use of Ehrhardt– Langer data gives a better agreement. At smaller temperatures the difference between simulated D/XB values using Ehrhardt–Langer or Brooks/Janev data decreases and is negligible at temperatures smaller than 5 eV. The extremely high D/XB values in the Brooks/Janev case at higher temperatures can mainly be attributed to the neglected reactions for charged radicals $CD_x^+$ in the Brooks database. From the resulting discrepancy of Brooks/Janov compared to measurements (as
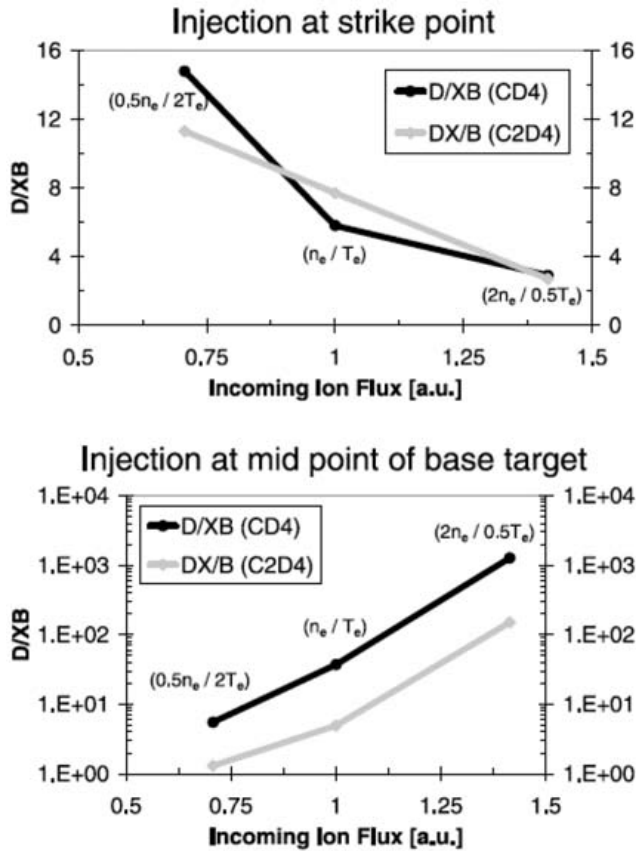
opposed to the Ehrhardt–Langer case) one can conclude that neglecting these reactions in the Brooks database is not justified at higher temperatures.

Fig. 14 presents calculated D/XB values for CD band emission from externally injected $CD_4$ and $C_2D_4$ molecules for two locations of injection in the JET divertor in dependence on the incoming particle flux. The flux is normalised to the reference case ($n_e$, $T_e$). Increasing the particle flux, injection at the strike point causes decreasing D/XB values (from 16 to 2). There is no significant difference in D/XB between $CD_4$ and $C_2D_4$ injection. Hydrocarbon injection at the mid point of the base target results in a completely different behaviour: D/XB increases with increasing flux and therefore decreasing temperature. Extremely high values are reached at the maximum flux (D/XB > 1000 for $CD_4$). This is a consequence of lower temperatures near the puffing location and the strong decrease of the rate coefficient for CD band excitation with decreasing temperature for $T_e$ smaller than 1 eV [30]. In addition, the D/XB values resulting from $C_2D_4$ injection are significantly smaller than for $CD_4$ injection.

For technical reasons experimental determinations of D/XB for $CD_4$ via CD and by means of puffing $CD_4$ into the edge plasma could not be completed in TEXTOR. However, similar experiments in JET have been performed with injection of $CD_4$ and $C_2H_4$ through different gas injection modules (GIMs) into the inner and outer divertor. A sketch of the geometry and the location of the GIMs is shown in Fig. 15.



**Figure 13.** D/XB for CD from $CD_4$ as a result of chemically eroded $CD_4$ at a TEXTOR test-limiter surface in dependence of $T_e$ and $n_e$: Ehrhardt–Langer data vs. Brooks/Janev data.
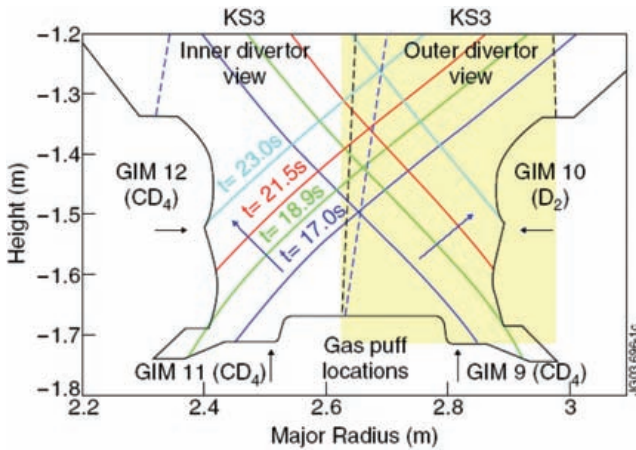
**Figure 14.** D/XB for CD from externally injected $CD_4$ and $C_2D_4$ into the divertor MkIIa of JET.



**Figure 15.** The magnetic configurations for four different times of the discharges used, showing the gas fuelling locations and fields of view (shaded and coloured area represents the inner and outer view, respectively) of the survey spectrometer (KS3).

A fixed amount of $CD_4$ was puffed through GIM 9, 11, 12 while the plasma was moved into the direction indicated in the figure. GIM 10 was used for reference discharges with $D_2$-puffs in order to find the correct amount for compensation and calibration versus the deuterium flux. The result for the behaviour of D/XB as a function of time (corresponding to different strike point locations) and derived for the inner divertor according to equation (2), is displayed in Fig. 16.
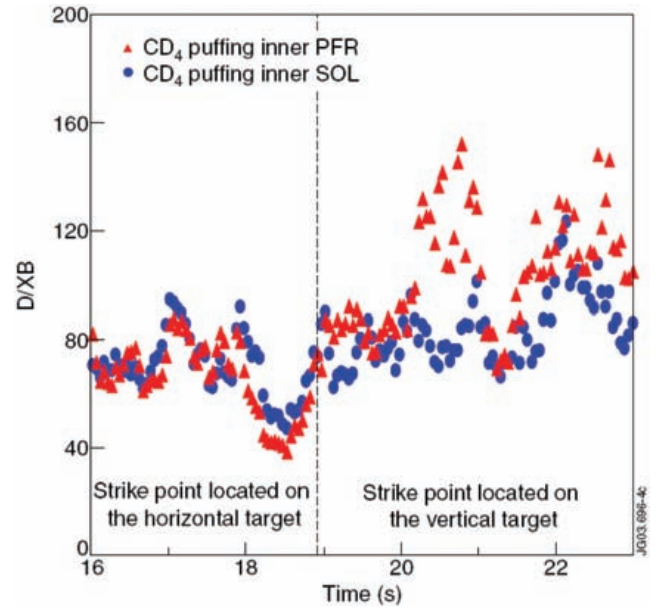


**Figure 16.** Time evolution of the D/XB-value for methane measured during the puffing of known $CD_4$ sources into the inner PFR. During 17 to 23.1s, the strike point was moved from horizontal target to the vertical divertor target.

The ratio increases from 70 to about 120 during the strike point sweep over horizontal and vertical target. The D/XB value between 18s and 19s decreases up to value of 40. During this time window, the strike point was moved over the inner divertor corner and the emission of $C_2$ Swan-band (at 516 nm [33,34]) becomes very strong, indicating the increase of non-methane hydrocarbons sources. These higher hydrocarbons may also contribute to the emission of CD photons after their catabolism [35]. This leads to an underestimation of the D/XB values in the time window between 18s and 19s. One should also have in mind that the plasma conditions in the inner divertor show a high electron density ($> 10^{20}m^{-3}$) and a low electron temperature ($< 10eV$).

Outer divertor $CD_4$ fuelling into the PFR shows a small increase of CD emission signal with the strike point on the horizontal divertor target, whereas the CD signal is doubled during the strike point sweep over the vertical target. This indicates the strong dependence of D/XB-value on the location of methane sources in the outer divertor. The D/XB-values with the strike point on the horizontal target are much smaller than D/XB-values on the vertical target which amounts to approximately 100 [25,36].

The latter authors have also performed intensive experiments to study the contribution of higher order hydrocarbons ($C_xH_y$ with $x \geq 2$) on the CD-value. These evaluations are still under critical discussion because the injection through GIM 9 into the PFR was found to be not so homogeneous as supposed. However, the injection through GIM 10 resulted in D/XB values for the molecular release of $C_2$ from these higher order hydrocarbons. The particle flux of $C_2$ radicals can be determined from the observation of the $d^3\Pi$ - $a^3\Pi_u$ transition - the so-called Swan-band. But the detection of the complete spectrum of the electronic

transition is challenging. In comparison to CD, more main diagonal transitions which are spread over a wider range can be observed, and non-diagonal transitions contribute significantly to the total intensity of the Swan-band. More information about the spectrum and examples are given in [37,38]. Due to practical reasons, only a minor part of the spectrum is observed - usually the band head of the (0-0) transition at 516.6 nm. However, a variety of different observation ranges and transitions, e.g. the (1-0) band at 565 nm, are observed additionally (TEXTOR [32] and JT60-U [38]). Further details about these measurements can be found in Refs. [25,39]

The variation of D/XB for the (0-0) transition at 516.6 nm of $C_2$ in JET during strike point variations and the simultaneous injection of $C_2H_4$ through GIM 10 is displayed in Fig. 17. The most reliable value is indicated by an ellipsoid when the strike point is located at GIM 10 and amounts to about 2000. This value is in good agreement with the one found earlier in hydrocarbon blow experiments in PISCES-A [3].

## 4.    Summary

For a number of particles appearing in fusion plasma boundary research rate coefficients for excitation and ionisation and/or so called "S(D)/XB" values have been either experimentally obtained and/or modelled. The results can be comprised for the individual species as following:

*Lithium and carbon:* excitation and ionisation of atoms have now been sufficiently well modelled to fit the experimentally obtained light emission profiles.

*Helium:* The inclusion of heavy particle collisions has led to a better fit of the experimental with the calculated line emission profiles. This resulted also in an increase of the boundary temperature by about a factor of 2.

*Boron:* Modelled S/XB values for B II fit well with experimental ones and agree also well among each other in the case of the triplet system.

*Oxygen:* S/XB values for a number O II lines in the blue wavelength range have been calculated. The ones known already agree with the new calculations.

*Silicon:* S/XB values for Si I and Si II have been calculated and experimentally determined. This has lead to corrections of values obtained by the van Regemorter formula.

*Hydrogen/deuterium:* Since a couple of years also collisional radiative models exist for the calculation of the corresponding D/XB- values. For few plasma conditions these could be experimentally verified. Extensive tables now allow also the determination of hydrogen molecular fluxes at various different plasma boundary conditions.

*Hydrocarbons:* The determination of D/XB values for CH (from $CH_4$)and $C_2$ (from $C_2H_y$) is still an ongoing business. The presence of extended surfaces near the source can lead to strong variations in these numbers. It was found that the "pure" values obtained earlier are in good agreement with latest experimental results from TEXTOR and JET.

## References

[1]    BOGEN, P., HARTWIG, H., HINTZ, E., HÖTHKER, K., LIE, Y.T., POSPIESZCZYK, A., SAMM, U., BIEGER, W., J. Nucl. Mater., **128 & 129** (1984) 157.
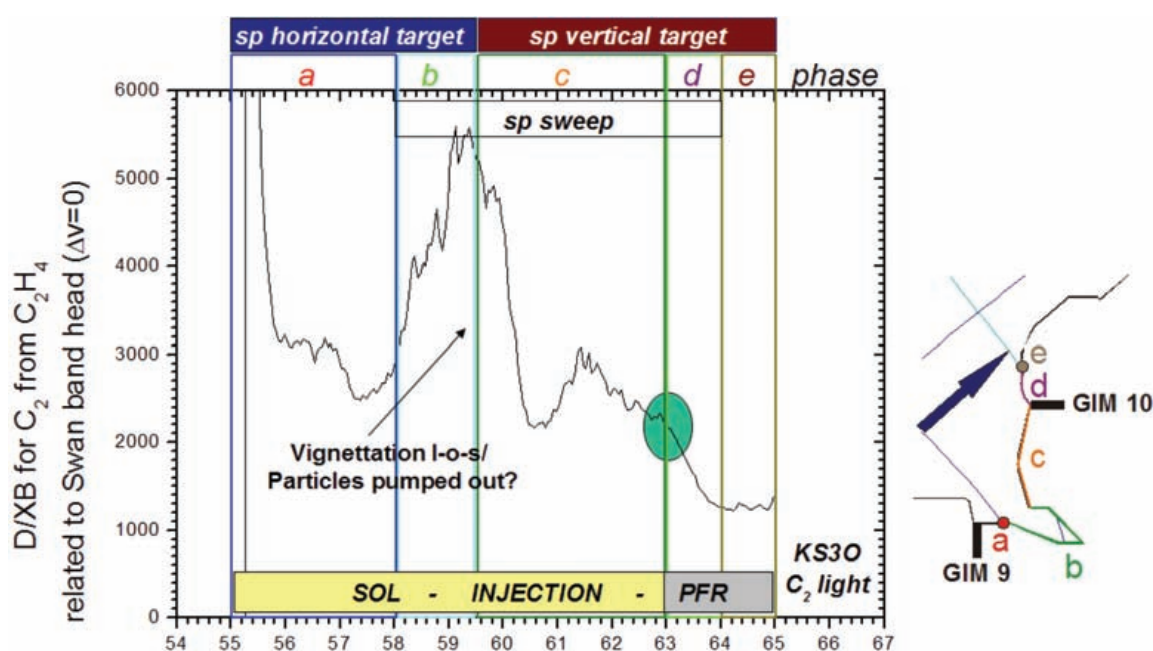
**Figure 17.** Variation of D/XB for $C_2$ in JET during strike point variations and the simultaneous injection of $C_2H_4$ through GIM 10. At the time of the ellipsoid the strike point is located in the position of injection.

[2] BEHRINGER, K., SUMMERS, H.P., DENNE, B., FORREST, M., STAMP, M., Plasma Phys. Control Fusion **31** (1989) 2059.

[3] POSPIESZCZYK, A., RA, Y., HIROOKA, Y., CONN, R.W., GOEBEL, D.M., LA-BOMBARD, B., NYGREN, R.E., *Spectroscopic studies of carbon containing molecules and their breakup in PISCES-A,* University of California at Los Angeles Report No. UCLA-PPG-1251, 1989; see National Technical Information Service Document No. DE91004936INZ. Copies may be ordered from The National Technical Information Service, Springfield, VA.

[4] POSPIESZCZYK, A., CHEVALIER, G., HIROOKA, Y., CONN, R.W., DOERNER, R., SCHMITZ, L., UCLA-PPG-1402, Dec. 1991 and Nucl. Instrum. Meth. Phys. Res. B **B72** (1992) 207.

[5] BEIGMAN, I.L., KOCSIS, G., POSPIESZCZYK, A., VAINSHTEIN, L.A., Plasma Phys. Control. Fusion **40** (1998) 1689.

[6] HUBER, A., BEIGMAN, I.L., BORODIN, D., MERTENS, Ph., PHILIPPS, V., POSPIESZCZYK, A., SAMM, U., SCHWEER, B., SERGIENKO, G., VAINSHTEIN, L., Plasma Phys. Control. Fusion **45** (2003) 89.

[7] SHEVELKO, V.P., VAINSHTEIN, L.A., 1993 *Atomic Physics for Hot Plasmas,* IOP Publishing, Bristol.

[8] BELL, K.L., GILBODY, H.B., HUGHES, J.G., KINGSTON, A.E., SMITH, F.J., J. Phys. Chem. **12 (**1983) 891.

[9] BEIGMAN, I.L., BORODIN, D., VAINSHTEIN, L., Opt. Spectr. **95** (2003) 493.

[10] WINTER, J., *Wall conditioning in fusion devices and its influence on plasma performance*, Plasma Phys. Control. Fusion **38** (1996) 1503

[11] TACHIEV, G., FROESE FISHER, C., J.Phys.B **32** (1999) 5805 http://www.vuse.vanderbilt.edu/~georgio/html-doc/center.html

[12] Atomic Data Analysis Structure, see also http://adas.phys.strath.ac.uk

[13] van REGEMORTER, H., Astrophys. J. **136** (1962) 906.

[14] BORODIN, D., BEIGMAN, I.L., VAINSHTEIN, L.A., POSPIESZCZYK, A., BREZINSEK, S., HUBER, A., Plasma Phys. Control. Fusion **44** (2002) 2251

[15] SAMM, U., BOGEN, P., ESSER, G., HEY, J.D., HINTZ, E., HUBER, A., KÖNEN, L., LIE, Y.T., MERTENS, Ph., PHILIPPS, V., et al, J. Nucl. Mater. **220–222 (**1995) 25.

[16] POSPIESZCZYK, A., SAMM, U., BERTSCHINGER, G., BOGEN, P., CLAASSEN, H.A., ESSER, G., GERHAUSER, H., HEY, J.D., HINTZ, E., KÖNEN, L., LIE, Y.T., RUSBÜLDT, D., SCHORN, R.P., SCHWEER, B., TOKAR, M., Phys. Plasmas **2 (**1995) 2272.

[17] HUBER, A., BEIGMAN, I.L., BORODIN, D., MERTENS, Ph., PHILIPPS, V., POSPIESZCZYK, A., SAMM, U., SCHWEER, B., SERGIENKO, G., VAINSHTEIN, L., Plasma Phys. Control. Fusion **45** (2003) 89.

[18] BREZINSEK, S., GREENLAND, P.T., HEY, J.D., LEHNEN, M., MERTENS, Ph., POSPIESZCZYK, A., SAMM, U., SCHWEER, B., SERGIENKO, G., VIETZKE, E., 28th Euro. Phys. Soc. Conf. Cont. Fus. Plasma Phys. Euro. Conf. Abst. **25A** (2001) 2077.

[19] POSPIESZCZYK, A., MERTENS, Ph., SERGIENKO, G., HUBER, A., PHILIPPS, V., REITER, D., RUSBÜLDT, D., SCHWEER, B., VIETZKE, E., GREENLAND, P.T., J. Nucl. Mater. **266-269** (1999) 138.

[20] BREZINSEK, S., GREENLAND, P.T., MERTENS, Ph., POSPIESZCZYK, A., REITER, D., SAMM, U., SCHWEER, B., SERGIENKO, G., J. Nucl. Mater. **313–316** (2003) 967.

[21] GREENLAND, P.T., Jül-Report No.: 3858, Forschungszentrum Jülich, Jülich 2001.

[22] BREZINSEK, S., SERGIENKO, G., POSPIESZCZYK, A., MERTENS, Ph., SAMM, U., GREENLAND, P.T., Plasma Phys. Control. Fusion **47** (2005) 615.

[23] WHYTE, D.G., BASTASZ, R., BROOKS, J.N., WAMPLER, W.R., WEST, W.P. WONG, C.P.C., BUZHINSKIJ, O.I., OPIMACH, I.V., J. Nucl. Mater. **269** (1999) 67.

[24] WHYTE, D.G., TYNAN, G.R., DOERNER, R.P., and BROOKS, J.N., Nucl. Fusion **41** (2001) 47.

[25] BREZINSEK, S., POSPIESZCZYK, A., KIRSCHNER, A, SERGIENKO, G., HUBER, A., PHILIPPS, V., MERTENS, Ph., U. SAMM, U., STAMP, M.F., MEIGS, A., GREENLAND, P.T., Physica Scripta. **T111** (2004) 42.

[26] EHRHARDT, A.B., LANGER, W.D., *Collisional Processes of Hydrocarbons in Hydrogen Plasmas*, PPPL-2477, Princeton University, 1987.

[27] BROOKS, J.N., WANG, Z., RUZIC, D.N., ALMAN, D.A., ANL/FPP/TM-297, Argonne National Laboratory, 1999.

[28] ALMAN, D.A., RUZIC, D.N., BROOKS, J.N., Phys. Plasmas **7**, (2000) 1421.

[29] JANEV, R.K., WANG, J.G., KATO, T., NIFS-DATA-64, National Institute for Fusion Science, Toki, 2001.

[30] NAUJOKS, D., COSTER, D., KASTELEWICZ, H., SCHNEIDER, R., J. Nucl. Mater. **266–269** (1999) 360.

[31] KIRSCHNER, A., BROOKS, J.N., PHILIPPS, V., WIENHOLD, P., POSPIESZCZYK, A., JANEV, R.K., SAMM, U., J. Nucl. Mater. **313-316** (2003) 444.

[32] POSPIESZCZYK, A., PHILIPPS, V., CASAROTTO, E., KÖGLER, U., SCHWEER, B., UNTERBERG, B., WESCHENFELDER, F., J. Nucl. Mater. **241–243** (1997) 833.

[33] POSPIESZCZYK, A., *Diagnostics of Edge Plasmas by Optical Methods,* in Atomic and Plasma-Material Interaction Processes in Controlled Thermonuclear Fusion, Janev, R.K. and Drawin, H.W. Eds*.,* Elsevier (1993) 213.

[34] PHILLIPS, J. G., *The Swan System of the C$_2$ Molecule,* UCLA Press, Los Angeles 1968.

[35] STAMP, M.F., ERENTS, S.K., FUNDAMENSKI, W., et al., J. Nucl. Mater. **290-293** (2001) 321.

[36] BREZINSEK, S., GREENLAND, P.T., POSPIESZCZYK, A., KIRSCHNER, A., SERGIENKO, G., MERTENS, Ph., PHILIPPS, V., SAMM, U., MEIGS, A., STAMP, M., 30th EPS Conference on Contr. Fusion Plasma Phys., St. Petersburg, 7-11 July 2003 ECA Vol. **27A**, O-2.4D.

[37] JANEV, R., REITER, D., *Collision processes of hydrocarbon species in hydrogen plasmas. 1. The methane family,* Forschungszentrum Jülich, Report Jül 3966, 2002.

[38] NAKANO, T., KUBO, H., HIGASHIJIMA, S., ASAKURA, N., TAKENAGA, H., SUGIE, T., ITAMI, K., Nucl. Fusion **42** (2002) 689.

[39] HUBER, A., BREZINSEK, S., COAD, P., ITAMI, K., JACHMICH, S., KIRSCHNER, A., MATTHEWS, G.F., MERTENS, Ph., PHILIPPS, V., POSPIESZCZYK, A., SCHWEER, B., SERGIENKO, G., STAMP, M.F., Physica Scripta **T111** (2004) 101.

# Measured line spectra and calculated atomic physics data for highly charged tungsten ions

*R. Radtke[1], C. Biedermann[1], G. Fussmann[1], J.l. Schwob[2], P. Mandelbaum[2] R. Doron[2]*

[1] Institut für Physik der Humboldt-Universität zu Berlin, Lehrstuhl Plasmaphysik, Newtonstraße 15, 12489 Berlin, Germany and Max-Planck-Institut für Plasmaphysik, EURATOM Association

[2] Racah Institute of Physics, The Hebrew University, 91904 Jerusalem, Israel

## Abstract

Using high-resolution X-ray and EUV spectrometry, we have performed measurements of the line emission from highly charged tungsten ions ranging from I-like $W^{21+}$ to V-like $W^{51+}$. The ions were produced in an electron beam ion trap (EBIT) operating with electron densities in the range $n_e < 10^{13}$ cm$^{-3}$. Our study encompassed a wide range of wavelengths spanning the region between about 5 and 1000 Å and we have compared the EBIT spectra with the results from *ab initio* calculations using the relativistic HULLAC package. A separate effort focused on HULLAC calculation of atomic structure data for tungsten ions with charge state q = 25-45, In-like $W^{25+}$ to Cu-like $W^{45+}$. We have calculated energy levels, radiative rate coefficients for E1, E2, M1 and M2 transitions, and electron impact collision strengths. Examples of our calculational results are given. Our measured line spectra and calculated atomic physics data are of particular relevance to the analysis and interpretation of spectral emission data from nuclear fusion plasmas.

## 1. Introduction

The increasing use of tungsten as target or wall material in nuclear fusion devices has induced new experimental and theoretical activity to gain data on its spectral emission under reactor relevant conditions. In the past two decades, graphite has almost exclusively been used for divertor plates or heat shields. However, it is estimated that intolerable amounts of carbon would be eroded in a fusion reactor where power fluxes to the target plates as high as 20 MW/m$^2$ are expected [1]. Tungsten offers a promising alternative to graphite because it exhibits excellent thermal properties such as high power handling capacity, high melting point, and large thermal shock resistance. In addition, its long erosion lifetime suggest that it may be the best solution for reducing the sputtering rates in a fusion reactor. Moreover, under high-density, low-temperature divertor conditions redeposition of tungsten can be very efficient due to the short ionization length of sputtered W atoms compared to the gyroradius of the $W^+$ ions in the confining magnetic field [2,3]. The latter implies that the production of higher ionization stages and associated problems of self-sputtering are in large part suppressed. On the negative side, if sputtered tungsten nonetheless penetrates into the central fusion plasma it will not be fully stripped at the high core electron temperatures ($T_e$ = 10-30 keV for ITER conditions) and raise the power losses by radiating line emission. This radiation from tungsten represents a serious problem since it limits the energy confinement and could quench the fusion reaction if the relative concentration of W ions in the core plasma is higher than about 10$^{-5}$ [4]. Control of possible tungsten impurities is thus an essential issue on the route towards the next large tokamak experiment.

In order to establish a quantitative method of measuring tungsten impurities in fusion plasmas and support modeling calculations, accurate atomic physics data is needed, including atomic transitions and its respective wavelengths, line intensities, and cross sections for ionization, recombination and excitation. The main interest at the present time is in the spectral emission from the high charge states of tungsten. So far most of the data on the tungsten radiation has been deduced from line-of-sight-integrated measurements on tokamak plasmas [5-8]. However, the spectral information in this case is strongly influenced by transport processes and the radial profile of electron temperature and density. Moreover, the number of ionization states that emit simultaneously is in general quite large which makes the identification and analysis of the impurity spectrum from tokamak-produced plasmas even more complex.

In the present measurements, we used an electron beam ion trap (EBIT) to produce tungsten ions and confine them for spectroscopic observations. EBIT operates with electron densities in the range $n_e \leq 10^{13}$ cm$^{-3}$ and has the advantage over experiments on tokamak plasmas that the ion's charge-state distribution can be controlled by varying the energy of the ionizing electron beam and that no integration over a range of electron temperatures and densities occurs. Theoretical analysis of the spectra from the ions in EBIT relies on collisional-radiative (CR) line intensities calculated by means of the multiconfiguration relativistic Hebrew University Lawrence Livermore Atomic Code (HULLAC) package [9,10]. *Ab initio* atomic structure data is calculated for tungsten ions with charge state q = 25-45, In-like W$^{25+}$ to Cu-like W$^{45+}$. In particular, we have calculated energy levels, radiative rate coefficients for E1, E2, M1 and M2 transitions, and electron impact collision strengths using the HULLAC method [9-11]. These data are relevant to high-temperature fusion plasmas and can be employed to construct synthetic spectra in the soft X-ray and vacuum ultraviolet (VUV) spectral ranges. In what follows below, we will first focus on the experimental setup at the EBIT device (Section 2). In Section 3, we present the results of our X-ray, EUV und VUV spectroscopic measurements and make a comparison with theoretical predictions. In Section 4, an excerpt of our calculated atomic physics data is given for illustration.

## 2. Experimental studies

Our measurements were performed at the Berlin electron beam ion trap and made use of the capability to vary the beam energy across the ionization thresholds and excite spectra of successive charge states. The electron beam in EBIT originates from an electron gun and is formed by accelerating and guiding electrons into the trap, an assembly of three cylindrical drift tubes floating at high potential. A pair of superconducting Helmholtz coils creates a 3-tesla magnetic field, which compresses the electron beam to a diameter of 70 μm as it passes through the trap region. Atoms injected into the trap are ionized successively by electron collisions and confined radially by the space charge of the electron beam. Axial confinement is provided within a 4-cm-long trapping region by the two end-drift tubes, which are biased positively with respect to the center segment. In addition to ionizing and trapping the ions, the beam also serves to excite them. The radiation produced from the trapped ions can then be observed through X-ray, VUV or visible spectroscopy. Tungsten is introduced to the EBIT as atoms emitted continuously from the dispenser type cathode of the electron gun. As the contaminant with the highest atomic number in EBIT (Z = 74) it concentrates in the trap during extended accumulation. To generate an even larger flow of tungsten atoms to the trap and accelerate the establishment of steady-state conditions, low-charged tungsten ions were produced by a metal vapor vacuum arc and extracted in a way that energetic ions from the arc were directed onto the cathode of electron gun to efficiently increase the sputtering of neutral W atoms. Although the atoms are ionized in the electron beam as they travel towards the drift tubes, there still remain enough atoms in the trapping region to be caught after an ionizing collision. For the conditions present in these measurements, an equilibrium in the photon flux from the trapped W ions was reached in less than 300 s.

The radiation emitted by the ions in EBIT was investigated by high-resolution X-ray and VUV spectroscopy using a vacuum flat-crystal Bragg spectrometer and a 2-m Schwob-Fraenkel grazing-incidence spectrometer, respectively. The Schwob-Fraenkel spectrometer [12] covers a wavelength range between 10 and 1000 Å and was specially designed and constructed at the Hebrew University for measurements with an EBIT. In the experiment presented here, the spectrometer was equipped with a 600 ℓ/mm grating set at a grazing angle of incidence of 2°. The photons emitted by the trapped ions were focused with a 6-m-curvature grazing-incidence mirror (mounted 21 cm from the EBIT axis) onto the entrance slit (18 μm) of the spectrometer. The EUV radiation was detected with a micro-channel plate/phosphor screen image-intensifier system that was coupled to a CCD camera with the dimensions of 1152 × 770 pixels and a pixel size of 22.5 μm. For the 18 μm wide slit the instrumental full-width-at-half-maximum (FWHM) is approximately 0.2 Å. *In situ* wavelength calibration of the spectrometer was performed using well known EUV lines from helium, nitrogen, neon, and argon ions. The x radiation was analyzed with a flexible vacuum flat-crystal spectrometer reflecting photons according to Bragg's law from a 75 × 45 mm$^2$ ADP crystal (2d = 10.648 Å), and the spectral information was recorded with a position-sensitive proportional counter. The spectrometer reaches a nominal resolution of $\lambda/\Delta\lambda \geq 2000$, necessary to resolve the X-ray spectra from tungsten in the 5-7 Å range. For calibrating the wavelength axis we used H-like and He-like lines from silicon which was introduced into EBIT by directing a gas flow of SiH$_4$ towards the trap.

Spectra were measured for electron-beam energies $E_b$ in the interval between about 500 eV and 5 keV sampling the radiation from I-like W$^{21+}$ to Ca-like W$^{54+}$ tungsten ions, using voltage increments of about 50 V in going from one $E_b$ value to the next. The beam current was limited throughout these measurements to 50 mA and lower to limit the beam-energy spread to approximately 30 eV FWHM. Each spectrum had an exposure time of about 1 h.
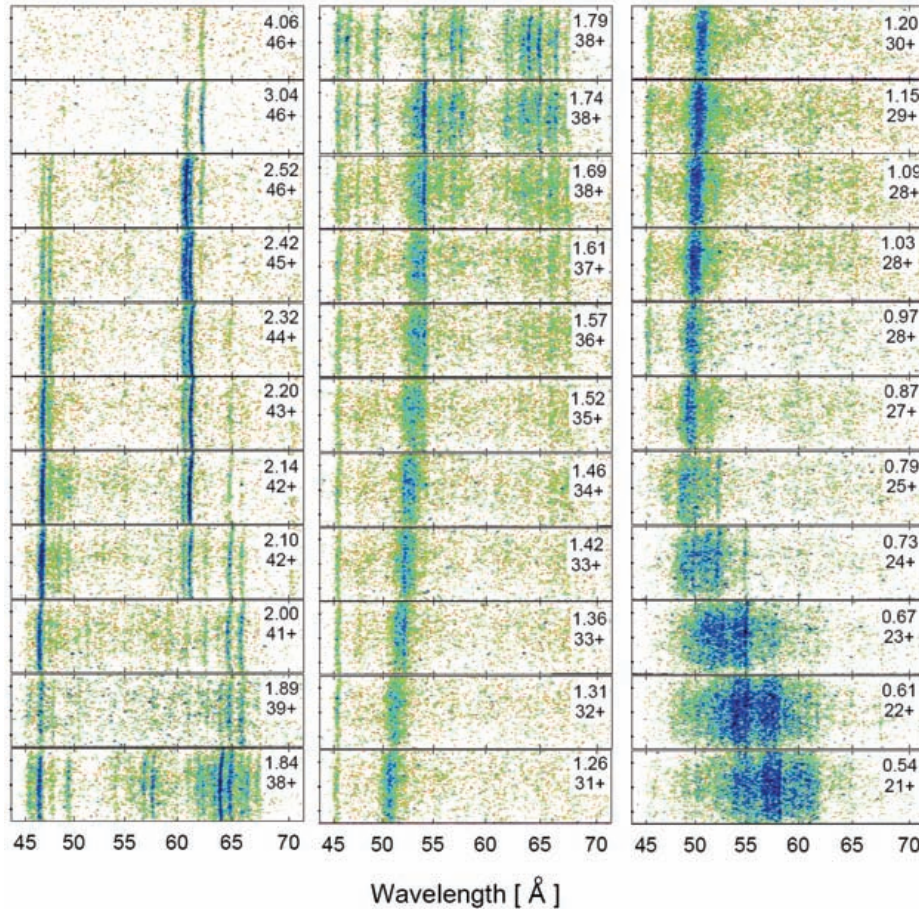
## 3. Tungsten spectra

### 3.1. EUV emission spectra

We now proceed with a survey of our EUV spectroscopic measurements and display in Fig. 1 CCD images

showing the emission from tungsten in the range 45-70 Å [13]. Each image represents a particular ion population in EBIT at the electron beam energy and charge number of the highest ionization stage marked to the right. For beam energies between about 4.0 and 1.7 keV, many line features can be observed in the spectra arising from resonance transitions in Cu-like $W^{45+}$ through Rb-like $W^{37+}$. For the sequence following the 1.7-keV spectrum, the population in EBIT is shifted to ions having open 4d or 4f subshells and we note a drastic change in the qualitative appearance of the spectrum as a function of $E_b$. The emission fuses into a narrow band near 50 Å and the band moves smoothly towards shorter wavelengths as decreasing charge states are progressively selected. This trend continues until $E_b$ becomes less than about 800 eV. Thereafter, the emission pattern disperses and shifts back to higher wavelengths.
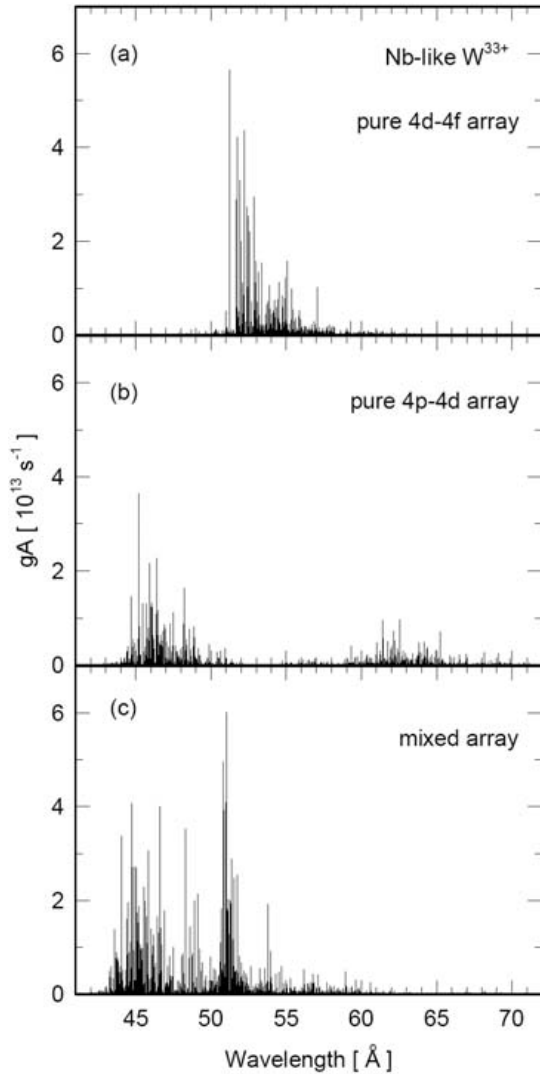
A theoretical analysis of the emission bands in terms of collisional-radiative line intensities has been made in Ref. [13]. The emphasis there was on the tungsten ions with charge 29+ to 37+ which clearly show the narrowing and shift of the band emission and thus may serve as a test case for modeling calculations. The ions in question exhibit $4p^54d^{n+1}$ and $4p^64d^{n-1}4f$ (n = 1-9) excited state configurations which connect to the $4p^64d^n$ ground configuration via resonance transitions. Using the HULLAC package, we

have made full intermediate coupling calculations to obtain the set of all possible transitions for the pure $4p^64d^n$ - $4p^54d^{n+1}$ and $4p^64d^n$ - $4p^64d^{n-1}4f$ as well as mixed $4p^64d^n$ - $[4p^54d^{n+1} + 4p^64d^{n-1}4f]$ transition array. As an example, we have plotted in Fig. 2 statistical-weight modelled spectra ($g_jA_{ji}$ products as a function of wavelength, where $A_{ji}$ is the Einstein coefficient for spontaneous emission from level j to level i and $g_j$ is the statistical weight of the upper level) for Nb-like $W^{33+}$. From Fig. 2 it is evident that in the mixed-configuration approximation the calculated array width shrinks due to quenching of the long-wavelength transitions from the $4p^54d^6$ configuration, but still cannot explain the observed narrow emission bands ($\Delta\lambda_{exp} \leq 2$Å). To resolve this is disparity a different set of calculations has been made using CR line intensities instead of gA products. The reason is that EBIT operates with electron densities in the range $n_e$ $< 10^{13}$ cm$^{-3}$ and as in tokamak plasmas the confined ions are in a state far from local thermodynamic equilibrium. Line intensities in this case are not proportional to gA products, but depend instead on the excitation rates of the ions which have to be obtained from a collisional-radiative model. Therefore, we have calculated CR line intensities from a steady-state rate equation taking excitation and de-excitation by electron collisions and electric as well as magnetic dipole and quadrupole radiation into account.



**Figure 1.** CCD images showing spectra from highly charged tungsten between 45 and 70 Å. The labels indicate the energy of the ionizing electron beam (in keV) and the highest possible charge state of tungsten for this beam energy.

Our calculations extend from very high ($n_e = 10^{22}$ cm$^{-3}$) to moderate and low electron densities ($n_e = 10^{12}$ cm$^{-3}$). A set of CR spectra for the mixed $4p^6 4d^3$ - [$4p^5 4d^4$ + $4p^6 4d^2 4f$] transition array of Y-like W$^{35+}$ is shown in Figs. 3(b)-3(e). The most striking effect of the collisional-radiative modeling is that at lower $n_e$ only a comparatively small portion of transitions within the array has sufficiently high intensity to contribute to the emission, in contrast to the gA distribution (Fig. 3(a)) and the results obtained at high density. As Fig. 3(e) exhibits, at $n_e = 10^{12}$ cm$^{-3}$ the spectrum has split into a single line at 45 Å and a structure at 52.5 Å comprised of a few strong lines. The calculated CR line intensities of the adjacent charge states to Y-like W$^{35+}$ show a similar variation with electron density. However, the prominent line group in each spectrum is displaced from the position of the analogous group for W$^{35+}$ and the displacement closely follows the trend of the shift for the emission bands in our experimental spectra. We have found experimental and theoretical evidence that more than ten ionization states of tungsten exhibit such narrow bands radiating in the range between 48 and 54 Å. Our results

explain thus the broad quasi-continuum band structure around 50 Å observed in the impurity spectrum from tokamak-produced plasmas [8] where, in contrast to EBIT, many more ionization states of tungsten emit simultaneously.

## 3.2. Magnetic dipole lines

A further field addressed in this section is the observation of magnetic dipole (M1) lines from highly charged tungsten. The lines originate from transitions between ground-term fine-structure levels and are located in the UV or VUV region of the spectrum. Studies of M1 lines from highly charged ions have important applications, for example in diagnosing high-temperature plasmas or testing atomic-structure calculations. We have undertaken a study of magnetic dipole lines from tungsten in Ru-like W$^{30+}$ to Rb-like W$^{37+}$ charge states. The lines arise from the $4p^6 4d^n$ (n = 1-8) ground state configurations and appear in the
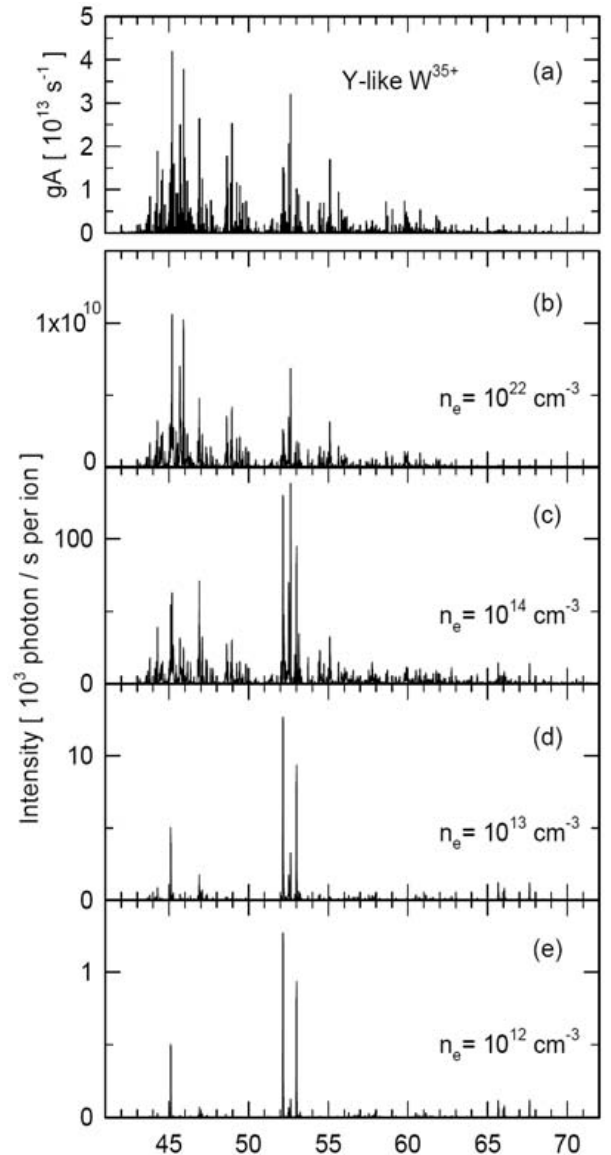


**Figure 2.** Calculated gA distributions for transitions in Nb-like W$^{33+}$; (c) shows the modelled distributions for the mixed array.



**Figure 3.** Calculated gA distribution (a), and modeled collisional radiative spectra for the mixed transition array of Y-like W$^{35+}$.

wavelength range from 640 to 730 Å. In our experiment, the energy of the ionizing electron beam was selected between 1.05 and 1.68 keV, and the radiation from the ions in EBIT was analyzed with the grazing-incidence spectrometer described above. From the measured two-dimensional CCD images, spectra were generated by binning a central 100 pixel wide strip and projecting the counts found in this strip onto the wavelength dispersive axis. Fig. 4 shows spectra of tungsten at eight energies optimized for the marked ion charge state. Typically, ions in one or two of the next lower and higher charge states are also present at each setting. The label on the right side of each spectrum indicates the energy of the beam in units of keV. Identification of the lines is based on the capability of EBIT to excite spectra of successive charge states by step-wise variation of the beam energy across the corresponding ionization thresholds. The identified lines for the eight measured charge states are shaded gray.
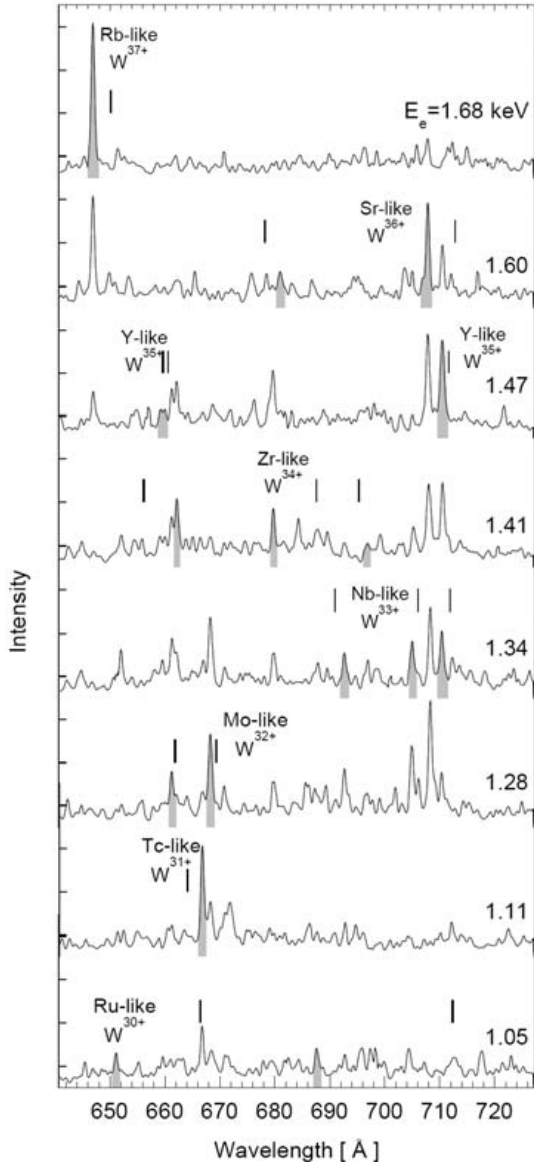
Note that all these lines appear well isolated in a relatively small wavelength range which makes them particularly suitable for diagnostic measurements. To support our identification, wavelengths and intensities were calculated for each tungsten ion from Ru-like $W^{30+}$ to Rb-like $W^{37+}$ using the HULLAC package combined with a collisional-radiative model. To begin with, a preliminary set of calculations was made to predict the wavelengths of the most intense lines. In calculating the population distribution among the levels of the $4p^6 4d^n$ (n = 1-8) ground configuration, we have included the two strongly mixing $4p^5 4d^{n+1}$ and $4p^6 4d^{n-1} 4f$ excited state configurations. These first calculations predicted that many bright M1 lines arising from forbidden transitions should be observed in the range between 500 and 900 Å. Based on these results a second set of calculations has then been made to achieve a higher degree of accuracy. We have included in the level energy calculations additional excitation channels, in particular $4p^6 4d^{n-2} 4f^2$, $4p^6 4d^{n-1} 5s$, $4p^6 4d^{n-1} 5d$, $4p^4 4d^{n+2}$, and $4p^5 4d^n 4f$. The inclusion of these configurations can have an important impact on the calculated transition wavelengths. However, there is no assurance that in the present calculation complete convergence was reached, since the number of levels (more than 4000) quickly surpasses our computational means. The wavelengths predicted by HULLAC for the measured eight charge states are shown in Fig. 4 by vertical marks. From the comparison with the experimental values, we infer that *ab initio* calculations for these lines can deliver results within about 1-3% of the correct numbers, depending on the transition.

Spectral lines show often differences in the density dependence implying that intensity ratios among these lines can be used for plasma diagnostic measurements. To generate line ratios for a Maxwell-Boltzmann electron temperature $T_e$, HULLAC calculations were performed with a view to line intensity ratios as density indicator. The lines in this case must arise from different upper levels within the same ionization state. Fig. 5 shows four intensity ratios of M1 lines to the resonant electric dipole line ($\lambda = 54.14$ Å) in Sr-like $W^{36+}$ as a function of the electron density. In the calculation a temperature $T_e = E_I$ is assumed, where $E_I = 1547$ eV is the ionization energy of Sr-like $W^{36+}$. The curves in Fig. 5 show that the ratios are very sensitive to the density in the range $n_e > 10^{14}$ cm$^{-3}$. Below $n_e \approx 10^{14}$ cm$^{-3}$ only the ratio R(598.01 Å/54.15 Å) is sensitive to the density. The qualitatively different behavior of the line intensity ratios can be explained by the density-dependent rates for populating and depopulating the levels within the ground configuration.

### 3.3. *Soft X-ray spectra*

To complement our measurement of tungsten EUV line emission, observations of the radiation from highly charged W ions were made in the soft X-ray range. Recent *ab initio* calculations for Rb-like $W^{37+}$ to Co-like $W^{47+}$ ions [14] predicted many lines in the band between 4 and 20 Å;



**Figure 4.** VUV spectra showing M1 lines of highly charged tungsten.
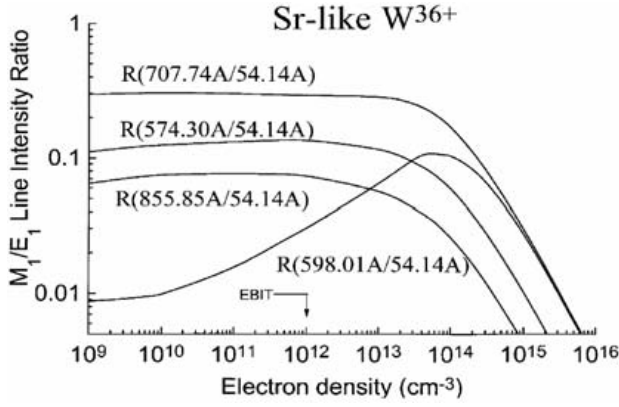
**Figure 5.** Intensity ratio of M1 to E1 lines for Sr-like $W^{36+}$ as a function of the electron density.

the most intense ones originate from 3d-4f transitions and are located near 5-6 Å. The identification of these lines is considered to be particularly important for monitoring tungsten impurities in tokamak fusion plasmas [15]. Our measurement concentrated on the soft X-ray lines from Zn-like $W^{44+}$ to Cr-like $W^{50+}$ ions, which are important for emission from plasmas at higher electron temperatures.

The measurements were carried out by employing a vacuum flat-crystal spectrometer equipped with an $75 \times 45$ mm$^2$ ADP crystal (2d = 10.648 Å). Fig. 6 shows spectra obtained with the electron beam set to 11 energies in the interval between 3.03 and 4.84 keV. There are several well-resolved line features, most of them could be attributed to W transitions predicted by Fournier [14,16]. In the lower beam-energy spectra, there is a prominent line at 5.673 Å, originating from a $3d^{10}$-$3d^9$4f transition in Ni-like $W^{46+}$. If the electron-beam energy is increased, we produce and excite Co-like $W^{47+}$ and Fe-like $W^{48+}$ in addition to the Ni-like $W^{46+}$ ions. The features from these ions incorporate contributions from a larger number of transitions since they are wider than expected for a single line. At even higher beam energies we could discern several other features belonging to Mn-like $W^{49+}$ and Cr-like $W^{50+}$ ions. The measured tungsten spectra are compared with theoretical data using Fournier's wavelength predictions for these charge states [14,16]. In Fig. 6, the wavelength predictions for Ni-like $W^{46+}$ through V-like $W^{51+}$ are overlaid in the 3.027-, 4.117-, 4.292-, 4.378-, 4.551- and 4.838-keV spectrum in order of increasing charge. The only notable difference between the experimental and theoretical spectra is the absence of a weak V-like feature that is predicted to be situated near 5.3 Å. All other lines in the measured spectra also appear in the simulated data.

## 4. Calculations

All the atomic physics data calculated in the present work were generated by using the multi-configuration relativistic Hebrew University Lawrence Livermore Atomic Code (HULLAC) package [9-11]. As a first step, for each tungsten ion ranging from In-like $W^{25+}$ (ground configuration

$4s^24p^64d^{10}4f^3$) to Cu-like $W^{45+}$ (ground configuration 4s) a set of atomic data has created including energy levels, radiative decay rate coefficients for E1, E2, M1 and M2 transitions, and electron impact effective collision strengths. As an example this information is shown for Cu-like $W^{45+}$ in Table I. For the complete range of ion states the data are collected in three Reports [17-19] which can be provided upon request by the authors. The data set for each ion consists of a header specifying the ionic species, isoelectronic sequence, ionization energy $E_I$ and a listing of the configurations included in the calculation. Next is the list of energy levels numbered according to increasing energies. For each energy level, the configuration, total angular momentum quantum number J and the energy in cm$^{-1}$ is given. Finally, for each couple of levels i and j (j > i), where i and j are the level numbers according to the energy level list, the calculated Einstein radiative decay rate coefficient

**Table I.** Example of atomic data for Cu-like $W^{45+}$ with a list of level energies, radiative decay rate coefficients and electron impact effective collision strengths

File: W45.dat
Isoelectronic sequence: CuI
Ionization Energy: $E_I$=2430 eV

The model includes the following configurations: $3p^63d^{10}4s$, 4p, 4d, 4f, 5s, 5p, 5d, 5f, $3p^63d^94s^2$, $3p^63d^94s4p$, $3p^63d^94s4d$, $3p^63d^94s4f$, $3p^63d^94p^2$, $3p^63d^94p4d$, $3p^63d^94d^2$, $3p^63d^94d4f$, $3p^63d^94d4f$, $3p^53d^{10}4s^2$, $3p^53d^{10}4s4p$, $3p^53d^{10}4s4d$, and $3p^53d^{10}4s4f$ (766 levels in total).

A. Energy levels

| # | Configuration | J | Energy (cm$^{-1}$) |
|---|---|---|---|
| 1 | $3p^63d^{10}4s$ | 1/2 | 0.00 |
| 2 | $3p^63d^{10}4p$ | 1/2 | 794047.69 |
| 3 | $3p^63d^{10}4p$ | 3/2 | 1610322.13 |
| 4 | $3p^63d^{10}4d$ | 3/2 | 2827249.00 |
| 5 | $3p^63d^{10}4d$ | 5/2 | 3000731.50 |
| 6 | $3p^63d^{10}4f$ | 5/2 | 4299222.00 |
| 7 | $3p^63d^{10}4f$ | 7/2 | 4342696.50 |
| 8 | $3p^63d^{10}5s$ | 1/2 | 7803587.50 |
| . | | | |
| . | | | |
| . | | | |
| 765 | $3p^53d^{10}4s4f$ | 7/5 | 22975698.00 |
| 766 | $3p^53d^{10}4s4f$ | 5/2 | 22978218.00 |

B. Radiative decay rate coefficients $A_{ij}$ and effective collision strengths

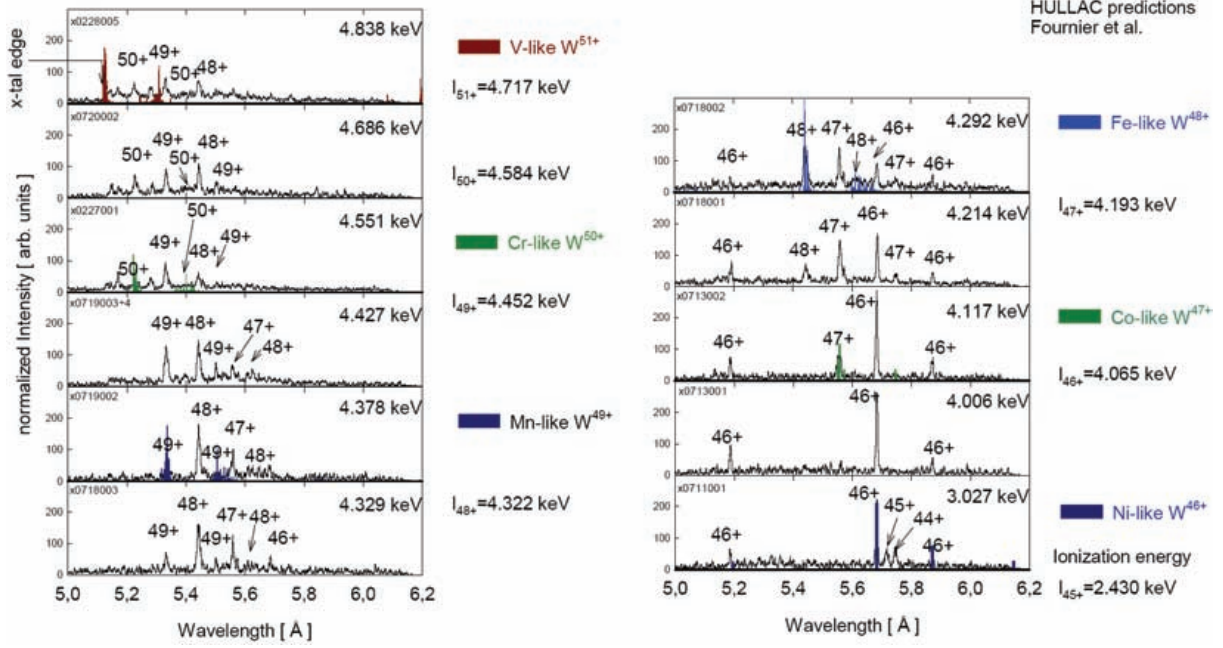| | | | Effective Collision Strength | | |
|---|---|---|---|---|---|
| i | j | $A_{ji}$ | $T_e$= 0.1$E_I$ | ... $E_I$ | ... 10$E_I$ |
| 1 | 2 | .488E+11 | 0.507E+00 | ... 0.540E+00 | ...0.101E+01 |
| 1 | 3 | .426E+12 | 0.814E+00 | ... 0.839E+00 | ...0.169E+01 |
| 1 | 4 | .120E+09 | 0.537E-01 | ... 0.559E-01 | ...0.659E-01 |
| . | | | | | |
| . | | | | | |
| 764 | 766 | .458E-06 | 0.101E-01 | ... 0.480E-02 | ...0.911E-03 |
| 765 | 766 | .351E-01 | 0.149E-01 | ... 0.103E-01 | ...0.108E-01 |

**Figure 6.** Measured and predicted soft X-ray spectra of highly charged tungsten.

$A_{ji}$ in $s^{-1}$ and the dimensionless effective collision strength $\gamma_{ij}$ is listed. $\gamma_{ij}$ is related to the electron impact excitation rate coefficient $Q_{ij}$ expressed in $cm^3$ $s^{-1}$ (defined for a Maxwellian electron energy distribution) by

$$\gamma_{ij} = \frac{Q_{ij}g_i T_e^{1/2}}{8.63 \times 10^{-6}} \times \exp\left(E_{ij}/kT_e\right)$$

where $g_i$ is the statistical weight of the lower level, $T_e$ the electron temperature in Kelvin, k the Boltzmann constant, and $E_{ij}$ the energy difference between levels i and j. $\gamma_{ij}$ is tabulated for a few discrete electron temperatures and can be interpolated for interim values owing to the smooth behavior as a function of $T_e$.

As a second step, we have calculated transition wavelengths and line intensities for each ion under consideration. The population $n_j$ of the ion in level j is obtained from the steady-state rate equation

$$\sum_{i<j} n_i n_e \sigma_{ij}^e v_e + \sum_{k>j} n_k \left(A_{kj} + n_e \sigma_{kj}^d v_e\right)$$

$$= n_j \left\{ \sum_{i<j}\left(A_{ji} + n_e \sigma_{ji}^d v_e\right) + \sum_{k>j} n_e \sigma_{jk}^e v_e \right\}$$

where the left-hand and right-hand sides of the equation represent the processes that populate and depopulate the level j. $\sigma_{ij}^e$ and $\sigma_{ji}^d$, respectively, are the energy-dependent electron-impact cross sections for excitation and deexcitation between levels i and j, and $v_e$ is the velocity of the mono-energetic electron beam. In solving the rate equation, electric as well as magnetic dipole and quadrupole radiative decays are taken into account. Once $n_j$ is obtained the line intensity $I_{ji}$, which represents the number of radiative

transitions per second and unit volume from the level j to the level i, is computed from

$$I_{ji} = n_j A_{ji}$$

All calculated wavelengths of the strongest lines in the EUV and VUV spectral range are summarized in Tables II through XXII. In addition, the levels (lower and upper), the type of transition, and the line intensities $I_{ji}$ are tabulated. The electron density and energy for which the data were calculated are $n_e = 10^{12}$ $cm^{-3}$ and $E = E_I$, where $E_I$ is the ionization energy of the ion under consideration. We have added an additional column containing experimental wavelength results from the Berlin EBIT for comparison in the 18 tables following Table IV (Pd-like $W^{28+}$ to Cu-like $W^{45+}$). Where the experimental spectra have revealed emission bands for the measured ions, the experimentally determined mean wavelength of the band is given in the $\lambda_{meas}$ column. With the predicted wavelengths and line intensities, the tables can be used as an aid for interpretation of spectral emission data from tokamaks and EBIT devices.

**Table II.** Calculated wavelengths, transitions and intensities for In-like $W^{25+}$. Ground configuration $4d^{10}4f^3$, $E_I$ = 782 eV, 378 levels are included from the $4f^3$, $4f^25s$, $4f^25p$, $4f^25d$ and $4f^25f$ configurations.

| λ(Å) | Lower | Upper | Type | Intensity |
|---|---|---|---|---|
| 49.395 | $4f^3_{5/2}$ (J = 9/2) | $[4f^2_{5/2}$ (4)$]5d_{3/2}$ (J = 7/2) | E1 | 83 |
| 109.42 | $4f^3_{5/2}$ (J = 9/2) | $[4f^2_{5/2}$ (4)$]5s$ (J = 7/2) | E1 | 69 |
| 111.70 | $[4f^2_{5/2}$ (4)$]4f_{7/2}$ (J = 7/2) | $[4f^2_{5/2}\,4f_{7/2}(3)]5s$ (J = 7/2) | E1 | 57 |
| 134.71 | $[4f^2_{5/2}$ (4)$]5d_{3/2}$ (J = 9/2) | $[4f^2_{5/2}$ (4)$]5f_{5/2}$ (J = 9/2) | E1 | 61 |
| 136.59 | $[4f^2_{5/2}$ (4)$]5d_{3/2}$ (J = 7/2) | $[4f^2_{5/2}$ (4)$]5f_{5/2}$ (J = 9/2) | E1 | 81 |
| 287.36 | $[4f^2_{5/2}$ (4)$]5s$ (J = 9/2) | $[4f^2_{5/2}$ (4)$]5p_{1/2}$ (J = 7/2) | E1 | 70 |
| 1825.1 | $[4f^2_{5/2}$ (4)$]4f_{7/2}$ (J = 11/2) | $[4f^2_{5/2}$ (4)$]4f_{7/2}$ (J = 13/2) | M1 | 62 |
| 2175.1 | $4f^3_{5/2}$ (J = 9/2) | $[4f^2_{5/2}$ (4)$]4f_{7/2}$ (J = 9/2) | M1 | 143 |
| 3728.8 | $[4f^2_{5/2}$ (2)$]4f_{7/2}$ (J = 3/2) | $4f_{5/2}\,[4f^2_{7/2}$ (4)$]$ (J = 3/2) | M1 | 57 |
| 5227.5 | $4f^3_{5/2}$ (J = 9/2) | $[4f^2_{5/2}$ (4)$]4f_{7/2}$ (J = 11/2) | M1 | 115 |
| 5838.0 | $[4f^2_{5/2}$ (4)$]4f_{7/2}$ (J = 11/2) | $4f_{5/2}\,[4f^2_{7/2}$ (6)$]$ (J = 13/2) | M1 | 61 |

**Table III.** Calculated wavelengths, transitions and intensities for Cd-like $W^{26+}$. Ground configuration $4d^{10}4f^2$, $E_I$ = 833 eV, 461 levels are included from the $4d^{10}4f^2$, $4d^94f^3$, $4d^{10}4f5s$, $4d^{10}4f5p$, $4d^{10}4f5d$, and $4d^{10}4f5f$ configurations.

| λ(Å) | Lower | Upper | Type | Intensity |
|---|---|---|---|---|
| 47.370 | $4d^{10}4f^2_{5/2}$ (J = 4) | $4d^9_{3/2}[4f^3_{5/2}(3/2)]$ (J = 3) | E1 | 1250 |
| 47.893 | $4d^{10}4f^2_{7/2}$ (J = 6) | $[4d^9_{3/2}4f_{5/2}(1)][4f^2_{7/2}(6)]$ (J = 6) | E1 | 1220 |
| 47.928 | $4d^{10}4f_{5/2}4f_{7/2}$ (J = 5) | $[4d^9_{3/2}[4f^2_{5/2}(4)]\,(5/2)]4f_{7/2}$ (J = 5) | E1 | 1570 |
| 48.143 | $4d^{10}4f^2_{5/2}$ (J = 4) | $4d^9_{3/2}[4f^3_{5/2}(9/2)]$ (J = 4) | E1 | 1460 |
| 50.376 | $4d^{10}4f_{5/2}4f_{7/2}$ (J = 4) | $[4d^9_{3/2}[4f^2_{5/2}(4)]\,(7/2)]4f_{7/2}$ (J = 5) | E1 | 1310 |
| 51.287 | $4d^{10}4f_{5/2}4f_{7/2}$ (J = 5) | $[4d^9_{3/2}[4f^2_{5/2}(4)]\,(7/2)]4f_{7/2}$ (J = 6) | E1 | 1250 |
| 51.803 | $4d^{10}4f^2_{5/2}$ (J = 4) | $[4d^9_{3/2}[4f^2_{5/2}(2)]\,(3/2)]4f_{7/2}$ (J = 5) | E1 | 1140 |

**Table IV.** Calculated wavelengths, transitions and intensities for Ag-like $W^{27+}$. Ground configuration $4d^{10}4f$, $E_I = 877$ eV, 157 levels are included from the $4d^{10}4f$, $4d^94f^2$, $4d^{10}5s$, $4d^{10}5p$, $4d^{10}5d$, $4d^{10}5f$ and $4d^94f5s$ configurations.

| $\lambda$(Å) | Lower | Upper | Type | Intensity |
|---|---|---|---|---|
| 47.298 | $4d^{10}4f_{5/2}$ | $4d^9_{3/2}[4f^2_{5/2}(4)]$ (J = 5/2) | E1 | 2040 |
| 47.475 | $4d^{10}4f_{7/2}$ | $[4d^9_{3/2}4f_{5/2}(1)]4f_{7/2}$ (J = 7/2) | E1 | 1910 |
| 47.719 | $4d^{10}4f_{7/2}$ | $[4d^9_{3/2}4f_{5/2}(1)]4f_{7/2}$ (J = 5/2) | E1 | 1330 |
| 47.777 | $4d^{10}4f_{5/2}$ | $4d^9_{3/2}[4f^2_{5/2}(2)]$ (J = 3/2) | E1 | 1420 |
| 47.827 | $4d^{10}5s$ | $[4d^9_{3/2}4f_{5/2}(1)]5s$ (J = 3/2) | E1 | 3790 |
| 47.838 | $4d^{10}5s$ | $[4d^9_{3/2}4f_{5/2}(1)]5s$ (J = 1/2) | E1 | 1880 |
| 49.702 | $4d^{10}4f_{7/2}$ | $[4d^9_{3/2}4f_{5/2}(1)]4f_{7/2}$ (J = 9/2) | E1 | 1710 |
| 50.262 | $4d^{10}4f_{5/2}$ | $4d^9_{3/2}[4f^2_{5/2}(4)]$ (J = 7/2) | E1 | 2110 |
| 159.45 | $4d^{10}5p_{3/2}$ | $4d^{10}5d_{5/2}$ | E1 | 493 |
| 175.26 | $4d^{10}5s$ | $4d^{10}5p_{3/2}$ | E1 | 3670 |
| 287.55 | $4d^{10}5s$ | $4d^{10}5p_{1/2}$ | E1 | 2380 |
| 3424.0 | $4d^{10}4f_{5/2}$ | $4d^{10}4f_{7/2}$ | M1 | 285 |

**Table V.** Measured and calculated wavelengths, transitions and intensities for Pd-like $W^{28+}$. Ground configuration $4d^94f$, $E_I = 1129$ eV, 87 levels are included from the $4p^64d^{10}$, $4p^54d^{10}4f$, $4p^64d^94f$, $4p^64d^95s$, $4p^64d^95p$, $4p^64d^95d$ and $4p^64d^95f$ configurations.

| $\lambda$meas(Å) | $\lambda$calc(Å) | Lower | Upper | Type | Intensity |
|---|---|---|---|---|---|
| | 48.001 | $4d^{10}$(J = 0) | $4p^6\,4d^9_{3/2}4f_{5/2}$ (J = 1) | E1 | 6430 |
| | 59.878 | $4d^{10}$(J = 0) | $4p^6\,4d^9_{5/2}4f_{7/2}$ (J = 1) | E1 | 213 |
| | 61.842 | $4d^{10}$(J = 0) | $4p^6\,4d^9_{5/2}4f_{7/2}$ (J = 2) | M2 | 178 |
| | 63.155 | $4d^{10}$(J = 0) | $4p^6\,4d^9_{5/2}4f_{5/2}$ (J = 2) | M2 | 262 |
| | 63.256 | $4p^6\,4d^9_{5/2}4f_{5/2}$ (J = 5) | $4p^5_{3/2}4d^{10}4f_{5/2}$ (J = 4) | E1 | 580 |
| | 63.389 | $4p^6\,4d^9_{5/2}4f_{7/2}$ (J = 6) | $4p^5_{3/2}4d^{10}4f_{7/2}$ (J = 5) | E1 | 179 |
| 784.94 | 796.4 | $4p^6\,4d^9_{5/2}4f_{5/2}$ (J = 5) | $4p^6\,4d^9_{3/2}4f_{5/2}$ (J = 4) | E2 | 91 |

**Table VI.** Measured and calculated wavelengths, transitions and intensities for Rh-like W$^{29+}$. Ground configuration $4p^6 4d^9$, $E_I = 1176$ eV, $4p^6 4d^9$, $4p^5 4d^{10}$, $4p^6 4d^8 4f$, $4p^6 4d^8 5s$, $4p^6 4d^8 5p$, $4p^6 4d^8 5d$, $4p^6 4d^8 5f$ and $4p^5 4d^9 4f$ configurations are included.

| λmeas(Å) | λcalc(Å) | Lower | Upper | Type | Intensity |
|---|---|---|---|---|---|
| band | 48.418 | $4d^9_{5/2}$ (J = 5/2) | $4d^4_{3/2}$ [$4d^4_{5/2}$ (4)] $4f_{7/2}$ (J = 7/2) | E1 | 2084 |
| 51.1 | 48.635 | $4d^9_{5/2}$ (J = 5/2) | $4d^3_{3/2} 4d^5_{5/2}$ (4) $4f_{5/2}$ (J = 3/2) | E1 | 1093 |
| | 48.762 | $4d^9_{5/2}$ (J = 5/2) | $4d^4_{3/2}$ [$4d^4_{5/2}$ (4)] $4f_{7/2}$ (J = 5/2) | E1 | 1435 |
| 756.64 | 757.600 | $4d^9_{5/2}$ (J = 5/2) | $4d^9_{3/2}$ (J = 3/2) | M1 | 165 |

**Table VII.** Measured and calculated wavelengths, transitions, and intensities for Ru-like W$^{30+}$. Ground configuration $4p^6 4d^8$, $E_I = 1227$ eV, 2674 levels are included from the $4p^6 4d^8$, $4p^5 4d^9$, $4p^6 4d^6 4f^2$, $4p^6 4d^7 5s$, $5d$, $4p^4 4d^{10}$, $4p^5 4d^8 4f$ and $4p^6 4d^7 4f$ configurations.

| λmeas(Å) | λcalc(Å) | Lower | Upper | Type | Intensity |
|---|---|---|---|---|---|
| | 48.945 | $4d^4_{3/2} 4d^4_{5/2}$ (J = 4) | $4d^3_{3/2}$[$4d^4_{5/2}$ (2)]7/2 $4f_{5/2}$ (J = 5) | E1 | 1781 |
| | 49.025 | $4d^4_{3/2} 4d^4_{5/2}$ (J = 2) | $4d^3_{3/2}$[$4d^4_{5/2}$ (2)]5/2 $4f_{5/2}$ (J = 3) | E1 | 681 |
| | 49.110 | $4d^4_{3/2} 4d^4_{5/2}$ (J = 0) | $4d^3_{3/2}$[$4d^4_{5/2}$ (0)]3/2 $4f_{5/2}$ (J = 1) | E1 | 234 |
| band | 49.150 | $4d^4_{3/2} 4d^4_{5/2}$ (J = 2) | $4d^3_{3/2}$[$4d^4_{5/2}$ (2)]7/2 $4f_{5/2}$ (J = 2) | E1 | 495 |
| 51.5 | 49.264 | $4d^4_{3/2} 4d^4_{5/2}$ (J = 4) | $4d^4_{3/2}$[$4d^3_{5/2}$ (3)]9/2 $4f_{7/2}$ (J = 4) | E1 | 1175 |
| | 49.269 | $4d^4_{3/2} 4d^4_{5/2}$ (J = 4) | $4d^3_{3/2}$[$4d^4_{5/2}$ (4)]11/2 $4f_{5/2}$ (J = 3) | E1 | 1092 |
| | 49.344 | $4d^4_{3/2} 4d^4_{5/2}$ (J = 4) | $4d^2_{3/2}$(0)$4d^5_{5/2}$ [5/2] $4f_{7/2}$ (J = 4) | E1 | 214 |
| | 49.399 | $4d^4_{3/2} 4d^4_{5/2}$ (J = 2) | $4d^3_{3/2}$[$4d^4_{5/2}$ (2)]7/2 $4f_{5/2}$ (J = 1) | E1 | 270 |
| 570.41 | 570.2 | $4d^4_{3/2} 4d^4_{5/2}$ (J = 4) | $4d^3_{3/2} 4d^5_{5/2}$ (J = 4) | M1 | 73 |
| 650.92 | 666.5 | $4d^3_{3/2} 4d^5_{5/2}$ (J = 3) | $4d^2_{3/2} 4d^6_{5/2}$ (J = 2) | M1 | 27 |
| 687.57 | 712.4 | $4d^4_{3/2} 4d^4_{5/2}$ (J = 2) | $4d^3_{3/2} 4d^5_{5/2}$ (J = 1) | M1 | 21 |
| 790.31 | 785.5 | $4d^4_{3/2} 4d^4_{5/2}$ (J = 2) | $4d^3_{3/2} 4d^5_{5/2}$ (J = 2) | M1 | 48 |
| 794.21 | 790.5 | $4d^4_{3/2} 4d^4_{5/2}$ (J = 4) | $4d^3_{3/2} 4d^5_{5/2}$ (J = 3) | M1 | 87 |

**Table VIII.** Measured and calculated wavelengths, transitions and intensities for Tc-like W$^{31+}$. Ground configuration $4p^64d^7$, $E_I = 1279$ eV, 410 levels were included from the $4p^64d^7$, $4p^54d^8$ and $4p^64d\,^64f$ configurations.

| λmeas(Å) | λcalc(Å) | Lower | Upper | Type | Intensity |
|---|---|---|---|---|---|
| band<br><br>51.9 | 49.569 | $4p^64d^7$ [J = 9/2] | $4p^64d^64f$ [J = 11/2] | E1 | 1694 |
| | 49.579 | $4p^64d^7$ [J = 5/2] | $4p^64d^64f$ [J = 5/2] | E1 | 129 |
| | 49.640 | $4p^64d^7$ [J = 5/2] | $4p^64d^64f$ [J = 7/2] | E1 | 360 |
| | 49.666 | $4p^64d^7$ [J = 5/2] | $4p^64d^64f$ [J = 5/2] | E1 | 125 |
| | 49.701 | $4p^64d^7$ [J = 3/2] | $4p^64d^64f$ [J = 5/2] | E1 | 285 |
| | 49.736 | $4p^64d^7$ [J = 9/2] | $4p^64d^64f$ [J = 9/2] | E1 | 1251 |
| | 49.791 | $4p^64d^7$ [J = 9/2] | $4p^64d^64f$ [J = 9/2] | E1 | 189 |
| | 49.793 | $4p^64d^7$ [J = 5/2] | $4p^64d^64f$ [J = 3/2] | E1 | 136 |
| | 49.951 | $4p^64d^7$ [J = 9/2] | $4p^64d^64f$ [J = 7/2] | E1 | 1134 |
| 666.76 | 664.107 | $4p^64d^7$ [J = 9/2] | $4p^64d^7$ [J = 9/2] | M1 | 123 |
| 804.88 | 809.690 | $4p^64d^7$ [J = 9/2] | $4p^64d^7$ [J = 7/2] | M1 | 108 |

**Table IX.** Measured and calculated wavelengths, transitions and intensities for Mo-like W$^{32+}$. Ground configuration $4p^64d^6$, $E_I = 1330$ eV, 4555 levels are included from the $4p^64d^6$, $4p^64d^44f^2$, $4p^64d^55s$, 5d, $4p^44d^8$, $4p^54d^64f$ and $4p^64d\,^54f$ configurations.

| λmeas(Å) | λcalc(Å) | Lower | Upper | Type | Intensity |
|---|---|---|---|---|---|
| band<br><br>52.2 | 50.114 | $4p^64d^6$ [J = 4] | $4p^64d^54f$ [J = 4] | E1 | 856 |
| | 50.149 | $4p^64d^6$ [J = 6] | $4p^64d^54f$ [J = 7] | E1 | 277 |
| | 50.175 | $4p^64d^6$ [J = 2] | $4p^64d^54f$ [J = 1] | E1 | 120 |
| | 50.179 | $4p^64d^6$ [J = 2] | $4p^64d^54f$ [J = 3] | E1 | 300 |
| | 50.218 | $4p^64d^6$ [J = 4] | $4p^64d^54f$ [J = 5] | E1 | 1046 |
| | 50.376 | $4p^64d^6$ [J = 4] | $4p^64d^54f$ [J = 5] | E1 | 193 |
| | 50.391 | $4p^64d^6$ [J = 2] | $4p^64d^54f$ [J = 2] | E1 | 230 |
| | 50.537 | $4p^64d^6$ [J = 4] | $4p^64d^54f$ [J = 4] | E1 | 265 |
| | 50.580 | $4p^64d^6$ [J = 4] | $4p^64d^54f$ [J = 3] | E1 | 703 |
| | 50.820 | $4p^64d^6$ [J = 6] | $4p^64d^54f$ [J = 6] | E1 | 108 |
| | 50.826 | $4p^64d^6$ [J = 4] | $4p^64d^54f$ [J = 3] | E1 | 88 |
| | 67.385 | $4p^64d^6$ [J = 4] | $4p^54d^7$ [J = 3] | E1 | 76 |
| | 68.754 | $4p^64d^6$ [J = 4] | $4p^54d^7$ [J = 4] | E1 | 77 |
| 661.08 | 661.9 | $4p^64d^6$ [J = 4] | $4p^64d^6$ [J = 5] | M1 | 258 |
| 668.19 | 669.4 | $4p^64d^6$ [J = 6] | $4p^64d^6$ [J = 6] | M1 | 101 |
| 803.03 | 807.7 | $4p^64d^6$ [J = 4] | $4p^64d^6$ [J = 4] | M1 | 270 |
| | 884.6 | $4p^64d^6$ [J = 4] | $4p^64d^6$ [J = 3] | M1 | 129 |

**Table X.** Measured and calculated wavelengths, transitions and intensities for Nb-like W$^{33+}$. Ground configuration 4p$^6$4d$^5$, E$_I$ = 1383 eV, 4168 levels are included from the 4p$^6$4d$^5$, 4p$^5$4d$^6$, 4p$^6$4d$^3$4f$^2$, 4p$^6$4d$^4$5s, 5d, 4p$^4$4d$^7$, 4p$^5$4d$^5$4f and 4p$^6$4d$^4$4f configurations.

| λmeas(Å) | λcalc(Å) | Lower | Upper | Type | Intensity |
|---|---|---|---|---|---|
| band 52.7 | 50.458 | 4p$^6$4d$^5$ (J = 5/2) | 4p$^6$4d$^4$4f (J = 5/2) | E1 | 125 |
| | 50.696 | 4p$^6$4d$^5$ (J = 5/2) | 4p$^6$4d$^4$4f (J = 7/2) | E1 | 869 |
| | 50.817 | 4p$^6$4d$^5$ (J = 11/2) | 4p$^6$4d$^4$4f (J = 13/2) | E1 | 207 |
| | 50.872 | 4p$^6$4d$^5$ (J = 9/2) | 4p$^6$4d$^4$4f (J = 11/2) | E1 | 133 |
| | 50.942 | 4p$^6$4d$^5$ (J = 5/2) | 4p$^6$4d$^4$4f (J = 7/2) | E1 | 173 |
| | 51.019 | 4p$^6$4d$^5$ (J = 5/2) | 4p$^6$4d$^4$4f (J = 3/2) | E1 | 174 |
| | 51.054 | 4p$^6$4d$^5$ (J = 5/2) | 4p$^5$4d$^6$ (J = 5/2) | E1 | 937 |
| | 51.305 | 4p$^6$4d$^5$ (J = 5/2) | 4p$^6$4d$^4$4f (J = 3/2) | E1 | 458 |
| | 51.346 | 4p$^6$4d$^5$ (J = 5/2) | 4p$^6$4d$^4$4f (J = 7/2) | E1 | 93 |
| | 51.362 | 4p$^6$4d$^5$ (J = 11/2) | 4p$^6$4d$^4$4f (J = 11/2) | E1 | 120 |
| 692.36 | 690.9 | 4p$^6$4d$^5$ (J = 5/2) | 4p$^6$4d$^5$ (J = 3/2) | M1 | 96 |
| 706.18 | 706.1 | 4p$^6$4d$^5$ (J = 5/2) | 4p$^6$4d$^5$ (J = 7/2) | M1 | 307 |
| 708.22 | 711.9 | 4p$^6$4d$^5$ (J = 5/2) | 4p$^6$4d$^5$ (J = 5/2) | M1 | 107 |
| | 993.2 | 4p$^6$4d$^5$ (J = 5/2) | 4p$^6$4d$^5$ (J = 5/2) | M1 | 420 |

**Table XI.** Measured and calculated wavelengths, transitions and intensities for Zr-like W$^{34+}$. Ground configuration 4p$^6$4d$^4$, E$_I$ = 1455 eV, 3163 levels are included from the 4p$^6$4d$^4$, 4p$^6$4d$^2$4f$^2$, 4p$^6$4d$^3$5s, 5d, 4p$^4$4d$^6$, 4p$^5$4d$^4$4f ,4p$^5$4d$^5$ and 4p$^6$4d$^3$4f configurations.

| λmeas(Å) | λcalc(Å) | Lower | Upper | Type | Intensity |
|---|---|---|---|---|---|
| band 53.2 | 51.381 | 4p$^6$4d$^4$ (J = 3) | 4p$^6$4d$^3$4f (J = 4) | E1 | 196 |
| | 51.549 | 4p$^6$4d$^4$ (J = 4) | 4p$^6$4d$^3$4f (J = 5) | E1 | 366 |
| | 51.742 | 4p$^6$4d$^4$ (J = 0) | 4p$^6$4d$^3$4f (J = 1) | E1 | 2928 |
| | 52.153 | 4p$^6$4d$^4$ (J = 4) | 4p$^6$4d$^3$4f (J = 4) | E1 | 231 |
| | 67.271 | 4p$^6$4d$^4$ (J = 0) | 4p$^5$4d$^5$ (J = 1) | E1 | 349 |
| 662.40 | 656.2 | 4p$^6$4d$^4$ (J = 1) | 4p$^6$4d$^4$ (J = 2) | M1 | 95 |
| 680.60 | 687.6 | 4p$^6$4d$^4$ (J = 1) | 4p$^6$4d$^4$ (J = 5) | M1 | 112 |
| 696.95 | 695.4 | 4p$^6$4d$^4$ (J = 2) | 4p$^6$4d$^4$ (J = 1) | M1 | 104 |
| 736.64 | 739.0 | 4p$^6$4d$^4$ (J = 4) | 4p$^6$4d$^4$ (J = 5) | M1 | 85 |
| 855.63 | 872.5 | 4p$^6$4d$^4$ (J = 0) | 4p$^6$4d$^4$ (J = 1) | M1 | 618 |
| 864.51 | 882.7 | 4p$^6$4d$^4$ (J = 4) | 4p$^6$4d$^4$ (J = 4) | M1 | 127 |

**Table XII.** Measured and calculated wavelengths, transitions and intensities for Y-like $W^{35+}$. Ground configuration $4p^64d^3$, $E_I$ = 1508 eV, 3000 levels are included from the $4p^64d^3$, $4p^64d4f^2$, $4p^64d^25d$, $4p^44d^5$ and $4p^54d^34f$ configurations.

| λmeas(Å) | λcalc(Å) | Lower | Upper | Type | Intensity |
|---|---|---|---|---|---|
| | 45.115 | $4p^64d^3$ (J=3/2) | $4p^54d^4$ (J=1/2) | E1 | 484 |
| | 46.913 | $4p^64d^3$ (J=9/2) | $4p^54d^4$ (J=9/2) | E1 | 76 |
| band 53.7 | 52.166 | $4p^64d^3$ (J=3/2) | $4p^64d^24f$ (J=5/2) | E1 | 1415 |
| | 52.529 | $4p^64d^3$ (J=7/2) | $4p^64d^24f$ (J=9/2) | E1 | 84 |
| | 52.642 | $4p^64d^3$ (J=9/2) | $4p^64d^24f$ (J=11/2) | E1 | 130 |
| | 53.015 | $4p^64d^3$ (J=3/2) | $4p^64d^24f$ (J=3/2) | E1 | 1055 |
| | 65.675 | $4p^64d^3$ (J=3/2) | $4p^54d^4$ (J=3/2) | E1 | 133 |
| | 67.634 | $4p^64d^3$ (J=3/2) | $4p^54d^4$ (J=5/2) | E1 | 133 |
| | 449.38 | $4d^3$ (J=3/2) | $[4d^2_{3/2}(0)]4d_{5/2}$ (J=5/2) | M1 | 65 |
| 563.82 | 565.42 | $[4d^2_{3/2}(2)]4d_{5/2}$ (J=3/2) | $4d_{3/2}[4d^2_{5/2}(4)]$ (J=5/2) | M1 | 56 |
| 566.54 | 568.78 | $[4d^2_{3/2}(0)]4d_{5/2}$ (J=5/2) | $4d_{3/2}[4d^2_{5/2}(0)]$ (J=3/2) | M1 | 17 |
| 615.34 | 617.66 | $[4d^2_{3/2}(2)]4d_{5/2}$ (J=9/2) | $4d_{3/2}[4d^2_{5/2}(4)]$ (J=11/2) | M1 | 31 |
| 629.85 | 630.10 | $[4d^2_{3/2}(2)]4d_{5/2}$ (J=3/2) | $4d_{3/2}[4d^2_{5/2}(2)]$ (J=3/2) | M1 | 41 |
| 622.30 | 636.29 | $4d^3$ (J=3/2) | $[4d^2_{3/2}(2)]4d_{5/2}$ (J=1/2) | M1 | 125 |
| 659.20 | 659.70 | $[4d^2_{3/2}(2)]4d_{5/2}$ (J=5/2) | $4d_{3/2}[4d^2_{5/2}(4)]$ (J=7/2) | M1 | 117 |
| 660.03 | 660.53 | $[4d^2_{3/2}(2)]4d_{5/2}$ (J=1/2) | $4d_{3/2}[4d^2_{5/2}(2)]$ (J=1/2) | M1 | 28 |
| 710.46 | 711.59 | $4d^3$ (J=3/2) | $[4d^2_{3/2}(2)]4d_{5/2}$ (J=3/2) | M1 | 366 |
| 756.64 | 752.74 | $[4d^2_{3/2}(2)]4d_{5/2}$ (J=7/2) | $4d_{3/2}[4d^2_{5/2}(4)]$ (J=9/2) | M1 | 23 |
| 774.76 | 775.35 | $[4d^2_{3/2}(2)]4d_{5/2}$ (J=9/2) | $4d_{3/2}[4d^2_{5/2}(4)]$ (J=9/2) | M11 | 37 |
| 822.68 | 832.25 | $4d^3$ (J=3/2) | $[4d^2_{3/2}(2)]4d_{5/2}$ (J=5/2) | M1 | 452 |

**Table XIII.** Measured and calculated wavelengths, transitions and intensities for Sr-like $W^{36+}$. Ground configuration $4p^64d^2$, $E_I$=1565 eV, 5000 levels are included from the $4p^64d^2$, $4p^64f^2$, $4p^64d5s$, $5p$, $5d$, $5f$, $4p^44d^4$, $4p^54d^24f$, $4p^64d4f$, and $4p^54d^3$ configurations.

| λmeas(Å) | λcalc(Å) | Lower | Upper | Type | Intensity |
|---|---|---|---|---|---|
| | 44.179 | $4p^64d^2_{3/2}$ (J = 2) | $4p^5_{1/2}4d^3_{3/2}$ (J = 1) | E1 | 353 |
| | 45.588 | $4p^64d^2_{3/2}$ (J = 0) | $4p^5_{1/2}4d^3_{3/2}$ (J = 1) | E1 | 191 |
| | 47.076 | $4p^64d^2_{3/2}$ (J = 2) | $4p^5_{1/2}4d^3_{3/2}$ (J = 2) | E1 | 759 |
| band | 52.772 | $4p^64d^2_{3/2}$ (J = 2) | $4p^64d_{3/2}4f_{5/2}$ (J = 1) | E1 | 146 |
| 54.14 | 53.209 | $4p^64d^2_{3/2}$ (J = 2) | $4p^64d_{3/2}4f_{5/2}$ (J = 3) | E1 | 1614 |
| | 54.796 | $4p^64d^2_{3/2}$ (J = 0) | $4p^64d_{3/2}4f_{5/2}$ (J = 1) | E1 | 361 |
| | 58.404 | $4p^64d^2_{3/2}$ (J = 2) | $4p^64d_{3/2}4f_{5/2}$ (J = 2) | E1 | 147 |
| | 63.148 | $4p^64d^2_{3/2}$ (J = 2) | $4p^5_{3/2}4d_{3/2}4d^2_{5/2}$ (J = 1) | E1 | 91 |
| | 65.588 | $4p^64d^2_{3/2}$ (J = 2) | $4p^5_{3/2}4d^2_{3/2\ 2}4d_{5/2}$ (J=2) | E1 | 199 |
| | 67.235 | $4p^64d^2_{3/2}$ (J = 2) | $4p^5_{3/2}4d^2_{3/2\ 2}4d_{5/2}$ (J=3) | E1 | 174 |
| | 450.68 | $4p^64d_{3/2}4d_{5/2}$ (J = 1) | $4p^64d^2_{5/2}$ (J = 0) | M1 | 33 |
| 526.19 | 526.94 | $4p^64d_{3/2}4d_{5/2}$ (J = 3) | $4p^64d^2_{5/2}$ (J = 2) | M1 | 6 |
| 541.20 | 547.51 | $4p^64d^2_{3/2}$ (J = 2) | $4p^64d_{3/2}4d_{5/2}$ (J = 1) | M1 | 19 |
| 574.30 | 580.31 | $4p^64d^2_{3/2}$ (J = 2) | $4p^64d_{3/2}4d_{5/2}$ (J = 2) | M1 | 236 |
| 598.01 | 593.69 | $4p^64d_{3/2}4d_{5/2}$ (J = 3) | $4p^64d^2_{5/2}$ (J = 4) | M1 | 58 |
| 635.89 | 633.90 | $4p^64d_{3/2}4d_{5/2}$ (J = 2) | $4p^64d^2_{5/2}$ (J = 2) | M1 | 23 |
| 680.60 | 678.29 | $4p^64d_{3/2}4d_{5/2}$ (J = 1) | $4p^64d^2_{5/2}$ (J = 2) | M1 | 9 |
| 707.74 | 712.75 | $4p^64d^2_{3/2}$ (J = 2) | $4p^64d_{3/2}4d_{5/2}$ (J = 3) | M1 | 550 |
| 795.09 | 798.29 | $4p^64d^2_{3/2}$ (J = 4) | $4p^64d^2_{5/2}$ (J = 4) | M1 | 15 |
| 855.85 | 854.94 | $4p^64d^2_{3/2}$ (J = 0) | $4p^64d_{3/2}4d_{5/2}$ (J = 1) | M1 | 106 |

**Table XIV.** Measured and calculated wavelengths, transitions and intensities for Rb-like W$^{37+}$. Ground configuration 4p$^6$4d, E$_I$ = 1618 eV, 286 levels are included from the 4p$^6$4d, 4p$^6$4f, 4p$^5$4d$^2$, 4p$^5$4d4f, 4p$^5$4f$^2$ and 4s4p$^6$4d4f configurations.

| λmeas(Å) | λcalc(Å) | Lower | Upper | Type | Intensity |
|---|---|---|---|---|---|
| | 44.793 | 4p$^6$4d$_{3/2}$ (J = 3/2) | 4p$^5_{1/2}$[4d$^2_{3/2}$ (J = 2)] J = 3/2 | E1 | 1110 |
| | 46.118 | 4p$^6$4d$_{3/2}$ (J = 3/2) | 4p$^5_{1/2}$[4d$^2_{3/2}$ (J = 0)] J = 1/2 | E1 | 320 |
| 49.52 | 49.057 | 4p$^6$4d$_{3/2}$ (J = 3/2) | 4p$^5_{1/2}$[4d$^2_{3/2}$ (J = 2)] J = 5/2 | E1 | 878 |
| 56.86 | 56.045 | 4p$^6$4d$_{3/2}$ (J = 3/2) | 4p$^6$4f$_{5/2}$ (J = 5/2) | E1 | 484 |
| 57.74 | 56.718 | 4p$^6$4d$_{3/2}$ (J = 3/2) | 4p$^5_{3/2}$[4d$^2_{5/2}$ (J = 4)] J = 5/2 | E1 | 181 |
| | 60.853 | 4p$^6$4d$_{3/2}$ (J = 3/2) | 4p$^5_{3/2}$4d$_{3/2}$ [J = 3]4d$_{5/2}$ J = 1/2 | E1 | 317 |
| | 60.905 | 4p$^6$4d$_{5/2}$ (J = 5/2) | 4p$^6$4f$_{7/2}$ (J = 7/2) | E1 | 28 |
| | 61.331 | 4p$^6$4d$_{5/2}$ (J = 5/2) | 4p$^6$4f$_{5/2}$ (J | E1 | 164 |
| | 62.138 | 4p$^6$4d$_{5/2}$ (J = 5/2) | 4p$^5_{3/2}$[4d$^2_{5/2}$ (J = 4)] J = 5/2 | E1 | 259 |
| 64.82 | 63.866 | 4p$^6$4d$_{5/2}$ (J = 5/2) | 4p$^5_{3/2}$4d$_{3/2}$ [J = 3]4d$_{5/2}$ J = 3/2 | E1 | 533 |
| | 89.541 | 4p$^6$4d$_{5/2}$ (J = 5/2) | 4p$^5_{3/2}$[4d$^2_{3/2}$ (J = 2)] J = 7/2 | E1 | 90 |
| 646.68 | 650.221 | 4p$^6$4d$_{3/2}$ (J = 3/2) | 4p$^6$4d$_{5/2}$ (J = 5/2) | M1 | 772 |

**Table XV.** Measured and Calculated wavelengths, transitions and intensities for Kr-like W$^{38+}$. Ground configuration 4s$^2$4p$^6$, E$_I$ = 1839 eV, 70 levels are included from the 4s$^2$4p$^6$, 4s$^2$4p$^5$4d, 4s$^2$4p$^5$4f, 4s$^2$4p$^5$5s, 4s$^2$4p$^5$5p, 4s$^2$4p$^5$5d, 4s$^2$4p$^5$5f, 4s4p$^6$4d and 4s4p$^6$4f configurations.

| λmeas(Å) | λcalc(Å) | Lower | Upper | Type | Intensity |
|---|---|---|---|---|---|
| | 21.621 | 4s$^2$ 4p$^5_{3/2}$4d$_{5/2}$ (J = 1) | 4s$^2$ 4p$^5_{3/2}$5p$_{3/2}$ (J = 0) | E1 | 83 |
| | 22.483 | 4s$^2$ 4p$^5_{1/2}$4d$_{3/2}$ (J = 1) | 4s$^2$ 4p$^5_{1/2}$5p$_{1/2}$ (J = 0) | E1 | 56 |
| 46.40 | 46.064 | 4s$^2$4p$^6$(J = 0) | 4s$^2$ 4p$^5_{1/2}$4d$_{3/2}$ (J = 1) | E1 | 2660 |
| | 56.073 | 4s$^2$ 4p$^5_{3/2}$4d$_{3/2}$ (J = 3) | 4s$^2$ 4p$^5_{3/2}$4f$_{7/2}$ (J = 2) | E1 | 120 |
| | 56.224 | 4s$^2$ 4p$^5_{3/2}$4d$_{3/2}$ (J = 1) | 4s$^2$ 4p$^5_{3/2}$4f$_{5/2}$ (J = 2) | E1 | 77 |
| | 57.022 | 4s$^2$ 4p$^5_{3/2}$4d$_{3/2}$ (J = 3) | 4s$^2$ 4p$^5_{3/2}$4f$_{5/2}$ (J = 2) | E1 | 97 |
| | 57.393 | 4s$^2$ 4p$^5_{3/2}$4d$_{3/2}$ (J = 2) | 4s$^2$ 4p$^5_{3/2}$4f$_{5/2}$ (J = 2) | E1 | 108 |
| | 58.664 | 4s$^2$ 4p$^5_{3/2}$4d$_{3/2}$ (J = 2) | 4s$^2$ 4p$^5_{3/2}$4f$_{5/2}$ (J = 3) | E1 | 93 |
| | 59.409 | 4s$^2$ 4p$^5_{3/2}$4d$_{3/2}$ (J = 3) | 4s$^2$ 4p$^5_{3/2}$4f$_{5/2}$ (J = 4) | E1 | 468 |
| 63.98 | 63.249 | 4s$^2$4p$^6$(J = 0) | 4s$^2$ 4p$^5_{3/2}$4d$_{5/2}$ (J = 1) | E1 | 2400 |
| | 68.335 | 4s$^2$ 4p$^5_{3/2}$4d$_{5/2}$ (J = 1) | 4s$^2$ 4p$^5_{3/2}$4f$_{7/2}$ (J = 2) | E1 | 219 |
| | 63.579 | 4s$^2$ 4p$^5_{3/2}$4d$_{3/2}$ (J = 3) | 4s 4p$^6$4d$_{3/2}$ (J = 2) | E1 | 121 |
| | 63.883 | 4s$^2$ 4p$^5_{1/2}$4d$_{3/2}$ (J = 1) | 4s$^2$ 4p$^5_{1/2}$4f$_{5/2}$ (J = 2) | E1 | 76 |
| | 80.897 | 4s$^2$4p$^6$(J = 0) | 4s$^2$ 4p$^5_{3/2}$4d$_{3/2}$ (J = 1) | E1 | 335 |
| | 128.05 | 4s$^2$4p$^5_{3/2}$4d$_{5/2}$ (J = 4) | 4p$^5_{1/2}$4d$_{5/2}$ (J = 3) | M1 | 32 |
| | 138.09 | 4s$^2$4p$^5_{3/2}$4d$_{5/2}$ (J = 3) | 4p$^5_{1/2}$4d$_{3/2}$ (J = 2) | M1 | 47 |
| 532.87 | 523.67 | 4s$^2$ 4p$^5_{3/2}$4d$_{3/2}$ (J = 3) | 4s$^2$ 4p$^5_{3/2}$4d$_{5/2}$ (J = 3) | M1 | 28 |
| 559.04 | 556.759 | 4s$^2$ 4p$^5_{3/2}$4d$_{3/2}$ (J = 2) | 4s$^2$ 4p$^5_{3/2}$4d$_{5/2}$ (J = 3) | M1 | 79 |
| | 585.986 | 4s$^2$ 4p$^5_{3/2}$4d$_{3/2}$ (J = 1) | 4s$^2$ 4p$^5_{3/2}$4d$_{5/2}$ (J = 2) | M1 | 59 |
| 799.23 | 798.080 | 4s$^2$ 4p$^5_{3/2}$4d$_{3/2}$ (J = 3) | 4s$^2$ 4p$^5_{3/2}$4d$_{5/2}$ (J = 4) | M1 | 120 |
| | 2758.8 | 4s$^2$ 4p$^5_{3/2}$4d$_{3/2}$ (J = 1) | 4s$^2$ 4p$^5_{3/2}$4d$_{3/2}$ (J = 2) | M1 | 103 |

**TABLE XVI.** MEASURED AND CALCULATED WAVELENGTHS, TRANSITIONS AND INTENSITIES FOR Br-LIKE W$^{39+}$. Ground configuration $4s^24p^5$, $E_I$=1894 eV, 195 levels are included from the $4s^24p^5$, $4s4p^6$, $4s^24p^44d$, $4s^24p^44d$, $4s^24p^44f$, $4s^24p^45s$, $4s^24p^45p$, $4s^24p^45d$, $4s^24p^45f$, $4s4p^54d$ and $4s4p^54f$ configurations.

| λmeas(Å) | λcalc(Å) | Lower | Upper | Type | Intensity |
|---|---|---|---|---|---|
| | 45.667 45.667 | $4p^5_{3/2}$ (J=3/2) (J=5/2) | $[4p^3_{3/2}\,4p_{1/2}](2)4d_{5/2}$ (J=5/2) | E1 | 133 |
| | 45.965 | $4p^5_{3/2}$ (J=3/2) (J=5/2) | $[4p^3_{3/2}\,4p_{1/2}](2)4d_{3/2}$ (J=1/2) | E1 | 476 |
| 46.81 | 46.119 | $4p^5_{3/2}$ (J=3/2) | $[4p^3_{3/2}\,4p_{1/2}](2)4d_{3/2}$ (J=5/2) | E1 | 1030 |
| | 46.124 | $4p^5_{3/2}$ (J=3/2) | $[4p^3_{3/2}\,4p_{1/2}](2)4d_{3/2}$ (J=3/2) | E1 | 623 |
| | 46.712 | $4p^5_{3/2}$ (J=3/2) | $[4p^3_{3/2}\,4p_{1/2}](2)4d_{5/2}$ (J=3/2) | E1 | 83 |
| | 50.014 | $4p^5_{3/2}$ (J=3/2) | $[4p^3_{3/2}\,4p_{1/2}](1)4d_{3/2}$ (J=5/2) | E1 | 55 |
| | 57.944 | $[4p^2_{3/2}\,4p^2_{1/2}](2)4d_{3/2}$ (J=5/2) | $[4p^2_{3/2}\,4p^2_{1/2}](2)4f_{5/2}$ (J=7/2) | E1 | 34 |
| | 58.672 | $[4p^2_{3/2}\,4p^2_{1/2}](2)4d_{3/2}$ (J=7/2) | $[4p^2_{3/2}\,4p^2_{1/2}](2)4f_{5/2}$ (J=7/2) | E1 | 38 |
| | 59.645 | $[4p^2_{3/2}\,4p^2_{1/2}](2)4d_{3/2}$ (J=7/2) | $[4p^2_{3/2}\,4p^2_{1/2}](2)4f_{5/2}$ (J=9/2) | E1 | 69 |
| | 60.282 | $4s^24p^5_{3/2}$ (J=3/2) | $4s4p^6$(J=1/2) | E1 | 247 |
| | 62.493 | $4s^24p^5_{3/2}$ (J=3/2) | $[4p^3_{3/2}\,4p_{1/2}](1)4d_{3/2}$ (J=5/2) | E1 | 36 |
| 64.74 | 63.798 | $4s^24p^5_{3/2}$ (J=3/2) | $[4p^2_{3/2}\,4p^2_{1/2}](2)4d_{5/2}$ (J=5/2) | E1 | 1020 |
| 65.76 | 64.851 | $4s^24p^5_{3/2}$ (J=3/2) | $[4p^2_{3/2}\,4p^2_{1/2}](2)4d_{5/2}$ (J=3/2) | E1 | 568 |
| | 66.652 | $4s^24p^5_{3/2}$ (J=3/2) | $[4p^2_{3/2}\,4p^2_{1/2}](0)4d_{5/2}$ (J=5/2) | E1 | 62 |
| | 68.691 | $[4p^2_{3/2}\,4p^2_{1/2}](2)4d_{5/2}$ (J=5/2) | $[4p^2_{3/2}\,4p^2_{1/2}](0)4f_{7/2}$ (J=7/2) | E1 | 68 |
| | 72.011 | $4s^24p^5_{3/2}$ (J=3/2) | $[4p^2_{3/2}\,4p^2_{1/2}](2)4d_{3/2}$ (J=1/2) | E1 | 41 |
| | 75.393 | $4s^24p^5_{3/2}$ (J=3/2) | $[4p^2_{3/2}\,4p^2_{1/2}](0)4d_{3/2}$ (J=3/2) | E1 | 72 |
| | 80.895 | $4s^24p^5_{3/2}$ (J=3/2) | $[4p^2_{3/2}\,4p^2_{1/2}](2)4d_{3/2}$ (J=5/2) | E1 | 138 |
| | 82.119 | $4s^24p^5_{3/2}$ (J=3/2) | $[4p^2_{3/2}\,4p^2_{1/2}](2)4d_{3/2}$ (J=3/2) | E1 | 40 |
| 131.8 | 133.609 | $4s^24p^5_{3/2}$ (J=3/2) | $4s^24p^5_{1/2}$ (J=1/2) | M1 | 101 |
| 698.37 | 687.875 | $[4p^2_{3/2}\,4p^2_{1/2}](2)4d_{3/2}$ (J=5/2) | $[4p^2_{3/2}\,4p^2_{1/2}](2)4d_{5/2}$ (J=7/2) | M1 | 40 |
| 774.76 | 759.439 | $[4p^2_{3/2}\,4p^2_{1/2}](2)4d_{3/2}$ (J=7/2) | $[4p^2_{3/2}\,4p^2_{1/2}](2)4d_{5/2}$ (J=9/2) | M1 | 103 |
| | | | | | |

**Table XVII.** Measured and calculated wavelengths, transitions and intensities for Br-like $W^{39+}$. Ground configuration $4s^24p^5$, $E_I = 1894$ eV, 195 levels are included from the $4s^24p^5$, $4s4p^6$, $4s^24p^44d$, $4s^24p^44d$, $4s^24p^44f$, $4s^24p^45s$, $4s^24p^45p$, $4s^24p^45d$, $4s^24p^45f$, $4s4p^54d$ and $4s4p^54f$ configurations.

| $\lambda$meas(Å) | $\lambda$calc(Å) | Lower | Upper | Type | Intensity |
|---|---|---|---|---|---|
| | 20.42 | $[4p^2_{1/2}\,4p_{3/2}](3/2)4d_{5/2}$ (J = 3) | $[4p^2_{1/2}\,4p_{3/2}](3/2)5p_{3/2}$ (J = 2) | E1 | 29 |
| | 46.092 | $[4p^2_{1/2}\,4p^2_{3/2}]$(J = 2) | $[4p_{1/2}\,4p^2_{3/2}(0)](1/2)4d_{3/2}$ (J = 1) | E1 | 397 |
| | 46.301 | $[4p^2_{1/2}\,4p^2_{3/2}]$(J = 0) | $[4p_{1/2}\,4p^2_{3/2}(2)](5/2)4d_{3/2}$ (J = 1) | E1 | 681 |
| 46.88 | 46.323 | $[4p^2_{1/2}\,4p^2_{3/2}]$(J = 2) | $[4p_{1/2}\,4p^2_{3/2}(2)](5/2)4d_{3/2}$ (J = 3) | E1 | 882 |
| | 46.366 | $[4p^2_{1/2}\,4p^2_{3/2}]$(J = 2) | $[4p_{1/2}\,4p^2_{3/2}(2)](3/2)4d_{5/2}$ (J = 2) | E1 | 37 |
| | 48.350 | $[4p^2_{1/2}\,4p^2_{3/2}]$(J = 2) | $[4p_{1/2}\,4p^2_{3/2}(0)](1/2)4d_{3/2}$ (J = 2) | E1 | 42 |
| | 50.387 | $[4p^2_{1/2}\,4p^2_{3/2}]$(J = 2) | $[4p_{1/2}\,4p^2_{3/2}(2)](5/2)4d_{3/2}$ (J = 3) | E1 | 36 |
| | 58.576 | $[4p^2_{1/2}\,4p^2_{3/2}]$(J = 2) | $4s4p^5_{3/2}$ (J = 1) | E1 | 97 |
| | 61.742 | $[4p^2_{1/2}\,4p^2_{3/2}]$(J = 0) | $4s4p^5_{3/2}$ (J = 1) | E1 | 131 |
| 62.60 | 62.337 | $[4p^2_{1/2}\,4p^2_{3/2}]$(J = 2) | $4s4p^2_{1/2}4p^3_{3/2}$ (J = 2) | E1 | 394 |
| | 64.049 | $[4p^2_{1/2}\,4p^2_{3/2}]$(J = 2) | $[4p^2_{1/2}\,4p_{3/2}](3/2)4d_{5/2}$(J = 1) | E1 | 86 |
| 65.81 | 64.791 | $[4p^2_{1/2}\,4p^2_{3/2}]$(J = 2) | $[4p^2_{1/2}\,4p_{3/2}](3/2)4d_{5/2}$(J = 3) | E1 | 830 |
| | 66.119 | $[4p^2_{1/2}\,4p_{3/2}](3/2)4d_{5/2}$ (J = 2) | $[4p^2_{1/2}\,4p_{3/2}](3/2)4f_{7/2}$ (J = 3) | E1 | 30 |
| | 67.854 | $[4p^2_{1/2}\,4p^2_{3/2}]$(J = 0) | $[4p^2_{1/2}\,4p_{3/2}](3/2)4d_{5/2}$ (J = 1) | E1 | 94 |
| | 68.307 | $[4p^2_{1/2}\,4p_{3/2}](3/2)4d_{5/2}$ (J = 3) | $[4p^2_{1/2}\,4p_{3/2}](3/2)4f_{7/2}$ (J = 4) | E1 | 82 |
| | 70.534 | $[4p^2_{1/2}\,4p^2_{3/2}]$(J = 2) | $[4p^2_{1/2}\,4p_{3/2}](3/2)4d_{5/2}$ (J = 2) | E1 | 112 |
| | 78.700 | $[4p^2_{1/2}\,4p^2_{3/2}]$(J = 2) | $[4p^2_{1/2}\,4p_{3/2}](3/2)4d_{3/2}$ (J = 1) | E1 | 38 |
| | 80.195 | $[4p^2_{1/2}\,4p^2_{3/2}]$(J = 2) | $[4p^2_{1/2}\,4p_{3/2}](3/2)4d_{3/2}$ (J = 2) | E1 | 61 |
| | 128.285 | $[4p^2_{1/2}\,4p^2_{3/2}]$(J = 2) | $[4p_{1/2}\,4p^3_{3/2}]$(J = 2) | M1 | 131 |
| | 134.913 | $[4p^2_{1/2}\,4p^2_{3/2}]$(J = 2) | $[4p_{1/2}\,4p^3_{3/2}]$(J = 1) | M1 | 77 |
| | 708.281 | $[4p^2_{1/2}\,4p_{3/2}](3/2)4d_{3/2}$ (J = 3) | $[4p^2_{1/2}\,4p_{3/2}](3/2)4d_{5/2}$ (J = 4) | M1 | 65 |

**Table XVIII.** Measured and calculated wavelengths, transitions and intensities for As-like $W^{41+}$. Ground configuration $4s^2 4p^3$, $E_I = 2003$ eV, 356 levels are included from the $4s^2 4p^3$, $4s4p^4$, $4p^5$, $4s^2 4p^2 4d$, $4s^2 4p^2 4f$, $4s^2 4p^2 5s$, $4s^2 4p^2 5p$, $4s^2 4p^2 5d$, $4s^2 4p^2 5f$, $4s4p^3 4d$, $4s4p^3 4f$ and $4s^2 4p4d^2$ configurations.

| $\lambda_{meas}$(Å) | $\lambda_{calc}$(Å) | Lower | Upper | Type | Intensity |
|---|---|---|---|---|---|
| | 45.874 | $4s^2 4p^2_{1/2} 4p_{3/2}$ (J = 3/2) | $4s^2 4p_{1/2} 4p_{3/2}(2)4d_{5/2}$ (J = 5/2) | E1 | 87 |
| | 46.690 | $4s^2 4p^2_{1/2} 4p_{3/2}$ (J = 3/2) | $4s4p^2_{1/2} 4p_{3/2}(2)4d_{3/2}$ (J = 3/2) | E1 | 274 |
| 47.16 | 46.694 | $4s^2 4p^2_{1/2} 4p_{3/2}$ (J = 3/2) | $4s4p^2_{1/2} 4p_{3/2}(2)4d_{3/2}$ (J = 1/2) | E1 | 692 |
| | 47.066 | $4s^2 4p^2_{1/2} 4p_{3/2}$ (J = 3/2) | $4s4p^2_{1/2} 4p_{3/2}(1)4d_{3/2}$ (J = 5/2) | E1 | 745 |
| | 50.544 | $4s^2 4p^2_{1/2} 4p_{3/2}$ (J = 3/2) | $4s^2 4p_{1/2} 4p_{3/2}(1)4d_{3/2}$ (J = 3/2) | E1 | 30 |
| | 60.255 | $4s^2 4p^2_{1/2} 4p_{3/2}$ (J = 3/2) | $4s 4p^2_{1/2} 4p^2_{3/2}$ (2) (J = 3/2) | E1 | 359 |
| 60.71 | 60.226 | $4s^2 4p^2_{1/2} 4p_{3/2}$ (J = 3/2) | $4s 4p^2_{1/2} 4p^2_{3/2}$ (0) (J = 1/2) | E1 | 108 |
| | 62.523 | $4s^2 4p_{1/2} 4p^2_{3/2}$ (2) (J = 3/2) | $4s^2 4p_{1/2} 4p_{3/2}(1)4d_{5/2}$ (J = 5/2) | E1 | 43 |
| | 62.548 | $4s^2 4p^2_{1/2}4d_{5/2}$ (J = 5/2) | $4s4p^2_{1/2} 4p_{3/2}$ (2)4d_{5/2} (J = 7/2) | E1 | 44 |
| 64.82 | 64.689 | $4s^2 4p^2_{1/2} 4p_{3/2}$ (J = 3/2) | $4s 4p^2_{1/2} 4p^2_{3/2}$ (2) (J = 5/2) | E1 | 461 |
| | 66.864 | $4s 4p^2_{1/2} 4p^2_{3/2}$ (2) (J = 3/2) | $4s4p^2_{1/2} 4p_{3/2}$ (1)4d_{5/2} (J = 5/2) | E1 | 22 |
| | 67.669 | $4s 4p^2_{1/2} 4p^2_{3/2}$ (2) (J = 5/2) | $4s4p^2_{1/2} 4p_{3/2}$ (2)4d_{5/2} (J = 7/2) | E1 | 27 |
| | 67.988 | $4s^2 4p^2_{1/2} 4d_{5/2}$ (J = 5/2) | $4s^2 4p^2_{1/2}4f_{5/2}$ (J = 7/2) | E1 | 38 |
| 70.15 | 69.963 | $4s^2 4p^2_{1/2} 4p_{3/2}$ (J = 3/2) | $4s^2 4p^2_{1/2} 4d_{5/2}$ (J = 5/2) | E1 | 249 |
| | 79.181 | $4s^2 4p^2_{1/2} 4p_{3/2}$ (J = 3/2) | $4s^2 4p^2_{1/2}4d_{3/2}$ (J = 3/2) | E1 | 59 |
| | 79.355 | $4s^2 4p_{1/2} 4p^2_{3/2}$ (2) (J = 5/2) | $4s^2 4p_{1/2} 4p_{3/2}(2)4d_{3/2}$ (J = 7/2) | E1 | 30 |
| | 108.760 | $4s^2 4p_{1/2} 4p^2_{3/2}$ (2) (J = 5/2) | $4s 4p^2_{1/2} 4p^2_{3/2}$ (2) (J = 3/2) | E1 | 26 |
| | 117.335 | $4s^2 4p_{1/2} 4p^2_{3/2}$ (2) (J = 3/2) | $4s 4p^2_{1/2} 4p^2_{3/2}$ (2) (J = 5/2) | E1 | 17 |
| | 122.276 | $4s^2 4p^2_{1/2} 4p_{3/2}$ (J = 3/2) | $4s^2 4p_{1/2} 4p^2_{3/2}$ (0) (J = 1/2) | M1 | 39 |
| | 131.394 | $4s^2 4p^2_{1/2} 4p_{3/2}$ (J = 3/2) | $4s^2 4p_{1/2} 4p^2_{3/2}$ (2) (J = 5/2) | M1 | 33 |
| | 139.811 | $4s^2 4p^2_{1/2} 4p_{3/2}$ (J = 3/2) | $4s^2 4p_{1/2} 4p^2_{3/2}$ (2) (J = 3/2) | M1 | 137 |

**Table XIX.** Measured and calculated wavelengths, transitions and intensities for Ge-like $W^{42+}$. Ground configuration $4s^24p^2$, $E_I = 2145$ eV, 207 levels are included from the $4s^24p^2$, $4s4p^3$, $4p^4$, $4s^24p4d$, $4s^24p4f$, $4s^24p5s$, $4s^24p5p$, $4s^24p5d$, $4s^24p5f$, $4s4p^24d$, $4s4p^24f$ and $4s^24d^2$ configurations.

| λmeas(Å) | λcalc(Å) | Lower | Upper | Type | Intensity |
|---|---|---|---|---|---|
| | 20.174 | $4s^24p_{1/2}\,4d_{3/2}$ (J = 1) | $4s^24p_{1/2}\,5p_{1/2}$ (J = 0) | E1 | 39 |
| 46.97 | 46.724 | $4s^24p^2_{1/2}$ (J = 0) | $4s^24p_{1/2}\,4d_{3/2}$ (J = 1) | E1 | 1740 |
| 61.30 | 60.707 | $4s^24p^2_{1/2}$ (J = 0) | $4s4p^2_{1/2}\,4p_{3/2}$ (J = 1) | E1 | 750 |
| | 65.913 | $4s4p^2_{1/2}\,4p_{3/2}$ (J = 2) | $4s4p^2_{1/2}\,4d_{5/2}$ (J = 2) | E1 | 63 |
| | 69.666 | $4s^24p_{1/2}\,4p_{3/2}$ (J = 2) | $4s^24p_{1/2}\,4d_{5/2}$ (J = 3) | E1 | 49 |
| | 72.158 | $4s4p^2_{1/2}\,4p_{3/2}$ (J = 1) | $4s4p^2_{1/2}\,4d_{5/2}$ ( J = 2) | E1 | 58 |
| | 82.323 | $4s^24p_{1/2}\,4p_{3/2}$ (J = 2) | $4s^24p_{1/2}\,4d_{3/2}$ (J = 2) | E1 | 53 |
| | 112.839 | $4s^24p_{1/2}\,4p_{3/2}$ (J = 2) | $4s4p^2_{1/2}\,4p_{3/2}$ (J = 1) | E1 | 86 |
| | 126.428 | $4s^24p_{1/2}\,4p_{3/2}$ (J = 1) | $4s4p^2_{1/2}\,4p_{3/2}$ (J = 2) | E1 | 72 |
| | 129.639 | $4s^24p^2_{1/2}$ (J = 0) | $4s^24p_{1/2}\,4p_{3/2}$ (J = 2) | M1 | 386 |
| | 132.462 | $4s^24p_{1/2}\,4p_{3/2}$ (J = 2) | $4s4p^2_{1/2}\,4p_{3/2}$ (J = 2) | E1 | 56 |
| | 135.991 | $4s^24p^2_{1/2}$ (J = 0) | $4s^24p_{1/2}\,4p_{3/2}$ (J = 1) | E1 | 139 |

**Table XX.** Measured and calculated wavelengths, transitions and intensities for Ga-like W$^{43+}$. Ground configuration $4s^24p$, $E_I$ = 2218 eV, 152 levels are included from the $4s^24p$, $4s^24d$, $4s^24f$, $4s^25s$, $4s^25p$, $4s^25d$, $4s^25f$, $4s4p^2$, $4s4p4d$, $4s4d^2$, $4s4p4f$, $4s4f^2$, $4s4d4f$ and $4p^3$ configurations.

| λmeas(Å) | λcalc(Å) | Lower | Upper | Type | Intensity |
|---|---|---|---|---|---|
| | 19.557 | $4s^24d$ (J = 3/2) | $4s^25p$ (J = 1/2) | E1 | 19 |
| 47.69 | 47.576 | $4s^24p$ (J = 1/2) | $4s^24d$ (J = 3/2) | E1 | 925 |
| 60.61 | 59.883 | $4s^24p$ (J = 1/2) | $4s4p^2_{1/2}$ (J = 1/2) | E1 | 571 |
| 61.29 | 60.865 | $4s^24p$ (J = 1/2) | $[4s4p_{1/2}(1)]4p_{3/2}$ (J = 3/2) | E1 | 609 |
| | 63.232 | $[4s4p_{1/2}(1)]4p_{3/2}$ (J = 3/2) | $4p_{1/2}[4p^2_{3/2}(2)]$ (J = 5/2) | E1 | 12 |
| | 63.788 | $[4s4p_{1/2}(0)]4p_{3/2}$ (J = 3/2) | $[4s4p_{1/2}(1)]4d_{5/2}$ (J = 3/2) | E1 | 20 |
| | 67.051 | $[4s4p_{1/2}(1)]4p_{3/2}$ (J = 5/2) | $[4s4p_{1/2}(1)]4d_{5/2}$ (J = 5/2) | E1 | 37 |
| | 68.151 | $4s^24p$ (J = 1/2) | $[4s4p_{1/2}(0)]4p_{3/2}$ (J = 3/2) | E1 | 39 |
| | 70.114 | $4s^24p$ (J = 3/2) | $4s^24d$ (J = 5/2) | E1 | 19 |
| | 72.351 | $[4s4p_{1/2}(1)]4p_{3/2}$ (J = 3/2) | $[4s4p_{1/2}(1)]4d_{5/2}$ (J = 5/2) | E1 | 23 |
| | 81.460 | $[4s4p_{1/2}(1)]4p_{3/2}$ (J = 5/2) | $[4s4p_{1/2}(1)]4d_{3/2}$ (J = 5/2) | E1 | 22 |
| | 112.577 | $4s^24p$ (J = 3/2) | $[4s4p_{1/2}(1)]4p_{3/2}$ (J = 1/2) | E1 | 21 |
| | 116.091 | $4s^24p$ (J = 3/2) | $[4s4p_{1/2}(1)]4p_{3/2}$ (J = 3/2) | M1 | 33 |
| | 126.570 | $4s^24p$ (J = 1/2) | $4s^24p$ (J=3/2) | M1 | 258 |
| | 126.655 | $4s^24p$ (J = 1/2) | $4s[4p^2_{1/2}(0)]$ (J = 1/2) | E1 | 333 |
| | 132.954 | $4s^24p$ (J = 3/2) | $[4s4p_{1/2}(1)]4p_{3/2}$ (J = 5/2) | E1 | 96 |
| | 147.655 | $4s^24p$ (J = 3/2) | $[4s4p_{1/2}(0)]4p_{3/2}$ (J = 3/2) | E1 | 28 |

**TABLE XXI.** MEASURED AND CALCULATED WAVELENGTHS, TRANSITIONS AND INTENSITIES FOR Zn-LIKE W$^{44+}$. Ground configuration $4s^2$, $E_I$=2372 eV, 98 levels are included from the $4s^2$, $4s4p$, $4s4d$, $4s4f$, $4p^2$, $4p4d$, $4p4f$, $4d^2$, $4d4f$, $4f^2$, $4s5s$, $4s5p$, $4s5d$ and $4s5f$ configurations.

| λmeas(Å) | λcalc(Å) | Lower | Upper | Type | Intensity |
|---|---|---|---|---|---|
| | 48.538 | $4s4p_{1/2}$ (J=1) | $4s4d_{3/2}$ (J=2) | E1 | 48 |
| 60.87 | 60.590 | $4s^2$ (J=0) | $4s4p_{3/2}$ (J=1) | E1 | 1690 |
| | 66.662 | $4s4p_{3/2}$ (J=2) | $4s4d_{5/2}$ (J=2) | E1 | 79 |
| | 73.846 | $4s4p_{3/2}$ (J=1) | $4s4d_{5/2}$ (J=2) | E1 | 41 |
| 132.75 | 132.010 | $4s^2$ (J=0) | $4s4p_{1/2}$ (J=1) | E1 | 811 |
| | 133.830 | $4s4p_{3/2}$ (J=2) | $4s4p_{1/2}$ (J=1) | M1 | 96 |

**TABLE XXII.** MEASURED AND CALCULATED WAVELENGTHS, TRANSITIONS AND INTENSITIES FOR Cu-LIKE W[45+]. Ground configuration 4s, $E_I$=2430 eV, 204 levels are included from the $3p^63d^{10}4s$, $3p^63d^{10}4p$, $3p^63d^{10}4d$, $3p^63d^{10}4f$, $3p^63d^{10}5s$, $3p^63d^{10}5p$, $3p^63d^{10}5d$, $3p^63d^{10}5f$, $3p^63d^94s^2$, $3p^63d^94s4p$, $3p^63d^94s4d$, $3p^63d^94s4f$, $3p^63d^94p^2$, $3p^53d^{10}4s^2$, $3p^53d^{10}4s4p$, $3p^53d^{10}4s4d$ and $3p^53d^{10}4p^2$ configurations.

| λmeas(Å) | λcalc(Å) | Lower | Upper | Type | Intensity |
|---|---|---|---|---|---|
| | 5.711 | $3p^63d^{10}4s$ (J=1/2) | $3p^63d^9_{3/2}4s(1)4f_{5/2}$ (J=3/2) | E1 | 67 |
| | 5.714 | $3p^63d^{10}4s$ (J=1/2) | $3p^63d^9_{3/2}4s(2)4f_{5/2}$ (J=1/2) | E1 | 35 |
| | 5.903 | $3p^63d^{10}4s$ (J=1/2) | $3p^63d^9_{5/2}4s(2)4f_{7/2}$ (J=3/2) | E1 | 23 |
| | 5.905 | $3p^63d^{10}4s$ (J=1/2) | $3p^63d^9_{5/2}4s(3)4f_{7/2}$ (J=1/2) | E1 | 11 |
| | 7.261 | $3p^63d^{10}4s$ (J=1/2) | $3p^63d^9_{3/2}4s(2)4p_{1/2}$ (J=3/2) | E1 | 12 |
| | 8.015 | $3p^63d^{10}4s$ (J=1/2) | $3p^63d^9_{5/2}4s^2$ (J=5/2) | E2 | 11 |
| | 16.137 | $3p^63d^{10}4p$ (J=3/2) | $3p^63d^{10}5s$ (J=1/2) | E1 | 14 |
| | 49.162 | $3p^63d^{10}4p$ (J=1/2) | $3p^63d^{10}4d$ (J=3/2) | E1 | 51 |
| 62.32 | 62.129 | $3p^63d^{10}4s$ (J=1/2) | $3p^63d^{10}4p$ (J=3/2) | E1 | 876 |
| | 71.849 | $3p^63d^{10}4p$ (J=3/2) | $3p^63d^{10}4d$ (J=5/2) | E1 | 78 |
| | 74.954 | $3p^63d^{10}4d$ (J=5/2) | $3p^63d^{10}4f$ (J=7/2) | E1 | 10 |
| 127.01 | 125.123 | $3p^63d^{10}4s$ (J=1/2) | $3p^63d^{10}4p$ (J=1/2) | E1 | 556 |

## References

[1] BROOKS, J.N., Fusion Technol. 18 (1990) 239.

[2] FIELD, A.R., FUSSMANN, G., GARCIA-ROSALES, C., HIRSCH, S., LIEDER, G., NAUJOKS, D., NEU, R., PITCHER, C.S., RADTKE, R., WENZEL, U., ASDEX Upgrade Team, J. Nucl. Mater. 220-222 (1995) 553.

[3] NAUJOKS, D., ASMUSSEN, K., BESSENRODT-WEBERPALS, S., DESCHKA, S., DUX, R., ENGELHARDT, W., FIELD, A.R., FUSSMANN, G., FUCHS, J.C., GARCIA-ROSALES, C., HIRSCH, S., IGNACZ, P., LIEDER, G., MAST, K.F., NEU, R., RADTKE, R., ROTH, J., WENZEL, U., ASDEX Upgrade Team, Nucl. Fusion 36 (1996) 671.

[4] PEACOCK, N.J., BARNSLEY, R., HAWKES, N.C., LAWSON, K.D., O'MULLANE, M.G., in Diagnostics for Experimental Thermonuclear Fusion Reactors, STOTT, P., GIUSEPPE, G., SINDONI, E., (Eds.), Plenum Press, New York 1996, 291.

[5] ISLER, R.C., NEIDIGH, R.V., COWAN, R.D., Phys. Lett. 63A (1977) 295.

[6] HINNOV, E., MATTIOLI, M., Phys. Lett. 66A (1978) 109.

[7] FINKENTHAL, M., HUANG, L.K., LIPPMANN, S., MOOS, H.W., MANDELBAUM, P., SCHWOB, J.L., KLAPISCH, M., TEXT Group, Phys. Lett. A 127 (1988) 255.

[8] ASMUSSEN, K., FOURNIER, K.B., LAMIG, J.M., NEU, R., SEELY, J.F., DUX, R., ENGELHARDT,W., FUCHS, J.C., ASDEX Upgrade Team, Nucl. Fusion 38 (1998) 967.

[9] BAR-SCHALOM, A., KLAPISCH, M., GOLDSTEIN, W.H., The HULLAC Code for Atomic Physis (1988), unpublished.

[10] BAR-SCHALOM, A., KLAPISCH, M., OREG, J., Phys. Rev. A 38 (1988) 1773.

[11] KLAPISCH, M., SCHWOB, J.L., FRANKEL, B.S., OREG, J., J. Opt. Soc. Am. 67 (1977) 148.

[12] BIEDERMANN, C, RADTKE, R., SCHWOB, J.L., MANDELBAUM, P., DORON, R., FUCHS, T., FUSSMANN, G., Physica Scripta T92 (2001) 85.

[13] RADTKE, R., BIEDERMANN, C., SCHWOB, J.L., MANDELBAUM, P., DORON, R., Phys. Rev. A 64 (2001) 012720.

[14] FOURNIER, K.B., At. Data Nucl. Data Tables 68 (1998) 1.

[15] NEU, R., FOURNIER, K.B., SCHLÖG, D., RICE, J., J. Phys. B 30 (1997) 5057.

[16] FOURNIER, K.B., private communication.

[17] MANDELBAUM, P, SCHWOB, J.L., DORON, R., Atomic Data for Highly Ionized Tungsten, Report LXUV 2001-5, Racah Institute of Physics, Hebrew University, Jerusalem.

[18] MANDELBAUM, P, SCHWOB, J.L., DORON, R., Atomic Data for Highly Ionized Tungsten, Report LXUV 2001-10, Racah Institute of Physics, Hebrew University, Jerusalem.

[19] MANDELBAUM, P, SCHWOB, J.L., DORON, R., Atomic Data for Highly Ionized Tungsten, Report LXUV 2001-11, Racah Institute of Physics, Hebrew University, Jerusalem.

# Vibrationally resolved processes in slow ion-molecule and atom-molecular ion collisions of hydrogenic species

*P.S. Krstić*

Oak Ridge National Laboratory, Physics Division, P.O. Box 2008, Oak Ridge, TN 37831-6372, USA

## Abstract

We have performed a series of comprehensive studies for the scattering of a proton on $H_2(v)$ and of a hydrogen atom on $H_2^+(v)$, for all initially vibrational excited states, $v$, of the relevant molecules. Final state resolved cross sections for charge transfer, excitation, dissociation, two-body association and elastic scattering have been calculated at the "same footing", in the range of the center-of-mass collision energies 0.5-10 eV, using a fully quantal, coupled-channel approach, and extended to 100 eV by the direct numerical solution of the time-dependent Schrödinger equation within the classical description of the projectile motion. An extensive vibrational basis set was used, defined in a large configuration space of the reactants, including a large number of dicretized vibrational continua (dissociation states), to account for the transitions through the "closed" channels as well as for the nuclear rearrangements at lower end of collision energies. A detailed picture was produced of all inelastic processes that involve two lowest, nonadiabatically coupled electronic surfaces of the $H_3^+$ molecule. The rotational dynamics of diatomic targets were treated with the sudden approximation. The obtained cross sections are in reasonable agreement with the sparse data available from literature, mostly for the initial ground vibrational state.

## 1. Introduction

In the edge/divertor region the temperatures are normally lower and there is a relatively high population of neutral species. Typical for this region is formation of molecules. Particularly important are $H_2(v)$ and $H_2^+(v)$ formed by associative desorption, collisional neutralization and excitation on the surface as well as hydrocarbons and hydrocarbon radicals, formed by chemical sputtering in the plasma facing carbon walls. These molecules are created with various isotopic combinations of H, and in excited vibrational states, $v$. Even if the population of vibrationally excited molecules in plasma is orders of magnitude smaller than for the ground, $v = 0$, state, the processes with $v > 0$ and $v = 0$ could be competitive. For example, the reaction $H_2(v) + H^+ \rightarrow H_2^+ + H$ is exoergic for $v \geq 4$ (for) $H$ and for $v \geq 6$ ($D$), thus increasing the charge transfer cross sections by two orders of magnitude (in comparison $v = 0$). Similarly, in the reaction, dissociation is more effective by two orders of magnitude from highly excited than from low-lying $v$.

The collision data for vibrationally excited molecules are decisively important for further advances in divertor modeling, for formation of the detached plasma regime, and for plasma diagnostics. Thus, infrared emission diagnostics of the divertor plasma critically depends on the collisional
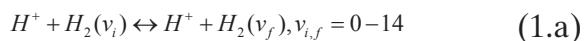
radiative models of the $H_2 / D_2$ plasma. A key role in the models is played by the vibrationally resolved cross sections of the included processes [1,2].

Several mechanisms of volume plasma recombination and formation of the detached plasma regime have been recognized in the tokamak plasma, of which Molecule Assisted Recombination (MAR) is currently believed to be the most effective. The data for various inelastic processes of hydrogen ions and atoms with vibrationally excited hydrogen molecules and molecular ions, specifically for charge transfer, are critically needed for MAR studies [1].

The proton-hydrogen molecule and hydrogen-molecular-ion systems are among the most fundamental ion-atom and ion-molecule two-electron collision systems. A typical collision event evolves through dynamically coupled electronic, vibrational and rotational degrees of freedom. Only scattered data have existed in the literature for vibrational excitation and charge transfer in the range of energies important for the divertor plasmas, mainly with the ground vibrational initial state of $H_2$ for $H^+ + H_2$ collisions, and almost no data were available for scattering of hydrogen on the molecular ion. These systems have been studied thoroughly only for the processes from the ground states (electronic, vibrational, rotational) as motivated by applications, as well as limited by experimental and theoretical

capabilities of the time. Also, these calculations were done within a manifold of bound vibrational states, thus neglecting the possible importance of inelastic processes through "closed" dissociative channels, as well as the dynamic change of the dissociative continuum edge with the position of the projectile. Only one comprehensive data set existed for the charge transfer and dissociation from excited vibrational states of $H_2$, calculated by the Trajectory Surface Hopping (TSH) method [3]. Due to classical nature of the TSH, this method might not give accurate data in the eV energy range.

Total and partial, initial and final vibrational state resolved cross sections for excitation [4-7] and charge transfer [4,7,8], dissociation (including dissociative energy and angular spectra) [9], association [10] and transport processes with excited molecules [5,6,11-14] have been calculated "on the same footing" using a fully-quantal, coupled-channel approach (FQCC) [4] in range of 0.5-10 eV collision energies. In addition, a hybrid, semiclassical split-operator approach (SCSO) [7], which assumes classical, straight-line trajectory of the projectile, but fully-quantal treatment of vibrational degrees of freedom as well as of electronic motion is employed for the center-of-mass energies above 20 eV (up to 100 eV). A list of studied inelastic processes is shown below:

$$H^+ + H_2(v_i) \leftrightarrow H^+ + H_2(v_f), v_{i,f} = 0-14 \qquad (1.a)$$

$$H^+ + H_2(v_i) \leftrightarrow H(1s) + H_2(v_f), v_i = 0-14, v_i = 0-18 \qquad (1.b)$$

$$H^+ + H_2(v_i) \leftrightarrow H^+ + H + H, v_i = 0-14 \qquad (1.c)$$

$$H + H_2^+(v_i) \leftrightarrow H + H_2^+(v_f), v_{i,f} = 0-18 \qquad (1.d)$$

$$H + H_2^+(v_i) \leftrightarrow H + H_2(v_f), v_i = 0-18, v_f = 0-14 \qquad (1.e)$$

$$H + H_2^+(v_i) \leftrightarrow H + H^+ + H, v_i = 0-18 \qquad (1.f)$$

$$H^+ + H + H \leftrightarrow H^+ + H_2(v_f), v_f = 0-14 \qquad (1.g)$$

$$H^+ + H + H \leftrightarrow H^+ + H_2^+(v_f), v_f = 0-19 \qquad (1.h)$$
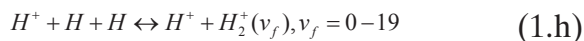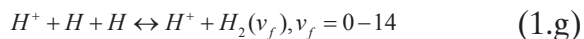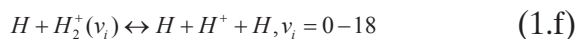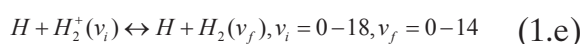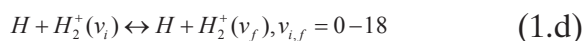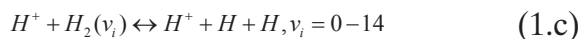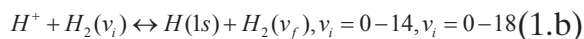
We solve the Schrödinger equation for both electronic and nuclear motion, on the two lowest, strongly coupled adiabatic electronic energy surfaces of $H_3^+$, expanding the nuclear wave function in a vibrational basis consisting of all bound and a large number of discretised continuum states. To include possible processes of nuclear particle interchange, a large configuration space of reactants was spanned [4,9]. Thus, the vibrational coordinate $\rho$ of the diatomic target, as well as the reactive coordinate $R$ (between the projectile and CM of the target) were extended up to 40 a.u. Because the extent of the highest bound vibrational wave functions of $H_2$ and $H_2^+$ is somewhat above 10 a.u., the

chosen space extent cover all reactive three-particle geometries. In the present work we use the sudden approximation for rotations, Infinite Order Sudden Approximation (IOSA) [15]. This approximation is applicable as long as the collision time is short compared to a typical rotation time, so that the rotation of a diatomic target may be considered frozen during a typical collision event. To account for the anisotropy of the energy surface, the calculation is repeated for various $(\vec{R}, \vec{\rho})$ angles, $\gamma$. The obtained cross sections are averaged over $\gamma$, in the interval 0-180º. This approximation works well in the eV region (and above) of center-of-mass collision energies, $E_{CM}$, and for molecular systems with a high degree of nuclear symmetry such as is $H_3^+$. Its accuracy is improved with the increase of the vibrational state $v_i$ as well as with increase of $E_{CM}$. For the range of collision energies considered here, and for excited initial vibrational states, the use of IOSA does not constitute a serious limitation of the calculations. The two lowest adiabatic electronic potential surfaces, on which the dynamics of the system is considered, are constructed with the Diatom-In-Molecule (DIM) method [16,17] using the best available potential curves for the diatomic fragments ($1s\sigma_g$ and $2p\sigma_u$ of $H_2^+$, and the ground state $^1\Sigma_g^+$ of $H_2$ [6]), which were calculated *ab initio* for a large number of diatomic internuclear distances [4] to provide a smooth interpolation of the DIM surfaces, reducing the numerical errors to a minimum (more than $10^7$ DIM geometries). The accurate potential curves of the fragments guarantee that the DIM potential energy surfaces (PES) tend asymptotically (in both $R$ and $\rho$) to the exact values, which provides correct boundaries for the scattering problem. Since DIM is the most accurate in isotropic regions of the PES its application here is also supported by the high degree of nuclear symmetry in the system studied. More details on construction of the present DIM surfaces can be found in [4]. In order to assess the accuracy of the obtained DIM surfaces we compare them with adiabatic surfaces for the ground and the first excited states of $H_3^+$ by utilizing a 54-state (11s,6p) Gaussian basis in the Unrestricted-Hartree-Fock–(full)-Configuration-Interaction (UHF-CI) approach, using GAMESS [19]. As a measure of the accuracy of the DIM PES we define rms of the relative deviations of the DIM ($E_{DIM}^{(i)}$) from the CI energies ($E_{CI}^{(i)}$) at the $i$ th PES, $\delta^{(i)} = (E_{DIM}^{(i)} - E_{CI}^{(i)})/E_{CI}^{(i)}$. The rms, $\bar{\delta}^{(i)}(R)$, is obtained by averaging of $\delta^{(i)}$ over $\rho$ in the interval (0.5,10) a.u. for fixed value of $R$ and is typically below 1%. The accuracy of the DIM PES decreases toward smaller $R$, where anisotropy increases. For the same reasons the accuracy decreases for smaller angles $\gamma$.

Some details of the methods used are shown in Section 2. The results for the manifold of inelastic processes are discussed in Sections 3-6. Finally, we present our conclusions in Section 7 "Atomic system of units is used in the text unless otherwise stated".

## 2. Theoretical approach: understanding the underlying physics

### 2.1. Fully-quantal coupled channel approach

The complete formulation of the low energy dynamics in the collision systems $H^+ + H_2(v_i)$ and $H + H_2^+(v_i)$ was given in our previous works [4,9,10]. Within the IOSA, and confining ourselves to the two lowest strongly coupled diabatic electronic states of $H_3^+$ system, the Schrödinger equation gives

$$[-\frac{1}{2\mu}\frac{\partial^2}{\partial R^2} - \frac{1}{2M}\frac{\partial^2}{\partial \rho^2} + W_{11} + \frac{\ell(\ell+1)}{2\mu R^2} - E]\Psi_1(R,\rho;\gamma)$$

$$+W_{12}\Psi_2(R,\rho;\gamma) = 0 \qquad (2)$$

$$[-\frac{1}{2\mu}\frac{\partial^2}{\partial R^2} - \frac{1}{2M}\frac{\partial^2}{\partial \rho^2} + W_{22} + \frac{\ell(\ell+1)}{2\mu R^2} - E]\Psi_2(R,\rho;\gamma)$$

$$+W_{21}\Psi_1(R,\rho;\gamma) = 0 \qquad (3)$$

where $E$ is the total energy of the system, $\ell$ is the angular momentum of the projectile motion, $W_{ij}$ are the coupling elements of diabatic Hamiltonian, $\mu$ and M are reduced masses of the triatomic and diatomic systems, respectively. dependent of the nuclear configuration, Fig. 1(a). The first of the considered two states represents the ground state of $H_3^+$ which for $R \rightarrow \infty$ has the dissociation limit $H^+ + H_2(^1\Sigma_g^+)$. The second of these two states is the first excited state of $H_3^+$ ion, which corresponds to the $H(1s) + H_2^+(1s\sigma_g)$ configuration, Fig 1(b). The second excited state of $H_3^+$ ion would be an anti-bonding state (of

different, triplet symmetry than the first two states) and corresponds to the $H(1s) + H_2^+(2\pi\sigma_u)$ configuration.

The $H^+ + H_2(v_i)$ charge transfer reaction for $v_i \leq 3$ although endoergic, has a low threshold energy (1.83 eV for $v_i = 0$), Fig. 1(b), and is strongly coupled to the mechanism of vibrational excitation to states that are high enough ($v_i \geq 4$) to overcome the barrier. Thus, this reaction is a second order process for $v_i < 4$ with an integral cross section that is more than ten times lower than the cross section for excitation to the first excited state of $H_2$ for collision energies less than 200 eV. On the other hand, charge transfer processes from higher excited states of $H_2$ are exoergic, often reflecting resonant features, with a significant role of nuclear particle exchange at eV energies, and may dominate inelastic transitions. Thus, the previously studied charge transfer (CT) processes from lower $v_i$ constitute a separate group of processes (evolving through different physical mechanisms) from those for $v_i \geq 4$. Concerning the differential cross sections, in order for the electron to make a transition to the excited surface ($H + H_2^+$) the $H_2$ bond must stretch while the projectile is still close enough to the $H_2$ molecule. This indicates that CT processes inherently lead to large angle scattering. Similarly, collisions that involve nuclear rearrangements will almost always result to scattering to large angles. On the other hand the charge transfer process from $H$ to $H_2^+$ is exoergic, i.e. there is no low-energy threshold, even from the ground $v_i = 0$ state of the target molecule.

As seen in Fig. 1(b), the two diabatic potential curves of $H_2^+ + H$ and $H^+ + H_2$, for $R \rightarrow \infty$ cross at $\rho \approx 2.5$ a.u. This reflects a general feature of the $H_3^+$ system that dominates collision dynamics on the two lowest potential
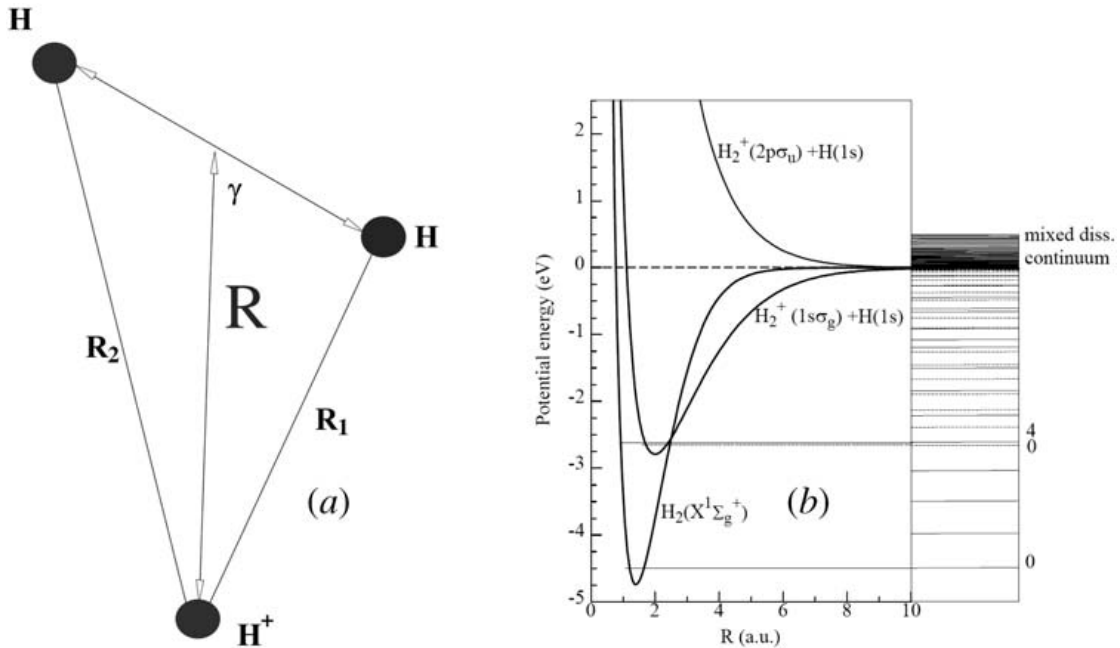


**Figure 1.** (a) Geometry of the $H_3^+$ collision system; (b) Diabatic potential curves of the $H_2^+ + H$ and $H^+ + H_2$, at fixed $R$, for $R \rightarrow \infty$ obtained from three lowest potential curves of $H_2$ and $H_2^+$; Vibrational energies of the ground $H_2$ and $H_2^+$ are also shown.

energy surfaces, the formation of an avoided intersection line (seam) between these two potential energy surfaces in the adiabatic representation of electronic states. For $\gamma = 90°$, the seam appears at $\rho = \rho_s \cong 2.5$ and $R > 4.5$, and along it the matrix elements of $\partial/\partial\rho$ between the adiabatic electronic states are almost delta functions of the vibrational coordinate (Fig. 2). This "numerically violent" behavior of matrix elements of $\partial/\partial\rho$ in the adiabatic electronic basis is the reason for using the diabatic representation of electronic states, Eqs. (2,3) on which the vibrational dynamics is considered. For other values of $\gamma$ the seam position changes slightly, but it remains narrow. Variation in the shape of the adiabatic energy surfaces and the coupling matrix elements as the collision geometry changes is quite significant. This indicates that the collision dynamics is strongly dependent on the orientation of molecular axis with respect to the vector of reactive coordinate, $\vec{R}$.

In the adiabatic limit of the perturber (projectile) motion, the kinetic energy operator of the projectile relative motion (including its angular component) can be removed from Eqs. (2,3), which yields an adiabatic eigenvalue problem for the coupled vibrational motion on the two diabatic electronic surfaces for each given diatomic orientation angle $\gamma$.

$$[-\frac{1}{2M}\frac{\partial^2}{\partial\rho^2}\mathbf{I} + \mathbf{W}(\rho,R) - \mathbf{E}(R)]\Phi(\rho,R) = 0 \quad (4)$$

where $\mathbf{W}$, $\mathbf{E}$, $\mathbf{I}$ are the 2x2 matrices and $\Phi$ eigenstate vector, defined for a fixed R. When $R \to \infty$, this "diabatic" eigenvalue problem is solved with finite quantization "volume" boundary conditions, $\Phi(\rho_{max}, R) = \Phi(\rho = 0, R) = 0$, where $\rho_{max} = 40$ a.u. As a consequence, the relevant vibronic continuum is discretized, although with this choice of large $\rho_{max}$ the density of the continuum states is very high even for several eV above the continuum edge, Fig. 1(b). This extensive vibrational basis set, including all bound vibrational states (35 on both $H_2$ and $H_2^+$ together) and several hundred (more than 800) discretized $H_2$ dissociative continua in a large configuration space (of 40 a.u., to include nuclear particle arrangements) was employed to solve Eqs. (2,3), reducing two coupled partial differential equations in $R$ and $\rho$ into a large set of ordinary second order coupled differential equations. The rotational dynamics of $H_2$ and

$H_2^+$ was treated within the sudden approximation [15] (Infinite Order Sudden Approximation, IOSA), implying that the collision center-of-mass energy, $E_{CM}$, is well above the value of a typical quantum of rotational excitation of the $H_2$ target (~0.01 eV).

The full calculations were performed for the 6 fixed orientations of the diatomic target (0-90º) and the results averaged at level of the cross sections. The FQCC equations were solved using Johnson logarithmic derivative method for each partial wave [20], which were matched to the plane-wave boundary conditions, using the K-matrix representations. Finally, the S-matrix is constructed from the K matrix, and this is used to calculate the cross sections for all inelastic and elastic processes [4]. We note that our data contain coherent sums over the direct and rearrangement channels (i.e. chemical reactions). The latter is particularly intensive for small angles $\gamma$, i.e. for almost collinear nuclear configurations.

Diagonalization of Eq. (4) for all fixed values of $R$ yield adiabatic vibronic potential curves which provides insight into vibrationally resolved transitions dynamics. The lowest 100 vibronic states of the $H_3^+$ (35 are bound) are shown in Fig. 3(a) for the $\gamma = 90º$ geometry as function of reactive coordinate R. These, in the dissociation limit, correspond to the states $H_2^+(v) + H$ and $H^+ + H_2(v)$ (the former are shown by dashed lines). The transitions between adiabatic vibronic states are caused by a number of nonadiabatic couplings of different types. All of these types of couplings have their origin in the operator $\partial/\partial R$ acting on the adiabatic vibronic functions, but they are all characterized by additional features arising from the local behavior of the adiabatic vibronic energies and nonadiabatic interactions. These features can be especially well elucidated if one considers the topology of adiabatic vibronic energies in the complex plane of reactive coordinate R. In Fig. 3(b) we show the nonadiabatic couplings $|U_{ij}(R)|$ for $\gamma = 90º$ and for all adjacent vibronic states ($j = i+1$, $j \leq 50$). First we note that the energies of states $v = 0 - 3$ do not "intersect" the energies of $v'$-states; the energy of state $v = 4$ closely approaches that of state $v' = 0'$ for $R \approx 7$ and for the larger values of $R$ the two curves become practically parallel and nearly resonant, indicating that the states are coupled by a Rosen-Zener-Demkov (RZD) nonadiabatic coupling
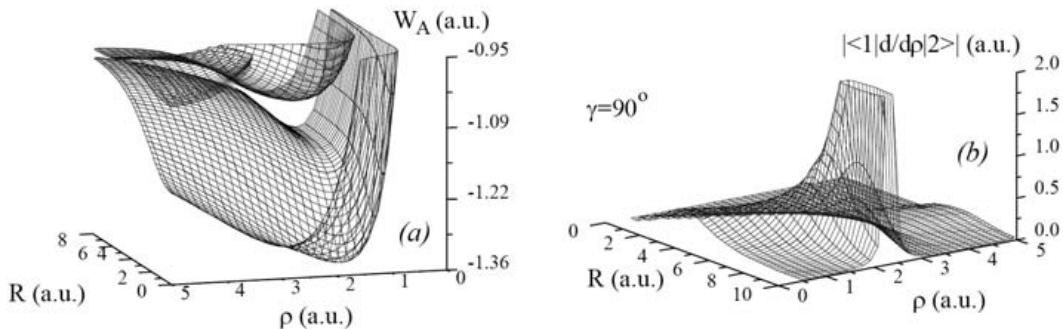


**Figure 2.** (a) 3D plots of the adiabatic electronic energies of the two electronic states considered; (b) 3D plots of matrix elements of $\partial/\partial\rho$ between the two adiabatic states.

mechanism. The energy of state $v = 4$ also has a narrow avoided crossing with the energy of state $v' = 1'$ at $R \sim 6.4$. At the position of avoided energy crossing of states $|4>$ and $|1'>$ the coupling matrix element between these two states shows a narrow and strongly pronounced peak (see Fig. 2(b)), a situation typical for the Landau-Zener (LZ) type of coupling between two adiabatic states. A general characteristic of LZ and Demkov couplings in an ion-atom collision is that they couple adiabatic states which are centered asymptotically on different centers. Here, these mechanisms couple vibronic states for different nuclear configurations, $H^+ + H_2$ and $H_2^+ + H$ causing electron transfer from $H_2$ onto $H^+$ (or vice versa).

By calculating the energies of these selected states in the complex plane of $R$ we find that the corresponding energy surfaces are pair-wise connected by branching points ("hidden crossings") [21,22] in the regions $Re\{R\} \sim 1$ (denoted here by $S^*$ series, similar to the S-type hidden crossings in the two-Coulomb center electron problem) and $Re\{R\} \sim 3$ (denoted here by $Q^*$.series, similar to the Q-type hidden crossings in the two-Coulomb center problem). The appearance of an $S^*$-type branch point is associated with the strong Coulomb repulsion of the projectile and target nuclei for small values of reactive coordinate, while $Q^*$ branch points are associated with the change of the character for adiabatic vibronic functions i.e., from predominantly three-

atomic on the left side of $Re\{R\} \approx 3$ to predominantly diatomic on its right side.

From the structure of adiabatic vibronic energy spectrum of $H_3^+$ ion (which at $R \to \infty$, in our case, goes over into the diatomic vibrational spectrum either of $H_2$ or $H_2^+$), and the fact that the radial coupling is the strongest for two successive adiabatic states (see the discussion above), it follows that the $S^*$-, $Q^*$-, and LZ-type of branch points form series along the entire part of discrete spectrum that lies above the initial vibronic state. Since the dissociation continuum states are also discretized these series of hidden crossings extend in the continuum. Therefore, such series of branch points (or series of strong radial couplings between the successive adiabatic vibronic states) promote the system into its dissociation continuum in the course of the collision. The RZD couplings, that require near-resonant energy conditions for the coupled states in order to be effective (conditions that cannot be met for any two successive states in the vibronic spectrum), do not form promotive series for dissociation. They, however, do participate in the overall vibrational dynamics.

We note that the continuum edge, defined by the first vibronic state which has asymptotically a positive energy (the thick solid line), is strongly deformed in the course of collision due to the deeper potential well of the $H_3^+$ ion (about -9.5 eV in this geometry) with respect to potential
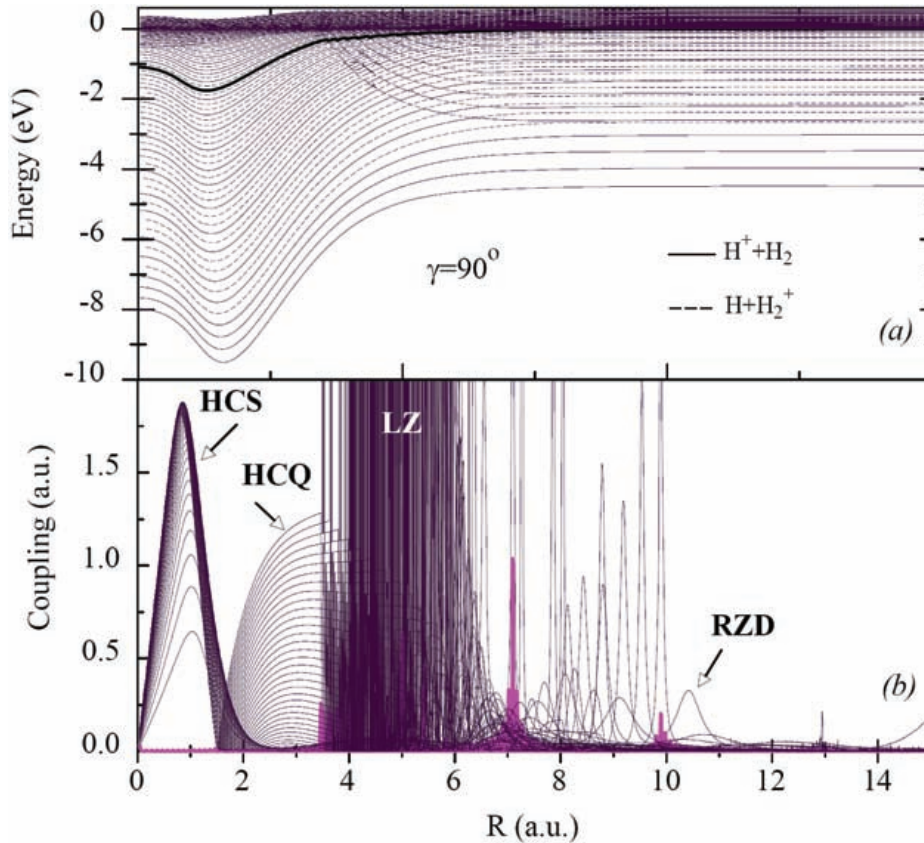


**Figure 3.** (a) Energy term diagram of adiabatic vibronic states when $\gamma = 90°$ and (b) nonadiabatic coupling matrix elements, $<i \mid \partial/\partial R \mid i+1>$, between successive states, with various types of nonadiabatic couplings between them; LZ-Landau-Zener; RZD - Rozen-Zener-Demkov; HCS and HCQ are the hidden crossings series (from [9]).

wells of $H_2$ or $H_2^+$. The deeper potential well of three-atomic collision complex can accommodate a larger number of bound states than the sum of bound states of its diatomic asymptotic fragments. The number of such Collisionally Induced Vibrational Bound States (CIVBS) [9] progressively increases when the projectile approaches the distance at which the potential energy of $H_3^+$ attains its minimum, and starts to decrease for still smaller $R$ (due to the increased nuclear repulsion).

Since LZ couplings between continuum states gradually shift toward lower R, they almost screen the main features of the nonadiabatic matrix elements in range 3.5-7 a.u.. The localization of the $S^*$-series of couplings, and the gradual shift of their maxima towards smaller R, are indications that this series constitutes a strong dissociation channel during the incoming stage of the collision. As the vibrational state increases the peak values of the coupling matrix elements tend to saturate, but their half-widths gradually decrease. This indicates that the higher vibrational states are dissociated more easily than the lower ones. The $S^*$ promotion series brings the system deeply in the continuum where it also remains after the collision. The $Q^*$-series of couplings is a relatively weak promotion channel during the receding stage of the collision. Finally, for the collision systems $H^+ + H_2(v \geq 4)$ and $H + H_2^+(v \geq 0)$ each of the initial states enters a series of successive LZ couplings during the incoming stage of the collision, that promote the system "diabatically" into the higher states and dissociation continuum following the position of the seam (see Fig. 1(b) and Fig. 2.) Because the LZ series enter the continuum edge at relatively large distances $R_d$, the wave packet has enough time to expand in the continuum before it passes the points $R_d$ again on the receding stage of the collision. The LZ diabatic promotion extends deeply into the continuum, leading to higher energies of dissociated fragments. Similarly, RZD couplings also extend into the continuum, as seen in Fig. 3(b). Because both LZ and RZD matrix elements couple the target and corresponding charge-transfer continuum states (as they do in the discrete spectrum), they tend to equilibrate the direct and charge transfer channels of the dissociation process. These mechanisms are of key importance for both processes of dissociation and association, discussed in next sections. The interplay between various promotion mechanisms is strongly dependent on $\gamma$.

### 2.2. Semiclassical split-operator approach

The fully quantal approach discussed above, is not practical at higher energies (few tens eV) because of a too large number of partial waves involved. An alternative [7] is to replace the partial wave with the impact parameter formalism, assuming a classical motion of the projectile. Electronic and vibrational motions are still treated quantally, on the two lowest adiabatic electronic surfaces of $H_3^+$, while IOSA and average over diatomic target angles is applied to

the diatomic target rotations. The resulting time-dependent Schrodinger equation is

$$\left(H_0 + \mathbf{V}\left(R(t),\rho\right)\right)\Psi\left(R(t),\rho,t\right) = i\frac{\partial\Psi\left(R(t),\rho,t\right)}{\partial t} \quad (5)$$

where R(t) is now a classical projectile trajectory defined here in the straight line approximation, $R = \sqrt{b^2 + v^2 t^2}$, V is the coupling matrix, and $\Psi$ is the state vector. The operator $H_0$ defines the unperturbed diatomic vibrational basis $\varphi$, Eq. (4) for $R \rightarrow \infty$, and V with property $V(R \rightarrow \infty) \rightarrow 0$ can be written in the form

$$\mathbf{V}(R,\rho) = \mathbf{V}_d + \rho V_{12}, \quad \rho = \begin{bmatrix} 0 & 1 \\ 1 & 0 \end{bmatrix} \quad (6)$$

where $\rho$ is the Pauli and $\mathbf{V_d}$ is the diagonal matrix, and $V_{12}$ represent diabatic coupling between the relevant diabatic states of $H_3^+$.

Eq. (5) is solved on a numerical mesh, employing the split-operator technique in the energy representation. Iterating the state vector in time from some large "-T" with a small step $\tau$ yields

$$\Psi_{n+1} = \exp(-i\mathbf{H}\tau)\Psi_n$$
$$\tau = \Delta t \quad (7)$$

where $\Psi_n = \Psi(t_n = -T + n\tau)$. Applying the well known Trotter operator relation

$$\exp[i(a+b)\tau] = \exp(ia\tau/2)\exp(ib\tau)\exp(ia\tau/2) + O(\tau^3) \quad (8)$$

to Eq. (7), using Eqs. (5) and (6), one obtains

$$\exp(-i(H_0 + V)\tau) =$$
$$\exp(-iH_0\frac{\tau}{2})\exp(-iV(t+\frac{\tau}{2})\tau)\exp(-iH_0\frac{\tau}{2}) + O(\tau^3) \quad (9)$$

where

$$\exp(-iV\tau) =$$
$$\exp(-iV_d\frac{\tau}{2})\exp(-i\rho V_{12}\tau)\exp(-iV_d\frac{\tau}{2}) + O(\tau^3) \quad (10)$$

Critical in the applications of Eqs. (9) and (10) are exponents with the differential and nondiagonal operators $H_0$ and $\rho V_{12}$, respectively. These are helped with the exact relations

$$\exp(-iH_{0i}\frac{\tau}{2}) = \sum_{k=0}^{\infty}\exp(-i\varepsilon_{ki}\frac{\tau}{2})|\varphi_{ki}(r)\rangle\langle\varphi_{ki}(r)| \quad (11)$$

and

$$\exp(-i\boldsymbol{\rho}V_{12}\tau) = \begin{bmatrix} \cos(V_{12}\tau)\mathbf{I} & -i\sin(V_{12}\tau)\mathbf{I} \\ -i\sin(V_{12}\tau)\mathbf{I} & \cos(V_{12}\tau)\mathbf{I} \end{bmatrix} \quad (12)$$

where i = 1,2 in Eq. (11), correspond to $H_2$ and $H_2^+$ vibrational bases $\left|\varphi_{k,i}(r)\right\rangle$, respectively. The summation over "k" in Eq. (11) assumes a discrete complete basis, which is here obtained limiting vibrational motion in ρ to the interval (0.4,20), which yields a discretized dissociative continuum. We truncate k to N = 400 for each "i", resulting in the vibrational basis of 400 states for each of $H_2$ and $H_2^+$ (35 bound and 765 quasi-continuum). The spatial ρ-discretization is done on a uniform mesh (0.4,20) with 400 nodes for each surface, yielding dimension of 2N = 800 for all relevant matrices in the iteration procedure. We note that nuclear rearrangement reactions, present at energies in the eV range are not significant at higher energies, which implies a smaller size of the numerical box, here 20 a.u.

It can be shown that our iteration procedure is unconditionally unitary and unconditionally convergent. Applying

$$\psi_{n+1} = M_{n+1}(\tau)\psi_n + O(\tau^3) \quad (13)$$

one can obtain the total wave function of the system after the collision, which evolved from an initial vibrational state, $\varphi_i$

$$\Psi_{n\to\infty} = M_n M_{n-1}...M_1\varphi_i = M\varphi_i \quad (14)$$

as well as an S-matrix element, $S_{ji}$, for transition from an arbitrary initial (i) to an arbitrary final (j) vibrational state of the system.

$$S_{ji} = \varphi_j^T M \varphi_i \quad (15)$$

The possibility to calculate the evolution operator M of the whole system, without specifying an initial state during the calculation is the main advantage of the proposed numerical procedure for treatment of the vibrationally resolved transitions from an arbitrary excited state. The final choice of the time step in calculating M, after checking the convergence, was τ = 0.002 a.u.

A check of quality of the obtained semi-classical data is matching of the cross sections with the fully-quantal results in the overlapping region of energies. The conclusion, after analysis of all transitions, is that the cross sections from the initially lowest vibrational states are overestimated when using the straight-line approximation for the projectile motion. Transitions which are dominated by non-tunneling mechanisms, like resonant, quasiresonant or endoergic collisions, seems to match well with the fully quantal results. For example, this is true for charge transfer from higher vibrationally excited states of $H_2$ in collision with $H^+$ as well as for all states of $H_2^+$ in collision with $H$.
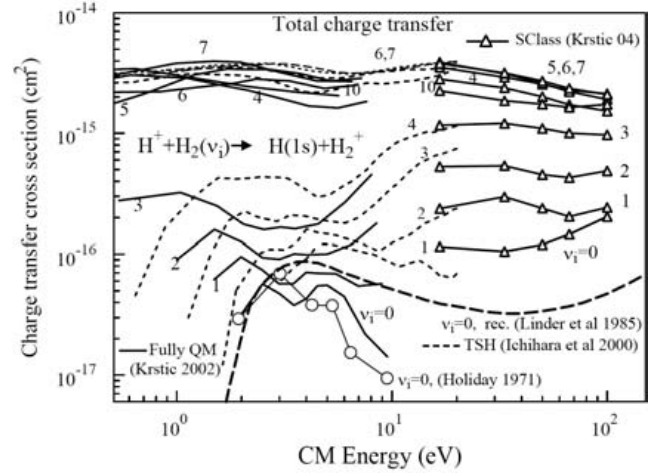


**Figure 4.** Charge transfer in $H_2(v_i)+H^+$ collisions, using fully quantal (solid lines) and semi-classical approaches (triangles), compared with TSH results of Ichihara et al. [3] (dashed lines), experiment of Holiday et al [23] (circles) and estimates of Linder et al [24] (thick dashed line) (from Ref. [7]).

## 3.    Charge transfer

The charge transfer cross sections (summed over final vibrational states) from excited vibrational states of $H_2$ in collisions with protons are shown in Fig. 4. Comparison with experimental data of Holiday [23] and Linder [24] shows good agreement at lowest energies, but lays between these two sets of data toward the higher energies. Data calculated by SCSO method (above 20 eV) are expected to overestimate the cross sections from lower initial states due to straight-line trajectory approximation, which is insensitive to repulsive potential barriers. Among all shown cross sections, charge transfers from the first three excited states constitute a separate group, as discussed in Section 2. The reason is that CT from the higher states is dominantly exoergic and often quasiresonant with the vibrational states of $H_2^+$ and therefore are large even at lowest energies. Comparison of our data with TSH ones of Ichihara shows a good agreement for the higher initial vibrational states, as could be expected from the classical nature of the TSH. It is interesting to note that quantal and the TSH calculations shows similar large contribution of the particle arrangement channels at low energies. As a contrast to Fig. 4, Fig. 5 shows charge transfer cross sections from excited states of $H_2^+$ in collision with $H$. This process is exoergic from all vibrational states (including the ground one). Matching the FQCC and SCSO data improves with increasing the excitation quantum number $v_i$. Decrease of the cross sections for high vibrational states is due to depletion of these states to the vibrational continuum (dissociation).

The partial charge transfer cross sections from the thirteenth excited state of $H_2^+$ to vibrational states of $H_2$ in collision $H + H_2^+$ are shown in Fig. 6, for various collision
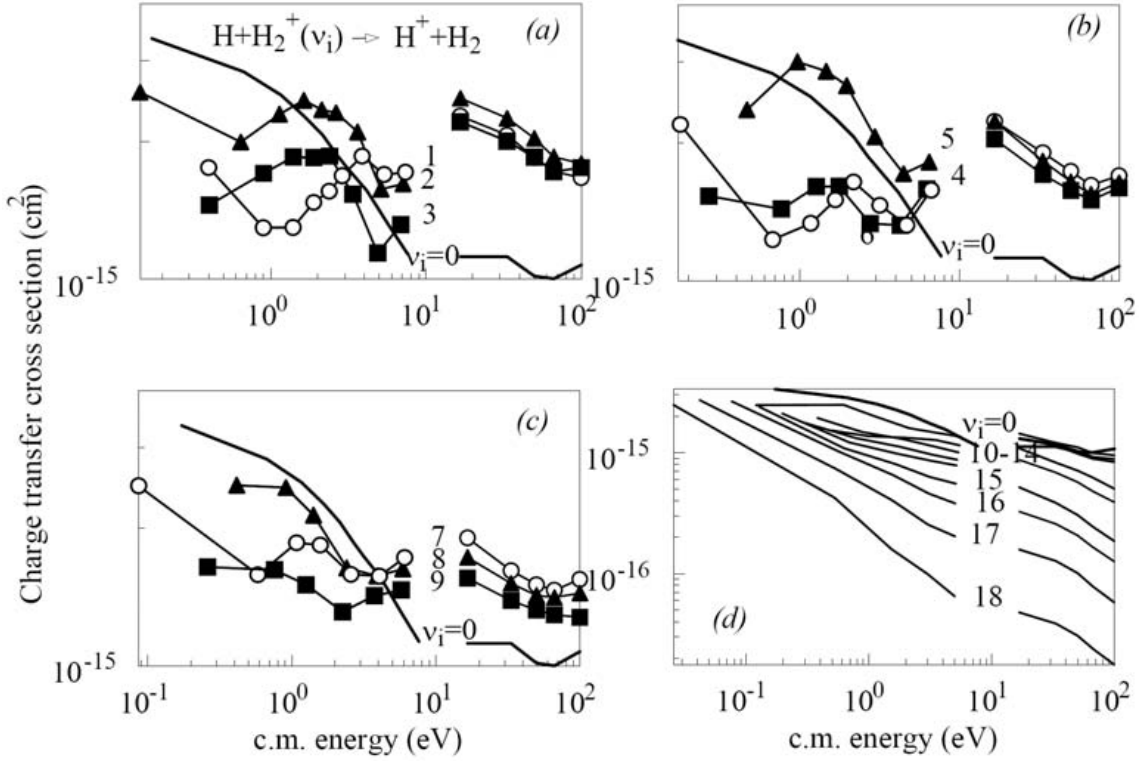
**Figure 5.** Charge transfer from vibrationally excited states of $H_2^+$ (from Ref. [4])
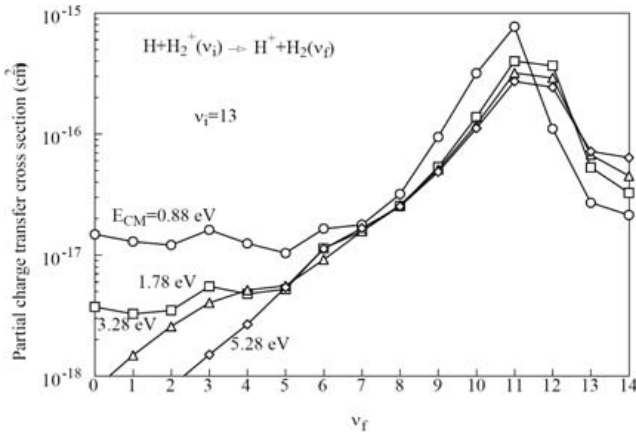


**Figure 6.** Partial cross sections for charge transfer in excited states of $H_2$ (from Ref. [4]).
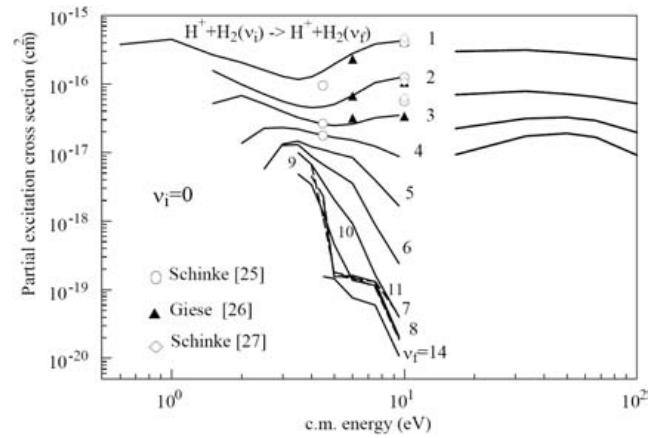


**Figure 7.** Vibrational excitation cross sections for collisions of protons on $H_2$ in the ground state.

energies. As expected, the distribution peaks around quasiresonance with eleventh excited state of $H_2$.
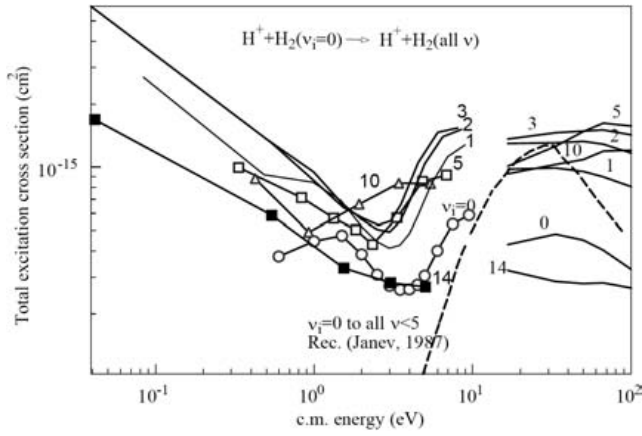
## 4.    Vibrational excitation

The excitation cross sections from ground vibrational state, $v_i = 0$, to various final, $v_f$, vibrational states of $H_2$ are shown in Fig. 7. These compare well with sparse literature data.

The matching of the fully quantal results at low energies with semiclassical, straight-line trajectory approxi-

mation results at higher energies becomes worse at large $v_f$, as expected.

The role of the particle rearrangements in the excitation process is of particular importance at lowest energies, as can be seen in Fig. 7. Our data contain coherent sum of the direct and arrangement channels. The previous calculations do not include rearrangement channels, under-estimating cross sections at lowest energies.

Total excitation cross sections, summed over all $v_f \neq v_i$ from various initial states of $H_2$ (in collision with proton) and of $H_2^+$ (in collision with $H$) are shown in Figs. 8 and 9, respectively. The relevant recommended cross section

**Figure 8.** Excitation cross section, summed over all final vibrational states, from various initial states of $H_2$ in collision with proton



**Figure 10.** Cross section for dissociation from varius excited states of $H_2$.



**Figure 9.** Excitation cross section, summed over all final vibrational states, from various initial states of $H_2^+$ in collision with H

for $H_2(v_i = 0)$ of Janev et al. [28] underestimates our curve, due to absence of rearrangement transitions in previous calculations.

## 5. Dissociation

Dissociation cross sections from various excited states of $H_2$ in collisions by protons and of $H_2^+$ in collisions with $H$ are shown in Figs. 10 and 11, respectively. As shown in Fig. 10, the agreement (matching) of the fully quantal with the TSH results of Ichihara [3] and our semi-classical data is good for higher initial excited states, but deteriorates (overestimate) significantly for lower $v_i$, as expected from the classical character of the TSH method as well as from the potential insensitivity of the straight-line trajectory approximation.

As shown in Fig. 1(b), the vibrational states separate to two disjunct, uncoupled sets that correspond to the vibrational states of two different Hamiltonians, $H_2$ and $H_2^+$. The same is true for the quasi-discrete states of positive

energy, that belong to the separate dissociative continua, those of $H_2$ and $H_2^+$. These states are strongly coupled mutually, thus enabling charge transfer and "excitation" in the continuum. The coupling of the dissociative states of $H_2$ and $H_2^+$ with the bound ones can be also realized in indirect way, by CT followed by dissociation. All the processes are accompanied by the reverse processes in either half of the collision. By "direct" dissociation (DD) we consider the process(es) that lead to the dissociating fragments in the dissociation states of their parent, i.e. of the diatomic molecule that supported the initial vibrational state. Similarly, charge transfer dissociation (CTD) is process that leads to dissociating fragments of "charge-transfer" produced molecule (rather than of parent one). An example of the DD process is dissociation if $H_2(v_i)$ into $H + H$ by proton impact. An example of CTD process would be the dissociation of $H_2(v_i)$ into $H + H^+$ by proton impact. Obviously, in this latter case the charged projectile will exit the scattering zone as a neutral $H$. These conclusions are also directly supported by the diagrams in Figs. 12(a) and 12(b), showing DD and CTD cross sections for various $v_i$ for $H^+ + H_2$ and $H + H_2^+$, respectively. It is obvious that the DD is a stronger process than CTD for $v_i = 14$ in Fig. 12(a), but the difference diminishes toward lower $v_i$. At $v_i = 6$ the contributions of DD and CTD to the total dissociation cross section are almost equal, and for even lower $v_i$ the CTD starts to be a more important process at the higher end of considered energy range. For the $H + H_2^+$ dissociation, the conclusions are somewhat opposite: for the higher $v_i$, CTD dominates the total dissociation by more than a factor 2; this dominance diminishes toward lower $v_i$, and for $v_i \leq 4$ the contributions of DDand CTD processes to the total dissociation cross section become practically equal. This consideration supports the assertion of the preceding section that DD and CTD are almost equilibrated by the strong mixing in the continuum. The DD process is slightly more intensive from the higher excited states of $H_2$, while CTD is slightly more intensive from the lower lying states.
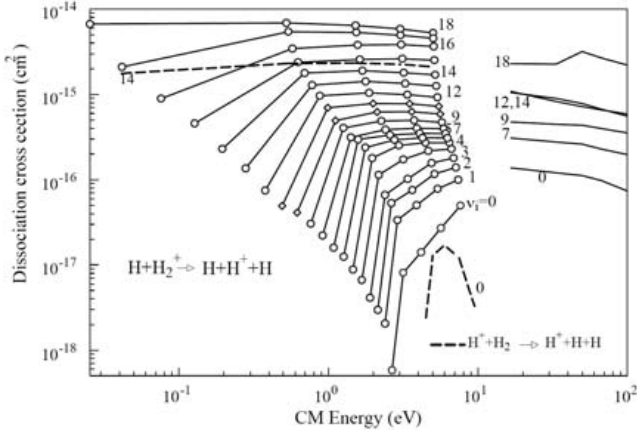
**Figure 11.** Cross section for dissociation from various excited states of $H_2^+$.



**Figure 12.** Comparison of the dissociation components, direct and CT dissociation cross sections for different initial vibrational states $v_i$ of the target, for (a) $H^+ + H_2 (v_i)$, and (b) $H + H_2^+ (v_i)$ collisions (from Ref. [9]).

In Fig. 13, we present the energy spectra for dissociation fragments of $H_2 (v_i)$ in collision with proton for various CM energies (as values $E_{REF}$ above the dissociation threshold $W(v_i)$, i.e. $E_{CM}^{(v_i)} = W(v_i) + E_{REF}$). and for a number of representative values of $v_i$. An obvious feature of these spectra is a pronounced cusp at the continuum edge for lower energies of the projectile. This feature is present for all initial states of the target molecule. The spectra extend close to $E_{REF}$, slowly decreasing with the fragment energy $E_k$, and then abruptly disappear, as required by the energy conservation.

We have also studied the distribution of dissociated fragments with respect to the angle $\gamma$. In Fig. 14 we show the angular distributions of dissociation fragments from the $H^+ + H_2$ dissociation (sum of DD and CTD channels) for the initial vibrational states $v = 0$ and 11 and a selected number of CM collision energies. The numbers on the concentric

circles indicate the values of dissociationcross section (in units of cm²). For the $v = 0$ case, a cosine-type distribution is apparent for the higher energies (7.5 and 9.5 eV), while with decreasing the collision energy the distributions become increasingly more isotropic. In the case of $v = 11$, however,
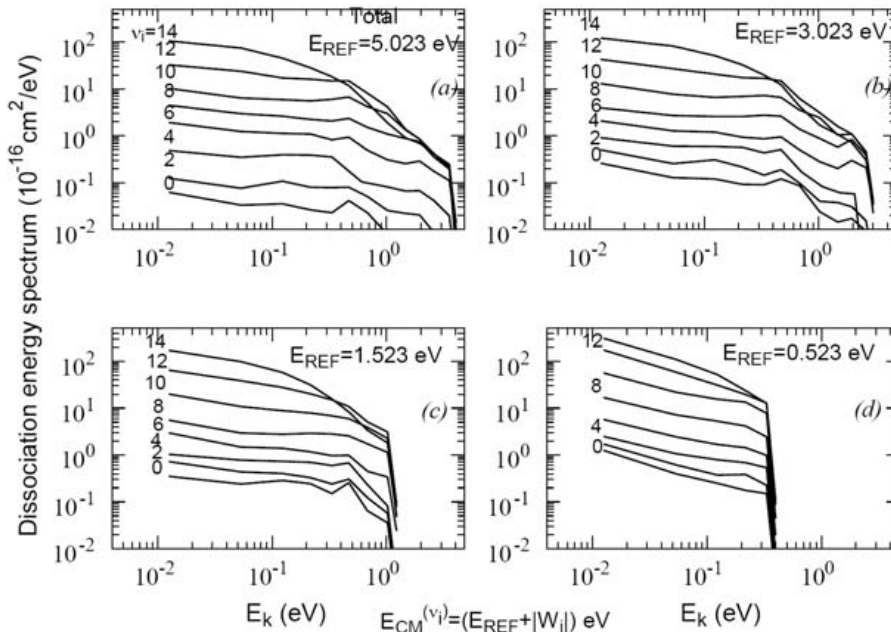


**Figure 13.** Total dissociation energy spectra for $H^+ + H_2 (v_i)$ system, for all $v_i$ at representative C.M. collision energies (from [9]).
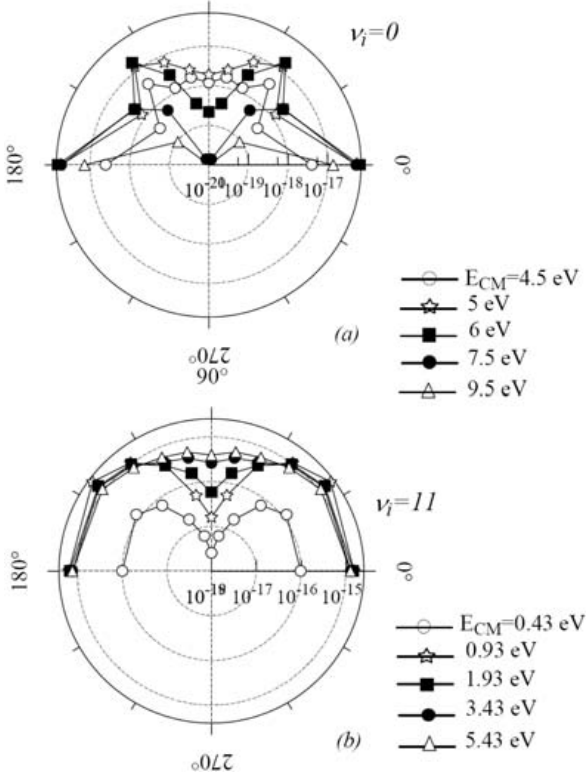
**Figure 14.** Angular distributions of dissociation fragments in $H^+$ + $H_2(v_i)$ collisions, for various CM collision energies and $v_i = 0,11$. (from Ref. [9]).

the situation is reversed. We conveniently represent the angular spectra of dissociation products in the form

$$S_E(\gamma) = F(E)\{\cos^\alpha(\gamma) + b_E(v)\sin(\gamma)\} \qquad (16)$$

where $\alpha$ and $b_E(v)$ can be obtained by fitting the cross section data to the above expression. It has been found that the parameter $\alpha$ does not depend on the energy and, to a high accuracy, has the form

$$\alpha(v) = 10.5(1 + 0.069v^{1.86})^{-1} \qquad (17)$$

The anisotropy parameter $b_E(v)$, however, has a very strong energy dependence, as can be seen also from Fig. 14, which for the considered values of $v$ has the form

$$\begin{aligned}
b_E(v=0) &= 6.296\exp(-1.723E^{0.44}), \\
b_E(v=11) &= 0.259\exp(-2.150E^{-0.95}).
\end{aligned} \qquad (18)$$

The angular distributions of fragments from the $H + H_2^+$ dissociation have similar features.

## 6. Three-body, diatomic association

We consider also the process of three-body, diatomic association, a process that may also be referred to using the quite general term three-body recombination. For cold hydrogen plasmas in particular, three-body, diatomic association occurs when two $H$ atoms associate, forming a

diatom ($H_2$), or a diatomic molecular ion ($H_2^+$), in the presence of a third heavy particle. In this non-radiative process, the heavy particle, here a proton or hydrogen atom, scatters on the associating system and plays the role of catalyzer for the reaction, enabling energy and momentum conservation between reactant and the product channels. Specifically, this process includes the reactions in Eq. (1.g) and (1.h).where any of the particles in the entrance channel can play the role of the scattered, catalyzing particle and $v$ denotes the vibrational quantum number of the associated diatomic. As discussed in connection with the study of collisional dissociation in $H^+ + H_2$ and $H + H_2^+$ systems, the dissociation during the incoming and outgoing parts of the collision takes place due to series of consecutive Landau-Zener (LZ) nonadiabatic couplings (at large $R$ distances), and series of hidden crossings at smaller $R$. The same series are operative under time reversal, and constitute the mechanisms for the associative reactions (1.g) and (1.h). The difference to the dissociation spectra calculations is in the boundary conditions, describing initial population of the continuum states, normalized here to the unit flux.

It should be emphasized that each of the reactions (1.g) and (1.h) contain two channels: direct association (DA) and charge transfer association (CTA),

$$H^+ + (H+H) \rightarrow H^+ + H_2(v), \qquad \text{(DA) (19)}$$

$$\rightarrow H + H_2^+(v) \qquad \text{(CTA) (20)}$$

$$H + (H^+ + H) \rightarrow H + H_2^+(v), \qquad \text{(DA) (21)}$$

$$\rightarrow H^+ + H_2(v) \qquad \text{(CTA) (22)}$$
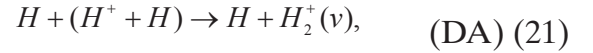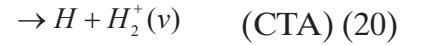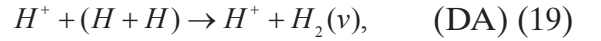
The rate coefficients for each of these channels are different. For a given projectile ($H^+$ or $H$) the CTA processes can be distinguished from the DA processes and are a consequence of charge transfer and particle exchange processes in the continuous and discrete vibronic spectrum. The CTA rates are about a factor two larger than those for the DA channel in the entire temperature range considered. As illustrated in Fig. 15 for T = 1,000 K, this is a consequence of the fact that higher vibrational states give the dominant contribution to the association rate, and that the density of these states in $H_2^+$ is higher than in $H_2$. The temperature dependences of the DA and CTA total rates, and their sum, can be fitted to the expressions

$$\langle K_3 \rangle_{H^+ + (H+H) \rightarrow P} = c_s \frac{C_P}{T^{\kappa_P}}.10^{-29} cm^6/s \qquad (23)$$

where $P$ stands for the reaction product (DA or CTA in Eqs. (19,20). Thus, $C_{DA} = 2.817$, $\kappa_{DA} = 1.141$ and $C_{CTA} = 3.397$, $\kappa_{CTA} = 1.051$, while for the total rate for association $C_{DA+CTA} = 5.858$, $\kappa_{DA+CTA} = 1.072$. The total and partial rates for the DA and CTA channels in $H + (H^+ + H)$ in Eqs. (21, 22) behave similarly to those for
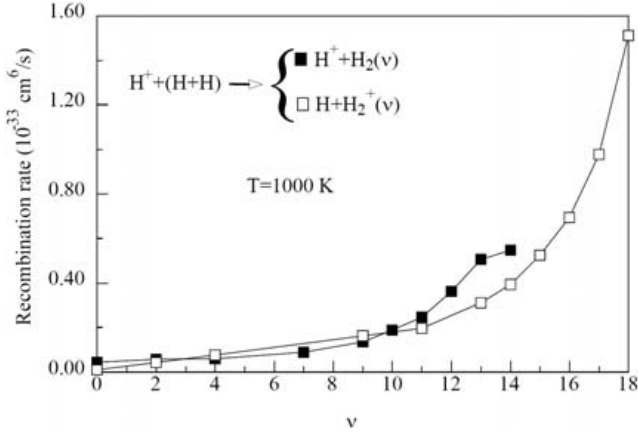
**Figure 15.** Final state resolved partial rate coefficients for three-body recombination of $H_2$ (DA) and $H_2^+$ (CTA) in the presence of $H^+$ at 1000 K (from Ref. [10]).



**Figure 16.** Total rate coefficients for creation of $H_2$ and $H_2^+$ in a hydrogen plasma (from Ref. [10]).

$H^+ + (H + H)$, except that now the DA process, association into $H_2^+$, dominates for the same reasons that CTA is the dominant process for proton projectiles. In this case, $C_{DA} = 1.429$, $\kappa_{DA} = 1.021$, $C_{CTA} = 1.201$, $\kappa_{CTA} = 1.083$, and $C_{DA+CTA} = 2.563$, $\kappa_{DA+CTA} = 1.041$. The total recombination rate in reaction $H + (H^+ + H)$ is about a factor two larger than for the $H + (H^+ + H)$ case, for all temperatures considered, which could be expected from the stronger polarization interaction between the associating particles and the charged projectile in the former case.

The division of the three-particle system into subsystems, $H^+ + (H + H)$ and $H + (H^+ + H)$ in the two basic collision arrangements is physically meaningful, and useful, only when the "projectile" can be clearly identified, e.g. by its energy or momentum. If this is not the case, that is, if all the particles in the system are characterized by the same temperature, then the association rates in the three-particle system for producing $H_2$ and $H_2^+$ are given by sums of the rates for DA and CTA reactions. These sums are displayed in Fig. 16 as well as the total association rate into either $H_2$ or $H_2^+$. In a thermal hydrogen plasma of approximately equal densities of neutral and ionized atoms the total three-body, diatomic association rate for production of $H_2^+$ is 1.8-2.5 times larger than the rate for association of $H_2$, for the considered range of temperatures. Also shown in Fig. 16 is the three-body recombination rate for neutral hydrogen, obtained by Orel [29] using a calculational method quite different than the present one, as well as experimental data of Jacobs for $H_2$ association in the $H + H + H$ collision system [30].

In summary, the calculated total association rates in the $H^+ + H + H$ system are about $5 \times 10^{-32} - 6 \times 10^{-34}$ cm$^6$/s for temperatures in the interval 300-20,000 K, and decrease as (approximately) $T^{-1}$ as temperature increases. This indicates that the three-body, diatomic association in $H^+ + H + H$ may be an important mechanism for $H_2$ and/or $H_2^+$ formation in astrophysical environments containing significant
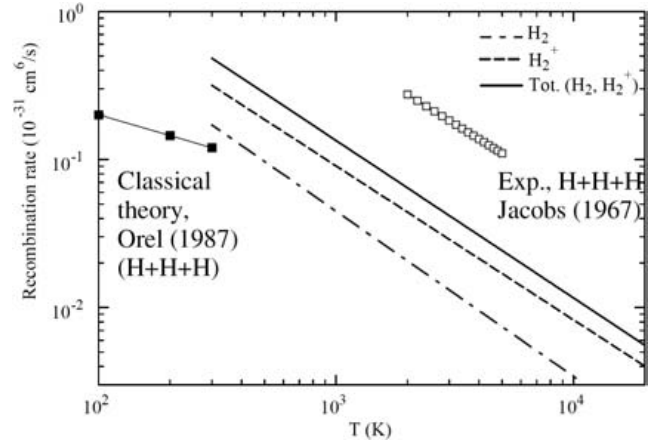
populations of protons and hydrogen atoms. In fusion divertor plasmas, however, even with temperatures as low as $\sim 1$ eV and typical plasma and gas densities of $10^{14}$ cm$^{-3}$, the three-body, diatomic association process yields total rate coefficient of $\approx 10^{-33}$ cm$^6$/s and the probability rate of $\approx 10^{-5}$ s$^{-1}$. Apparently, this will not play a significant role in volume plasma recombination in the presence of more powerful competing processes (such as the three-body recombination in $e + H^+ + e$, for instance).

## 7. Conclusions

Since our calculation of all inelastic and elastic processes has been done at the "same footing", it is of interest to show the interplay of these processes in function of collision energy. Fig. 17 shows the momentum transfer and viscosity cross sections along with the charge transfer (ct), dissociation (dis), and total excitation-de-excitation cross sections ($\sum$ vib), for a four initial states $v_i$ of $H^+ + H_2(v_i)$. For $v_i = 0$, charge transfer and dissociation cross sections stay well below the momentum transfer and viscosity cross sections. In the energy range considered, the main contributions to the total vibration cross section comes from the lower vibrational states.

This picture changes for $v_i = 4$ for which the charge transfer cross section dominates (being larger than the one for total vibrational excitation). At the higher end of the collision energies even dissociation becomes a strong process. Thus, for these higher $v$, calculation of the elastic cross sections without taking into account inelastic processes could lead to serious inaccuracies. For $v_i = 7$ the cross sections for all inelastic processes are larger than the momentum transfer and viscosity cross sections and, for $v_i = 12$, they are larger by more than an order of magnitude. In the case of the $H + H_2^+(v_i)$ system displayed in Fig. 18, cross sections for the charge transfer processes dominate over the mometum transfer and viscosity cross sections
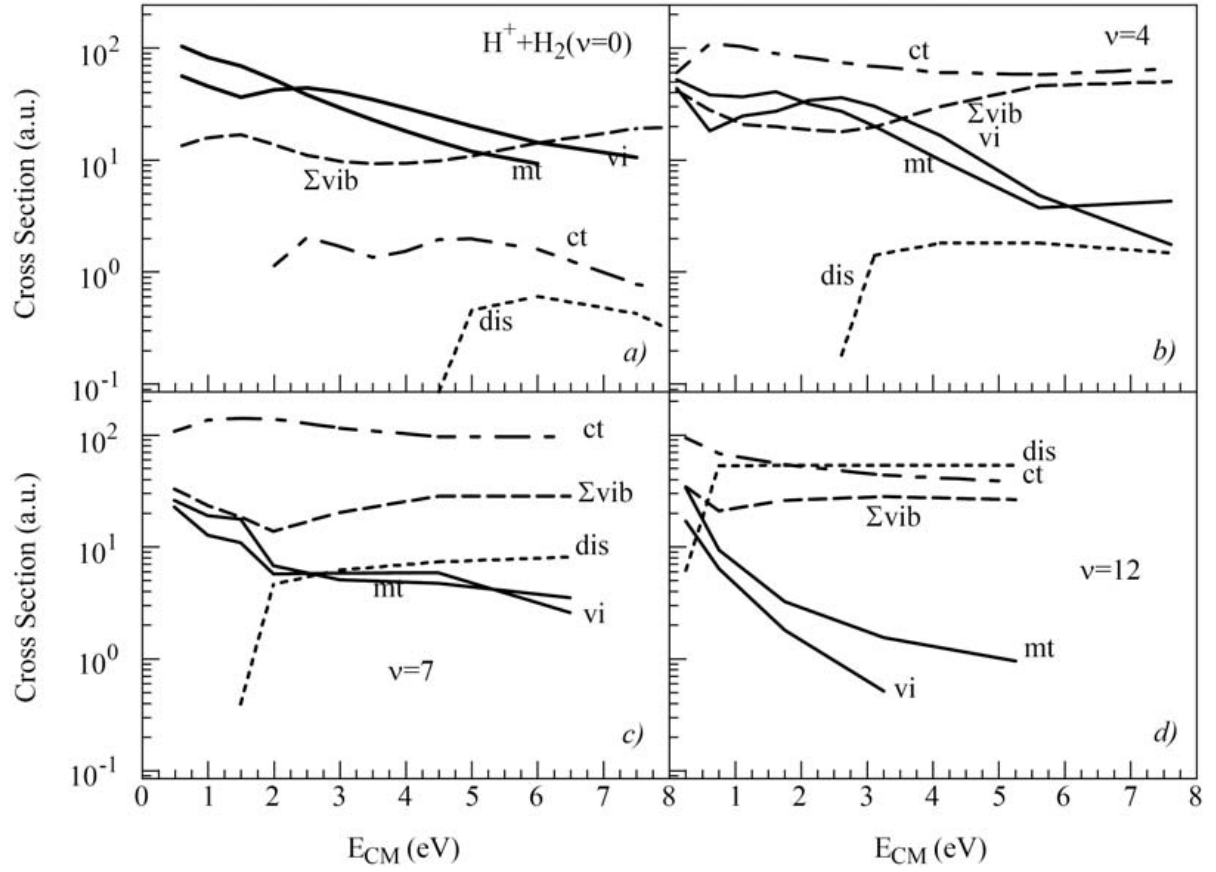
**Figure 17.** Comparison of momentum transfer and viscosity cross sections for representative excited vibrational states in $H^+ + H_2(v)$ collision with inelastic processes from the same vibrational state (from Ref. [14]).
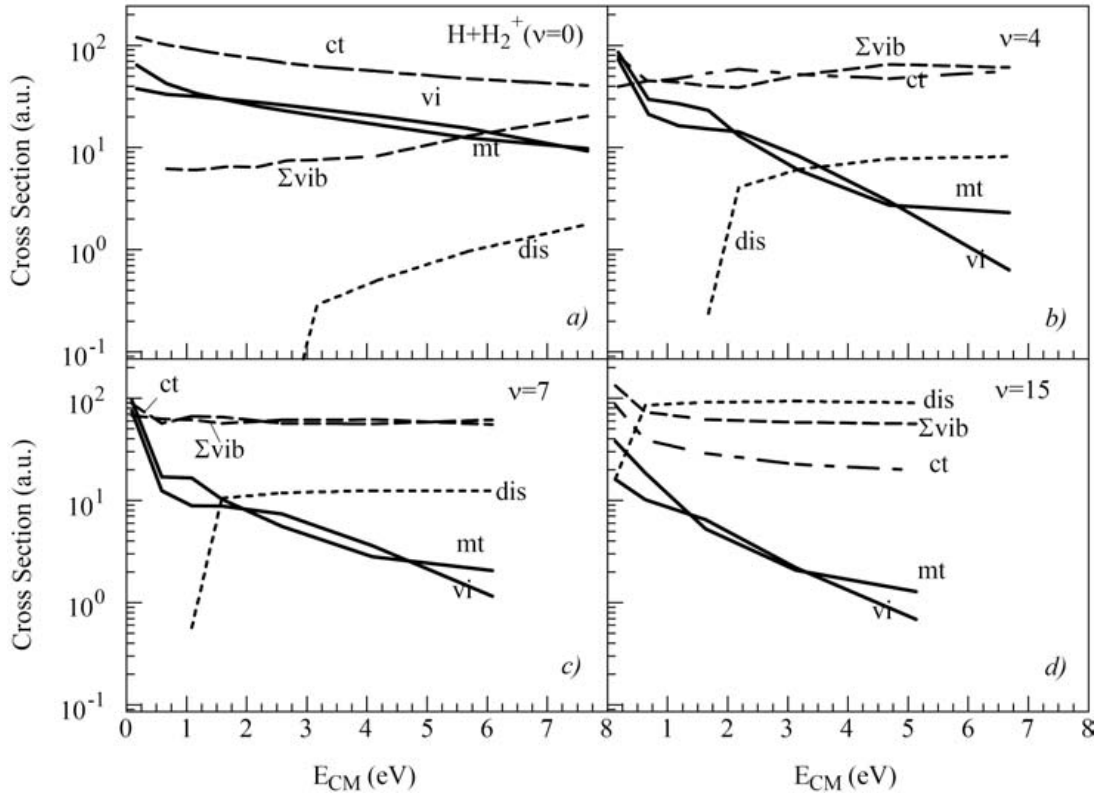


**Figure 18.** The same as Fig. 17, but for $H + H_2^+$ (from Ref. [14]).

already for the ground state. For higher $v_i$ the total excitation cross section as well as dissociation become dominating processes, suppressing the elastic scattering channel and its transport-relevant moments. It is interesting to note that for $v_i \geq 4$, the total excitation–de-excitation and charge transfer cross sections are similar in magnitude, since both are dominantly manifested from exoergic, almost resonant transitions. For the highest vibrational states, charge transfer is suppressed by a large probability of dissociation due to the closeness of the vibrational energy levels to the continuum edge.

The database produced contains all mentioned elastic and inelastic processes for the $H + H_2^+$ and that for $H^+ + H_2$ collision systems (0.5-100 eV) in form of partial and total, initial and final vibrational state resolved cross sections, all obtained at the "same footing". This currently represents the most comprehensive quantum-mechanically obtained set of inelastic data for collisions that involve hydrogen atoms, ions and molecules. These are available in tabular form at the Controlled Fusion Atomic Data Center (CFADC) web site (www-cfadc.phy.ornl.gov). While the cross sections below 10 eV of CM collision energy are calculated accurately, using only IOSA approximation, the results obtained in the semiclassical framework (above 20 eV) show drawbacks which is characteristics to the straight-line trajectory approximation. In order to study rovibrationally resolved processes at low collision energies, with various isotopic combinations of H and, with resolution of particle rearrangement channels consistently, rotational dynamics has to be fully treated.

## Acknowledgments

## References

[1]    KRASHENINNIKOV, S., Phys. Scr. **T96** (2002) 7.

[2]    PIGAROV, A.YU., Phys. Scr. **T96** (2002) 16.

[3]    ICHIHARA, A., IWAMOTO, O., JANEV, R.K., J. Phys. B **33** (2000) 4747.

[4]    KRSTIĆ, P.S., Phys. Rev. A 66 (2002) 042717.

[5]    KRSTIĆ, P.S., SCHULTZ, D.R., J. Phys. B **32** (1999) 2415.

[6]    KRSTIĆ, P.S., SCHULTZ, D.R., Atomic and Plasma-Material Interaction Data for Fusion **8** (1999) 1.

[7]    KRSTIĆ, P.S., "Vibrationally resolved collisions in cold hydrogen plasma", Nuclear Instruments and Methods 2005 (Proc. CAARI2004, Fort Worth, Texas).

[8]    KRSTIĆ, P.S., SCHULTZ, D.R., JANEV, R.K., Phys. Scr. **T96** (2002) 61-71.

[9]    KRSTIĆ, P.S., JANEV, R.K., Phys. Rev. A 67 (2003) 022708.

[10]   KRSTIĆ, P.S., JANEV, R.K., SCHULTZ, D.R., J. Phys. B 36 (2003) L249.

[11]   KRSTIĆ, P.S., SCHULTZ, D.R., "Atomic and molecular transport processes in a cool hydrogen plasma," in *Atomic Processes in Plasmas,* R.C. Mancini and R.A. Phaneuf (Eds.), AIP Conference Proceedings **547** (2000) 53.

[12]   KRSTIĆ, P.S., SCHULTZ, D.R., "Atomic and Molecular Databases for Fusion Divertor Plasma," Proc. 3rd ICAMDATA, Gatlinburg, TN, edited by D.R. Schultz et al, (AIP, New York, 2002).

[13]   KRSTIĆ, P.S., "Nearly adiabatic atomic physics: Methods-Data-Devices," Proceedings, 21st Symposium on Physics of Ionized Gases (SPIG), edited by N. Bibic et al. (Nis, Yug., 2002).

[14]   KRSTIĆ, P.S., SCHULTZ, D.R., J. Phys. B. **36** (2003) 385.

[15]   BAER, M., NAKAMURA, H., J. Chem Phys. **66** (1987) 1363, and references therein.

[16]   ELLISON, F.O., J. Am. Chem. Soc. **85** (1963) 3540.

[17]   PRESTON, R.K., TULLY, J.C., J. Chem. Phys. **54** (1971) 4297.

[19]   SCHMIDT, M.W., BALDRIDGE, K.K., BOATZ, J.A., ELBERT, S.T., GORDON, M.S., JENSEN, J.H., KOSEKI, S., MATSUNAGA, N., NGUYEN, K.A., SU, S., WINDUS, T.L., DUPUIS, M., MONTGOMERY, J.A., "General atomic and molecular electronic structure system," J. Comput. Chem. **14** (1993) 1347.

[20]   JOHNSON, B., J. Comp. Phys. **13** (1973) 445.

[21]   SOLOV'EV, E.A., Usp. Fiz. Nauk, **157** (1989) 437 [Sov. Phys. Usp., **32** (1989) 228].

[22]   KRSTIĆ, P.S., SCHULTZ, D.R., JANEV, R.K., J. Phys. B, (1996) 1941.

[23]   HOLLIDAY, M.G., MUCKERMAN, J.T., FRIEDMAN, L., J. Chem. Phys. **54** (1971) 1058.

[24]   LINDER, F., JANEV, R.K., BOTERO, J., in "Atomic and Molecular Processes in Fusion Edge Plasmas," Janev, R.K. (Ed.), Plenum Press, New York, 1995, p. 397.

[25]   SCHINKE, R., MCGUIRE, P., Chem. Phys **31** (1978) 391.

[26]   GIESE, C.F., GENTRY, W.R., Phys.Rev.A **10** (1974) 2156.

[27]   SCHINKE, R., Chem. Physics **24** (1977) 379.

[28]   JANEV, R.K., LANGER, W.D., EVANS, JR, K., POST, JR, D.E., in "Elementary Processes in Hydrogen-Helium Plasmas", Springer-Verlag, New York (1987).

[29]   OREL, A.E., J. Chem. Phys. **87** (1987) 314.

[30]   JACOBS, T.A., GIEDT, R.R., COHEN, N., J. Chem. Phys. **47** (1967) 54.

# Electron capture cross sections in collisions of N²⁺ and O²⁺ with H

*P. Barragán, L.F. Errea, L. Fernández, A. Macías, L. Méndez, I. Rabadán, A. Riera*

Laboratorio Asociado al CIEMAT de Física Atómica y Molecular en Plasmas de Fusión,
Departamento de Química, Universidad Autónoma de Madrid, 28049 Madrid, Spain

## Abstract

*Ab initio* total and partial cross sections for electron capture proccess in collisions of ground and metastable ¹⁴N²⁺ and ¹⁶O²⁺ with H(1s) are presented. Calculations are performed in a wide energy range from $1\times10^{-5}$ to 20 keV/amu, using both quantal and semiclassical treatments, and a molecular basis set that includes 80 and 39 states for NH²⁺ and OH²⁺ systems, respectively. Partial cross sections and branching ratios to the different channels are also presented.

## 1. Introduction

Electron capture (EC) in ion-atom(molecule) collisions are important processes in astrophysical and fusion plasmas. However, the measurement of cross sections for these processes is often difficult due to the presence of unknown quantities of metastable species in the ion beam, and only recently, double translational energy techniques have allowed to measure EC cross sections for ions in both ground and metastable states (see Refs. [1] and [2]).

In particular, N²⁺ beams from usual ion sources are, in principle, a mixture of unknown proportions of ground state ($2s^22p\ ^2P^o$) and metastable ($2s2p^2\ ^4P$) ions and, accordingly, the following EC reactions can take place in N²⁺+H beam experiments:

$$N^{2+}(2s^22p\ ^2P^o) + H(1s) \rightarrow N^+ + H^+ \qquad (1)$$
$$N^{2+}(2s2p^2\ ^4P) + H(1s) \rightarrow N^+ + H^+ \qquad (2)$$
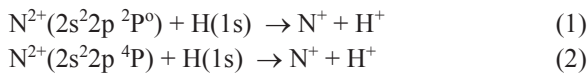
Similarly, O²⁺ beams can contain ground state ($2s^22p^2\ ^3P$) and metastable ($2s^22p^2\ ^1D$ and $2s^22p^2\ ^1S$) ions, and the following EC reactions can take place:

$$O^{2+}(2s^22p^2\ ^3P) + H(1s) \rightarrow O^+ + H^+ \qquad (3)$$
$$O^{2+}(2s^22p^2\ ^1D) + H(1s) \rightarrow O^+ + H^+ \qquad (4)$$
$$O^{2+}(2s^22p^2\ ^1S) + H(1s) \rightarrow O^+ + H^+ \qquad (5)$$
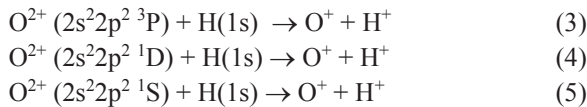
The calculation in the range $0.1 < E < 20$ keV/amu requires the use of a large molecular basis set in order to consider collisions from both ground and metastable ions. In this energy range, we have employed a semiclassical treatment in terms of molecular expansions, as detailed in Ref. [3] and [4]. At $E \approx 0.1$keV/amu we have employed both semiclassical and quantal treatments, as described in Ref. [4]. This calculation is relevant from the theoretical point of view since semiclassical and quantal results have been only compared for a few collisions. For $10^{-3} < E < 10^2$ eV/amu, only the quantal formalism has been employed. Our calculation is particularly relevant at these low energies, where present experimental techniques (merged beams experiments [5]) only yield total cross sections and cannot be applied at energies lower than 10 eV/amu. Although for one-electron systems (see Ref. [6] and references therein) some calculations have recently been carried out using hyperspherical coordinates, this method is not easily extended to many-electron systems [7] and we have applied the common reaction coordinate as explained in Ref. [4].

From the computational point of view, our treatment employs a molecular expansion, which involves the previous evaluation of potential energy curves and dynamical couplings of the corresponding quasimolecule. For many-electron systems, this calculation requires the adaptation of quantum chemistry packages. In particular, for collisions involving metastable species, several initial states must be considered, and one has to include a relatively large number of molecular states, which must be evaluated with the same precision in a wide range of internuclear separations; this is a non standard task for those packages, and their application to dynamical problems have been considered in previous works ([8], [9] and [10].)

## 2. Methodology

In the calculations we have applied the methods explained in detail in Refs. [3] and [4], and the references cited in these papers. We only summarize the basic equations of the quantal and semiclassical approaches in this section.

## 2.1. Semiclassical Eikonal approach

In this treatment one assumes that the nuclei follow straight–line trajectories, $R = b + vt$, with impact parameter $b$ and velocity $v$, while the electronic motion is described by the semiclassical equation:

$$\left( H_{el} - i\frac{\partial}{\partial t} \right)\Psi = 0 \qquad (6)$$

where $H_{el}$ is the clamped-nuclei Born-Oppenheimer electronic Hamiltonian. The function $\Psi$ is expanded in the form:

$$\Psi = D\sum_k a_k(t)\phi_k \exp\left( -i\int_{-\infty}^{t} \varepsilon_k dt' \right) \qquad (7)$$

where $D$ is a common translation factor, and $\phi_k$ are eigenfunctions of $H_{el}$ with energy $\varepsilon_k$. Substitution of this expansion in Eq. (6) leads to a system of first order differential equations, whose solutions are the coefficients $a_k(t)$; this system is solved with the initial condition $a_i(t = -\infty) = 1$ for a collision where the system is initially in the state $\phi_i$, and from these coefficients one obtains the probability $P_{ij}$ for transition to state $\phi_j$ and the corresponding total cross section $\sigma_{ij}$:

$$\sigma_{ij}(v) = 2\pi\int_0^\infty bP_{ij}db = 2\pi\int_0^\infty \left| a_j - \delta_{ij} \right|^2 db \qquad (8)$$

## 2.2. Quantal approach

In the quantal approach one has to solve the stationary Schrödinger equation

$$H\Psi^Q = E_{CM}\Psi^Q \qquad (9)$$

where $H$ is the non-relativistic Hamiltonian operator and $E_{CM}$ is the impact energy in the centre of mass reference frame. As in the semiclassical case, a molecular expansion is employed:

$$\Psi^Q(r,\xi) = \sum_k \chi_k(\xi)\phi_k(r,\xi) \qquad (10)$$

where $\xi$ is the common reaction coordinate that ensures that a truncated expansion fulfills the collision boundary conditions. Substitution of this expansion in the Schrödinger equation leads to a system of second order differential equations for the nuclear wavefunctions $\chi_j$. Solution of this system and comparison with the asymptotic solutions (Ricatti-Bessel or Coulomb functions) yields the S-matrix elements $S_{ij}^J$, where $J$ is the total angular momentum quantum number. The total cross section for $I \rightarrow j$ trasition is given by:

$$\sigma_{ij}(v) = \frac{\pi}{k_i^2}\sum_J (2J+1)\left| S_{ij}^J - \delta_{ij} \right|^2 \qquad (11)$$

with $k_i$ the initial momentum, which is the quantal equivalent of Eq. (8).

## 3. Molecular calculations

Molecular states (MS), $\phi_j$, and energies, $\varepsilon_j$, have been calculated using a multireference configuration interaction method (MRCI) with the program MELD [11]. This method starts with a SCF calculation in a basis of Gaussian type orbitals (GTOs); this provides a set of molecular orbitals (MOs) which are then used to construct the reference configurations. Each reference configuration is a symmetry- and spin-adapted linear combination of a few Slater determinants built up from products of the MOs. The configuration interaction (CI) space includes all single and double excitations from the reference set. The calculations have been performed within the Cs symmetry point group, which means that $\Sigma^+$, $\Pi_+$, $\Delta_+$, …, MS appear as A' states while $\Sigma^-$, $\Pi_-$, $\Delta_-$, … are A" states, where the subindexes $\pm$ indicate the symmetry of the corresponding state under reflection in the collision plane.

In the present calculations, the GTO basis sets were taken from [12] and consist of {5s,4p,3d,2f} contracted GTOs for nitrogen, {4s,3p,1d} for hidrogen and {4s,3p,2d} for oxygen. The MOs for both systems were obtained with restricted SCF calculations for four electrons systems ($NH^{4+}$, $OH^{5+}$), so that the 2p orbitals obtained are not occupied (hence, degenerate). For each subsystem, the CI space was built from a set of (at most) 80 reference configurations. To limit the final number of configurations in the CI, we have applied the following restrictions: (i) frozen core approximation: all configurations have the MO 1σ doubly occupied; (ii) doubly excited configurations are selected using second order perturbation theory. The set of reference configurations was generated following an iterative process (see Ref. [3]), which insures that the most important configurations in the MS of interest are included in the reference set at each value of $R$.

In Tables I and II we compare the calculated energies for the states of the ions $N^{2+}$, $N^+$, $O^{2+}$ and $O^+$ involved in thecollsions with the spectroscopic values of Ref. [13]. The impartance of this comparison will be clear later on. We also include the molecular states that correlate with each atomic level.

## 4. Total EC cross section in $N^{2+}( 2s^2 2p\ ^2P^o)+H(1s)$ collisions

We have calculated the total cross sections for the EC reaction (1) by employing a 56–term molecular basis set; this basis includes the triplet and singlet MS of Table I. The cross section is obtained as:

$$\sigma = 1/12\ [\sigma(1\ ^1\Sigma^+) + \sigma(1\ ^1\Pi_+) + \sigma(1\ ^1\Pi_-)] +$$
$$3/12\ [\sigma(1\ ^3\Sigma^+) + \sigma(1\ ^3\Pi_+) + \sigma(1\ ^3\Pi_-)] \qquad (12)$$

where $\sigma\ (i)$ are the cross sections for the capture reaction with initial channel $i$. Our cross sections (tabulated values are available at [14], are compared in Fig. 1 with

experimental results and previous theoretical values for energies $E < 20 \text{keV/amu}$, where ionization is negligible. This log-log plot shows a linear decrease in the energy range $0.1 < E < 10 \text{eV/amu}$, which can be qualitatively explained by employing the Langevin model (similar behaviour has been found in Refs. [15] and [16]). Explicitly, the cross section in this region is approximately given by $0.2\sigma_L$, with (in atomic units) $\sigma_L = 2\pi(\alpha/E)^{1/2}$. The sharp peaks at low energies can be ascribed to shape resonances (see also Fig. 2a). In the present calculation, we have increased the accuracy of the numerical integration procedure with respect

to the previous work of Barragán *et al.* [4], and we have not found the peak obtained in that calculation, and also in ref. [17], at $E \approx 0.2 \text{eV/amu}$.

With respect to the comparison with previous results, our cross sections agree, at low energies, with the 2-state model of Bienstock *et al.* [16], and are systematically higher than those of the calculation of Herrero *et al.* [17], who only included triplet MS in the molecular basis. However, we have found that the difference between both calculations is mainly due to small differences in the molecular wave functions, which become relevant at low impact energies.

**Table I.** Asymptotic atomic limit of the molecular states (MS) used for the NH$^{2+}$ system. The values are the energy differences (in eV) between the corresponding channel and channel 1 (for singlets and triplets) or channel 2 (for quintets)

| i | Channel | This work | | MS |
|---|---------|-----------|---|-----|
| 1 | N$^{2+}$(2s$^2$2p $^2$P$^o$) | 0.000 | 0.000 | $^{1,3}\Sigma^+$, $^{1,3}\Pi$ |
| 2 | N$^{2+}$(2s2p$^2$ $^4$P) | 7.045 | 7.090 | $^{1,3}\Sigma^-$, $^{1,3}\Pi$ |
| 3 | N$^{2+}$(2s2p$^2$ $^2$D) | 12.410 | 12.525 | $^{1,3}\Sigma^+$, $^{1,3}\Pi$, $^{1,3}\Delta$ |
| 4 | N$^{2+}$(2s2p$^2$ $^2$S) | 16.219 | 16.242 | $^{1,3}\Sigma^+$ |
| 5 | N$^+$(2s$^2$2p$^2$ $^3$P) | -29.470 | -29.600 | $^3\Sigma^-$, $^3\Pi$ |
| 6 | N$^+$(2s$^2$2p$^2$ $^1$D) | -27.512 | -27.701 | $^1\Sigma^+$, $^1\Pi$, $^1\Delta$ |
| 7 | N$^+$(2s$^2$2p$^2$ $^1$S) | -25.337 | -25.547 | $^1\Sigma^+$ |
| 8 | N$^+$(2s2p$^3$ $^3$D$^o$) | -17.976 | -18.164 | $^3\Sigma^-$, $^3\Pi$, $^3\Delta$ |
| 9 | N$^+$(2s2p$^3$ $^3$P$^o$) | -15.856 | -16.059 | $^3\Sigma^+$, $^3\Pi$ |
| 10 | N$^+$(2s2p$^3$ $^1$D$^o$) | -11.369 | -11.723 | $^1\Sigma^-$, $^1\Pi$, $^1\Delta$ |
| 11 | N$^+$(2s$^2$2p3s $^3$P$^o$) | -11.102 | -11.138 | $^3\Sigma^+$, $^3\Pi$ |
| 12 | N$^+$(2s$^2$2p3s $^1$P$^o$) | -11.050 | -11.103 | $^1\Sigma^+$, $^1\Pi$ |
| 13 | N$^+$(2s2p$^3$ $^3$S$^o$) | -9.996 | -10.367 | $^3\Sigma^-$ |
| 14 | N$^+$(2s$^2$2p3p $^1$P) | -9.143 | -9.191 | $^1\Sigma^-$, $^1\Pi$ |
| 15 | N$^+$(2s$^2$2p3p $^3$D) | -8.906 | -8.954 | $^3\Sigma^+$, $^3\Pi$, $^3\Delta$ |
| 16 | N$^+$(2s2p$^3$ $^1$P$^o$) | -8.534 | -8.924 | $^1\Sigma^+$, $^1\Pi$ |
| 17 | N$^+$(2s$^2$2p3p $^3$S) | -8.604 | -8.660 | $^3\Sigma^+$ |
| 18 | N$^+$(2s$^2$2p3p $^3$P) | -8.400 | -8.452 | $^3\Sigma^-$, $^3\Pi$ |
| 19 | N$^+$(2s2p$^3$ $^5$S$^o$) | -30.746 | -30.889 | $^5\Sigma^-$ |
| 20 | N$^+$(2s2p$^2$3s $^5$P) | -11.190 | -11.200 | $^5\Sigma^-$, $^5\Pi$ |
| 21 | N$^+$(2s2p$^2$3p $^5$D$^o$) | -8.923 | -8.963 | $^5\Sigma^-$, $^5\Pi$, $^5\Delta$ |
| 22 | N$^+$(2s2p$^2$3p $^5$P$^o$) | -8.669 | -8.720 | $^5\Sigma^+$, $^5\Pi$ |

**Table II.** Same as in Table I but for OH$^{2+}$ system. Values are energy differences (in eV) between the corresponding channel and channel 1

| i | Channel | This work | | MS |
|---|---------|-----------|---|-----|
| 1 | O$^{2+}$(2s$^2$2p$^2$ $^3$P) | 0.000 | 0.000 | $^{2,4}\Sigma^-$, $^{2,4}\Pi$ |
| 2 | O$^{2+}$(2s$^2$2p$^2$ $^1$D) | 2.718 | 2.514 | $^2\Sigma^+$, $^2\Pi$, $^2\Delta$ |
| 3 | O$^{2+}$(2s$^2$2p$^2$ $^1$S) | 5.570 | 5.355 | $^2\Sigma^+$ |
| 4 | O$^{2+}$(2s2p$^3$ $^5$S$^o$) | 7.178 | 7.480 | $^4\Sigma^-$ |
| 5 | O$^+$(2s2p$^4$ $^4$P) | -20.006 | -20.289 | $^4\Sigma^-$, $^4\Pi$ |
| 6 | O$^+$(2s2p$^4$ $^2$D) | -13.995 | -14.566 | $^2\Sigma^+$, $^2\Pi$, $^2\Delta$ |
| 7 | O$^+$(2s$^2$2p$^2$3s $^4$P) | -12.093 | -12.180 | $^4\Sigma^-$, $^4\Pi$ |
| 8 | O$^+$(2s$^2$2p$^2$3s $^2$P) | -11.568 | -11.728 | $^2\Sigma^-$, $^2\Pi$ |
| 9 | O$^+$(2s2p$^4$ $^2$S) | -10.218 | -10.857 | $^2\Sigma^+$ |
| 10 | O$^+$(2s$^2$2p$^2$3p $^2$S$^o$) | -9.464 | -9.861 | $^2\Sigma^-$ |
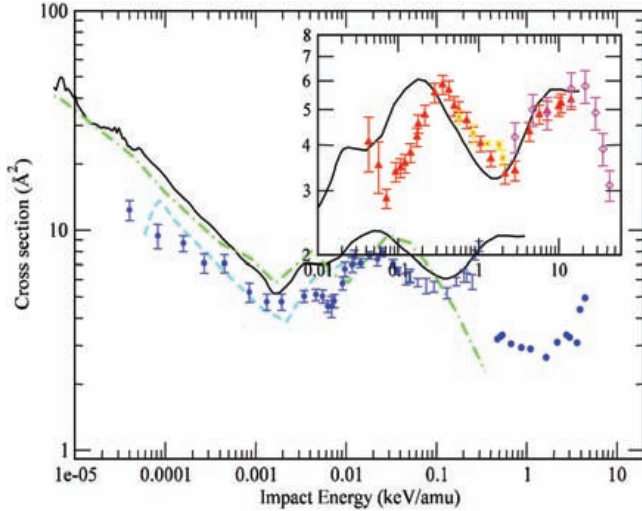


**Figure 1.** Total EC cross sections in N$^{2+}$(2s$^2$2p $^2$P$^o$)+H(1s) collisions. Present calculations with solid lines. Experimental results, ■ [20], ♦ [21], ▲ [18], ● [19]. Other theoretical results, — . —. [16], – – – – [17].

Since our energies are slightly lower than those of [17], and show better agreement with the spectroscopic atomic levels, we conclude that our calculation is more precise at low impact energies. At $E \approx 0.2$keV/amu, our total cross section shows a local maximum, while the maximum of the experimental data of Wilkie *et al.* [18] is shifted to $E \approx 0.5$keV/amu. On the other hand, for $E < 2$keV/amu, our cross section lays parallel and is about 25% higher than that of Pieksma *et al.* [19]. Finally, for energies between 2 and 20keV/amu, our present results are in very good agreement with the measurements of Refs. [18], [20] and [21]. At high energies ($E >$ 2keV/amu), triplet states dissociating into channels 5 and 11, and singlet states dissociating into channels 6, 7, 10 and 12 become accessible, so that the 2-state model of Bienstock *et al.* [16] is not appropriate.

## 5. Total EC cross section in N$^{2+}$(2s2p$^2$ $^4$P)+H(1s) collisions

Total cross sections for reaction (2) are obtained with the relation:

$$\sigma = 1/8[\sigma(2\ ^3\Sigma^-) + \sigma(2\ ^3\Pi_+) + \sigma(2\ ^3\Pi_-)] + 5/24\ [\sigma(2\ ^5\Sigma^-) + \sigma(2\ ^5\Pi_+) + \sigma(2\ ^5\Pi_-)] \qquad (13)$$

We have employed in this calculation the set of 35 triplet states also used for reaction (1), and 15 quintet MS. The ensuing cross sections are compared in Fig. 2 with those for reaction (1). At $E < 0.01$keV/amu, and $E > 1$keV/amu, cross sections for reactions (1) and (2) show similar values and energy dependences, indicating that a contamination of the initial beam by metastable ions would be unnoticeable by comparing experimental and theoretical total EC cross sections. On the contrary, for $0.01 < E < 1$keV/amu, the presence of metastable ions in the experiment would be more easily noticed in the total cross section. In this respect, the good agreement of our total cross section for reaction (1) with the experiments of [18], [20] and [21] for $E > 1$keV/amu indicates that there was a very small proportion of metastable N$^{2+}$ ions in the corresponding initial beams. On the other hand, the disagreement of the cross section measured in [19] with other data in the region $0.01 < E <$ 1keV/amu might be attributed to a larger proportion of metastable ions in that experiment. However, a proportion of 40% of metastable ions is required to get good agreement with the experiment of Pieksma *et al.* [19], who did not find any evidence of such a high proportion of metastable ions. For $E > 2$keV/amu, where the cross sections for reactions (1) and (2) are very similar, we obtain good agreement between all experiments and our calculation.
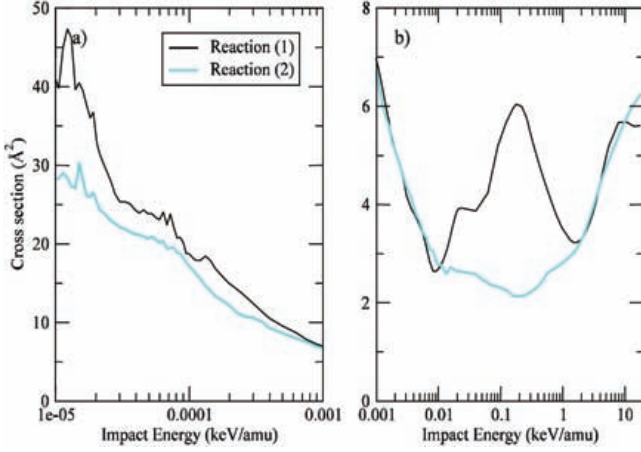
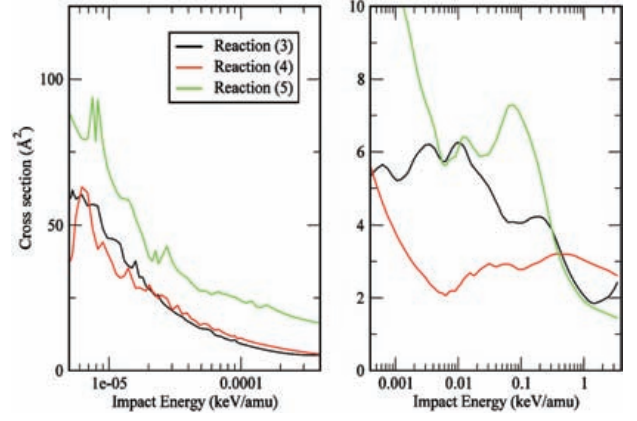**Figure 2.** Total cross sections for reactions given in (1) and (2).



**Figure 4.** Comparison between the total EC cross sections in $O^{2+}$+ H(1s) collisions from various $O^{2+}$ initial states.

## 6.    Total EC cross section in $O^{2+}$+H(1s) collisions

Our calculated total cross sections for reactions (3), (4) and (5) are plotted in Figs. 3 and 4. The overall shape of the total cross section for reaction (3) (see Fig. 3) is similar to that found for reaction (1), with a Lagevin-type behaviour at $1 \times 10^{-5} < E < 3 \times 10^{-4}$ keV/amu. The oscillations of the cross section in the region $2 \times 10^{-4} < E < 0.02$ keV/amu are due to interference effects between transitions in the double avoided crossing between the energies of MS $1^4\Pi$ (one of the entrance channels) and $5^4\Pi$. We obtain good agreement between our theoretical EC cross sections from $O^{2+}(^3P)$ ions with experimental data of [22], and worse agreement is found by assuming a contamination of the initial beam by metastable $O^{2+}(^1D)$ or $O^{2+}(^1S)$ ions. Therefore, our results indicate that there was not beam contamination in the experiment of Ref. [22].

## 7.    State-selective EC cross sections

Cross sections for several exit channels are presented in Figs. 5 and 6, where we plot the contribution ratio to the total EC cross section of each individual channel, calculated as

$$\gamma_i = \frac{\sigma_i}{\sum_j \sigma_j} \times 100$$

with $i$ and $j$ running over the EC channel index.

As explained in detail in Ref. [4], the relative values of the partial cross sections of Fig. 5 for reaction (1) can be qualitatively explained by only taking into account transitions from the entrance channels to states of channel 8. At high $v$, other triplet states (channels 5 and 11) are populated. Besides, we obtain good agreement (see Ref. [4]) between the calculated partial cross sections for the most populated exit channels (8 $^3D^o$ and 9 $^3P^o$) and the experimental data of Refs. [2] and [18].

In the case of reaction (2), and at low $v$, the dominant exit channels (11 $^3P^o$ and 13 $^3S^o$) are populated in the avoided crossings of the potential energy curves at $R \approx 6.1$ and 8.1 a.u., respectively. The ratios of Fig. 5 are due to the initial statistical mixture: the states correlating to 11 $^3P^o$ are populated in the avoided crossing at $R \approx 6.1$ a.u., which appears in the $^3\Pi$ subsystem, whose statistical weight is 2/8, while the MS (13 $^3\Sigma^-$) correlating to 13 $^3S^o$ is populated in the avoided crossing at $R \approx 8.1$ a.u. and the statistical weight of the $^3\Sigma^-$ subsystem is 1/8 (see Eq. (13)). As in the case of reaction (1), for energies above 1keV/amu, other channels (9 $^3P^o$, 8 $^3D^o$, 20 $^5P$, 21 $^5D^o$) become accessible.

With respect to the $OH^{2+}$ system, at low energies (below 1.25 keV/amu), the EC process (3) involves the capture of the target electron into the 2p orbital with simultaneous excitation of a 2s electron to the 2p orbital (exit channels 5 and 6 of Table II). This result agrees with the translation energy spectra of [25], which exhibit a single peak for reaction (3) at $E < 0.5$ keV/amu. At higher energies,
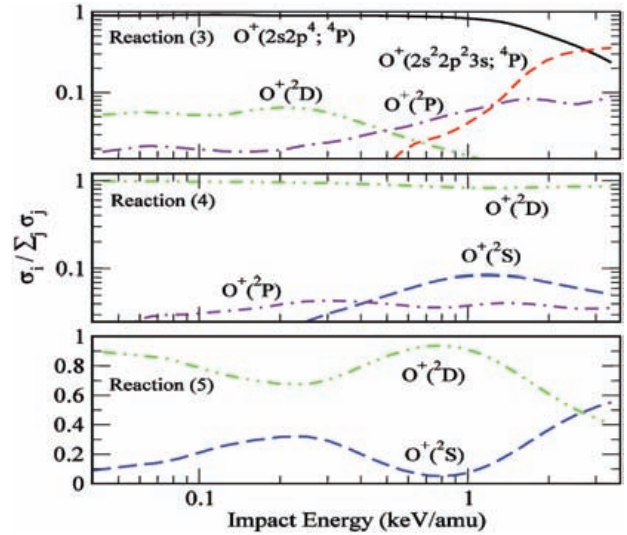


**Figure 3.** Total EC cross sections in O2+(3p)+H(1s) collisions ◆, experimental data of Ref. [20]; ■, calculations of Ref. [23]; ●, calculations of Ref. [24]
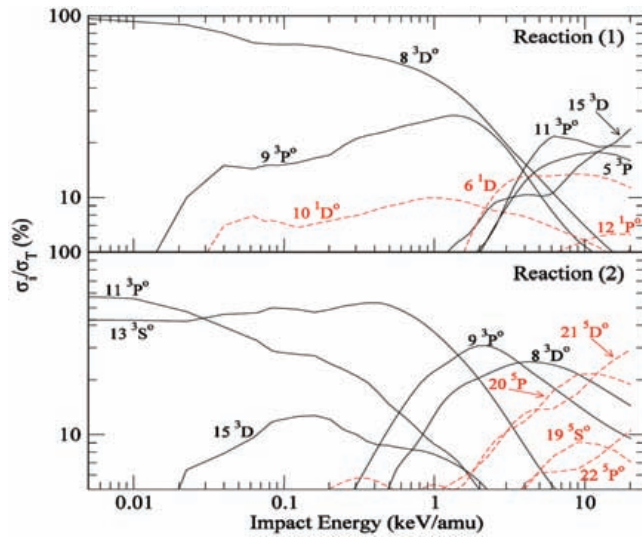
**Figure 5.** Branching ratio to EC channels in reactions (1) and (2); N⁺ products are indicated in these panels.



**Figure 6.** Branching ratio to EC channels in reactions (3), (4) and (5); O⁺ products are indicated in these panels.

the capture into the 3s orbital (channels 7 and 8) becomes competitive with the previous process, and these transitions are responsible for the increase of the total cross section in Fig. 3 for $E > 1.25$keV/amu. The branching ratios for reactions (4) and (5) have been explained in detail in Ref. [3] in terms of transitions between the MS involved, and will not be repeated here. However, we will point out that our results are consistent with the experiment of McLaughlin *et al.* [25], who found a peak in the translation energy spectra at $\Delta E \approx 3.4$ eV, which can be assigned to the formation of $O^+(^2D)$ in reaction (4).

## 8. Conclusions

We have evaluated total and partial EC cross sections for collisions of doubly charged ions ($O^{2+}$ and $N^{2+}$) with H(1s), which can be relevant in edge plasma diagnostics. We have employed large molecular expansions, which allowed us to cover a wide energy range, and to consider collisions of both ground state and metastable ions. We have obtained very large cross sections for reactions (1) – (5) at $E < 0.1$eV/amu, where we also see narrow peaks due to resonances. In general, EC processes at these energies populate a single exit channel. At very low energies, radiative EC, not considered in our calculation, could be relevant, and would limit the practical application of our cross sections. We have compared the calculated cross sections with beam experiments data where available, and discussed the influence of metastable ions in those measurements. Partial cross sections, which are required for charge exchange spectroscopy, have also been evaluated, and are presented as branching ratios for the reactions considered.

## References

[1] VOULOT, D., GILLEN, D.R., THOMPSON, W.R., GILBODY, H.B., MCCULLOUGH, R.W., ERREA, L., MACÍAS, A., MÉNDEZ, L., RIERA, A., J. Phys. B **33** (2000) L187.

[2] VOULOT, D., GILLEN, D.R., KEARNS, D.M., MCCULLOUGH, R.W., GILBODY, H.B., J. Phys. B **34** (2001) 1039.

[3] CABELLO, C.N., ERREA, L.F., FERNÁNDEZ, L., MÉNDEZ, L., MACÍAS, A., RABADÁN, I., RIERA, A., J. Phys. B **36** (2003) 307.

[4] BARRAGÁN, P., ERREA, L.F., MÉNDEZ, L., MACÍAS, A., RABADÁN, I., RIERA, A., Phys. Rev. A **70** (2004) 022707.

[5] MROCZKOWSKI, T., SAVIN, D.W., REJOUB, R., KRSTIC, P.S., HAVENER, C.C., Phys. Rev. A **68** (2003) 032721.

[6] LEE, T.G., LE, A.-T., LIN, C.D., J. Phys. B **36** (2003) 4081.

[7] LE, A., LIN, C.D., ERREA, L.F., MÉNDEZ, L., RIERA, A., PONS, B., Phys. Rev. A **69** (2004) 062703.

[8] CASTILLO, J.F., COOPER, I.L., ERREA, L.F., MÉNDEZ, L., RIERA, A., J. Phys. B **27** (1994) 5011.

[9] CASTILLO, J.F., ERREA, L.F., MACÍAS, A., MÉNDEZ, L., RIERA, A., J. Chem. Phys. **103** (1995) 2113.

[10] ERREA, L.F., MACÍAS, A., MÉNDEZ, L., RABADÁN, I., RIERA, A., J. Phys. B **33** (2000) L615.

[11] DAVIDSON, E., *Modern Techniques in Computational Chemistry,* CLEMENTI, E., Ed. (Leiden: ESCOM Publishers B V) (1990)

[12] WIDMARK, P.O., MALMQVIST, P., ROOS, B., Theor. Chim. Acta **77** (1990) 291.

[13] MOORE, C.E., Atomic Energy Levels Natl Stand. Ref. Data Series NBS Circular vol 1 (Washington, DC: US Government Printing Office) (1971)

[14] http://tcam.qui.uam.es/publicaciones/datos

[15] PIEKSMA, M., GARGAUD, M., McCARROLL, R., HAVENER, C.C., Phys. Rev. A **54** (1996) R13.

[16] BIENSTOCK, S., DALGARNO, A., HEIL, T.G., Phys. Rev. A **33** (1986) 2078.

[17] HERRERO, B., COOPER, I.L., DICKINSON, A.S., FLOWER, D.R., J. Phys. B **28** (1995) 711.

[18] WILKIE, F.G., YOUSIF, F.B., MCCULLOUGH, R.W., GEDDES, J., GILBODY, H.B., J. Phys. B **18** (1985) 479.

[19] PIEKSMA, M., BANNISTER, M.E., WU, W., HAVENER, C.C., Phys. Rev. A **55** (1997) 3526.

[20] PHANEUF, R.A., MEYER, F.W., McKNIGHT, R.H., Phys. Rev. A **17**, (1978) 534.

[21] SEIM, W., MÜLLER, A., WIRKNER-BOTT, I., SALZBORN, E., J. Phys. B **14** (1981) 3475.

[22] PHANEUF, A., ALVAREZ, I., MEYER, F.W., CRANDALL, D.H., Phys. Rev. A **26** (1982) 1892.

[23] BUTLER S.E., HEIL, T.G., DALGARNO, A., Astrophys. J. **241** (1980) 442.

[24] HONVAULT, P., GARGAUD, M., BACCHUS-MONTABONEL, M., MCCARROLL, R.M., Astron. & Astrophys. **302** (1995) 931.

[25] MCLAUGHLIN, T.K., WILSON, S.M., MCCULLOUGH, R.W., GILBODY, H.B., J. Phys. B **23** (1990) 737.

# Atomic data for $H^+$+He(1s$^2$), He(NLM) collisions: single ionisation, excitation and charge exchange cross sections

*K. Dimitriou[1], F. Aumayr[1], K. Katsonis[2], HP. Winter[1], M.I. Chibisov[3], R.K. Janev[4], X. Urbain[5], F. Brouillard[5]*

[1] Institut für Allgemeine Physik, TU Wien, Wiedner Hauptstraße 8-10, A–1040 Wien, Austria

[2] Laboratoire de Physique des Gaz et des Plasmas, Universite de Paris-Sud, 91405 Orsay, France

[3] Russian Research Center "Kurchatov Institute", Moscow, Russia

[4] Macedonian Academy of Sciences and Arts, 1000 Skopje, Macedonia

[5] Department de Physique, Universite Catholique de Louvain, Louvain-la-Neuve, Belgium

## Abstract

Classical trajectory Monte Carlo (CTMC) calculations have been performed for single ionisation and excitation of ground-state helium atoms by protons in the impact energy region of 5 - 200 keV. The calculated data are compared with available experimental data: for ionisation they are close to each other, while for excitation the calculated data are larger by up to a factor of two. For excitation into high quantum numbers we observe a $n^{-3}$ scaling law for our CTMC calculations. In addition, cross sections for excitation and charge exchange in slow collisions of protons with He(1s,NLM) excited atoms (N = 2,3,4) have been calculated in the collision velocity range $10^6 – 10^8$ cm/s by using the molecular orbital close-coupling (MOCC) method, with analytically calculated coupling matrix elements in the asymptotic region of internuclear distance. There are no results from other sources for these cross sections for comparison. The cross section data obtained in CTMC and MOCC calculations are presented in graphical and tabular form.

## 1.    Introduction

Collisions between protons and helium atoms, frequently encountered in fusion plasma devices, are of relevance for both fundamental and applied research. Knowledge of accurate ionisation, excitation and electron capture cross sections for such collisions is of interest for plasma diagnostics and modelling, in particular for fusion plasma diagnostics by fast helium beam emission spectroscopy (He-BES [1]), and also provides a test for different theoretical and experimental methods. In the present work, the available atomic database for the following reactions is considered.

Single ionisation ($\sigma_{si}$)   $H^+ + He(1s^2) \rightarrow H^+ + He^+ + e^-$       (I)

Single excitation ($\sigma_{se}$)   $H^+ + He(1s^2) \rightarrow H^+ + He(1s, n\ ^1L)$  (II)

Previously compiled experimental and theoretical data have been collected and listed in tabular form. Proton impact energies ($E$) from 5 to 200 keV are considered here, and are of direct interest for fast helium beam emission spectroscopy (He-BES) of fusion plasmas.

Fast He-BES attempts to measure the profiles of electron density and electron temperature across a magneti-cally confined fusion plasma, by observing various HeI emission lines along a fast neutral helium beam injected into the plasma. Emission from and attenuation of the injected He beam is caused by collisions with plasma electrons and ions, and therefore the evaluation of electron density and temperature requires an intricate modelling procedure for which as many relevant collision processes as possible have to be taken into account. Detailed compilations of pertinent cross sections, covering a larger energy range ($10 < E < 10^3$ keV), can be found for reactions (I) in Rudd *et al.* (1985) [2] and Gilbody (1992) [3], and for reactions (II) in Fritsch (1991, 1992) [4,5] and de Heer *et al.* (1992) [6]. Our main contribution here is the inclusion in the database results from the more recent theoretical work available in the literature, based on both quantum and classical calculations, as well as more recent data obtained by the CTMC method.

In addition to reactions (I) and (II) above, the available cross section data for excitation and charge exchange processes in slow collisions of protons with excited helium atoms will be presented in the collision velocity range $10^6 – 10^8$ cm/s. The processes considered are:

Single excitation ($\sigma_{exc}$)       $H^+ + He(1s, NLM)^S \rightarrow H^+ + He(1s, N'L'M')^S$(III)

Single charge exchange ($\sigma_{cx}$)  $H^+ + He(1s, NLM)^S \rightarrow H(nlm) + He^+(1s)$     (IV)
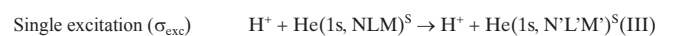
where {N,n} = 2, 3, 4, and N,L,M (and n,l,m) are the usual quantum numbers. The superscript S in the excited atom designation represents the total spin of excited atom (2S+1 = 1, 3; singlet, triplet). In the considered collision velocity range, the only cross section data for processes (III) and (IV) are from the theoretical MOCC calculations of Chibisov et al. (2001) [7] (N, n = 3) and Chibisov et al. (2002) [8] (N, n = 2, 3). For collision velocities higher than a few times $10^8$ cm/s, theoretical cross section calculations for the excitation process (III) have been performed by Fritsch (1991, 1992) [4,5] (for NLM=$2^1$S initial state only) by using the atomic-orbital close coupling (AOCC) method, and by Igarashi and Shirai (1996) [9] (for N = 2, 3, 4 initial states) using the first Born and Glauber approximations.

The original results presented in this article have been obtained by the authors by using the CTMC method for the processes (I) and (II), and the MOCC method for the processes (III) and (IV). We give a brief account of these computational methods, as applied to the studied processes, in the next section.

## 2. Computational methods

### 2.1. CTMC calculations of processes (I) and (II)

A complete theoretical study of proton collisions by helium atoms requires a four-body formulation, where all particles interact by Coulomb potentials. The two electrons on the helium atom are strongly correlated and both of them have to be taken into account in the collision dynamics. However, even for this simple collision system, theoretical calculations for the collision energies of present interest become extremely difficult whenever both electrons and their Coulomb interaction are explicitly treated. In the present work, a three-body Hamiltonian formulation has been chosen for the description of collision dynamics. The three particles considered here are (a) the incoming proton, (b) the one ("effective") target electron and (c) the He$^+$ core. We have performed two sets of calculations, where the electron - He$^+$ core interaction is described (1) by a pure Coulomb potential with effective charge $Z_{eff}$ = 1.6785, and (2) by the model potential proposed by Reinhold and Falcon (1986) [10]. In both cases, the initial configuration of the helium atom ground state has been constructed according to the two-body micro-canonical distribution. The three-body CTMC (3CTMC) model used in the present work has been developed in the Laboratory of Gas and Plasma Physics at the University of Paris-Sud, where preliminary data have been obtained by Katsonis and Maynard (1991) [11], and it has been systematically used in order to evaluate atomic data for ion-atom collisions [12]. The model describes the dynamics of one effective target electron. In the helium case, the presence of two equivalent electrons is taken into account in the cross section calculations within the independent electron approximation (IEA).

The IEA cross sections for single ionisation, $\sigma_{si}$, and single excitation, $\sigma_{se(n)}$, are expressed in terms of one-electron probabilities $P^k_j$:

$$\sigma_{si} = 2 \cdot \sigma^c_{si} \cdot P_{se} = 2 \cdot \sigma^c_{si} \cdot (1 - P^c_{si} - P^c_{sec}) \qquad (1)$$

$$\sigma_{se(n)} = 2 \cdot \sigma^c_{se(n)} \cdot P^c_{n=1} = 2 \cdot \sigma^c_{se(n)} \cdot (1 - P^c_{si} - P^c_{sec} - \Sigma_{n>1} P^c_n) \qquad (2)$$

$P^c_{si}$, $P^c_{sec}$, $P^c_n$ and $P^c_{se}$ denote respectively the one electron probabilities for

- single ionisation – reaction (I),
- single electron capture,
- single excitation into energy level with principal quantum number *n* and
- total single excitation ($P^c_{se} = \Sigma_n P^c_n$),

as calculated by the 3CTMC model. $\sigma^c_{si}$, $\sigma^c_{sec}$, $\sigma^c_{se(n)}$ and $\sigma^c_{se}$ are the corresponding cross sections. Eq. (1) applies when one electron is ejected (but not captured by the projectile) and the other electron stays on the target, while Eq. (2) is used when only one electron is excited; the other remains in the ground level. $P^c_n$ is calculated by classifying the electron trajectories according to the following rule [13]:

$$0.5(E_n + E_{n+1}) < E_{cl} < 0.5(E_n + E_{n-1}) \qquad (3)$$

where $E_{cl}$ is the classical binding energy at the end of each collision event, leading to excitation of the target. All classical binding energies lying within the above interval belong to the energy level $E_n$. This energy level is defined as the average of the energies of the singlet states, corresponding to the same principal quantum number *n*. Calculations are performed for one-electron transitions into energy levels with *n* = 4, 5 and 6, where the 'hydrogenic' approximation is expected to be more reliable than for the lower exited states. For comparison, we also used an expression proposed in [14], which has been derived from the density in the classical phase space volume. However, no considerable differences have been found for the excitation of the energy levels considered here. For each collision energy, $8 \cdot 10^5$ trajectories have been numerically integrated, the maximum statistical error being 7% for single ionisation and 20 % for the least probable excitation channel considered here (*n* = 6). Later on, we shall compare the present results with the collected experimental and theoretical data.

### 2.2. MOCC calculations of processes (III) and (IV)

One of the main features of the H$^+$ + He(NLM) (we omit the designation of 1s electron hereafter) collision system at low energies is that charge exchange states H(nlm)

(n > 1) are Stark splitted at large internuclear distances R by the field of He$^+$ ion. The energies of these Stark states vary at large R as $\pm R^{-2}$ and at certain distances they intersect the diabatic energies of H$^+$ + He(NLM) covalent states (pseudo-crossings, in the adiabatic picture), and these are the regions of internuclear distance where non-adiabatic transitions take place most probably. Another feature of the considered collision system is that at large values of R, the strongest (dominant) interaction is that between the Stark and covalent states with n = N, as shown in Ref. [7]. The multipole coupling between the He excited states or direct coupling of Stark states with n' ≠ n are significantly weaker or completely negligible. Two consequences follow from these features: (i) the electron capture from any initial state of the {N} manifold takes place dominantly to states of the manifold {n} = {N}, which can be expected also from the energy quasi-resonance of particular states of these manifolds, and (ii) the excitation (or de-excitation) of excited He states appears to be a two-step process: on the incoming stage of the collision the strong covalent-Stark state couplings populate the charge exchange states, and on the receding stage of the collision the same type of couplings (i.e. by re-capture) populate other (N'L'M') excited states. In the low energy collision region, this two-step excitation mechanism is by far stronger than the direct (e.g. dipole induced) transitions between excited He states [7].

The MOCC equations describing the collision dynamics in the system are obtained from the time dependent Schrödinger equation by expanding the total wave function of the excited electron (the effects of the 1s core electron are taken into account by using the experimental values for the excited state energies in He) in terms of covalent states (with expansion coefficients $a_{NLM}(t)$) and Stark states (n$_1$,n$_2$,m) (expansion coefficients $b_{nn1m}(t)$), where n$_1$,n$_2$,m are the parabolic quantum numbers and n = n$_1$+n$_2$+m+1. The coupled equations have the usual form

$$i\, db_{nn1m}/dt = \Sigma_{NL}\, a_{NLM}(t)\, V_{NLM}{}^{nn1m}(R)\, exp\,[i\,\Phi(t)] \quad (4)$$

$$i\, da_{NLM}/dt = \Sigma_{nn1}\, b_{nn1m}(t)\, V_{nn1m}{}^{NLM}(R)\, exp[-i\Phi(t)] \quad (5)$$

$$a_{NLM}(t \to \infty) = \delta_{NLM,NoLoMo}\,, \quad b_{nn1m}(t \to \infty) = 0 \quad (6)$$

where $V_{NLM}{}^{nn1m} = V_{nn1m}{}^{NLM}$ is the coupling matrix element between the covalent and Stark states, $\Phi(t)$ is an energy phase, and (N$_0$L$_0$M$_0$) is the initial state. $V_{NLM}{}^{nn1m}$ has been calculated (in closed analytic form) asymptotically (for large R) exactly in [7], and it is proportional to $\delta_{Mm}$. This means that Eqs. (4) - (5) are decoupled in the magnetic quantum number and have to be solved separately for each specific initial M value. At the same time, this means that rotational coupling, inducing transitions between the m ≠ M states, is not included in the above system of coupled equations (we

note that $V_{NLM}{}^{nn1m}$ depends on the modulus of M (= m) only). Furthermore, the phase $\Phi(t)$ is a purely energy phase and does not contain terms describing the electron momentum transfer during the collision, i.e. no electron translational factors, ETFs, are included in Eqs. (4) and (5). In the considered collision velocity region the nuclear motion can be described in the linear trajectory approximation, R(t) = {ρ$^2$ + (vt)$^2$}$^{1/2}$, where ρ is the impact parameter and ν is the collision velocity. The energy phase $\Phi(t)$ within the dipole approximation for the expansion of energies $E_H(t)$ and $E_{He}(t)$ has the form

$$\Phi(t) = (E_H{}^0 - E_{He}{}^0)\, t - [d\,/(v\rho)]\,\{(\pi/2) + arctan(vt/\rho)\}\,,\ d = -(3/2)\,n\,(n_1 - n_2) \quad (7)$$

where $E_H{}^0$ and $E_{He}{}^0$ are the unperturbed energies of corresponding atomic states, and $d$ is the dipole moment of (n$_1$,n$_2$,m) Stark state.

When solving the coupled Eqs. (4) and (5) with the boundary conditions (6), the excitation probabilities $P_{NLMo}$ (ρ) = |a$_{NLMo}$(+∞)|$^2$ are obtained directly, and after integration over the impact parameter ρ the corresponding cross section is obtained. However, from the solutions of Eqs. (4) and (5) one can obtain only the charge exchange probabilities $P_{nn1Mo}$(ρ) for population of the Stark states. In order to obtain the charge exchange probabilities for populating specific angular momentum (spherical) states of H, one has to project the (n$_1$n$_2$m) Stark states onto the angular momentum (nlm) states, and thus obtain the charge exchange probability $P_{nlMo}$(ρ). Its integration over ρ gives the corresponding charge exchange cross section.

## 3. Single ionisation of ground state He by proton impact

The collected data for ionisation are listed in Table 1. We are particularly interested here in pure single ionisation - reaction (I), though cross sections for

transfer ionisation ($\sigma_{ti}$)   H$^+$ + He(1s$^2$) → H + He$^{2+}$ + e$^-$   (V)

double ionisation ($\sigma_{di}$)   H$^+$ + He(1s$^2$) → H$^+$ + He$^{2+}$ + 2e$^-$ (VI)

and total free electron production ($\sigma_-$ = $\sigma_{si}$ + $\sigma_{ti}$ + 2$\sigma_{di}$), are also addressed.

### 3.1. Experimental data

Experimental data for ionisation have been discussed in detail by Rudd *et al.* (1985) [2] and by Gilbody (1992) [3]. However, only few experimental methods can provide accurate data for pure single ionisation, especially at low energy collisions (< 15 keV). Very accurate measurements (within 10%) for individual channels (I), (V) and (VI) have been performed by the Belfast group [12, 13] using the cross beam coincidence counting (CBCC) technique. Experimental studies based on the parallel plate capacitor (PPC)

technique provide cross sections for the total free electron production (see for example in [14]), including contributions from the channels (I), (V), and (VI). Large discrepancies (up to 50%) between several investigators using the above technique have been encountered in the literature. Fig. 1 presents the detailed measurements for free electron production performed by Rudd *et al.* (1983) [15] in comparison with the pure single ionisation cross sections of Shah *et al.* (1989) [13]. As expected the former cross sections are slightly larger than the latter ones in the energy range from 15 to 200 keV, but they are too large for lower collision e for pure single ionisation. The coincidence counting measurements of Afrosimov *et al.* (1969) [16] for pure single ionisation (not shown) deviate considerably from the previous data. The recommended data by Rudd *et al.* (1985) [2] for $\sigma_-$ are close to the values of Rudd *et al.* (1983) [15], while the recommended data by Barnett (1990) [17] for $\sigma_{si}$ are considerably larger than the values of Rudd *et al.* (1983) [15] and Shah *et al.* (1989) [13] at collision energies $E < 40$ keV, where transfer and double ionisation are of minor importance for pure single ionisation. The coincidence counting measurements of Afrosimov *et al.* (1969) [16] for pure single ionisation (not shown) deviate considerably from the previous data. The recommended data by Rudd *et al.* (1985) [2] for $\sigma_-$ are close to the values of Rudd *et al.* (1983) [15], while the recommended data by Barnett (1990) [17] for $\sigma_{si}$ are considerably larger than the values of Rudd *et al.* (1983) [15] and Shah *et al.* (1989) [13] at energy collisions $E < 40$ keV.

## 3.2. Calculated data

A considerable theoretical effort has been achieved during the last fifteen years in evaluating cross sections for proton collisions with helium atoms. Elaborate quantum-mechanical and classical calculations have been developed in order to obtain a better physical insight of the collision processes (I), (V), and (VI). CTMC studies for ionisation processes have been early performed by McDowell and co-workers [21] and by Zaifman and Maor (1986) [22]. Four-body CTMC calculations of Wetmore and Olson (1988) [23], where electron-electron correlation is ignored, and of Montemayor and Schiwietz (1989) [24], where a radial correlation between the two electrons is included, give improved results for pure single ionisation cross sections at collision energies higher than 100 keV. Still, transfer ionisation is not satisfactory described. A considerable improvement has been proposed by Cohen (1996) [25] using the so-called Quasi-classical trajectory Monte Carlo (QTMC) method, which emphasises the stability of the helium atom.

Fig. 1 includes our results, based on two different types of potentials (see Section 2.1), and the ones obtained by Cohen (1996) [25] for pure single ionisation (I). A better agreement with the experiment is obtained by our calcula-

tions when pure Coulomb interactions are considered. This is in agreement with the general observation that Coulomb potential, being better justified physically, should be used in CTMC calculations [26]. In the present case, the initial electronic radial distribution according to the model potential presents a cut-off at a distance between the electron and the He$^+$ core smaller than the one corresponding to the pure Coulomb case [10]. Consequently, the electron is restricted into a smaller collision volume; contributions to ionisation cross sections coming from large impact parameters, which are important at low energies, are therefore suppressed. Our three-body CTMC calculations reproduce quite successfully the form of experimental single ionisation cross section; the position of the maximum is located at 80 keV, being close to the experimental one at 100 keV. At this energy region, our results are about 25% higher than the data of Shah et al. (1989) [16]. They are in good agreement with experimental data in the energy region around 20 keV, but smaller by ~30% at lower energies. We note that our results are near to those of Schultz and Olson (1988) [27] (not shown) at the higher collision energies
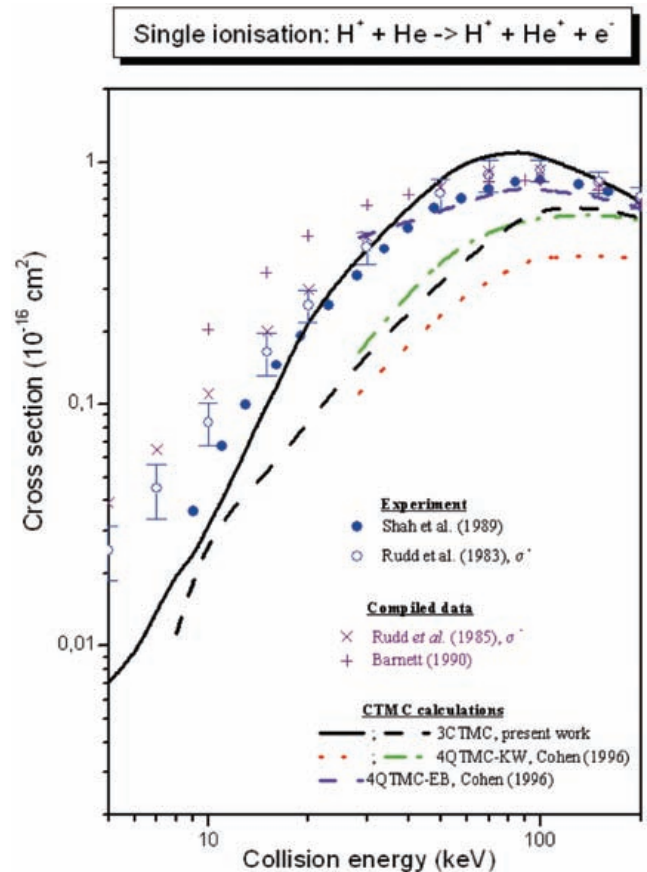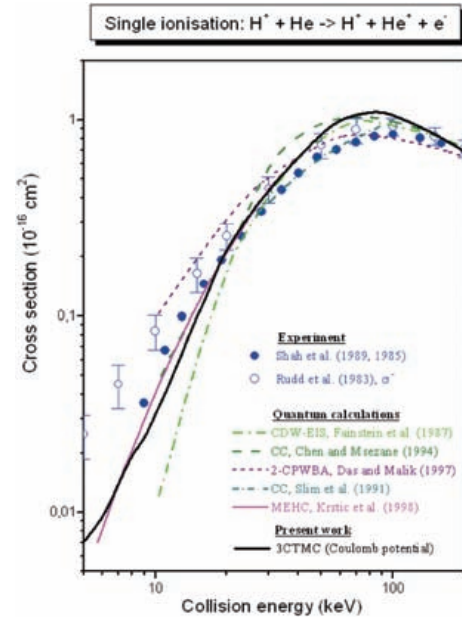


**Figure 1.** Single ionisation cross sections as a function of collision energy. Experimental data: full circles, Shah et al. (1989) [16]; open circles Rudd et al. (1983) [18]. Compiled data: crosses, Rudd et al. (1985) [2] and Barnett (1990) [20]. CTMC calculations: black solid line, present work using Coulomb potential between e$^-$ and He$^+$ core; black dashed line, present work using model potential between e$^-$ and He$^+$ core; dot, dash-dot and dash lines, Cohen (1996) [25].

considered here. Quantum-mechanical calculations, based on several approximations, have been extensively performed for evaluating the pure single ionisation cross section. Fig. 2 compares results obtained by

 – Continuum Distorted Wave Eikonal Initial State (CDW-EIS) approximation of Fainstein *et al.* (1987) [28],
 – Close Coupling approach of Slim *et al.* (1991) [29] and Chen and Msezane (1994) [30],
 – Two Channel Plane Wave Born Approximation (2-CPWBA) of Das and Malik (1997) [31]
 – Multi-Electron Hidden Crossing theory (MEHC) of Krstić *et al.* (1998) [32].

Also included in Fig. 2 are our 3CTMC results for the pure Coulomb case and experimental data of Shah *et al.* (1989) [16] and Rudd *et al.* (1983) [18]. Calculations of Sahoo *et al.* (2000) [33] using the impact parameter Born approximation (IPBA, not shown) are in agreement with the measurements of Rudd *et al.* [18]. The above quantum-mechanical calculations agree with the measurements in different energy regions, reflecting the range of validity of each approximation.



**Figure 2.** Single ionisation cross sections as a function of collision energy. Experimental data: as in Fig. 1. Theory: dash dot line, CDW-EIS calculations from Fainstein et al. (1987) [28]; dashed line, CC calculations from Chen and Msezane (1994) [30]; short dash line, 2-CPWBA calculations from Das and Malik (1997) [31]; short dash-dot line, CCAO calculations from Slim et al. (1991) [29], solid line MEHC theory from Krstic et al (1998) [32], black solid line, 3CTMC calculations, present work.

**Table 1.** Ionization data for $H^+$ + He ground state collisions

| Energy range (keV) | Quantities | Experimental (**E**), Theoretical (**T**), Review Data (**R**) | References |
|---|---|---|---|
| 5 - 50 | $\sigma_{si}$, $\sigma_{di}$, $\sigma_{ti}$, $\sigma_{sec}$ | CC (**E**) | [19] |
| 5 - 4·10³ | $\sigma_-$, $\sigma_+$ | PPC (**E**) | [18] |
| 5 - 5·10³ | $\sigma_-$, $\sigma_+$ | **R** | [2] |
| 6 - 30 | $\sigma_{si}$, $\sigma_{di}$ | MEHC (**T**) | [32] |
| 9 - 100 | $\sigma_{si}$, $\sigma_{di}$, $\sigma_{ti}$, $\sigma_{sec}$ | CBCC/ToF (**E**) | [16] |
| 10 - 140 | $\sigma_-$, $\sigma_{aec}$ | PPC (**E**) | [17] |
| 10 - 10³ | $\sigma_{si}$, $\sigma_-$ | R | [3] |
| 10 - 10³ | $\sigma_{si}$, $P_{si}(b)$ | CCAO (**T**) | [30] |
| 10 - 5·10³ | $\sigma_{si}$, $\sigma_-$ | **R** | [20] |
| 10 - 5·10³ | $\sigma_{si}$, $\sigma_{di}$ | 2-CPWBA (**T**) | [31] |
| 10 - 5·10⁴ | $\sigma_{si}$ | CDWEIS (**T**) | [28] |
| 25 - 100 | $\sigma_{si}$, $\sigma_{sec}$ | CCAO (**T**) | [29] |
| 25 - 125 | $\sigma_-$ | CTMC (**T**) | [21] |
| 25 - 200 | $\sigma_{asi}$, $\sigma_{sec}$ | CTMC (**T**) | [22] |
| 25 - 625 | $\sigma_{si}$, $d\sigma_{si}/d\Omega$ | CTMC (**T**) | [27] |
| 25 – 1.6·10³ | $\sigma_{si}$, $d\sigma_{si}/d\Omega$ | IPBA (**T**) | [33] |
| 25 - 2·10³ | $\sigma_{si}$, $\sigma_{ti}$, $\sigma_{di}$, $\sigma_{sec}$ | QTMC (**T**) | [25] |
| 50 - 2380 | $\sigma_{si}$, $\sigma_{di}$, $\sigma_{ti}$, $\sigma_{sec}$ | CBCC/ToF (**E**) | [15] |
| 60 - 10³ | $\sigma_{si}$, $\sigma_{di}$, $\sigma_{sec}$, $\sigma_-$, $d\sigma_{si}/d\Omega$ | CTMC (**T**) | [10] |
| 60 - 10³ | $\sigma_{si}$, $\sigma_{ti}$, $\sigma_{di}$, | CTMC (**T**) | [23] |
| 60 –1.5·10³ | $d^2\sigma_{si}/d\Omega dE$, $d^2\sigma_{di}/d\Omega dE$ | CTMC (**T**) | [24] |

**Table 2.** Excitation data for H+ + He ground state collisions

| Energy range (keV) | Transitions | Quantities | Experimental Data (E), Theoretical Data (T), Review Data (R) | References |
|---|---|---|---|---|
| 1 - 150 | $1s^2 \rightarrow 1s\, n\,^1$S ($n$ = 3, 4, 5, 6)<br>$1s\, n\,^1$P ($n$ = 3, 4, 5)<br>$1s\, n\,^1$D ($n$ = 3, 4, 5, 6) | $\sigma_e$ | O (E) | [37] |
| 1 - 100 | $1s^2 \rightarrow 1s\, 2\,^1$L (L = S, P) | $\sigma_e$ | CCAO-MO (T) | [57] |
| 1 - $10^3$<br>5 - $10^3$<br>2.3 - $10^3$ | $1s^2 \rightarrow 1s\, 4\,^1$L (L = S, P, D)<br>$1s\, 3\,^1$L (L = S, P, D)<br>$1s\, 2\,^1$L (L = S, P, D) | $\sigma_e$ | (R) | [20] |
| 5 - 80 | $1s^2 \rightarrow 1s\, n\,^1$P ($n$ = 2, 3, 4) | $\sigma_e$ | CCAO (T) | [4] |
| 5 - $10^3$ | $1s^2 \rightarrow 1s\, n\,^1$S ($n$ = 2, 3, 4, 5)<br>$1s\, n\,^1$P ($n$ = 2, 3, 4, 5)<br>$1s\, n\,^1$D ($n$ = 3, 4, 5) | $\sigma_e$ | CCAO (T), R | [5] |
| 5 - 2·$10^3$ | $1s^2 \rightarrow 1s\, n\,^1$P ($n$ =2, 3) | $\sigma_e$ | FBA (T) | [45] |
| 5 - 5·$10^3$ | $1s^2 \rightarrow 1s\, n\,^1$S ($n$ = 2 - 7)<br>$1s\, n\,^1$P ($n$ = 2 - 6)<br>$1s\, n\,^1$D ($n$ = 3 –6) | $\sigma_e$ | FBA (T) | [41] |
| 6 - 30 | $1s^2 \rightarrow 1s\, 2\,^1$L (L = S, P) | $\sigma_e$ | 8s-CCMO (T) | [56] |
| 6.25 - 625 | $1s^2 \rightarrow 1s\, 2\,^1$L (L = S, P) | $\sigma_e$ | MSIPA(T) | [46] |
| 10 - 300 | $1s^2 \rightarrow 1s\, 2\,^1$L (L = S, P) | $\sigma_e$ | SBA (T) | [47] |
| 10 - 500 | $1s^2 \rightarrow 1s\, 2\,^1$L (L = S, P) | $\sigma_e$ | EDWB A | [48] |
| 10 - $10^3$ | $1s^2 \rightarrow 1s\, n\,^1$L<br>($n$ = 2, 3, 4, 5, L = S, P, D)<br>$1s\, 2\,^1$S $\rightarrow 1s\, 2\,^1$P<br>$1s\, 2\,^1$S $\rightarrow 1s\, 3\,^1$L(L= S, P, D) | $\sigma_e$ | SEDWA (T) | [53] |
| 10 - $10^4$ | $1s^2 \rightarrow 1s\, 2\,^1$L (L = S, P)<br>$1s\, 3\,^1$L (L = P, D) | $\sigma_e$ | MSIPA(T) | [49] |
| 15 - 500 | $1s^2 \rightarrow 1s\, 2\,^1$L (L = S, P) | $\sigma_e$ | TDHF(T) | [50] |
| 20 -100 | $1s^2 \rightarrow 1s\, 2\,^1$L (L = S, P) | $\sigma_e$, $\sigma_{sec}$ | CCAO (T) | [55] |
| 20 – 500 | $1s^2 \rightarrow 1s\, n\,^1$S ($n$ = 4, 5, 6)<br>$1s\, n\,^1$P ($n$ = 3, 4, 5, 6)<br>$1s\, n\,^1$D ($n$ = 3, 4, 5) | $\sigma_e$ | O (E) | [34] |
| 20 - $10^3$ | $1s^2 \rightarrow 1s\, 2\,^1$l (L = S, P) | $\sigma_e$, $d\sigma_e/d\Omega$ | SEA (T) | [52] |
| 20 - $10^3$ | $1s^2 \rightarrow 1s\, n\,^1$P ($n$ = 2, 3, 4) | $\sigma_e$, $d\sigma_e/d\Omega$ | SEDWA (T) | [54] |
| 25 -100 | $1s^2 \rightarrow 1s\, 2\,^1$L (L = S, P) | $\sigma_e$, $d\sigma_e/d\Omega$ | EL (E), MSIPA(T) | [44] |
| 25 - 100 | $1s^2 \rightarrow 1s\, 2\,^1$L (L = S, P) | $\sigma_e$, $d\sigma_e/d\Omega$ | EL (E) | [43] |
| 25 - 125 | $1s^2 \rightarrow 1s\, 2\,^1$L (L = S, P) | $\sigma_i$, $\sigma_e$, $d\sigma_e/d\Omega$ | EL (E) | [42] |
| 25 - 500 | $1s^2 \rightarrow 1s\, 2\,^1$L (L = S, P) | $\sigma_e$ | SOPA (T) | [51] |
| 60 - 400 | $1s^2 \rightarrow 1s\, n\,^1$L<br>($n$ = 4, 5, L = S, D) | $\sigma_e$ | O (E) | [36] |
| 100 - $10^3$ | $1s^2 \rightarrow 1s\, n\,^1$S ($n$ = 3, 4, 5)<br>$1s\, n\,^1$P ($n$ = 3, 4, 5)<br>$1s\, n\,^1$D ($n$ = 3, 4) | $\sigma_e$ | O (E) | [38] |
| 150 - $10^3$ | $1s^2 \rightarrow 1s\, n\,^1$P ($n$ =2, 3, 4) | $\sigma_e$ | O (E) | [40] |
| 150 - $10^3$ | $1s^2 \rightarrow 1s\, n\,^1$S ($n$ = 4, 5, 6, 7)<br>$1s\, n\,^1$P ($n$ = 3, 4, 5, 6) | $\sigma_e$ | O (E) | [35] |
| 200 - $10^3$ | $1s^2 \rightarrow 1s\, 3\,^1$P<br>$1s\, 4\,^1$L (L = S, D) | $\sigma_e$ | O (E) | [39] |

SYMBOLS AND ACRONYMS USED IN TABLES 1 AND 2

Quantities

$\sigma_e$: Single excitation cross section.

$\sigma_{si}$: Single ionization cross section.

$\sigma_{sec}$: Single electron capture cross section.

$\sigma_{ti}$: Transfer ionization cross section.

$\sigma_{di}$: Double ionization cross section.

$\sigma_{asi}$: Apparent single ionisation cross section ($\sigma_{sec} + \sigma_{si}$).

$\sigma_-$: Total free electron production cross section ($\sigma_{si} + \sigma_{ti} + 2\sigma_{di}$).

$\sigma_+$: Total positive ion production cross section ($\sigma_- + \sigma_{sec} + 2\sigma_{dec}$).

$d\sigma_e/d\Omega$: Differential cross section for single excitation.

$d\sigma_{si}/d\Omega$: Differential cross section for single ionization.

$d\sigma_{sec}/d\Omega$: Differential cross section for single electron capture.

$d^2\sigma_{si}/d\Omega dE$: Differential cross section for single ionization.

$d^2\sigma_{di}/d\Omega dE$: Differential cross section for double ionization.

$P_i(b)$: Ionization probability.

Methods: Experimental (**E**), Theoretical (**T**)

(E)

**CBCC**: Cross Beam Coincidence Counting measurement.

**CC:** Coincidence Counting measurement.

**EL**: Energy Loss measurement.

**O**: Optical measurement.

**PPC**: Parallel Plate Capacitor measurement.

**ToF**: Time of Flight measurement.

(T)

**CCAO**: Close Coupling Atomic Orbital method.

**CCMO**: Close Coupling Molecular Orbital method.

**CCAO-MO**: Close Coupling Atomic Orbital – Molecular Orbital matching method.

**2-CPWBA**: Two Channels Plane Wave Born Approximation.

**CDWEIS**: Continuum Distorted Wave Eikonal Initial State approximation.

**EDWBA**: Eikonal Distorted Wave Born Approximation.

**CTMC**: Classical Trajectory Monte Carlo method.

**FBA**: First Born Approximation.

**IPBA:** Impact Parameter Born Approximation.

**MEHC**: Multi-Electron Hidden Crossing theory.

**MSIPA**: Multi-State Impact Parameter Approximation.

**QCTMC**: Quasi-Classical Trajectory Monte Carlo method.

**SBA**: Second Born Approximation.

**SEA**: Symmetric Eikonal Approximation.

**SEDWA**: Symmetric Eikonal Distorted Wave Approximation.

**SOPA**: Second Order Potential Approximation.

**UFBA**: Unitarized First Born Approximation.

**TDHF**: Time dependent Hartree-Fock method.

**8s-:** Eight states

## 4. Excitation of He ground state ions by proton impact

The status of the atomic database on helium excitation by proton impact has been discussed in detail by Fritsch (1991, 1992) [4, 5] and de Heer *et al.* (1992) [6]. We give here a brief account of this work, and additionally include the recent quantum-mechanical calculations performed in the last ten years together with our CTMC calculations. The collected data for one-electron transitions from the ground state of helium atom into the singlet states ($n^1$L), where $n = 2$ - 6 and L = S, P, D, are listed in Table 2.

### 4.1. Experimental data

Experimental studies of one-electron excitation transitions for $H^+$ + He collisions have been performed in the 1960s and 1970s, based mainly on optical techniques. Fritsch [4, 5] and de Heer *et al.* (1992) [6] pointed out an inconsistency in the experimental data for single excitation into $n^1$L states, for $n = 3, 4, 5$ and L = S, P, D, at intermediate to low collision energies ($10 < E < 300$ keV). Absolute cross sections for the same transitions measured by different investigators [34-40] show the same energy dependence in the overlapping region around 150 keV, but they considerably differ in magnitude. According to Fritsch and to de Heer and collaborators, a consistent set of excitation cross sections for each individual transition can be obtained by using as guidance the corresponding experimental data at high energies ($E > 500$ keV), which either directly or after renormalization agree with the results of the Born approximation [41]. For high energies, the data of Hasselkamp *et al.* (1971) [39] and Hippler and Schartner (1974) [40] can be considered as reliable because they converge to the ones calculated by the Born approximation, while for energies below 100 keV the data of van den Bos *et al.* (1968) [37] are close to the average cross sections. Note that excitation into $2^1$P states seems to be well established in experimental studies of Park and Schowengardt (1969) [42], Park *et al.* (1978) [43], Hippler and Schartner (1974) [40] and Kvale *et al.* (1985) [44] agreeing well in the collision energy range from 25 to 1000 keV, except near 25 keV. The only available experimental data for the less investigated transition from the ground state to the metastable singlet state $2^1$S, are those of Kvale *et al.* (1985) [44], based on the energy loss technique, for the energy range from 25 to 100 keV.
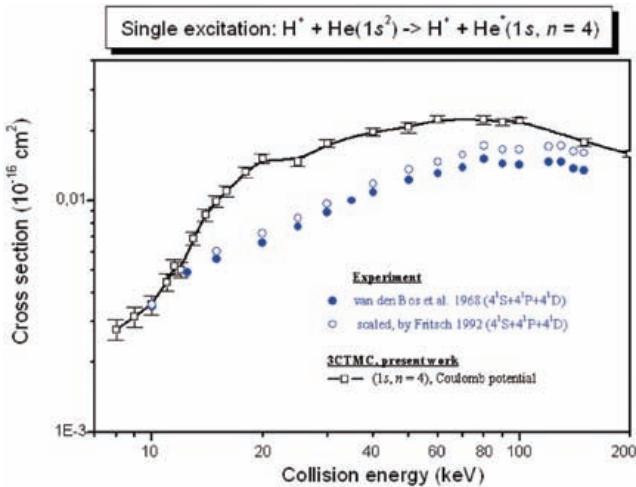
### 4.2. Theoretical data

Quantum-mechanical calculations of excitation cross sections have been performed in the late 1960s and early 1970s [45-51]. However, the results of different investigators frequently deviate from each other, especially for $E < 100$ keV. Recent calculations based on the Symmetric-Eikonal (SE) approximation [52-54] give improved results for transitions to ($n^1$L) states ( $n = 2, 3, 4, 5$ and L = S, P, D)
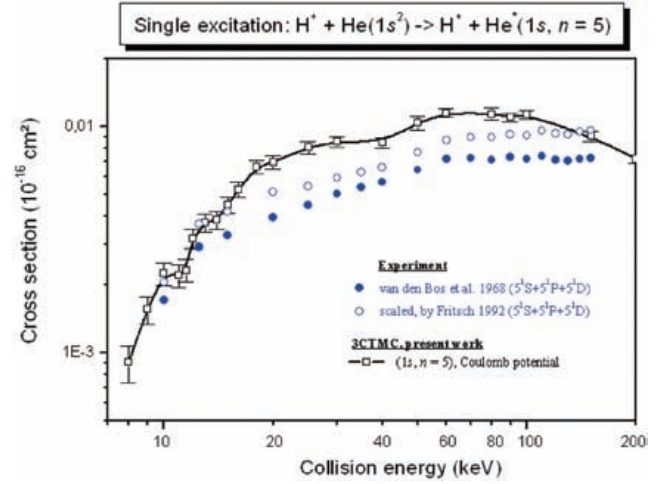
in the collision energy range around 100 keV, and they converge to the results of the Born approximation at high $E$.

For collision energies lower than 100 keV the calculations of Rodriguez *et al.* (1997) [54], where both electrons are explicitly treated, are in better agreement with the scaled experimental data. However, these calculations do not predict the oscillatory feature of the low energy cross sections observed experimentally [34, 37], which seems to be more pronounced for transitions into high excited states $n$ with large angular momentum values ($^1$D states). The oscillatory behaviour of the cross sections is also supported by AOCC calculations of Fritsch for excitation of $2^1$S, $3^1$S, $2^1$P, $3^1$P and $3^1$D states, which are in excellent agreement (except for the $2^1$S state) with the scaled experimental data at collision energies between 5 and 30 keV. The AOCC calculations of Slim *et al.* (1991) [55] also show a structure of the cross sections for $2^1$S and $2^1$P transitions, but at higher energies. Cross sections for excitation into $2^1$S and $2^1$P states have been calculated by Kimura (1985) [56] and Kimura and Lin (1986) [57], using the MOCC and AOCC-MOCC matching method, respectively. For each individual channel both calculations lie within the experimental errors of Kvale *et al.* (1985) [44], but they do not exhibit any oscillatory structures.

Although several CTMC models have been used for calculating ionisation and single electron capture cross sections, none of them has been applied to study helium excitation by proton impact. Total excitation cross sections into energy levels with $n = 4$, 5 and 6, covering the energy region from 8 to 200 keV, have been calculated with the 3CTMC model described in Section 2.1. Calculations are performed for the case where the interactions between three particles are purely of Coulomb type. Figs. 3 and 4 show the CTMC results for excitation into energy levels with $n = 4$ and 5, together with the sum of measured excitation cross



**Figure 4.** Excitation cross sections into energy level with $n$ =5 as a function of collision energy; symbols as in Fig. 3.
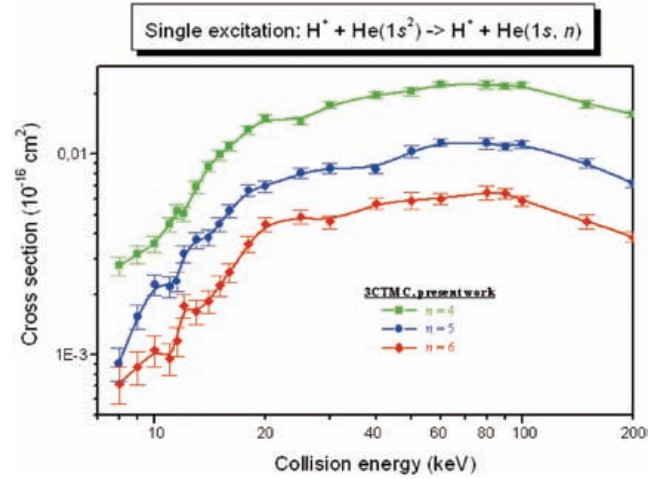


**Figure. 5.** Excitation cross sections into energy levels with $n = 4$, 5, 6 obtained by the 3CTMC model as a function of collision



**Figure 3.** Excitation cross sections into energy level with $n = 4$ as a function of collision energy. Experimental data: full circles, van den Bos (1968)[37]; crosses, scaled data by Fritsch (1992) [5]. 3CTMC calculations: open squares connected by solid line, present work.
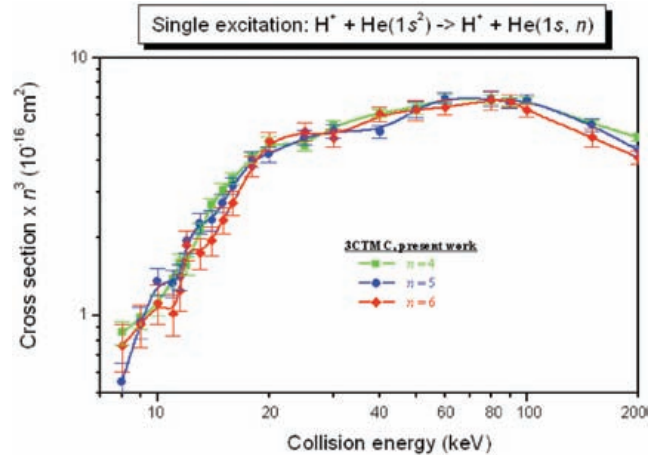


**Figure 6.** Scaled excitation cross sections into energy levels with $n = 4$, 5, 6 obtained by the 3CTMC model as a function of collision energy.

sections of van den Bos (1968) [37] for transitions to $4^1S$, $4^1P$ and $4^1D$ and $5^1S$, $5^1P$ and $5^1D$ states, respectively. Also included are the scaled data by Fritsch (1992) [5]. Note that the oscillatory structure observed in each individual channel (S, P and D) is suppressed when we add the corresponding cross sections. The CTMC cross sections for the channels $n = 4$ and 5 are larger than the experimental and scaled ones. For transitions to $n = 4$, CTMC results are larger up to a factor of two at 20 keV, but they converge to the scaled data at the high and low collision energy limits considered here. This discrepancy can be attributed to the fact that the single excitation process, where correlation effects between the two electrons are important, cannot be properly described by a simple 'hydrogenic' representation of the helium within the independent electron approximation. However, a better agreement is obtained for excitation into energy levels with $n = 5$, supporting the fact that classical calculations are expected to be more valid for higher quantum numbers. In Fig. 5 we display our results for transitions into $n = 4, 5, 6$. As expected, excitation cross sections decrease for transitions into high energy levels. Moreover the cross sections follow a $n^{-3}$ dependence, particularly at high energies, as it is also shown in scaled form in Fig. 6. This $n^{-3}$ dependence of excitation cross sections for high n-values reflects the dominance of the dipole component of the interaction potential that the CTMC method takes fully into account. In a quantum-mechanical formulation of the problem, the $n^{-3}$ dependence of excitation cross sections for dipole allowed transitions to high n-levels in charged particle-atom collisions appears in explicit form (see, e.g., [58]).

## 5. Excitation and electron capture in collisions of protons with excited helium atoms

The system of coupled Eqs. (4)-(5) has been solved numerically subject to the boundary conditions (6) for all the states that asymptotically represent the excited states of the helium atom with N = 2,3,4 and the hydrogen atom Stark states with principal quantum numbers n = 2,3,4. For the coupling interaction $V_{NLM}^{nn1m}(R)$, the analytic expression derived in [7] has been used, and the nuclear motion has been described in the straight-line approximation. Because of the conservation of the projection of angular momentum on the internuclear axis during the collision (M = M' = m) in the present formulation of the problem, it was sufficient to solve the system of coupled equations separately for each fixed initial value of M. Since in heavy particle collisions the total spin is also conserved, the system of equations (4)-(5) had to be solved also for a fixed value of S as well.

As argued in Section 2.2, the dominant interactions in the considered collision system at large internuclear distances are those coupling the covalent states, that converge to the (NLM) states of He in the separated atom limit, and the Stark states ($n_1 n_2 m$), having the same values of

principal quantum number, n = N. However, the radial couplings of the states with n ≠ N do have an effect on the magnitude of calculated cross sections and, therefore, all states of the manifolds {N},{n} = 2,3,4 had to be included in the expansion basis. Within the adopted basis set one can obtain reliable cross section results only for the states with N' = 2, 3 (excitation, de-excitation) and the states with n = 2,3 (charge exchange), since the results for the population of N', n = 4 states have to be considered as unreliable due to the fact that the couplings of these states with the N', n = 5 states have not been taken into account, i.e. the states N', n = 5 have not been included in the expansion basis. For this reason we present here only the results for initial states with N = 2, 3. We should also note that because of the dominance of the covalent – Stark state couplings between the states with n = N, the excitation cross sections with N' = N, and charge exchange cross sections with n = N are by orders of magnitude higher than those between the states with N' ≠ N and n ≠ N. Therefore, in what follows, we present only the cross sections for transitions between the states N' = n = N.
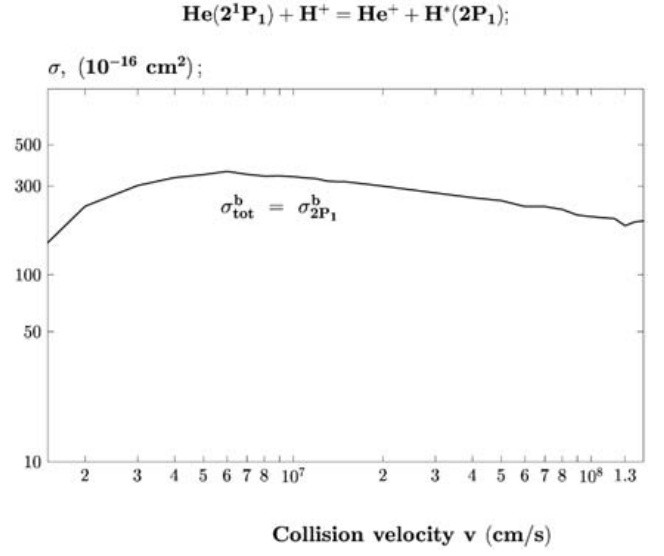
### 5.1. Excitation and charge exchange cross sections from N = 2 initial states

In this sub-section we adopt the notation $(1s; NLM)^S = (N^{2S+1}L_M)$ for the initial excited helium state, and $Nl_M$ or $nl_M$ for the final states in the excitation and charge exchange processes, respectively, where the conservation of total spin, S (= 0, 1), and the projection of orbital angular momentum on the internuclear axis (m = M' = M) have been taken into account, and N = n = 2. In this notation, there are six initial N = 2 excited states of the He atom: $2^1S_0$, $2^1P_0$, $2^1P_1$, $2^3S_0$, $2^3P_0$ and $2^3P_1$ (keeping in mind that M is the modulus of the magnetic quantum number). For a specified initial state, the cross section for a process of type λ will be designated as $\sigma^\lambda_{2lm}$, where λ = a and λ = b designate the excitation and charge exchange process, respectively, and m = M.
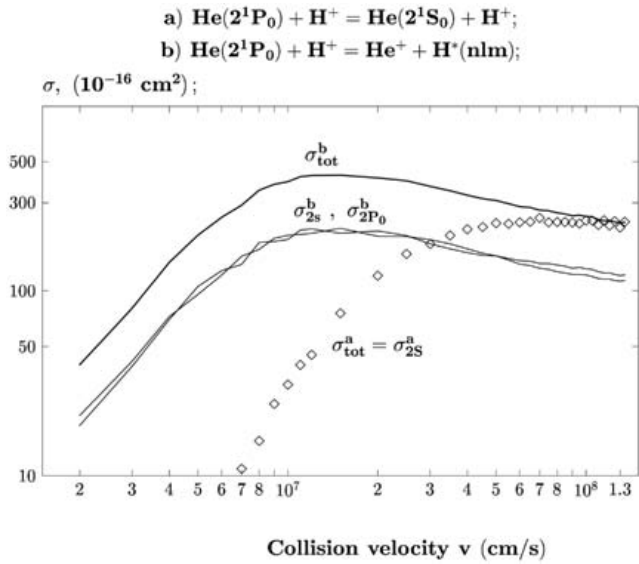
The excitation and charge exchange cross sections from the singlet initial states $2^1L_M$ are shown in Figs. 7 – 9, while those for the triplet initial states $2^3L_M$ are given in Figs. 10 – 12. The labels $\sigma^\lambda_{2lm}$ near each curve designate the type of the process (λ) and the final state ($2l_M$) of the active electron. A general characteristics of all $\sigma^\lambda_{2lm}$ cross sections is that they all have broad maxima in a certain collision velocity region, attaining values of the order of (200–400) x $10^{-16}$ cm². For lower collision velocities, the cross sections decrease very rapidly (exponentially), a characteristics of the adiabatic evolution of the collision system in this velocity region. The velocity at which the cross section maximum appears is related to the energy difference of the initial and final state (the reaction energy defect); the smaller this difference, the smaller the velocity at which the cross section maximum appears. For the $2^1P_1$ initial state, the difference between its energy and the energy of the n = 2 hydrogen level is smaller than for all other $2^{2S+1}L_M$ states,

$$He(2^1S_0) + H^+ = He^+ + H^*(2S_0, 2P_0);$$
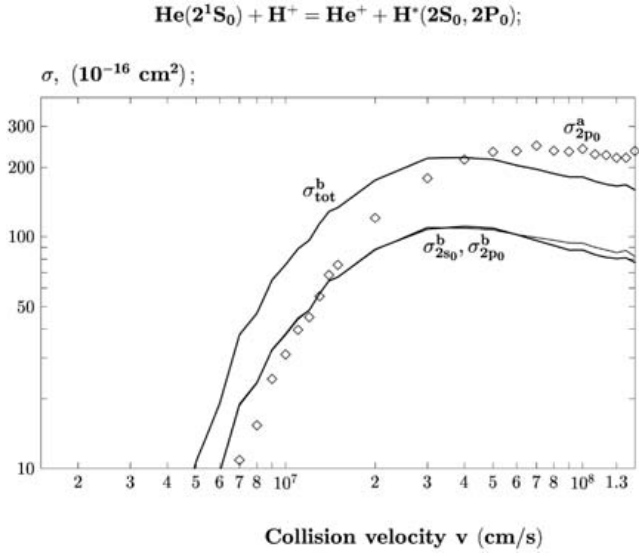


**Figure 7.** Excitation (superscript a) and charge exchange (superscript b) cross sections for the initial $2\,^1S_0$ helium excited state.

a) $He(2^1P_0) + H^+ = He(2^1S_0) + H^+;$
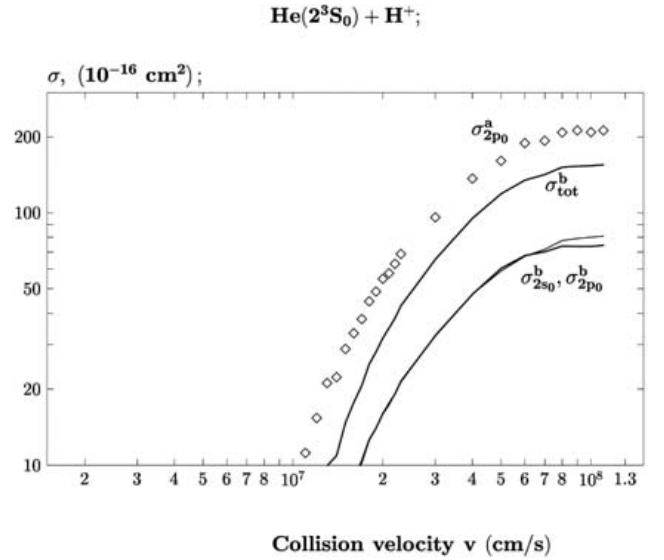b) $He(2^1P_0) + H^+ = He^+ + H^*(nlm);$



**Figure 8.** Same as in Fig. 7, but for the initial $2^1P_0$ excited state.

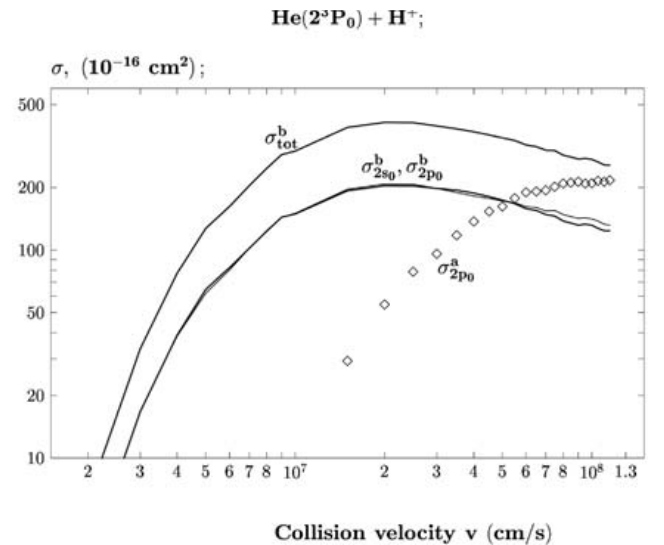and the cross section maximum appears at collision velocities around $6 \times 10^6$ cm/s.

It should be noted that because of the M' = m = M selection rule, only the charge exchange channel (λ = b) is open for the $2^{1,3}P_1$ initial states.

*5.2. Excitation and charge exchange cross sections from N=3 initial states*

In the case of N = 3, there are six singlet ($3^1L_M$) and six triplet ($3^3L_M$) (L = 0, 1, 2; M = 0, ..., L) states. The number of excitation and de-excitation transitions within the {N = 3} manifold for each specified ($3^{1,3}L_M$) initial state is very large. Similarly large is the number of charge exchange transitions to the states of the {n = 3} manifold from a given

$$He(2^1P_1) + H^+ = He^+ + H^*(2P_1);$$



**Figure 9.** Electron capture into $H(2p_1)$ state in proton collisions with $He(2^1P_1)$.

$$He(2^3S_0) + H^+;$$



**Figure 10.** Same as in Fig. 7, but for the $2\,^3S_0$ initial state.

$$He(2^3P_0) + H^+;$$



**Figure 11.** Same as in Fig. 7, but for the $2^3P_0$ initial state.
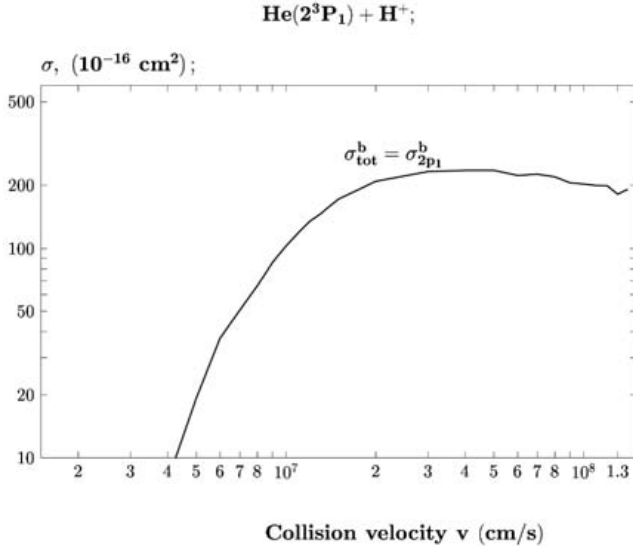
$He(2^3P_1) + H^+;$



**Figure 12.** Same as in Fig. 9, but for the $2^3P_1$ initial state.
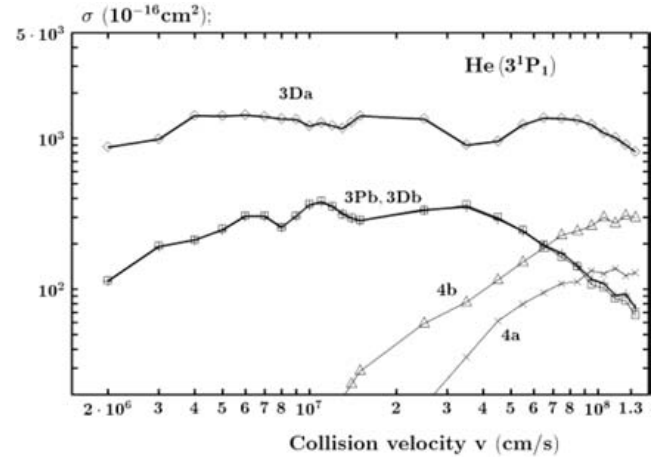


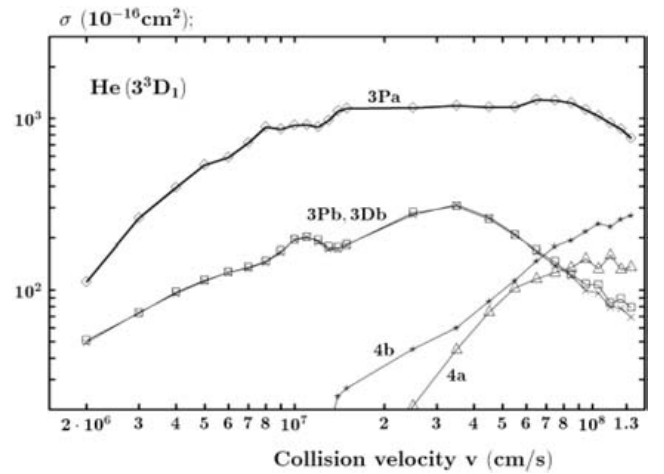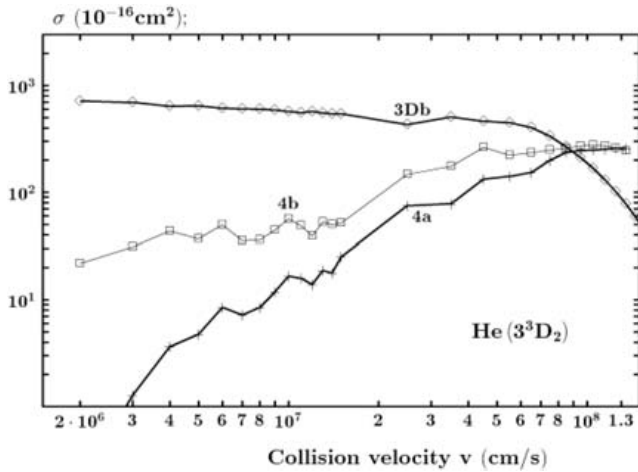**Figure 15.** Same as in Fig. 13, but for the $3^1P_1$ initial state.
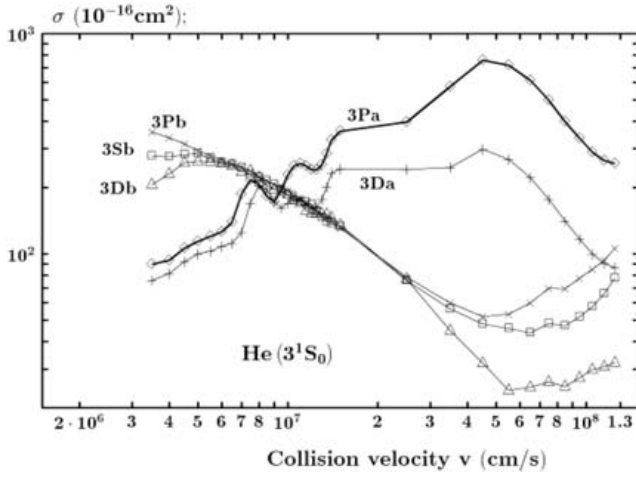


**Figure 13.** Excitation (label a) and charge exchange (label b) cross sections for the initial $3^1S_0$ excited state of He.
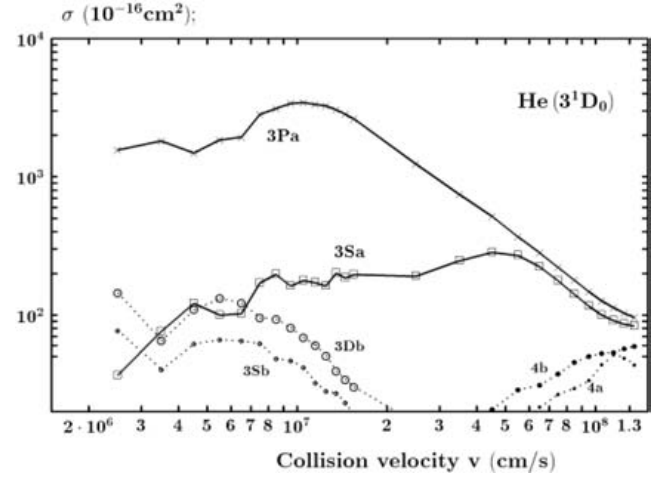


**Figure 16.** Same as in Fig. 13, but for the $3^1D_0$ initial state.
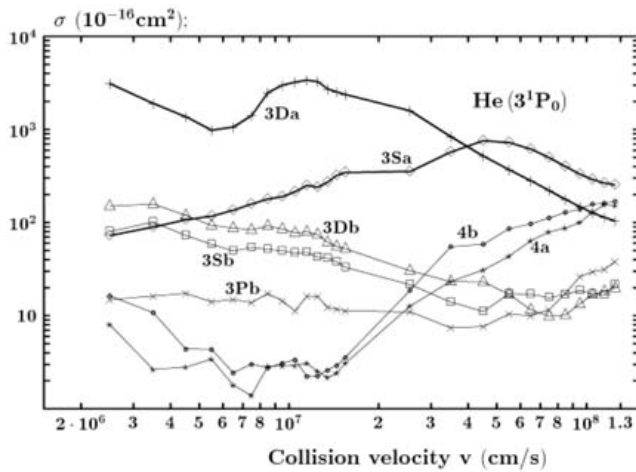


**Figure 14.** Same as in Fig. 13, but for the $3^1P_0$ initial state.
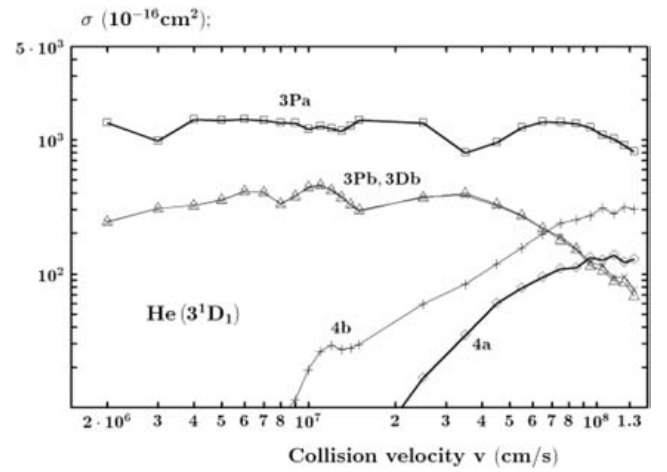


**Figure 17.** Same as in Fig. 13, but for the $3^1D_1$ initial state.
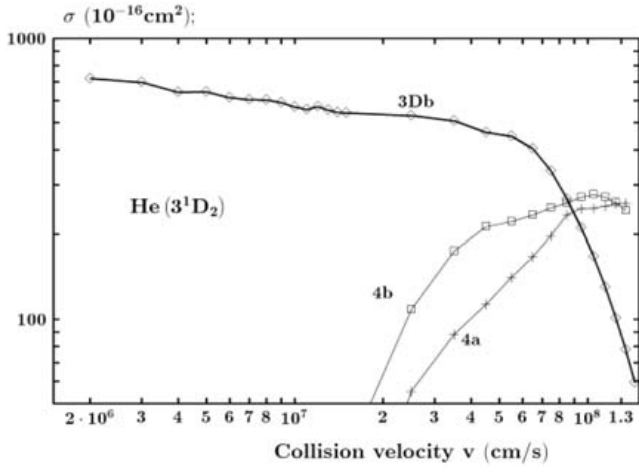
**Figure 18.** Same as in Fig. 13, but for the $3^1D_2$ initial state.
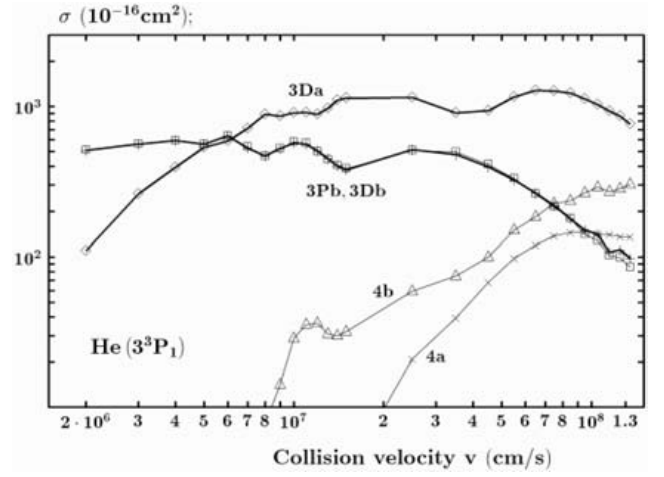


**Figure 21.** Same as in Fig.13, but for the $3^3P_1$ initial state.
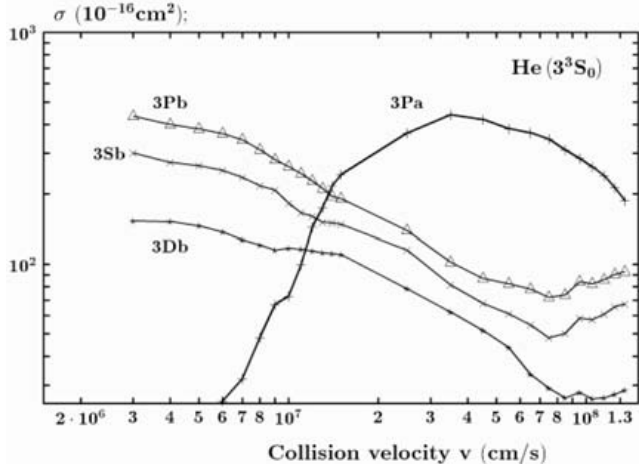


**Figure 19.** Same as in Fig. 13, but for the $3^3S_0$ initial state.
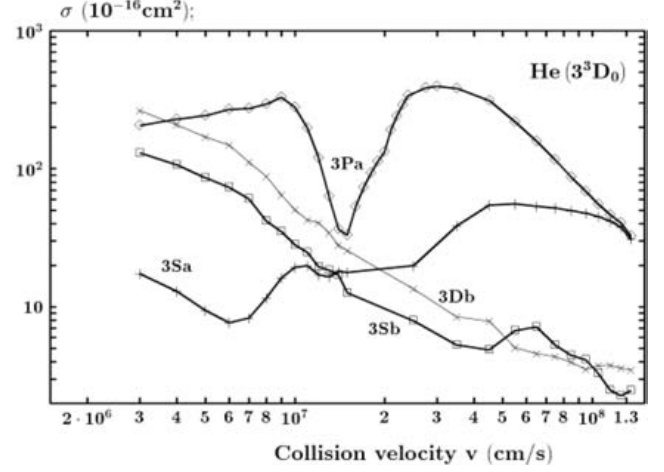


**Figure 22.** Same as in Fig. 13, but for the $3^3D_0$ initial state.
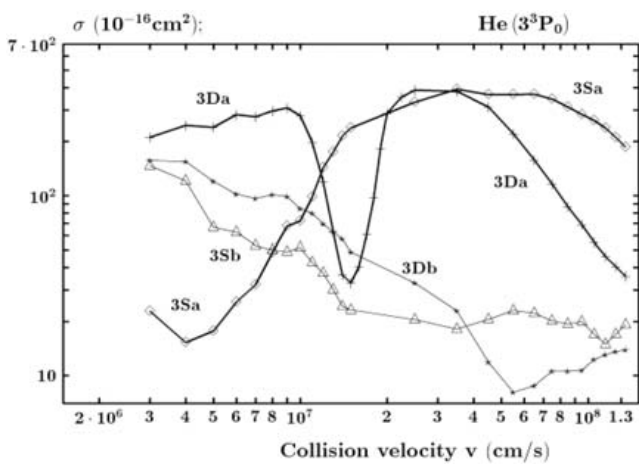


**Figure 20.** Same as in Fig. 13, but for the $3^3P_0$ initial state.



**Figure 23.** Same as in Fig. 13, but for the $3^3D_1$ initial state.

**Figure 24.** Same as in Fig. 13, but for the $3^3D_2$ initial state.

initial $(3^{1,3}L_M)$ initial state. The cross sections for excitation (label *a*) and charge exchange (label *b*) to the {N = 3} and {n = 3} sub-levels for the singlet initial $3^1L_M$ states are shown in Figs. 13 – 18, and those for excitation and electron capture from the triplet initial $3^3L_M$ states are shown in Figs. 19 - 24. The numerical values for these cross sections can be obtained on request from one of the authors (Chibisov, e-mail: chib@tokamak.ru). In the designation (nlm) for the product He or H atom n is equal either to 3 or 4, *m* is always equal to the value M of the initial state, and the value of angular quantum number *l* is indicated on the labels of cross section curves. These labels show also the value of the principal quantum number n, and the type of process (*a* or *b*). It can be seen from these figures that the cross sections for population of N, n = 3 excitation or charge exchange states are generally large (order of magnitude $10^{-13}$–$10^{-14}$ cm$^2$), and as a rule larger than the cross sections for the {N = 3} manifold of initial states. The electron capture cross section from $3^{1,3}D_2$ initial states to the $3d_2$ final state (Figs. 18 and 24, respectively) has a velocity behaviour typical for resonant charge exchange reactions. For some of the initial states, the total excitation cross section (denoted as 4a) and total charge transfer cross section (denoted as 4b) for transitions to N = 4 and n = 4 manifolds of states are shown. These cross sections, while being small at low collision velocities, can become comparable to the cross sections for transitions to N, n = 3 states at collision velocities around $10^8$ cm/s. As discussed earlier, however, since the N, n = 5 manifolds of states have not been included in the expansion basis of the calculations in Ref. [8], the total excitation and electron capture cross section to N = 4, n = 4 levels cannot be considered reliable.

## 6.    Conclusions

The status of the atomic database of single ionisation and excitation cross sections for proton collisions with neutral helium atoms has been reviewed for collision energies relevant to He beam diagnostics (5 - 200 keV). We have mainly focused on the compilation of quantum-mechanical and classical calculations performed during the last ten years. In addition, we performed CTMC calculations within the independent electron approximation, especially at the comparably low collision energies considered here. A fairly good agreement between our calculated single ionisation cross sections and the experimental ones has been obtained at collision energies from 10 up to 200 keV. Moreover, the CTMC calculations are in agreement with quantum-mechanical calculations in different collision energy regions. On the other hand, the one electron transitions into excited energy levels cannot be properly described by a three-body classical formulation within the independent electron approximation, as demonstrated here for transitions to *n* = 4, 5 levels. However, for the transition to *n* = 5, a better agreement of the CTMC results is obtained with the scaled data of Fritsch, in accordance with the expectation that the validity of the classical description increases with increasing of principal quantum number *n* of electronic state.

In this work we have also presented cross sections for excitation and charge exchange in proton collisions with excited helium atoms obtained by employing the MOCC method in the collision velocity range $10^6 – 10^8$ cm/s. While cross section data exist for all excitation and charge exchange transitions from the initial states with N = 2, 3 to all {N'} = 2,3 (excitation) and {n} = 2,3 (charge exchange) manifolds of states, only cross sections for transitions from {N} = 2 states to {N'} = 2 and {n} = 2 manifolds of states have been presented here, adding sources and the way of access to the other data.

## References

[1]    MENHART, S., PROSCHEK, M., FALTER, H.-D., ANDERSON, H., SUMMERS, H., STAEBLER, A., FRANZEN, P., MEISTER, H., SCHWEINZER, J., JONES, T.T.C., COX, S., HOWKES, N., AUMAYR, F., WINTER, HP, J. Nucl. Mat. **290-293** (2001) 673.

[2]    RUDD, M., KIM, Y.-K., MADISON, D.H., GALLAGHER, J.W., Rev. Mod. Phys. **57** (1985) 965.

[3]    GILBODY, H.B., Nucl. Fusion Suppl. **3** (1992) 55.

[4]    FRITSCH, W., Phys. Lett. A **160** (1991) 64.

[5]    FRITSCH, W., Nucl. Fusion Suppl. **3** (1992) 41.

[6]    DE HEER, F.J., HOEKSTRA, R., SUMMERS, H.P., Nucl. Fusion Suppl. **3**, 47 (1992).

[7]    CHIBISOV, M.I., JANEV, R.K., URBAIN, X., BROUILLARD, F., J. Phys. B: Atom. Mol. Opt. Phys. **34** (2001) 2631.

[8]    CHIBISOV, M.I., JANEV, R.K., URBAIN, X., BROUILLARD, F., J. Phys. B: Atom. Mol. Opt. Phys. **35** (2002) 5081.

[9]    IGARASHI, A., SHIRAI, T., Phys. Scr. **T62** (1996) 95.

[10]   REINHOLD, C.O., FALCON, C.A., Phys. Rev. A **33** (1986) 3859.

[11]   KATSONIS, K., MAYNARD, G., IAEA AGM on "A+M Data for Fusion Plasma Impurities", Report INDC(NDS)-257, Vienna, November 1991.

[12] KATSONIS, K., MAYNARD, G., J. Physique IV **1**, C1-313 (1991); KATSONIS, K., MAYNARD, G., JANEV, R.K., Phys. Scr. **T37** (1991) 80, MAYNARD, G., JANEV, R.K., KATSONIS, K., J. Phys. B: Atom. Mol. Opt. Phys. **25** (1992) 437.

[13] BRANSDEN, B.H., McDOWELL, M.R.C., ìCharge Exchange and the Theory of Ion – Atom Collisions", Clarendon Press, Oxford, 1992.

[14] OLSON, R.E., Phys. Rev. A **24** (1981) 1726; BECKER, R.L., MacKELLAR, A.D., J. Phys. B: Atom. Mol. Opt. Phys. **17** (1984) 3923.

[15] SHAH, M.B., GILBODY, H.B., J. Phys. B: At. Mol. Opt. **18** (1985) 899.

[16] SHAH, M.B., McCALLION, P., GILBODY, H.B., J. Phys. B: At. Mol. Opt. **22** (1989) 3037.

[17] DE HEER, F.J., SCHUTTEN, J., MOUSTAFA, H., Physica **32** (1966) 1766.

[18] RUDD, M., DUBOIS, R.D., TOBUREN, L.H., RATCLIFFE, C.A., GOFFE, T.V., Phys. Rev. A **28** (1983) 3244.

[19] AFROSIMOV, V.V., MAMAEV, Y.A., PANOV, M.N., FEDORENKO, N.V., Sov. Phys.-ZETP **14** (1969) 109.

[20] BARNETT, C.F., At. Data Fusion **1**, ORNL-6086/V1 (1990).

[21] PEACH, G., WILLIS, S.L., McDOWELL, M.R.C, J. Phys. B: At. Mol. Opt. **18** (1985) 3921; WILLIS, S.L., PEACH, G., McDOWELL, M.R.C., BANERJI, J., J. Phys. B: At. Mol. Opt. **18** (1985) 3939.

[22] ZAIFMAN, D., MAOR, D., Phys. Rev. Lett. **56** (1986) 320.

[23] WETMORE, A.E., OLSON, R.E., Phys. Rev. A **38** (1988) 5563.

[24] MONTEMAYOR, V.J., SCHIWIETZ, G., Phys. Rev. A **40** (1989) 6223.

[25] COHEN, J.S., Phys. Rev. A **54** (1996) 573.

[26] KATSONIS, K., VARVOGLIS, H., J. Phys. B: At. Mol. Opt. Phys. **28** (1995) L483.

[27] SCHULTZ, D.R., OLSON, R.E., Phys. Rev. A **38** (1988) 1866.

[28] FAINSTEIN, P.D., PONCE, V.H., RIVOLA, R.D., Phys. Rev. A **36** (1987) 3639.

[29] SLIM, H.A., HECK, E.L., BRANSDEN, B.H., FLOWER, D.R., J. Phys. B: At. Mol. Opt. **24** (1991) L421.

[30] CHEN, Z., MSEZANE, A.Z., Phys. Rev. A **49** (1993) 1752.

[31] DAS, T., MALIK, F.B., J. Phys. B: At. Mol. Opt. **30** (1997) 1223.

[32] KRSTIC, P.S., SCHULTZ, D.R., BENT, G., J. Phys. B: At. Mol. Opt. **31** (1998) 183.

[33] SAHOO, S., DAS, R., SIL, N.C., MUKHERJEE, S.C., ROY, K., Phys. Rev. A **62** (2000) 22716.

[34] DENIS, A., DUFAY, M., GAILLARD, M., C.R.A.S.P. B **264** (1966) 440.

[35] THOMAS, E.W., BENT, G.D., Phys. Rev. **164** (1967) 143.

[36] ROBINSON, J.M., GILBODY, H.B., Proc. Phys. Soc. **92** (1967) 589.

[37] VAN DEN BOS, J., WINTER, G.J., DE HEER, F.J., Physica 40 (1968) 357.

[38] SCHARMANN, A., SCHARTNER, K.H., Z. Phys. **228** (1969) 254.

[39] HASSELKAMP, D., HIPPLER, R., SHARMANN, A., SCHARTNER, K.-H., Z. Phys. **248** (1971) 254.

[40] HIPPLER, R., SCHARTNER, K.-H., J. Phys. B: At. Mol. Opt. **7** (1974) 618.

[41] BELL, K.L., KENNEDY, D.J., KINGSTON, A.E., J. Phys. B: At. Mol. Opt. **1** (1968) 1037.

[42] PARK, J.T., SCHOWENGARDT, F.D., Phys. Rev. A **185** (1969) 152.

[43] PARK, J.T., GEORG, J.M., PEACHER, J.L., ALDAG, J.E., Phys. Rev. A **18** (1978) 48.

[44] KVALE, T.J., SEELY, D.G., BLANKENSHIP, D.M., REDD, E., GAY, T.J., KIMURA, M., RILLE, E., PEACHER, J.L., PARK, J.T., Phys. Rev. A 32 (1985) 1369.

[45] SEDDON, G.J., BANYARD, K.E., J. Phys. B: At. Mol. Opt. **7** (1974) 2476.

[46] FLANNERY, M.R., J. Phys. B: At. Mol. Opt. **3** (1970) 306.

[47] HOLT, A.R., HUNT, J., MOISEIWITSCH, B.L., J. Phys. B: At. Mol. Opt. **4** (1971) 1318.

[48] JOACHAIN, C.J., VANDERPOORTEN, R., J. Phys. B: At. Mol. Opt. **7** (1974) 817.

[49] VAN DEN BOS, J., Phys. Rev. **181** (1969) 191.

[50] GRAMLICH, K., GR‹N, N., SCHEID, W., J. Phys. B: At. Mol. Opt. **19** (1969) 1457.

[51] BEGUM, S., BRANSDEN, B.H., COLEMAN, J., J. Phys. B: At. Mol. Opt. **6** (1973) 837.

[52] OLIVERA, G.H., RAMIREZ, C.A., RIVOLA, R.D., Phys. Rev. A **47** (1993) 1000.

[53] GULYAS, L., FAINSTEIN, P.D., Phys. Rev. A **56** (1997) 1321.

[54] RODRIGUEZ, V.D., RAMIREZ, C.A., RIVOLA, R.D., MIRAGLIA, J.E., Phys. Rev. A **55** (1997) 4201.

[55] SLIM, H.A., HECK, E.L., BRANSDEN, B.H., FLOWER, D.R., J. Phys. B: At. Mol. Opt. **24** (1991) 1683.

[56] KIMURA, M., Phys. Rev. A **31** (1985) 2158.

[57] KIMURA, M., LIN, C.D., Phys. Rev. A **34** (1986) 176.

[58] PERCIVAL, I.C., RICHARDS, D., Adv. At. Mol. Phys. **11** (1975) 2.

# Cross sections for electron capture and excitation processes in collisions between the hydrogen-like $He^+$(1s) and $B^{4+}$(1s), $C^{5+}$(1s), $N^{6+}$(1s), $O^{7+}$(1s) ions

*V.K. Nikulin, N.A. Guschina*

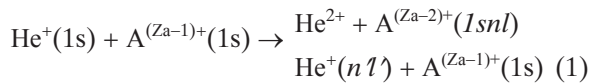A.F. Ioffe Physical-Technical Institute, St. Petersburg, Russian Federation

## Abstract

Cross sections for electron capture from the $He^+$(1s) ion and for excitation of the $He^+$(1s) ion in collisions with hydrogen-like $B^{4+}$(1s), $C^{5+}$(1s), $N^{6+}$(1s), $O^{7+}$(1s) ions have been obtained for the first time (collision energies $E_c$ of the $He^+$ ion are in the range 0.2 to 3 MeV). The calculations of cross sections were undertaken by the close-coupling equation method on the basis set of two-electron quasimolecular states.

Cross sections for single-electron capture into singlet and triplet 1snl ($2 \leq n \leq 5$) states of $B^{3+}$, $C^{4+}$, $N^{5+}$, $O^{6+}$ ions differ insignificantly due to weak exchange interaction between ground and excited quasimolecular states. In $He^+$(1s) - $C^{5+}$(1s), $N^{6+}$(1s), $O^{7+}$(1s) collisions the main contribution at $E_c > 1$ MeV to total cross section for excitation of $He^+$(1s) ion is due to electron excitation $1s \rightarrow 2p_0$. In $He^+$(1s) - $B^{4+}$(1s) collision significant contribution to the total cross section for excitation at $E_c < 1.0$ MeV is due to electron excitation $1s \rightarrow 3d_0$; at $E_c > 1.0$ MeV the process of electron excitation $1s \rightarrow 2p_{\pm 1}$ becomes the main one.

## 1. Introduction

In the central plasma region of controlled nuclear fusion devices, reactions occurring in collisions of $He^+$ ions with hydrogen-like impurity ions $B^{4+}$, $C^{5+}$, $N^{6+}$, $O^{7+}$ ($A^{(Za-1)+}$) within the MeV collision energy range are of great importance:

$$He^+(1s) + A^{(Za-1)+}(1s) \rightarrow \begin{array}{l} He^{2+} + A^{(Za-2)+}(1snl) \\ He^+(n\ell') + A^{(Za-1)+}(1s) \end{array} \quad (1)$$

Direct experimental research of these collisions with strong Coulomb repulsion between ions is difficult, and these reactions have not yet been studied theoretically. We report calculations of total and partial cross sections for charge transfer and excitation in reactions (1), at collision energies of $He^+$ ions ranging from 0.2 to 3 MeV.

The resulting data are necessary for modeling of alpha-particles behaviour in plasma and for spectroscopic diagnostics of high-temperature plasma. Emission from the excited impurity ions and $He^+$ ions, formed after collision, is of interest for plasma core spectroscopic diagnostics.

## 2. Theoretical method

### 2.1. Two-electron quasimolecular states

Computation of cross sections for single-electron capture and excitation in reactions (1) were performed by means of the impact parameter approximation and solving the close-coupling equations on the basis set of two-electron quasimolecular states.

Two-electron quasimolecular states $\phi_j$ are calculated in the single configuration approximation constructed using the single-electron Screened Diatomic Molecular Orbitals (SDMO) $\psi_j$:

$$\phi_j(r_1, r_2, R) = \frac{1}{\sqrt{2(1+S_{0j}^2)}} (\psi_0(r_1; R) \ \psi_j(r_2; R)$$
$$\pm \psi_0(r_2; R)) \equiv [\psi_0, \psi_j] \quad (2)$$

where R is the internuclear distance, $r_1$, $r_2$ are the coordinates of electrons, and $\psi_0$ is an orbital 1sσ or 1sσ' describing in the limit of separated atoms the 1s electron state of the ion $A^{(Za-1)+}$ or $A^{(Za-2)+}$. We use the classification of single-electron SDMOs by spherical quantum numbers (nlm) of united atom states. Signs "+" and "-" represent singlet and triplet two-electron states of quasimolecule; $S_{0j}$ is

the overlapping intergral of the SDMO $\psi_0$ and $\psi_j$, which are the solutions of the two-centre problem

$$(H_0(k) + V_{eff}^j(r_k; R))\ \psi_j(r_k) = \varepsilon_j(R)\ \psi_j(r_k),$$

$$H_0(k) = (-\frac{\nabla_k^2}{2} - \frac{Z_a}{r_{ak}} - \frac{Z_b}{r_{bk}}) \quad\quad (3)$$

The effective potential $V_{eff}^j$ is given in parametric form [2]:

$$V_{eff}^j(r_k; R) = \frac{1}{2}[\frac{a_1^j - b_1^j}{r_{ak}} + \frac{a_1^j + b_1^j}{r_{bk}} + \frac{\tilde{a}_1^j + Ra_0^j}{r_{ak}r_{bk}} + \frac{b_2^j(r_{ak} - r_{bk})^2}{Rr_{ak}r_{bk}}],$$

where $r_{ak}$, $r_{bk}$ are distances from the k electron to the nuclei with charges $Z_a$ and $Z_b$ ($Z_b = Z_{He}$), respectively. The basic set of two-electron diabatic states $\phi_j = [\psi_0, \psi_j]$ used to calculate the reactions (1) is shown in Table I.

**Table I.** The Basic Set of Two-Electron Diabatic States $\phi_j(r_1, r_2; R)$ (SDMO $2p\sigma$, $3d\sigma$, $4f\sigma$ in $\phi_1$ describe 1s electronic state of He$^+$ ion at $R \rightarrow \infty$)

| He$^+$ + B$^{4+}$ | He$^+$ + C$^{5+}$, N$^{6+}$ | He$^+$ + O$^{7+}$ | |
|---|---|---|---|
| the entrance channels He$^+$(1s) + A$^{(Za-1)}$(1s) | | | |
| $\phi_1 = [1s\sigma, 2p\sigma]$ | $\phi_1 = [1s\sigma, 3d\sigma]$ | $\phi_1 = [1s\sigma, 4f\sigma]$ | |
| The charge-transfer channels He$^{2+}$ + A$^{(Za-2)+}$(1snl) | | | |
| | | | (nl) |
| $\phi_2 = [1s\sigma', 3d\sigma]$ | $\phi_2 = [1s\sigma', 2p\sigma]$ | $\phi_2 = [1s\sigma', 2p\sigma]$ | $2p_0$ |
| $\phi_3 = [1s\sigma', 4f\sigma]$ | $\phi_3 = [1s\sigma', 4f\sigma]$ | $\phi_3 = [1s\sigma', 3d\sigma]$ | $3d_0$ |
| $\phi_5 = [1s\sigma', 6h\sigma]$ | $\phi_4 = [1s\sigma', 5g\sigma]$ | $\phi_4 = [1s\sigma', 5g\sigma]$ | $4f_0$ |
| $\phi_{10} = [1s\sigma', 7i\sigma]$ | $\phi_6 = [1s\sigma', 7i\sigma]$ | $\phi_5 = [1s\sigma', 6h\sigma]$ | $5g_0$ |
| $\phi_6 = [1s\sigma', 2p\pi]$ | - | - | $2p_{\pm 1}$ |
| $\phi_7 = [1s\sigma', 3d\pi]$ | $\phi_7 = [1s\sigma', 3d\pi]$ | $\phi_7 = [1s\sigma', 3d\pi]$ | $3d_{\pm 1}$ |
| $\phi_9 = [1s\sigma', 5g\pi]$ | $\phi_8 = [1s\sigma', 4f\pi]$ | $\phi_8 = [1s\sigma', 4f\pi]$ | $4f_{\pm 1}$ |
| - | $\phi_{10} = [1s\sigma', 6h\pi]$ | $\phi_9 = [1s\sigma', 5g\pi]$ | $5g_{\pm 1}$ |
| the excitation channels He$^+$(n'l') + A$^{(Za-1)+}$(1s) | | | |
| | | | (n'l') |
| $\phi_4 = [1s\sigma', 5g\sigma]$ | $\phi_5 = [1s\sigma', 6h\sigma]$ | $\phi_6 = [1s\sigma', 7i\sigma]$ | $2p_0$ |
| $\phi_8 = [1s\sigma', 4f\pi]$ | $\phi_9 = [1s\sigma', 5g\pi]$ | $\phi_{10} = [1s\sigma', 6h\pi]$ | $2p_{\pm 1}$ |
| $\phi_{11} = [1s\sigma', 8k\sigma]$ | - | - | $3d_0$ |

Among single-electron orbitals $\psi_j$ ($j \neq 0$) used to calculate reactions (1), there were SDMOs describing the 1s and $2p_{0,\pm 1}$ electronic states of a He$^+$ ion and the $2p_0$, $3d_{0,\pm 1}$, $4f_{0,\pm 1}$, and $5g_{0,\pm 1}$ electronic states of an A$^{(Za-2)+}$(1snl) ion in the limits of well separate nuclei. In the computation of He$^+$(1s) - B$^{4+}$(1s) collisions the excitation channel $3d_0$-state of He$^+$ ion, the nearest to the channel of single-electron capture into 1s5g-states of B$^{3+}$ ion, was also taken into

account. In this computation the single effective potential $V^1_{eff}$ has been used, based on the parameter definition scheme described in Ref. [3]. To compute single-electron orbitals $1s\sigma$ and $1s\sigma'$ with highly different energy values which describe the 1s-eleon state in A$^{(Za-1)+}$ and A$^{(Za-2)+}$ ions at the limit of separated atoms, special effective potentials $V^0_{eff}$ were used. Their parameter definition scheme is given in Ref. [4].

Energies of two-electron states $\phi_j(r_1, r_2; R)$

$$E_j(R) = <\phi_j(r_1, r_2; R) \mid H \mid \phi_j(r_1, r_2; R)> \quad (4)$$

have been calculated by means of the first order of perturbation theory [5], and are shown in Figs. 1-4.

A change from $Z_a = 5$ to $Z_a = 6$ and from $Z_a = 7$ to $Z_a = 8$ entails change of quasimolecular state $\phi_1(r_1, r_2; R)$, which describes at $R \rightarrow \infty$ the entrance channel in reactions (1). Atomic limits for two-electron states of He$^+$(1s) + N$^{6+}$(1s) system, as shown in the Table I, were formulated on the basis of the following consideration: at the collision velocities under analysis, the probabilities of transitions between states $[1s\sigma', 6h\sigma]$-$[1s\sigma', 7i\sigma]$ and $[1s\sigma', 5g\pi]$-$[1s\sigma', 6h\pi]$ in the neighbourhood of their pseudocrossings at
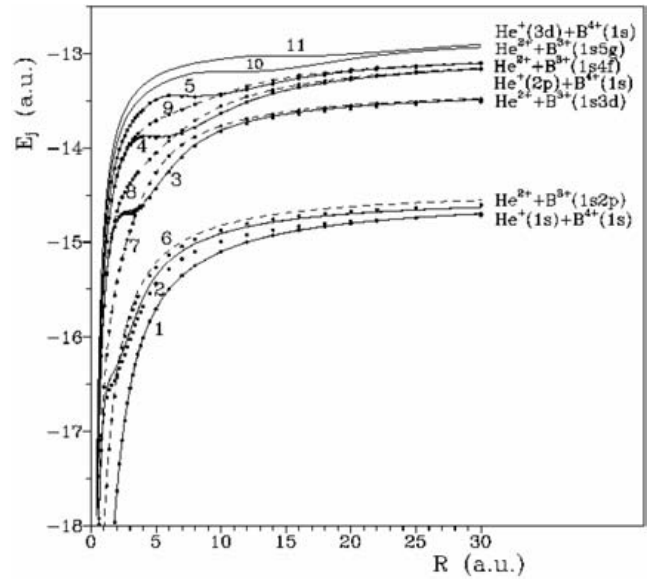


**Figure 1.** The energies $E_j(R)$ of two-electron singlet ($^1\Sigma_j$ - solid line, $^1\Pi_j$ - broken line) and triplet ($\bullet$) diabatic states $\phi_j$ ($j = 1 - 11$) for the He$^+$(1s) + B$^{4+}$(1s) system.
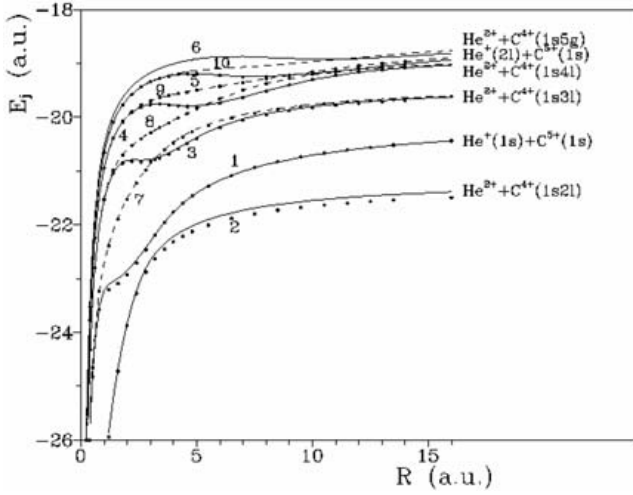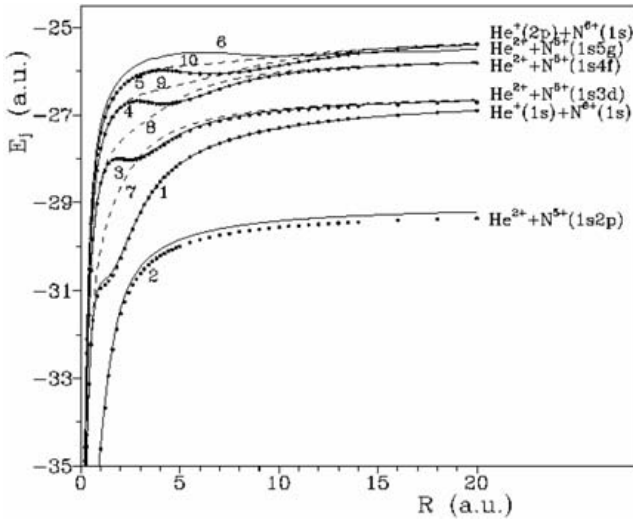
Entrance channel$\phi_1 = [1s\sigma, 2p\sigma]$ (1)

Charge-transfer channels:
$\phi_2 = [1s\sigma', 3d\sigma]$ (2), $\phi_6 = [1s\sigma', 2p\pi]$ (6),
$\phi_3 = [1s\sigma', 4f\sigma]$ (3), $\phi_7 = [1s\sigma', 3d\pi]$ (7),
$\phi_5 = [1s\sigma', 6h\sigma]$ (5), $\phi_9 = [1s\sigma', 5g\pi]$ (9),
$\phi_{10} = [1s\sigma', 7i\sigma]$ (10).

Single excitation channels:
$\phi_4 = [1s\sigma', 5g\sigma]$ (4), $\phi_8 = [1s\sigma', 4f\pi]$ (8),
$\phi_{11} = [1s\sigma', 8k\sigma]$ (11).

**Figure 2.** The energies $E_j(R)$ of two-electron singlet ($^1\Sigma_j$ - solid line, $^1\Pi_j$ - broken line) and triplet ($\bullet$) diabatic states $\phi_j$ (j = 1 - 10) for the $He^+(1s) + lC^{5+}(1s)$ system.
Entrance channel $\phi_1 = [1s\sigma, 3d\sigma]$ (1).
Charge-transfer channels:
   $\phi_2 = [1s\sigma', 2p\sigma]$ (2),
   $\phi_3 = [1s\sigma', 4f\sigma]$ (3),  $\phi_7 = [1s\sigma', 3d\pi]$ (7),
   $\phi_4 = [1s\sigma', 5g\sigma]$ (4),  $\phi_8 = [1s\sigma', 4f\pi]$ (8),
   $\phi_6 = [1s\sigma', 7i\sigma]$ (6),  $\phi_{10} = [1s\sigma', 6h\pi]$ (10).
Single excitation channels:
   $\phi_5 = [1s\sigma', 6h\sigma]$ (5), $\phi_9 = [1s\sigma', 5g\pi]$ (9).

R ~ 18 a.u. and R ~ 16 a.u. (see Fig. 3) equals 1; as a result the correlation diagram for the $He^+(1s) + N^{6+}(1s)$ system is similar to the diagram for the $He^+(1s) + C^{5+}(1s)$ system. Our calculations show that energies of the singlet and triplet states differ insignificantly in all considered systems because of the low exchange interaction between lower and excited electronic states.

### 2.2.  Close-coupling equation method

Within the close-coupling equation method, the problem reduces to the determination of the electron wave function $\Psi(r_1, r_2, t)$, that satisfies the nonstationary Schrödinger equation
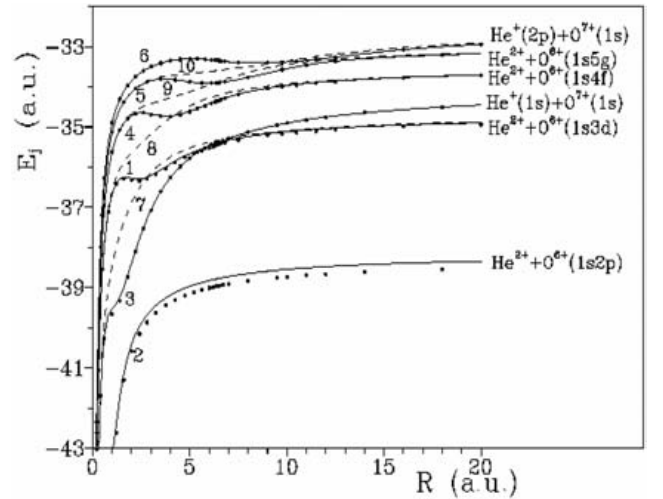
$$i \frac{\partial \Psi(r_1, r_2, t)}{\partial t} = H'(r_1, r_2, R(t)) \Psi(r_1, r_2, t) \tag{5}$$

where H′ is the total electron Hamiltonian

$$H' = H + \frac{Z_a Z_b}{R(t)}, \quad H = \sum_{k=1,2} H_o(k) + \frac{1}{r_{12}} \tag{6}$$

$$\Psi(r_1, r_2, t) = \sum_{j=1}^{n} a_j(t) \phi_j(r_1, r_2, R) \exp(-i \int_0^t [E_j(R) + \frac{Z_a Z_b}{R}] dt') \tag{7}$$

and $r_{12}$ is a distance between electrons.



**Figure 3.** The energies $E_j(R)$ of two-electron singlet ($^1\Sigma_j$ - solid line, $^1\Pi_j$ - broken line) and triplet   ($^3\Sigma_j$ - $\bullet$) diabatic states $\phi_j$ (j = 1 - 10) for the $He^+(1s) + N^{6+}(1s)$ system.
a.      Entrance channel$\phi_1 = [1s\sigma, 3d\sigma]$ (1).
Charge-transfer channels:
   $\phi_2 = [1s\sigma', 2p\sigma]$ (2),
   $\phi_3 = [1s\sigma', 4f\sigma]$ (3), $\phi_7 = [1s\sigma', 3d\pi]$ (7),
   $\phi_4 = [1s\sigma', 5g\sigma]$ (4), $\phi_8 = [1s\sigma', 4f\pi]$ (8),
   $\phi_5 = [1s\sigma', 6h\sigma]$ (5), $\phi_9 = [1s\sigma', 5g\pi]$ (9).
c.      Single excitation channels:
   $\phi_6 = [1s\sigma', 7i\sigma]$ (6),  $\phi_{10} = [1s\sigma', 6h\pi]$ (10).



**Figure 4.** The energies $E_j(R)$ of two-electron singlet ($^1\Sigma_j$ - solid line, $^1\Pi_j$ - broken line) and triplet   ($^3\Sigma_j$ - $\bullet$) diabatic states $\phi_j$ (j = 1 - 10) for the $He^+(1s) + O^{7+}(1s)$ system.
Entrance channel $\phi_1 = [1s\sigma, 4f\sigma]$ (1).
Charge-transfer channels:
   $\phi_2 = [1s\sigma', 2p\sigma]$ (2),
   $\phi_3 = [1s\sigma', 3d\sigma]$ (3), $\phi_7 = [1s\sigma', 3d\pi]$ (7),
   $\phi_4 = [1s\sigma', 5g\sigma]$ (4), $\phi_8 = [1s\sigma', 4f\pi]$ (8),
   $\phi_5 = [1s\sigma', 6h\sigma]$ (5), $\phi_9 = [1s\sigma', 5g\pi]$ (9).
Single excitation channels:
   $\phi_6 = [1s\sigma', 7i\sigma]$ (6), $\phi_{10} = [1s\sigma', 6h\pi]$ (10).

Wave function $\Psi(r_1, r_2, t)$ can be expanded into a series on the basis of a set of two-electron single configuration states:

If at $t \to -\infty$ ($R \to \infty$), the initial state of collision system $He^+(1s) + A^{(Za-1)+}(1s)$ is

$$\phi_1(r_1, r_2) = \lim_{t \to -\infty} \phi_1(r_1, r_2; R(t))$$

(with the energy $E_1(R = \infty)$), then

$$\Psi(r_1, r_2, t)_{|t \to -\infty} \to \phi_1(r_1, r_2) \exp(-iE_1(\infty)t). \qquad (8)$$

Substitution of Eq. (7) into Eq. (5) and taking Eq. (8) into consideration gives a set of linear differential equations to determine $a_j$ coefficients. For an orthogonal set of two-electron basis functions and the Coulomb trajectory of a nucleus motion, these equations can be re-arranged to give the following form [6]:

$$\frac{da_j(\tau)}{d\tau} = -\sum_{k \neq j} a_k(\tau) \{ \frac{\tau}{R - \gamma} R_{jk} + \frac{\rho}{R(R - \gamma)} L_{jk}$$

$$+ \frac{i}{\upsilon} \frac{R}{R - \gamma} H_{jk} \} \exp(-\frac{i}{\upsilon} \int_0^\tau (E_k - E_j) \frac{R}{R - \gamma} d\tau) \qquad (9)$$

$$(R(\tau) = (\tau^2 + \gamma^2 + \rho^2)^{1/2} + \gamma; \; -\infty < \tau < \infty)$$

with these initial conditions

$$a_j(-\infty) = \delta_{1j} \exp(-i\nu_1), \qquad (10)$$

where

$$\nu_1 = \exp(\frac{1}{\upsilon} \int_0^\infty [E_1(R) - E_1(\infty) + \frac{Z_a Z_b}{R}] \frac{R}{R - \gamma} d\tau).$$

In Eq. (9) $\rho$ is the impact parameter, and $\upsilon$ is the relative velocity of the nuclear motion, $\gamma = Z_a Z_b / (\mu \upsilon^2)$, $\mu$ - reduced mass; $R_{jk} = \langle \phi_j | d/dR | \phi_k \rangle$, $L_{jk} = \langle \phi_j | iL_y | \phi_k \rangle$ and $H_{jk} = \langle \phi_j | H | \phi_k \rangle$ are matrix elements of dynamic (radial and rotational) and potential coupling between two-electron states (2).

The transition amplitude from the initial state $\phi_1(\mathbf{r}_1, \mathbf{r}_2)$ to the final state

$\phi_j(r_1, r_2) = \lim_{R \to \infty} \phi_j(r_1, r_2; R)$ for given impact parameter $\rho$ and collision velocity $\upsilon$ is

$$b_j(\rho, \upsilon) = \lim_{t \to \infty} \langle \phi_j(r_1, r_2) | \Psi(r_1, r_2, t) \rangle \exp(iE_j(\infty)t)$$

$$= a_j(\infty) \exp(-i\nu_j), \qquad (11)$$

where

$$\nu_j = \frac{1}{\upsilon} \int_0^\infty [E_j(R) - E_j(\infty) + \frac{Z_a Z_b}{R}] \frac{R}{R - \gamma} d\tau. \qquad (12)$$

In applying the quasi-molecular model to describe atomic collisions (i.e., in solving the close-coupling equations), the problem arises of electron momentum transfer in the course of charge exchange. Since the pioneering study [7], this problem has not yet been rigorously solved even when considering single-electron quasi-molecular processes. It was shown in Ref. [7] that, because of ignoring the electron momentum translation in the course of nucleus motion, the basis functions (electron states) in an expansion of Eq. (7) turn out to be coupled to each other for any nucleus positions. Hence, when the number n of the terms in the basis set is finite, the calculated results depend strongly on the set size. To eliminate the nonphysical coupling between the states, it was proposed in Ref. [7] to use basis molecular function of Eq. (2) multiplied by the translation factors in the form of plane waves in Eq. (7). Many different forms of the translation factors have been proposed for quasi-molecular and atomic bases, as well as for single-electron and two-electron colliding systems and for heteronuclear and homonuclear quasi-molecules.

In this study, an alternative approach proposed in Ref. [8] for single-electron quasi-molecules is used to take into account momentum transfer. A special coordinate system for electrons is used to calculate the matrix elements of the dynamic coupling of the states. It was shown in Ref. [8] that, if the coordinate origin in a heteronuclear quasi-molecule $He^{2+}$- H(1s) is set at the centroid of the charges on the inter-nuclear axis (equipotential point - a natural boundary that separates the electrons belonging to one nucleus from the electrons belonging to the other), the transition probabilities calculated as a function of the impact parameter and the total cross sections are close to those calculated after allowance for the translation factor in the form of a plane wave.

For two-electron quasi-molecules considered in this study, this approach was verified in our recent paper [9] by calculating the reverse processes to reactions (1). The results of our calculation were close to the results of quasi-molecular calculations performed in the low-energy range with allowance for the translation factor, and in the high-energy range using an atomic model. Moreover, the approach used in Ref. [9] provides the best agreement with the available experimental data over a wide energy range.

As matrix elements of dynamic and potential coupling between singlet and triplet states are equal to zero, the system of close-coupling Eqs. (10) for reactions (1) splits into two independent systems for singlet and triplet entrance channels.

Matrix elements of dynamic coupling $d^s_{ij}$ and $d^t_{ij}$ between singlet (s) and triplet (t) two-electron states are the same and can be expressed via the matrix elements of radial ($R_{ij}$) and rotational ($L_{ij}$) coupling between the single-electron SDMO $\psi_i$ and $\psi_j$:

$$R_{ij} = \langle \psi_i | d/dR | \psi_j \rangle, \quad if \; m_i - m_j = 0; \qquad (13)$$

$$L_{ij} = \langle \psi_i | iL_y | \psi_j \rangle, \quad if \; |m_i - m_j| = 1.$$

Expressions were obtained without allowance for a minor non-orthogonality between the ground $\psi_o = (1s\sigma, 1s\sigma')$ and excited ($\psi_i$, $\psi_j$) states. The overlapping integral $S_{1s\sigma,1s\sigma'}$ was taken to be equal to one. For example, in the worst case of the $He^+(1s) - B^{4+}(1s)$ collision system, the values of $S_{1s\sigma,2p\sigma}$ and $S_{1s\sigma,3d\sigma}$ are less than $2\times10^{-2}$ and $S_{1s\sigma,1s\sigma'} = 0.996 \div 0.998$ at all R.

Detailed information relative to matrix elements of dynamic and potential coupling for the collision systems under consideration is presented in our preliminary reports [10] and [11]. For example, only the following twelve most significant matrix elements of the dynamic coupling for the $He^+- C^{5+}$ and $He^+- N^{6+}$ collision systems were retained in the close-coupling equations written on the basis of ten two-electron states listed in Table I:

$R_{12} = <3d\sigma|d/dR|2p\sigma>$, $R_{13} = <3d\sigma|d/dR|4f\sigma>$,
$R_{14} = <3d\sigma|d/dR|5g\sigma>$, $R_{15} = <3d\sigma|d/dR|6h\sigma>$,
$R_{34} = <4f\sigma|d/dR|5g\sigma>$, $R_{35} = <4f\sigma|d/dR|6h\sigma>$,
$R_{36} = <4f\sigma|d/dR|7i\sigma>$, $R_{45} = <5g\sigma|d/dR|6h\sigma>$,
$R^N_{46} = <5g\sigma|d/dR|7i\sigma>$, $R_{56} = <6h\sigma|d/dR|7i\sigma>$,
$R_{89} = <4f\pi|d/dR|5g\pi>$, $R_{9,10} = <5g\pi|d/dR|6h\pi>$.

The first three "transfer" matrix elements $R_{12}$, $R_{13}$, and $R_{14}$, between the entrance channel and charge-transfer channels (Table I) vanish asymptotically (Fig. 8, Ref. [10]). In calculations of the transfer matrix elements as discussed above, a special coordinate system for electron ("equipotential point frame" [8]) was used.

However, the "excitation" matrix element $R_{15}$ calculated in the equipotential point frame possesses physically spurious asymptotic behaviour (Fig. 8, Ref. [10]) tending to a constant, and the attainment of convergence for the integrated solution of close-coupling equations becomes impossible. Therefore, the radial couplings between the entrance channel ($\phi_1$) and the channels ($\phi_j$) for the excitation into the $2p_0$ state of a $He^+$ ion that did not vanish at $R \rightarrow \infty$ were artificially cut off using an exponentially decaying function:

$R'_{1j}(R) = R_{1j}(R_c) \exp[-\beta(R - R_c)]$      for $R > R_c$;
$R'_{1j}(R) = R_{1j}(R)$               for $R \leq R_c$,

where j = 4 for $He^+- B^{4+}$ collision system, j = 5 for $He^+- C^{5+}$ and $He^+- N^{6+}$ collision systems and j = 6 for $He^+- O^{7+}$ collision system (Table I). For all of the systems under study, the constants $R_c$ and $\beta$ were set to be about 7.0 and 0.3 a.u., respectively.

Only two out of the rest of the eight matrix elements $R_{34}$ and $R_{36}$ have spurious asymptotic behaviour (Fig. 11, Ref. [10]) . These eight matrix elements are responsible for the probability redistribution between charge-transfer and excitation channels. However, the results of integration of close-coupling equations are independent of whether matrix elements $R_{34}$ and $R_{36}$ are cut off or not.

All the computations of SDMO, two-electron states energies and matrix elements of dynamic and potential interaction between them are performed by using program package developed by the authors [12].

## 3. Results and discussions

For a given collision velocity $\upsilon$, partial cross-sections of population of two-electron singlet and triplet states $\phi_j(r_1,r_2) = \lim_{R\rightarrow\infty} \phi_j(r_1,r_2;R)$ were calculated by means of the formula

$$\sigma_j(\upsilon) = 2\pi \int_0^\infty d\rho \, | b_j(\rho,\upsilon)|^2 \qquad (14)$$

where $b_j(\rho, \upsilon)$ are the transition amplitudes (12) from the initial state $\phi_1(r_1,r_2)$ to the final state $\phi_j(r_1,r_2)$ (the small non-orthogonality of the two-electron states ($< \phi_i|\phi_j > < 10^{-3}$) was not taken into account in the close-coupling equations (10)). The "TANGO" [13] program was used to integrate the close-coupling equations (kindly provided by Antoine Salin).

*3.1. Cross sections for single-electron capture and excitation for $He^+(1s) - B^{4+}(1s)$ collision*

A calculation of partial cross sections $\sigma_j(\upsilon)$ (14) for $He^+(1s)$ ions colliding with $B^{4+}(1s)$ ions was carried out using the basic set of singlet two-electron states only. Total $\sigma_{sec}$ and partial $\sigma_{sec}(n)$ cross sections for single-electron capture (sec) into singlet 1snl-states (n = 2 - 5) of $B^{3+}$ ion were determined:

$$\sigma_{sec} = \sum_{n=2-3} \sigma_{sec}(n), \qquad (15)$$

where

$\sigma_{sec}(2) = \sigma_2(2p_0) + \sigma_6(2p_{\pm1})$,
$\sigma_{sec}(3) = \sigma_3(3d_0) + \sigma_7(3d_{\pm1})$,
$\sigma_{sec}(4) = \sigma_5(4f_0) + \sigma_9(4f_{\pm1})$,
$\sigma_{sec}(5) = \sigma_{10}(5g_0)$

total $\sigma_{exc}$ and partial $\sigma_{exc}(2)$, $\sigma_{exc}(3)$ excitation (exc) cross sections of $He^+$ ion:

$$\sigma_{exc} = \sum_{n=2-5} \sigma_{exc}(n), \qquad (16)$$

where

$\sigma_{exc}(2) = \sigma_{exc}(2p_0) + \sigma_{exc}(2p_{\pm1}) = \sigma_4(2p_0) + \sigma_7(2p_{\pm1})$,
$\sigma_{exc}(3) = \sigma_{exc}(3d_0) = \sigma_{11}(3d_0)$.

The basic set of 11 singlet two-electron quasimolecule states were used at projectile energies $E_c$ of $He^+$ ion ranging from 0.2 to 2 MeV. Results are shown in Tables II and IIa, and in Figs. 5 and 6.

Contributions to the total single-electron capture and excitation cross sections of the single-electron capture processes and excitation into triplet quasimolecular states are discussed in the following section.

### 3.2. Cross sections for single-electron capture and excitation for $He^+(1s)$ - $C^{5+}(1s)$ collision

Solutions of the close-coupling equation system for the $He^+ + C^{5+}$ quasimolecule on the basic set of 10 two-electron quasimolecilar states were determined for both the singlet and triplet entrance channel. Total $\sigma_{sec}$ and partial $\sigma_{sec}(n)$ cross sections for single-electron capture into singlet and triplet 1snl-states with n = 2 - 5 of $C^{4+}$ ion were calculated by the formula:

$$\sigma_{sec} = \sum_{n=2-5} \sigma_{sec}(n),\qquad(17)$$

where

$$\sigma_{sec}(2) = \sigma_2(2p_0), \quad \sigma_{sec}(3) = \sigma_3(3d_0) + \sigma_7(3d_{\pm1}),$$
$$\sigma_{sec}(4) = \sigma_4(4f_0) + \sigma_8(4f_{\pm1}), \quad \sigma_{sec}(5) = \sigma_6(5g_0) + \sigma_{10}(5g_{\pm1});$$

total $\sigma_{exc}$ and partial $\sigma_{exc}(2p_{0,\pm1})$ excitation cross sections of $He^+$ ion were calculated as follows:

$$\sigma_{exc} = \sigma_{exc}(2p_0) + \sigma_{exc}(2p_{\pm1}),$$

where
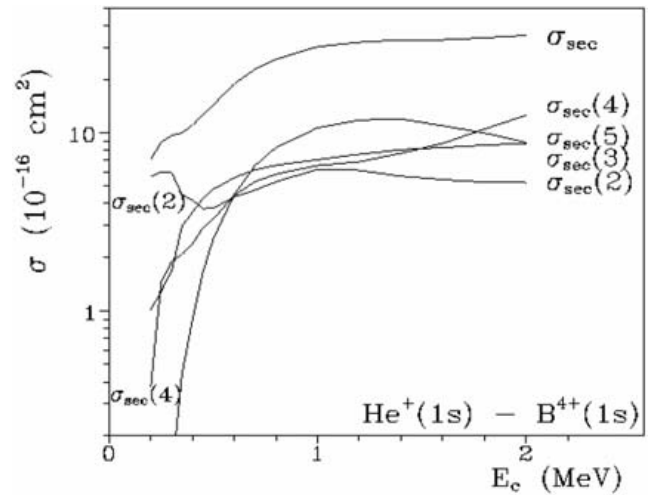
$$\sigma_{exc}(2p_0) = \sigma_5(2p_0), \quad \sigma_{exc}(2p_{\pm1}) = \sigma_9(2p_{\pm1}).$$

The calculations show that partial cross sections for the single-electron capture and excitation, determined on the basic set of singlet and triplet $He^+ + C^{5+}$ quasimolecule states, exhibited insignificant differences (for comparsion, total cross sections for charge transfer and excitation into singlet and triplet quasimolecular states are shown in Figs. 7 and 8). These observations occur because the energies of the singlet and triplet states only differ by a small amount due to their low exchange interaction, and the matrix elements of the dynamic interaction between singlet ($d^s_{ij}$) and triplet ($d^{tr}_{ij}$) states are equal. The results of the calculation of the partial (for singlet entrance channel) and total (for singlet and triplet entrance channels) cross sections for charge

transfer and excitation processes are shown in Tables III and IIIa, and in Figs. 7 and 8.

**Table II.** The Partial $\sigma_{sec}(n)$ and Total $\sigma_{sec}$ Cross Sections for Single-Electron Capture of Singlet 1snl-States of $B^{3+}$ in $He^+(1s) + B^{4+}(1s)$ Collisions

| $E_C$ (MeV) | $\sigma_{sec}(n=2)$ ($10^{-16}$ cm$^2$) | $\sigma_{sec}(n=3)$ ($10^{-16}$ cm$^2$) | $\sigma_{sec}(n=4)$ ($10^{-16}$ cm$^2$) | $\sigma_{sec}(n=5)$ ($10^{-16}$ cm$^2$) | $\sigma_{sec}$ ($10^{-16}$ cm$^2$) |
|---|---|---|---|---|---|
| 0.20 | 5.65 | 1.01 | 0.38 | 0.05 | 7.08 |
| 0.25 | 6.02 | 1.39 | 1.47 | 0.07 | 8.86 |
| 0.30 | 5.95 | 1.69 | 1.90 | 0.13 | 9.67 |
| 0.35 | 4.49 | 2.99 | 2.07 | 0.45 | 10.00 |
| 0.40 | 4.18 | 3.58 | 2.38 | 0.90 | 11.04 |
| 0.45 | 3.75 | 4.27 | 2.92 | 1.66 | 12.60 |
| 0.50 | 3.76 | 4.81 | 3.27 | 2.53 | 14.37 |
| 0.60 | 4.36 | 5.59 | 4.44 | 4.47 | 18.87 |
| 0.70 | 4.76 | 6.19 | 5.32 | 6.55 | 22.81 |
| 0.80 | 5.29 | 6.56 | 5.85 | 8.24 | 25.94 |
| 1.00 | 6.23 | 7.06 | 6.54 | 10.67 | 30.51 |
| 1.20 | 6.14 | 7.57 | 6.87 | 11.79 | 32.37 |
| 1.40 | 5.70 | 8.03 | 7.68 | 11.97 | 33.38 |
| 1.60 | 5.46 | 8.25 | 8.72 | 1.095 | 33.38 |
| 1.80 | 5.28 | 8.52 | 10.48 | 9.98 | 34.26 |
| 2.00 | 5.24 | 8.73 | 12.53 | 8.83 | 35.33 |



**Figure 5**. The total $\sigma_{sec}$ and partial $\sigma_{sec}(n)$ cross sections for the single-electron capture in $He^+(1s) + B^{4+}(1s)$ collisions: $\sigma_{sec} = \sum_{n=2-5} \sigma_{sec}(n)$; $\sigma_{sec}(2) = \sigma_2(2p_0)+\sigma_6(2p_{\pm1})$, $\sigma_{sec}(3) = \sigma_3(3d_0)+\sigma_7(3d_{\pm1})$, $\sigma_{sec}(4) = \sigma_4(4f_0)+\sigma_9(4f_{\pm1})$, $\sigma_{sec}(5) = \sigma_{10}(5g_{\pm1})$.

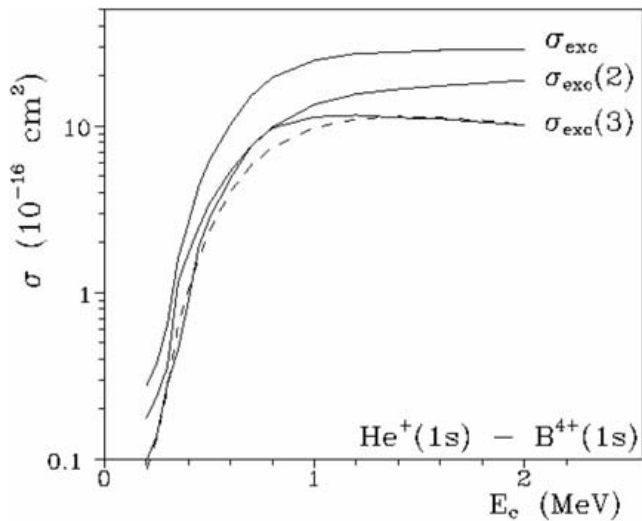**Table IIa.** The Partial $\sigma_{exc}(2p_l)$, $\sigma_{exc}(3d_0)$ and Total $\sigma_{exc}$ Cross Sections for He$^+$(1s) Ion Excitation in He$^+$(1s) + B$^{4+}$(1s) Collisions for the Singlet Entrance Channel

| $E_C$ (MeV) | $\sigma_{exc}(2p_0)$ ($10^{-16}$ cm$^2$) | $\sigma_{exc}(2p_{\pm 1})$ ($10^{-16}$ cm$^2$) | $\sigma_{exc}(3d_0)$ ($10^{-16}$ cm$^2$) | $\sigma_{exc}$ ($10^{-16}$ cm$^2$) |
|---|---|---|---|---|
| 0.20 | 0.09 | 0.09 | 0.10 | 0.28 |
| 0.25 | 0.11 | 0.13 | 0.14 | 0.38 |
| 0.30 | 0.10 | 0.26 | 0.29 | 0.65 |
| 0.35 | 0.52 | 0.63 | 0.45 | 1.60 |
| 0.40 | 0.69 | 1.04 | 0.90 | 2.62 |
| 0.45 | 0.86 | 1.62 | 1.90 | 4.38 |
| 0.50 | 1.07 | 2.35 | 2.79 | 6.21 |
| 0.60 | 1.31 | 4.05 | 4.86 | 10.22 |
| 0.70 | 1.77 | 5.84 | 7.60 | 15.22 |
| 0.80 | 2.37 | 7.45 | 9.75 | 19.57 |
| 1.00 | 3.67 | 9.79 | 11.35 | 24.81 |
| 1.20 | 4.58 | 11.02 | 11.62 | 27.22 |
| 1.40 | 5.19 | 11.42 | 11.23 | 27.83 |
| 1.60 | 6.21 | 11.24 | 11.06 | 28.52 |
| 1.80 | 7.30 | 10.80 | 10.55 | 28.66 |
| 2.00 | 8.60 | 10.22 | 10.14 | 28.95 |

Total cross sections for single-electron capture ($\Sigma_{sec}$) and excitation ($\Sigma_{exc}$) in the He$^+$(1s) - C$^{5+}$(1s) collision are equal:

$$\Sigma_{sec} = 0.25\ \sigma^s_{sec} + 0.75\ \sigma^{tr}_{sec} \text{ and } \Sigma_{exc}(2p_l)$$
$$= 0.25\ \sigma^s_{exc} + 0.75\ \sigma^{tr}_{exc}, \tag{18}$$

where $\sigma^s_{sec}$, $\sigma^s_{exc}$ and $\sigma^{tr}_{sec}$, $\sigma^{tr}_{exc}$ are the total cross sections for charge transfer and excitation, calculated for the singlet and triplet two-electron quasimolecule states, respectively.
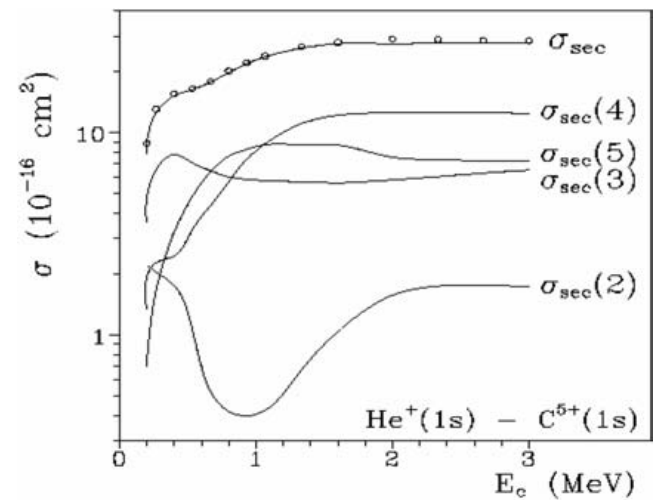
### 3.3. Cross sections for single-electron capture and excitation for He$^+$(1s) - N$^{6+}$(1s), O$^{7+}$(1s) collisions

Taking into account the results of detailed research on the He$^+$(1s) - C$^{5+}$(1s) collision process, the calculations of single-electron capture and excitation cross sections for He$^+$(1s) ions colliding with B$^{4+}$(1s), N$^{6+}$(1s) and O$^{7+}$(1s) ions were performed using the basic set of singlet two-electron states only. Cross sections calculated on the basis of these given conditions describe the statistically weighted total

**Table III.** The Partial $\sigma_{sec}(n)$ and Total $\sigma_{sec}$ Cross Sections for the Single-Electron Capture of Singlet 1snl-States of C$^{4+}$ in He$^+$(1s) + C$^{5+}$(1s) Collisions ($\sigma_{sec}^{tr}$ – Total Cross Section for the Single-Electron Capture Triplet 1snl-States of C$^{4+}$ Ions)

| $E_C$ (MeV) | $\sigma_{sec}(n=2)$ ($10^{-16}$ cm$^2$) | $\sigma_{sec}(n=3)$ ($10^{-16}$ cm$^2$) | $\sigma_{sec}(n=4)$ ($10^{-16}$ cm$^2$) | $\sigma_{sec}(n=5)$ ($10^{-16}$ cm$^2$) | $\sigma_{sec}(\sigma^{tr}_{sec})$ ($10^{-16}$ cm$^2$) |
|---|---|---|---|---|---|
| 0.200 | 2.21 | 3.64 | 1.35 | 0.70 | 7.90 (8.48) |
| 0.267 | 2.05 | 6.55 | 2.27 | 1.65 | 12.52 |
| 0.400 | 1.76 | 7.80 | 2.46 | 3.23 | 15.24 |
| 0.533 | 1.07 | 7.10 | 3.30 | 4.84 | 16.31 |
| 0.667 | 0.53 | 6.49 | 4.35 | 6.40 | 17.77 |
| 0.800 | 0.42 | 6.04 | 5.70 | 7.65 | 19.81 |
| 0.933 | 0.40 | 5.88 | 7.42 | 8.27 | 21.96 |
| 1.067 | 0.43 | 5.78 | 8.84 | 8.72 | 23.76 |
| 1.333 | 0.67 | 5.71 | 11.07 | 8.72 | 26.16 |
| 1.600 | 1.04 | 5.64 | 12.20 | 8.67 | 27.55 (27.91) |
| 2.000 | 1.57 | 5.84 | 12.58 | 7.56 | 27.56 (29.05) |
| 2.333 | 1.74 | 6.05 | 12.58 | 7.35 | 27.73 |
| 2.667 | 1.76 | 6.32 | 12.52 | 7.25 | 27.84 |
| 3.000 | 1.73 | 6.53 | 12.47 | 7.25 | 27.99 |



**Figure 6.** The total $\sigma_{exc}$ and partial $\sigma_{exc}(n)$ cross sections for the He$^+$(1s) ion excitation in He$^+$(1s) + B$^{4+}$(1s) collisions: $\sigma_{exc} = \sigma_{exc}(2) + \sigma_{exc}(3)$; $\sigma_{exc}(2) = \sigma_{exc}(2p_0) + \sigma_{exc}(2p_{\pm 1}) = \sigma_4 + \sigma_{10}$, $\sigma_{exc}(3) = \sigma_{exc}(3d_0) = \sigma_{11}$ (broken line - partial $\sigma_{exc}(2p_{\pm 1})$ cross section).



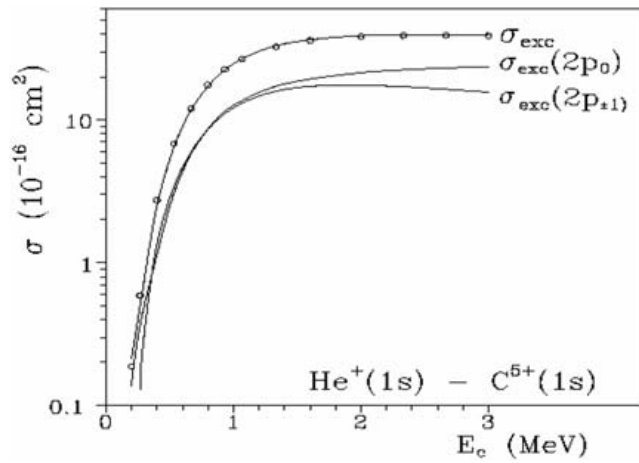**Figure 7.** The total $\sigma_{sec}$ and partial $\sigma_{sec}(n)$ cross sections for the single-electron capture in He$^+$(1s) + C$^{5+}$(1s) collisions: $\sigma_{sec} = \sum_{n=2-5}\sigma_{sec}(n)$; $\sigma_{sec}(2) = \sigma_2(2p_0)$, $\sigma_{sec}(3) = \sigma_3(3d_0) + \sigma_7(3d_{\pm 1})$, $\sigma_{sec}(4) = \sigma_4(4f_0) + \sigma_8(4f_{\pm 1})$, $\sigma_{sec}(5) = \sigma_6(5g_0) + \sigma_{10}(5g_{\pm 1})$

cross sections (20) of charge transfer and excitation for the $He^+(1s)$ - $B^{4+}(1s)$, $N^{6+}(1s)$, $O^{6+}(1s)$ collisions with a high degree of accuracy.

**Table IIIa.** The Partial $\sigma_{exc}(2p_l)$ and Total $\sigma_{exc}$ Cross Sections for the $He^+(1s)$ Ion Excitation in $He^+(1s) + C^{5+}(1s)$ Collisions for the Singlet Entrance Channel ($\sigma_{exc}^{tr}$ – Total Excitation Cross Section for the Triplet Entrance Channel)

| $E_C$ (MeV) | $\sigma_{exc}(2p_0)$ $(10^{-16}$ cm$^2)$ | $\sigma_{sec}(2p_{\pm1})$ $(10^{-16}$ cm$^2)$ | $\sigma_{exc}(\sigma_{exc}^{tr})$ $(10^{-16}$ cm$^2)$ |
|---|---|---|---|
| 0.200 | 0.07 | 0.14 | 0.21 (0.34) |
| 0.267 | 0.13 | 0.36 | 0.49 (0.59) |
| 0.400 | 1.35 | 1.14 | 2.49 (2.73) |
| 0.533 | 3.38 | 3.04 | 6.42 (6.79) |
| 0.667 | 5.90 | 5.70 | 11.60 (11.95) |
| 0.800 | 8.65 | 8.53 | 17.17 (17.58) |
| 0.933 | 11.46 | 11.06 | 22.52 (22.55) |
| 1.067 | 13.69 | 13.14 | 26.83 (26.71) |
| 1.333 | 17.17 | 15.87 | 33.04 (32.61) |
| 1.600 | 19.30 | 17.17 | 36.47 (36.10) |
| 2.000 | 21.44 | 17.50 | 38.94 (38.44) |
| 2.333 | 22.45 | 17.08 | 39.53 (39.18) |
| 2.667 | 23.12 | 16.39 | 39.51 (39.26) |
| 3.000 | 23.52 | 15.62 | 39.14 (38.96) |

Total and partial cross sections for single-electron capture and excitation of collisions between $He^+(1s)$ ions and $N^{6+}(1s)$ ions were calculated by means of Eqs. (17) and (18). The data are shown in Tables IV and IVa, and in Figs. 9 and 10.

When the cross sections for single-electron capture and excitation of collisions between $He^+(1s)$ ions and $O^{7+}(1s)$ ions were calculated, Eqs. (18) and (19) for the partial cross sections $\sigma_{sec}(5)$ and $\sigma_{exc}(2p_l)$ were changed in the following way:

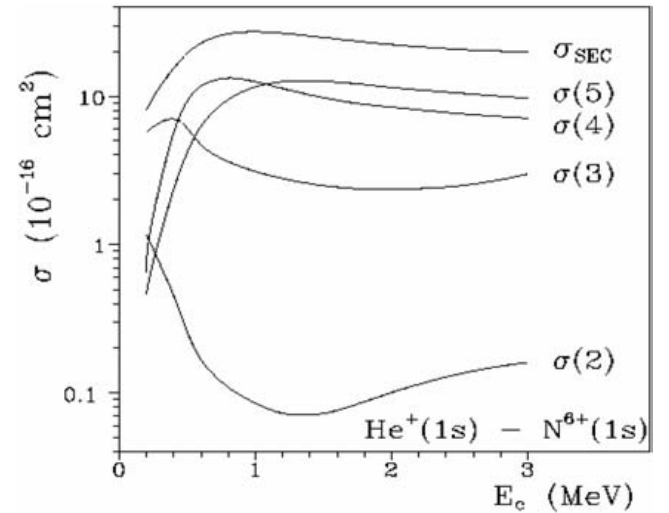$$\sigma_{sec}(5) = \sigma_5(5g_0)+\sigma_9(5g_{\pm1}) \quad \text{and} \quad \sigma_{exc}(2p_0) = \sigma_6(2p_0),$$
$$\sigma_{exc}(2p_{\pm1}) = \sigma_{10}(2p_{\pm1}).$$

The data are shown in Tables V and Va, and in Figs. 11 and 12.

**Table IV.** The Partial $\sigma_{sec}(n)$ and Total $\sigma_{sec}$ Cross Sections for the Single-Electron Capture of Singlet 1snl-States of $N^{5+}$ in $He^+(1s) + N^{6+}(1s)$ Collisions

| $E_C$ (MeV) | $\sigma_{sec}(n=2)$ $(10^{-16}$ cm$^2)$ | $\sigma_{sec}(n=3)$ $(10^{-16}$ cm$^2)$ | $\sigma_{sec}(n=4)$ $(10^{-16}$ cm$^2)$ | $\sigma_{sec}(n=5)$ $(10^{-16}$ cm$^2)$ | $\sigma_{sec}$ $(10^{-16}$ cm$^2)$ |
|---|---|---|---|---|---|
| 0.20 | 1.15 | 5.73 | 0.66 | 0.47 | 8.01 |
| 0.40 | 0.45 | 7.02 | 5.66 | 2.34 | 15.48 |
| 0.60 | 0.17 | 4.72 | 11.71 | 6.24 | 22.84 |
| 0.80 | 0.11 | 3.61 | 13.25 | 9.51 | 26.48 |
| 1.00 | 0.08 | 3.10 | 12.52 | 11.58 | 27.28 |
| 1.20 | 0.07 | 2.78 | 11.29 | 12.54 | 26.68 |
| 1.50 | 0.07 | 2.49 | 9.78 | 12.63 | 24.96 |
| 1,70 | 0.08 | 2.37 | 8.96 | 12.13 | 23.54 |
| 2.00 | 0.10 | 2.35 | 8.44 | 11.46 | 22.35 |
| 2.50 | 0.13 | 2.48 | 7.64 | 10.50 | 20.74 |
| 3.00 | 0.16 | 2.98 | 7.10 | 9.68 | 19.92 |



**Figure 8.** The total $\sigma_{exc}$ and partial $\sigma_{exc}(2p_l)$ cross sections for $1s \rightarrow 2p_l$ electron excitation of the $He^+(1s)$ ion in $He^+(1s) + C^{5+}(1s)$ collisions: $\sigma_{exc} = \sigma_{exc}(2p_0)+ \sigma_{exc}(2p_{\pm1})$; $\sigma_{exc}(2p_0) = \sigma_5$, $\sigma_{exc}(2p_{\pm1}) = \sigma_9$ (total excitation cross section $\sigma_{exc}^{tr}$ calculated on the basis of the triplet quasimolecular state)
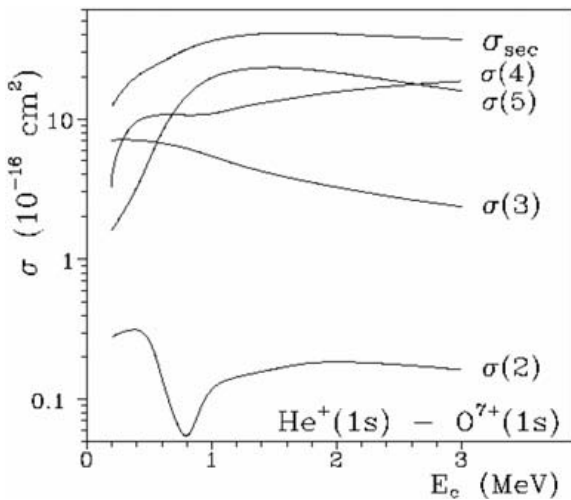


**Figure 9.** The total $\sigma_{sec}$ and partial $\sigma_{sec}(n)$ cross section for the single-electron capture in $He^+(1s) + N^{6+}(1s)$ collisions: $\sigma_{sec} = \sum_{n=2-5} \sigma_{sec}(n)$; $\sigma_{sec}(2) = \sigma_2(2p_0)$, $\sigma_{sec}(3) = \sigma_3(3d_0) + \sigma_7(3d_{\pm1})$, $\sigma_{sec}(4) = \sigma_4(4f_0) + \sigma_8(4f_{\pm1})$, $\sigma_{sec}(5) = \sigma_6(5g_0) + \sigma_{10}(5g_{\pm1})$.
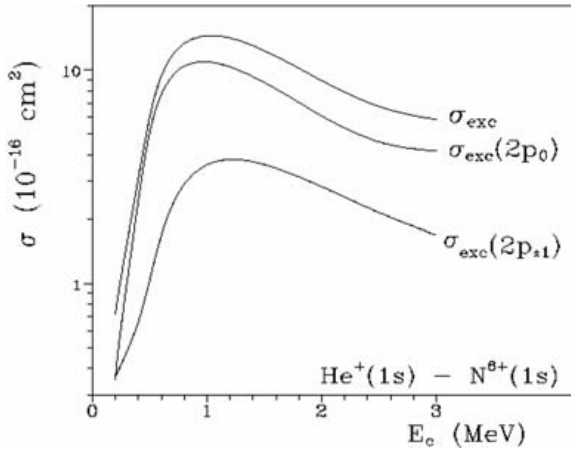
**Figure 10.** The total $\sigma_{exc}$ and partial $\sigma_{exc}(2p_l)$ cross sections for the $1s \rightarrow 2p_l$ electron excitation of He$^+$(1s) ion in He$^+$(1s) + N$^{6+}$(1s) collisions: $\sigma_{exc} = \sigma_{exc}(2p_0) + \sigma_{exc}(2p_{\pm1})$; $\sigma_{exc}(2p_0) = \sigma_5(2p_0)$, $\sigma_{exc}(2p_{\pm1}) = \sigma_9(2p_{\pm1})$.

**Table IVa.** The Partial $\sigma_{exc}(2_l)$ and Total $\sigma_{exc}$ Cross Sections of the He$^+$(1s) Ion Excitation in He$^+$(1s) + N$^{6+}$(1s) Collisions for the Singlet Channel

| $E_C$ (MeV) | $\sigma_{exc}(2p_0)$ ($10^{-16}$ cm$^2$) | $\sigma_{exc}(2p_{\pm1})$ ($10^{-16}$ cm$^2$) | $\sigma_{exc}$ ($10^{-16}$ cm$^2$) |
|---|---|---|---|
| 0.20 | 0.36 | 0.36 | 0.72 |
| 0.40 | 2.45 | 0.66 | 3.11 |
| 0.60 | 7.66 | 1.68 | 9.34 |
| 0.80 | 10.44 | 2.90 | 13.34 |
| 1.00 | 10.93 | 3.60 | 14.52 |
| 1.20 | 10.35 | 3.80 | 14.16 |
| 1.50 | 8.75 | 3.60 | 12.35 |
| 1.70 | 7.32 | 3.23 | 10.56 |
| 2.00 | 6.09 | 2.84 | 8.93 |
| 2.50 | 4.61 | 2.14 | 6.75 |
| 3.00 | 4.18 | 1.69 | 5.87 |



**Figure 11.** The total $\sigma_{sec}$ and partial $\sigma_{sec}(n)$ cross sections for the single-electron capture in He$^+$(1s) + O$^{7+}$(1s) collisions: $\sigma_{sec} = \sum_{n=2-5} \sigma_{sec}(n)$; $\sigma_{sec}(2) = \sigma_2(2p_0)$, $\sigma_{sec}(3) = \sigma_3(3d_0) + \sigma_7(3d_{\pm1})$, $\sigma_{sec}(4) = \sigma_4(4f_0) + \sigma_8(4f_{\pm1})$, $\sigma_{sec}(5) = \sigma_5(5g_0) + \sigma_9(5g_{\pm1})$.

**Table V.** The Partial $\sigma_{sec}(n)$ and Total $\sigma_{sec}$ Cross Sections for the Single-Electron Capture of Singlet 1snl-States of O$^{6+}$ in He$^+$(1s) + O$^{7+}$(1s) Collisions

| $E_C$ (MeV) | $\sigma_{sec}(n = 2)$ ($10^{-16}$ cm$^2$) | $\sigma_{sec}(n = 3)$ ($10^{-16}$ cm$^2$) | $\sigma_{sec}(n = 4)$ ($10^{-16}$ cm$^2$) | $\sigma_{sec}(n = 5)$ ($10^{-16}$ cm$^2$) | $\sigma_{sec}$ ($10^{-16}$ cm$^2$) |
|---|---|---|---|---|---|
| 0.20 | 0.28 | 7.05 | 3.29 | 1.59 | 12.22 |
| 0.40 | 0.31 | 7.04 | 9.56 | 3.22 | 20.13 |
| 0.60 | 0.14 | 6.70 | 10.69 | 7.98 | 25.51 |
| 0.80 | 0..05 | 6.15 | 10.65 | 14.64 | 31.49 |
| 1.00 | 0.11 | 5.40 | 10.89 | 19.73 | 36.14 |
| 1.25 | 0.15 | 4.59 | 12.23 | 22.57 | 39.53 |
| 1.50 | 0.16 | 4.02 | 13.38 | 23.28 | 40.85 |
| 1.75 | 0.18 | 3.59 | 14.54 | 22.65 | 40.95 |
| 2.00 | 0.18 | 3.25 | 15.59 | 21.39 | 40.42 |
| 2.50 | 0.18 | 2.72 | 17.32 | 18.46 | 38.68 |
| 3.00 | 0.16 | 2.36 | 18.60 | 15.86 | 36.98 |

**Table Va.** The Partial $\sigma_{exc}(2p_l)$ and Total $\sigma_{exc}$ Cross Sections for the He$^+$(1s) Ion Excitation in He$^+$(1s) + O$^{7+}$(1s) Collisions for the Singlet Entrance Channel

| $E_C$ (MeV) | $\sigma_{exc}(2p_0)$ ($10^{-16}$ cm$^2$) | $\sigma_{sec}(2p_{\pm1})$ ($10^{-16}$ cm$^2$) | $\sigma_{exc}$ ($10^{-16}$ cm$^2$) |
|---|---|---|---|
| 0.20 | 0.92 | 0.29 | 1.21 |
| 0.40 | 1.38 | 1.23 | 2.60 |
| 0.60 | 3.93 | 3.28 | 7.21 |
| 0.80 | 6.54 | 4.67 | 11.21 |
| 1.00 | 8.72 | 5.35 | 14.07 |
| 1.25 | 11.10 | 5.59 | 16.68 |
| 1.50 | 12.77 | 5.56 | 18.33 |
| 1.75 | 14.32 | 5.45 | 19.77 |
| 2.00 | 15.87 | 5.33 | 21.20 |
| 2.50 | 18.98 | 5.12 | 24.10 |
| 3.00 | 21.84 | 4.99 | 26.83 |
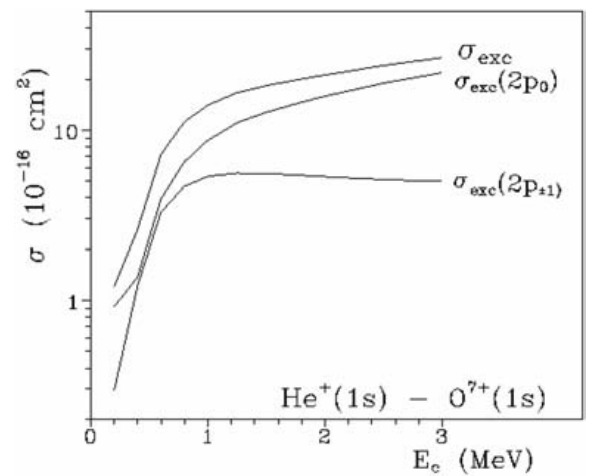


**Figure 12.** The total $\sigma_{exc}$ and partial $\sigma_{exc}(2p_l)$ cross sections for the $1s \rightarrow 2p_l$ electron excitation of the He$^+$(1s) ion in He$^+$(1s) + O$^{7+}$(1s) collisions: $\sigma_{exc} = \sigma_{exc}(2p_0) + \sigma_{exc}(2p_{\pm1})$; $\sigma_{exc}(2p_0) = \sigma_6(2p_0)$, $\sigma_{exc}(2p_{\pm1}) = \sigma_{10}(2p_{\pm1})$.

## 4. Conclusion

New data have been obtained on the total and partial cross sections for single-electron capture and excitation of the projectile in collision between hydrogen-like $He^+(1s)$ and $B^{4+}(1s)$, $C^{5+}(1s)$, $N^{6+}(1s)$, $O^{7+}(1s)$ ions over a range of collision energies $E_c$ from 0.2 to 3.0 MeV. The maximum value of the total cross section for single-electron capture ($40.9 \times 10^{-16}$ cm$^2$) was obtained in the $He^+(1s)$ - $O^{7+}(1s)$ collision at $E_c$ = 1.75 MeV. The maximum value of the excitation total cross section of the $He^+$ ion ($39.5 \times 10^{16}$ cm$^2$) was obtained in a collision between $He^+(1s)$ and $C^{5+}(1s)$ ions at $E_c$ = 2.33 MeV. In the $He^+(1s)$ + $B^{4+}(1s)$, $N^{6+}(1s)$, $O^{7+}(1s)$ collisions, cross sections for single-electron capture are larger than the cross section for excitation over the whole range of considered collision energies, and for the $He^+(1s)$ + $C^{5+}(1s)$ collision is only larger when $E_c$ < 0.9 MeV. At low collision energies in all of the systems considered with the exception of $He^+(1s)$ + $B^{4+}(1s)$, the main single-electron capture occurs in the 1s3l-states of $A^{(Z_A-2)+}$ ions. As $E_c$ increases (a) in $He^+(1s)$ + $C^{5+}(1s)$ collisions, the main single-electron capture occurs in the 1s5l- and then the 1s4l-states of $C^{4+}$ ion; (b) in $He^+(1s)$ + $N^{6+}(1s)$ collisions, single-electron capture occurs in the 1s4l- and then the 1s5l-states of $N^{5+}$ ions; (c) in $He^+(1s)$ + $O^{7+}(1s)$ collisions, most of single-electron capture occurs in the 1s4l- and then the 1s5l-states followed by the 1s4l-states of the $O^{6+}$ ion. At low collision energies $E_c$, in the $He^+(1s)$ + $B^{4+}(1s)$ collision, the main single-electron capture involves the 1s2l-state of $B^{3+}$ ion; whereas for all other collisions, the partial cross section for single-electron capture in the 1s2p-state of the $A^{(Z_A-2)+}$ ion is small over the whole range of collision energies considered:

$$\sigma^C_{sec}(2) < 2.0\ 10^{-16}\ \text{cm}^2,\ \sigma^N_{sec}(2) < 1.\ 10^{-16}\ \text{cm}^2\ \text{and}$$
$$\sigma^0_{sec}(2) < 0.3\ 10^{-16}\ \text{cm}^2.$$

For the $He^+(1s)$ + $B^{4+}(1s)$ collision, capture in the 1s3l- followed by the 1s5l-states of $B^{3+}$ ion are the most significant $E_c$ increases. We list below the $E_c$ intervals (in MeV) for every system in which the maximun values of the partial single-electron capture cross sections in n-states of $A^{(Z_A-2)+}(1snl)$ ions were obtained (maximum values for the partial cross sections $\sigma(n)$ (in $10^{-16}$ cm$^2$) over each interval are listed in parentheses):

|  | n = 2 | n = 3 |
|---|---|---|
| $B^{3+}(1snl)$ | $E_c$ < 0.4 (6.00) | - |
| $C^{4+}(1snl)$ | - | $E_c$ < 0.7 (7.8) |
| $N^{5+}(1snl)$ | - | $E_c$ < 0.4 (7.0) |
| $O^{6+}(1snl)$ | - | $E_c$ < 0.4 (7.1) |

| n = 4 | n = 5 |
|---|---|
| $0.4 < E_c < 0.7$ (6.2) | $E_c > 0.7$ (12.6) |
| $E_c > 1.0$ (12.6) | $0.7 < E_c < 1.0$ (8.7) |
| $0.4 < E_c < 1.1$ (13.3) | $E_c > 1.1$ (12.6) |
| $0.4 < E_c < 0.70$ (10.7) | $0.7 < E_c < 2.6$ (23.3) |
| $E_c > 2.6$ (20.3) |  |

The excitation of the $He^+$ ion in $He^+(1s)$ + $C^{5+}(1s)$, $N^{6+}(1s)$, $O^{7+}(1s)$ collisions occurs mainly in the $2p_0$-state. A significant contribution to the total cross section in the $He^+(1s)$ - $B^{4+}(1s)$ collision is made by excitation in the $3d_0$-state of the $He^+$ ion.

## References

[1] TAWARA, H., "Roles of Atomic and Molecular Processes in Fusion Plasma Researches", NIFS- DATA-25, May 1995, Nagoya, Japan.

[2] NIKULIN, V.K., GUSCHINA, N.A., J. Phys B: Atom. Mol. Phys. **11** (1978) 3553.

[3] NIKULIN, V.K., GUSCHINA, N.A., Tech. Phys. **44** (1999) 12 (translated from Russian).

[4] NIKULIN, V.K., GUSCHINA, N.A., SAMOYLOV, A.V., TSAREV, Yu.N.,"The method of the effective potential for many-electron quasimolecules. Ne$^{q+}$- Ne (q = 1, 2, 4) collisions." Preprint of Ioffe Physical-Technical Institute N 811, Leningrad, 1983.

[5] NIKULIN, V.K., SAMOYLOV, A.V., Phys. Lett. **89A** (1982) 235.

[6] NIKULIN, V.K., GUSCHINA, N.A., Optics and spectroscopy **80** (1996) 378 (translated from Russian).

[7] BATES, D.R., McCARROLL, R., Proc. Roy. Soc. A **245** (1958) 175.

[8] HATTON, G.J., LANE, N.F., WINTER, T.G., J. Phys. B: Atom. Mol. Phys. **12** (1979) L571.

[9] NIKULIN, V.K., GUSCHINA, N.A., Atom. Plasma-Mater. Interact. Data Fusion **10** (2002) 95.

[10] NIKULIN, V.K., GUSCHINA, N.A., "Theoretical study of electron capture and excitation processes in collisions between the hydrogen-like $He^+$ and $C^{5+}$, $N^{6+}$ ions". Preprint of Ioffe Physical-Technical Institute N 1764, St. Petersburg, 2003.

[11] NIKULIN, V.K., GUSCHINA, N.A., TSAREV, Yu.N., "Theoretical study of electron capture and excitation processes in collisions between $He^+$ and $B^{4+}$, $C^{5+}$, $N^{6+}$, $O^{7+}$ hydrogen-like ions". Preprint of Ioffe Physical-Technical Institute N 1772, St. Petersburg, 2004.

[12] GUSCHINA, N.A., NIKULIN, V.K., "The program package for inelastic process computation in slow ion-atom collisions". Preprint of Ioffe Physical-Technical Institute N 1717, St. Petersburg, 1998.

[13] PIACENTINI, R.D., SALIN, A., Comput. Phys. Commun. **12** (1976) 199.

# Radiative lifetime of high Rydberg states perturbed by a neutral atom

*M.I. Chibisov[1], R.K. Janev[2], I.I. Fabrikant[3], X. Urbain[4], F. Brouillard[4]*

[1] RRC "Kurchatov Institute", Nuclear Fusion Institute, Kurchatov str. 1, Moscow 123182, Russia

[2] Macedonian Academy of Sciences and Arts, P.O. Box 428, 1000 Skopje, Macedonia

[3] University of Nebraska, Department of Physics and Astronomy, Lincoln, NE-68588, USA

[4] Department de Physique, Unite PAMO, Chemin du cyclotron 2, B-1348 Louvain-la-Neuve, Belgium

## Abstract

The radiative lifetimes of high Rydberg states perturbed by a neutral atom have been investigated. Calculations have been performed for the "active" states within the $N^2$ Rydberg manifold with principal quantum numbers N = 20, 25, 30, 35. The energies of these "active" states are shifted with respect to the unperturbed Coulomb energies. Their lifetimes are found to depend on internuclear distance R between the Rydberg and perturbing atom. In the limit of asymptotically large distances R, the calculated radiative lifetime is equal to that of corresponding Stark state, whereas in the limit R → 0, this parameter is equal to that of the spherical S-state for a given N. However at distances about half of the size of Rydberg electron orbit, the calculated radiative lifetimes are 3-5 times larger than these limit values.

## 1.    Introduction

Recently [1-3], we have constructed an adiabatic wave function for the system A(nLm) + B, where A(nLm) is a highly excited atom and B is a ground state perturbing atom. We found that these wave functions differ significantly from the original (unperturbed) Coulomb spherical or parabolic wave functions. The origin of this difference lies in the degeneracy of the Coulomb energy levels [4, 5].

We have studied the radiative lifetime of high Rydberg states perturbed by a neutral atom. Previously, the $N^2$ manifold of the initially degenerate states of a Rydberg electron (with principal quantum number N) has been shown to have only one state, conditionally designated as "active", that experiences dramatic changes due to perturbation by a ground state neutral atom[1-3, 6, 7]. The energy of the "active" state is shifted from the initial Coulomb energy level, and the molecular dissociation energy of this state is the largest [6, 7]. N other adiabatic states are "quasi-active" states: their energies are equal to the unperturbed Coulomb energies, but their wave functions acquire a dependence on the internuclear distance R(t) (i.e. on time). The remaining N(N - 1) - 1 states of the $N^2$ manifold of degenerate states are "passive"; their wave functions are equal to the initial (unperturbed) Coulomb wave functions and their energies remain unchanged (constant). The present calculations show that the radiative lifetime of the "active" states with N = 20, 25, 30, 35 are 3-5 times larger than the radiative lifetime of Rydberg electron in states with initial Coulomb spherical or parabolic wave functions with the same N values.

## 2.    Radiative lifetime

The total probability of radiation when a Rydberg electron transits from an initial N state to all states with n < N is given by [8, 9] (in atomic units):

$$A_N = \frac{4}{3c^3} S_N(R); \qquad S_N(R) = \sum_{n=1}^{N-1} (\Delta E_n^N)^3 \sum_{l=0}^{n-1} [<nl|\,r\,|N>]^2; \qquad (1)$$

where c is the speed of light (c = 137.0343 in atomic units). The energy difference $\Delta E_n^N$ between the N and n levels can be taken to be equal to that of the unperturbed degenerate states. The radiative lifetime of the N state is then

$$T_N(R) = \frac{4.668 \cdot 10^{-11} \text{ sec}}{S_N(R)}. \qquad (2)$$

### 2.1.  Complete Ortonormal Basis of Adiabatic Wave Functions

In previous work [1-3, 10, 11], the wave functions of an "active" state were shown to be well represented by:

$$\psi_n(R, r) = \sum_{l=0}^{n-1} \sum_{m=-l}^{+l} J_{nlm}(R)\,\phi_{nlm}(r); \qquad J_{nlm}(R) = \frac{\phi_{nlm}(R)}{\sqrt{Q_n(R)}}; \qquad (3)$$

where

$$Q_n(R) = \sum_{l=0}^{n-1} \sum_{m=-l}^{+l} |\phi_{nlm}(R)|^2 = 2Z \int_R^{\infty} \phi_{n0}^2(r)dr; \qquad (4)$$

and the subscript n0 corresponds to the spherical wave function with zero angular momentum quantum numbers l =

m = 0 [5]. Wave function (3) describes the S-wave scattering of the Rydberg electron on the atom B.

The functions that are orthogonal to the wave function of "active" state $\psi_n(R,r)$ are [2, 3]

$$\psi_{nlm}(R,r) = \phi_{nlm}(r) - J_{nlm}(R)\,[\psi_n(R,r) + \phi_{n\lambda\mu}(r)]; \quad (5)$$

where the $\phi_{m\lambda\mu}$ function is orthogonal to $\psi_n(R,r)$ from the outset, so that $J_{n\lambda\mu}(R) = 0$.

Each of the functions (5) is orthogonal to $\psi_n(R,r)$ and all other functions. If the z axis of the coordinate system is directed along the internuclear vector **R,** only the functions with m = 0 are present in Eq. (5) because $\phi_{nlm}(R) = 0$ for $m \neq 0$.

### 2.2. Dipole matrix elements

Let us calculate the radiation from the "active" state with principal quantum number N when the Rydberg electron undergoes transitions to all final states n with n < N. The matrix elements of $z = r\cos(\theta)$ between the wave functions of "active" states are

$$M_1(N, n, R) = <\psi_n(R,r)| z |\psi_N(R,r)>$$
$$= \sum_{l=0}^{n-1} J_{n/0}(R)[J_{N,l1,0}(R)\frac{(l+1)\cdot(r)_{N,l+1}^{n,l}}{\sqrt{(2l+1)(2l+3)}} \quad (6)$$
$$+ J_{N,l1,0}(R)\frac{l\cdot(r)_{N,l-1}^{n,l}}{\sqrt{(2l+1)(2l-1)}}]$$

where the radial matrix element is defined as

$$(r)_{N,l-1}^{n,l} = \int_0^\infty f_{n,l}(r)f_{N,l-1}(r)r^3\,dr; \quad (7)$$

and $f_{nl}(r)$ is the Coulomb radial spherical function. This matrix element has been calculated by Gordon [12]

$$(r)_{N,l-1}^{n,l} = \frac{(-1)^{n-l}}{4Z(2l-1)!}\cdot\sqrt{\frac{(N+l)!(n+l-1)}{(N-l-1)!(n-l)!}}$$
$$\times \frac{(4nN)^{l+1}(N-n)^{N+n-2l-2}}{(N+n)^{N+n}}$$
$$\times [F(-N+l+1, -n+l+1; 2l; -4nN/(N-n)) - \left(\frac{N-n}{N+n}\right)^2$$
$$\times F(-N+l-1, -n+l+1; 2l; -4nN/(N-n)^2)];$$
$$(8)$$

where F(a, b, c; z) is the hypergeometric function. We use a transformation of these matrix elements to undertake the numerical calculations by employing the relation [5]:

$F(a, b; c; z) = (1 - z)^{-a} F(a, c - b; c; z/(z - 1))$. Eq.(8) can then be written as

$$(r)_{N,l-1}^{n,l} = \frac{(-1)^{n-l}}{4Z(2l-1)!}\cdot\sqrt{\frac{(N+l)!(n+l-1)}{(N-l-1)!(n-l)!}}$$
$$\times \frac{(4nN)^{l+1}(N-n)^{N-n-2}}{(N+n)^{N+n}}$$
$$\times [(\frac{N-n}{N+n})^2 F(-N+l+1, n+l; 2l; 4nN/(N+n)^2)$$
$$- F(-N+l-1, n+l; 2l; 4nN/(N+n)^2)];$$
$$(9)$$

In Eq. (8) the absolute value of the argument of the hypergeometric function is very large: $4nN/(N-n)^2 \approx 4N^2$ when $n \to N-1$. However in Eq. (9), this argument is always smaller than one, and therefore Eq.(9) can be conveniently used for arbitrarily large values of principal quantum number N.

The matrix elements between the initial state wave function $\psi_N$ and the orthogonalized wave function (5) with principal quantum numbers n < N can be calculated in the form

$$M_2(N,n,l,R) = <\psi_{n/0}(R,r)| z |\psi_N(R,r)>$$
$$= J_{N,l+1,0}(R)\frac{(l+1)\cdot(r)_{N,l+1,0}^{nl}}{\sqrt{(2l+3)(2l+1)}} \quad (10)$$
$$+ J_{N,l+1,0}(R)\frac{l\cdot(r)_{N,l-1,0}^{nl}}{\sqrt{(2l+1)(2l-1)}} - J_{n/0}(R)M_1(N,n,R);$$

where the matrix element $M^1(N,n,R)$ is given by Eq. (6).

The radiation of photons polarized along the x and y axes is given by the matrix elements

$$<n, l, m = \pm 1 | x | \psi_N> = <n, l, m = \pm 1 | y | \psi_N>$$
$$= \pm\frac{1}{2}\sqrt{\frac{l(l+1)}{2l+1}}[J_{N,l+1,0}(R)\cdot\frac{(r)_{N,l+1}^{nl}}{\sqrt{2l+3}} \quad (11)$$
$$- J_{N,l+1,0}(R)\cdot\frac{(r)_{N,l-1}^{nl}}{\sqrt{2l-1}}].$$

The sum of the squared moduli of these matrix elements that appear in the total radiation probability is

$$|M_3(N, n, l, R)|^2 = \qquad (12)$$
$$\frac{l(l+1)}{2l+1}\cdot[J_{N,l1,0}(R)\cdot\frac{(r)_{N,l+1}^{nl}}{\sqrt{2l+3}} - J_{N,l1,0}(R)\cdot\frac{(r)_{N,l-1}^{nl}}{\sqrt{2l-1}}]^2$$

The radiative lifetime of the "active" state $\psi_N(R,r)$ is given by the sum of squared moduli of all above matrix elements, i.e.
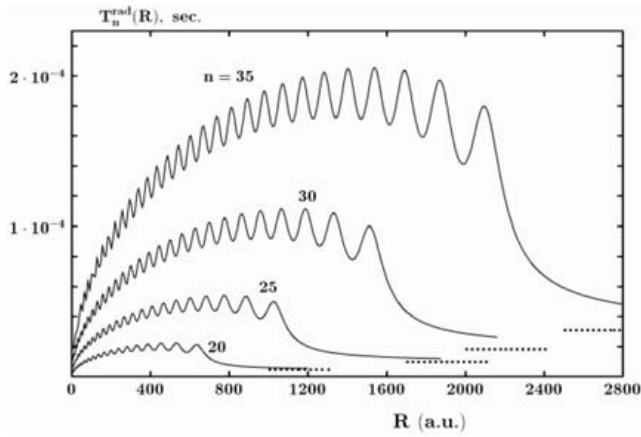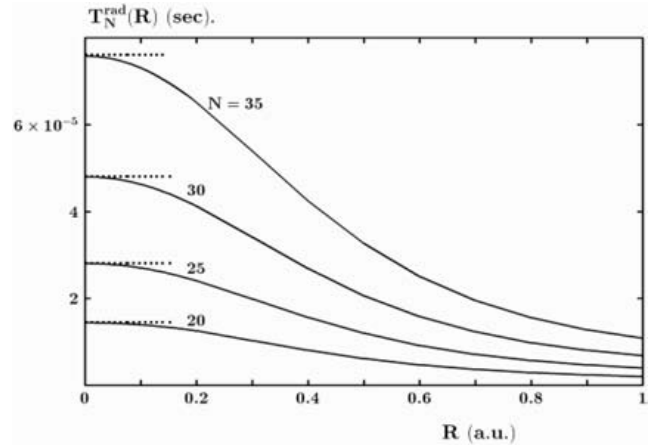
**Figure 1.** Radiative lifetimes of Rydberg states perturbed by a neutral atom as a function of internuclear distance R for principal quantum numbers N = 20, 25, 30, 35 (full lines). Dotted lines are the radiative life times of Stark states with the largest quantum number $n_1$ = N - 1, see Table 1. The wave functions of these states are the limits of the wave functions (3) of "active" states at R $\rightarrow \infty$ .



**Figure 2.** Same as Fig. 1, but for small internuclear distances, R $\rightarrow$ 0. Dotted lines are the radiative lifetimes of spherical S-states (see Table 1) adopted by the wave functions (3) when R $\rightarrow$ 0.

$$S_N(R) = \sum_{n=1}^{N-1} (\Delta E_n^N)^3 \{|M_1(N, n, R)|^2$$
$$+ \sum_{l=0}^{n-1} [|M_2(N, n, l, R)|^2 + |M_3(N, n, l, R)|^2]\}. \qquad (13)$$

## 3.    Results

The radiative lifetimes of high Rydberg states perturbed by a neutral atom and calculated by the above formula are shown in Figs. 1 and 2 as functions of the inter-nuclear distance R. Oscillations occur in the radiative lifetimes (Fig. 1) due to the oscillating functions $J_{nlm}(R)$ (of different frequencies) that are present in matrix elements $M_1(R)$ and $M_2(R)$. For comparison, we list in Table 1 values of the radiative lifetimes of the initial (unperturbed) parabolic and spherical states. These values are shown in Figs. 1 and 2 as dotted lines, and show that the influence of a perturbing atom on the radiative lifetime of a high Rydberg state is significant. At internuclear distances of the order of half the size of the orbit of Rydberg electron, the radiative lifetimes of the Rydberg states with N = 20 – 35 are 3-5 times larger than the lifetimes of the corresponding unperturbed states.

These studies have an obvious relevance in the interpre-tation of the experimental optical observations [13]: a perturbing neutral atom may significantly change the natural linewidth of the radiation from a Rydberg atom. In particular, due to the interaction of the Rydberg atom with a perturbing neutral atom, the linewidth of the radiation acquires a dependence on their mutual distance. Furthermore, the resulting information is important in experimental attempts to detect the so-called trilobite states investigated in Ref. [6, 7].

**Table I.** Radiative lifetimes ($10^{-5}$ sec) of spherical and stark Rydberg states with principal quantum number N

| N | Spherical S-state | Stark states with $n_1$ = N-1, $n_2$ = m = 0 |
|---|---|---|
| 20 | 1.441 | 0.4408 |
| 25 | 2.768 | 0.9498 |
| 30 | 4.738 | 1.789 |
| 35 | 7.478 | 3.066 |

## References

[1]    CHIBISOV, M.I., ERMOLAEV, A.M., BROUILLARD, F., CHERKANI, M., Phys. Rev. Lett., **84** (2000) 451; Zh. Exp. Teor. Phys., **117** (2000) 313 (JETP **90** (2000) 276); J. Phys. B, **34** (2001) 49.

[2]    CHIBISOV, M.I., Zh. Exp. Teor. Phys., **120** (2001) 291 (JETP **93** (2001) 256).

[3]    CHIBISOV, M.I., Uspekhi Fizichesk. Nauk, **172** (2002) 3 (Physics-Uspekhi **45** (2002) 1).

[4]    OMONT, A., J. Physique, **38** (1977) 1343.

[5]    LANDAU, L.D., LIFSHITZ, E.M., Quantum Mechanics. Nonrelativistic Theory, Moscow, "Nauka", 1989 (in Russian).

[6]    CHIBISOV, M.I., KHUSKIVADZE, A.A., FABRIKANT, I.I., J. Phys. B, **35** (2002) L193.

[7]    KHUSKIVADZE, A.A., CHIBISOV, M.I., FABRIKANT, I.I., Phys. Rev. A **66** (2002) 042709.

[8]     BETHE, H.A., SALPETER, E.E., Quantum Mechanics of One- and Two-Electron Atoms, Springer-Verlag, Berlin-Heidelberg, 1957.

[9]     LEBEDEV, V.S., BEIGMAN, I.L., Physics of Highly Excited Atoms and Ions, Springer-Verlag, Berlin-Heidelberg, 1998.

[10]    KERESELIDZE, T.M., CHIBISOV, M.I., Zh. Exp. Teor. Fiz. **68** (1975) 12 (JETP **41** (1975) 6).

[11]    DEMKOV, YU.N., OSTROVSKI, V.N., Zero Range Potential Approach in Atomic Physics, Leningrad State University Press, Leningrad, 1975.

[12]    GORDON, W., Ann. Phys. **2**(1929)1031.

[13]    SOBELMAN, I.I., Introduction to the Theory of Atomic Spectra, GIFML, Moscow, 1963 (in Russian).